University of Calgary

PRISM Repository **https://prism.ucalgary.ca**

The Vault Open Theses and Dissertations

2014-06-05

Tracking Thermal and Structural Properties of Melt-Freeze Crusts in the Seasonal Snowpack

Smith, Michael Andrew

Smith, M. A. (2014). Tracking Thermal and Structural Properties of Melt-Freeze Crusts in the Seasonal Snowpack (Doctoral thesis, University of Calgary, Calgary, Canada). Retrieved from https://prism.ucalgary.ca. doi:10.11575/PRISM/28497

http://hdl.handle.net/11023/1566

Downloaded from PRISM Repository, University of Calgary

UNIVERSITY OF CALGARY

Tracking Thermal and Structural Properties of Melt-Freeze Crusts in the Seasonal Snowpack

by

Michael Andrew Smith

A DISSERTATION

SUBMITTED TO THE FACULTY OF GRADUATE STUDIES

IN PARTIAL FULFILLMENT OF THE REQUIREMENTS FOR THE

DEGREE OF DOCTOR OF PHILOSOPHY

DEPARTMENT OF CIVIL ENGINEERING

CALGARY, ALBERTA

May, 2014

© Michael Andrew Smith 2014

Abstract

Persistent weak layers present a particular challenge for avalanche forecasters due to their long lifetime and the difficulty of obtaining observations once they are deeply buried. Melt-freeze crusts are one type of persistent weak layer that is often associated with deep slab avalanches during late winter or spring. This study seeks to improve the understanding of the thermal and structural properties of melt-freeze crusts by tracking them from formation through to isothermal conditions in the spring.

Specific Surface Area (SSA) was tracked weekly using near-infrared digital photography for nine natural crusts and four cold lab crusts during the winters of 2008-09 and 2009-10. Image analysis techniques were adapted from existing methods in order to track the mean SSA for specific structures within crusts, as well as vertical profiles of SSA across crust boundaries. Few temporal trends were identified even in the presence of strong diurnal slope normal temperature gradients, but the ratio of mean SSA between crusts and adjacent layers did reveal relative changes in the structure.

The thermal conductivity was tracked for six natural and five cold lab crusts during the winter of 2009-10 using a heated needle probe. Thermal conductivity of two cold lab crusts increased during freezing and subsequently decreased in the presence of strong vertical temperature gradients, while that of natural crusts had no discernible trends under weak temperature gradients. Trends of increasing thermal conductivity in adjacent layers were well correlated with increasing density as in previous studies but with a positive offset that may be attributable to the warmer snow temperatures in this study relative to past studies.

The SNOWPACK model was used to model the formation and evolution of spatially uniform crusts at a flat study plot as well as on a virtual slope. Persistent model cold temperature biases were found on the virtual slope, which resulted in delays in settling and densification relative to observations. A warm model bias was found for the flat simulation,

and settling and layer water content exceeded what was observed. Both biases were likely related to meteorological inputs.

Acknowledgements

First and foremost I would like to thank my supervisor Bruce Jamieson, whose timely advice and seemingly endless patience have allowed me to complete this dissertation.

My fellow graduate students at ASARC kept the mood light after long days in the field and put in long, cold hours in the pit while gathering the data for study: Thomas Exner, Katherine Johnston, Cam Ross, Cora Shea and Dave Tracz. The dry humour and sage advice of Post-Doc Sascha Bellaire helped me steer through the final season of field work, while ASARC technicians Catherine Brown, Ali Haeri and Mark Kolasinski were always helpful in gathering data and refining field methods.

The staff of the Avalanche Control Section at Glacier National Park, specifically forecasters Bruce McMahon and Jeff Goodrich, provided invaluable logistical support and guidance during my three winters of work. Without their assistance this study could not have been completed. Mike Wiegele and his staff at Mike Wiegele heli-skiing have been long-time supporters of snow science and of ASARC in particular. The snow safety staff at Kicking Horse Mountain Resort were unfailingly accommodating in providing an alternate venue when conditions did not cooperate at Rogers Pass.

I would like to thank Charles Fierz for his help in getting SNOWPACK up and running, and for helping me to understand the guts of the model. John Kelly and Ilya Storm of the Canadian Avalanche Centre were also instrumental in pushing me toward using the SNOWPACK model as part of my research.

For help with seemingly endless edits and revisions I must once again thank Bruce Jamieson as well as ASARC Post-Doc Michael Schirmer for his valuable insight late in the writing process.

I must also thank the long list of avalanche professionals and researchers who provided ideas, insight and inspiration. You're too numerous to list, but I hope to repay the favor as

I move forward. Finally I'd like to thank my family and friends who never gave up on me even when completion seemed years away.

Table of Contents

List of Tables

List of Figures and Illustrations

Chapter 1

Introduction

Snow is an intriguing material to study: Unlike many materials, it exists within several degrees (or at most several tens of degrees) of its melting point; Unlike metamorphic rock, snow may undergo significant metamorphism over the course of several hours, often to the chagrin of avalanche forecasters. According to data published by the Canadian Avalanche Centre (CAA, 2014) and drawn from Jamieson et al. (2010) avalanches in Canada were responsible for an average of 14 fatalities per year from 1996 -2007. This represents an increase of 4 fatalities per year over the previous 10-year period (Jamieson and Geldsetzer, 1996). Several winters since then have exceeded the average with the majority of victims comprised of winter recreationists.

Numerous regional or national public avalanche forecast centres provide public avalanche bulletins in hopes of educating users and reducing the number of incidents. Avalanche forecasters typically draw on professional experience to synthesize information from avalanche professionals and, increasingly, public observations. Class I data, the "stability factors" (McClung and Schaerer, 2006) include the most direct signs of snowpack stability such as recent avalanche activity and stability or explosives tests. Class II data, the "snowpack factors", include past avalanche observations and information from snow profiles (see Section 1.1. Class III data are the "meteorological factors" such as recent precipitation, wind and temperature.

In Canada and the United States the avalanche danger is communicated via the North American Public Avalanche Danger Scale. There are five possible levels of danger, from "Low" to "Extreme" and within each level the forecaster communicates travel advice, the size and distribution of avalanches, and the likelihood of avalanches. The likelihood is further

divided into natural and human-triggered avalanches.

The largest and most destructive avalanches are slab avalanches, wherein a failure within the snowpack releases an overlying cohesive slab of snow. Reduced to the most simple factors, stress applied to a given layer exceeds its strength. From the standpoint of forecasting, the likelihood of an avalanche may be reduced to two factors: The probability of a localized failure in a particular layer, and the probability that the failure will propagate (the propagation propensity, Gauthier and Jamieson (2008)) far enough for the overlying slab to fail. Triggering may occur through heavy snowfall, dynamic loading by a skier or snowmobiler, explosives or warming, leading to increased strain rates within weak layers. Propagation propensity is a property of both the failure layer and the overlying slab, where energy is released through shear failure and weak layer collapse (Heierli and Zaiser, 2008) and if the energy released exceeds the fracture toughness of the failure layer, the failure will continue to propagate.

One particular challenge for all avalanche professionals is the persistent weak layer (PWL). As its name suggests this is a weakness in the snowpack that is buried and persists for weeks or even months. Oftentimes such layers will become deeply buried and unreactive for long periods before suddenly becoming reactive once again. A PWL is often difficult to observe due to its depth in the snowpack and forecasters are left with little information or warning to when it may release slab avalanches.

Melt-freeze crusts, especially those that form early in the winter, are a frequent source of concern (e.g. Smith et al., 2008) that may lie dormant throughout the winter before failing as the snowpack weakens, or as it is stressed by large dynamic loads such as cornice failures. Crusts are unique from other snow grain types in their microstructure, persistence and ability to resist compaction. This may contribute to the formation of weak facet layers while freezing, as a strong temperature gradient is maintained between the wetted layer and a new snow layer above (e.g. Jamieson and Fierz, 2004) and also once buried due to their

relatively high thermal conductivity and lower vapour permeability (Jamieson, 2006). Thick or stiff crusts may also act as a bed surface for avalanches, where shear stress is concentrated (Habermann et al., 2008). Numerous studies have documented the formation and role of melt-freeze crusts in avalanches (Buhler, 2013; Conlan and Jamieson, 2012; Jamieson and Langevin, 2004; Jamieson, 2004a,b, 2006) and initial efforts have been made to understand their formation and evolution through field and cold lab studies as well as modeling (e.g. Jamieson and Fierz, 2004; Smith et al., 2008).

The goal of this study is to better understand the structure and temporal evolution of melt-freeze crusts in the seasonal snowpack. The remainder of this chapter will provide a brief introduction to the science of snow including the deposition, layering and metamorphism of the seasonal snowpack. The research goals and methods will be outlined and the study area introduced. The remaining chapters will examine in detail the various aspects of the study.

1.1 The Seasonal Snowpack

In North America the seasonal snowpack in mountainous regions is typically in place from October through April or May. During this time the snow may go through several cycles of accumulation, ablation, melting and re-freezing. Most precipitation particles have a dendritic form which is quickly broken down through the action of wind, sun, compaction and metamorphic processes, leading to the formation of a layered snowpack consisting of well-bonded rounded grains, angular faceted grains, stiff melt-freeze forms and feathery surface hoar. Snowpack structure may also be highly spatially variable due to local variations in weather, topography and vegetation.

Characterization of the seasonal snowpack is usually done via snow profile (Figure 1.1 and Table 1.1) whereby a field worker exposes a pit wall of the snowpack. Layers are defined by grain type, density, crystal form and hand hardness (CAA, 2007), and may also depend on whether the objective is stability evaluation or research, where even small variations may be

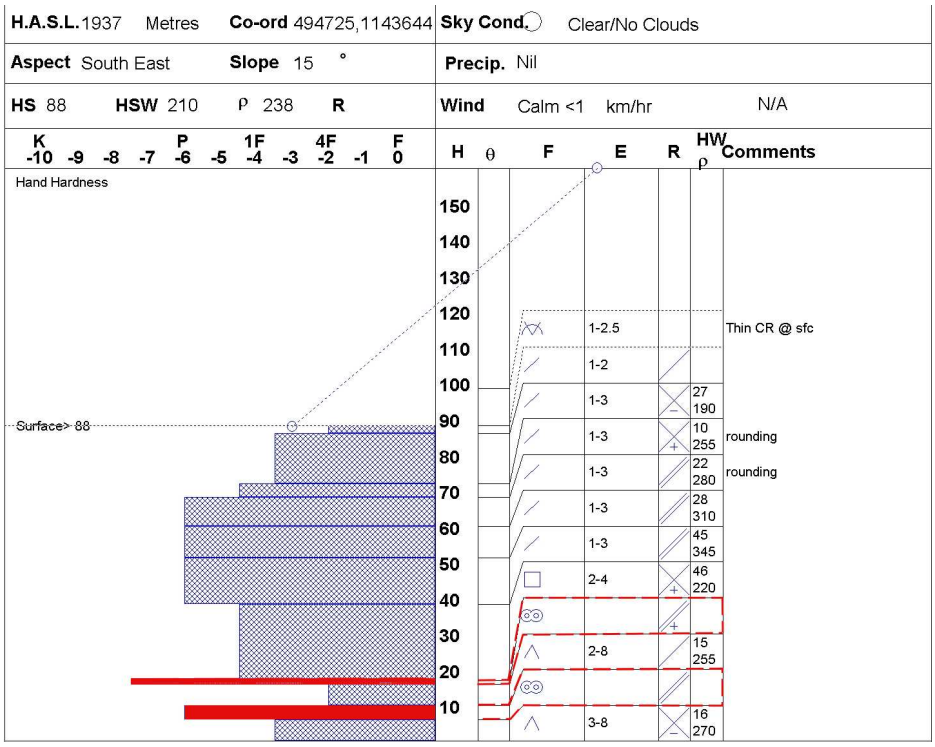

Figure 1.1: *An example of a snow profile, plotted using the commercial program SNOWPRO. Crusts are highlighted in red and denoted by the "bicycle chain" symbol. Layer properties including depth (H), moisture (θ), grain type (F) and extent (E), resistance (R) and layer density (ρ) are given in tabular form on the right side of the profile and resistance and temperature are plotted graphically on the left. See Table 1.1 for detail on properties recorded during a snow profile.*

of interest. Potential weak layers way be identified by the presence of certain grain types, by sharp transitions in hardness which would tend to concentrate stress, or by testing a layer's propensity for failure initiation or propagation. Deep layers in particular may be tested using the Deep Tap Test (CAA, 2007) or Propagation Saw Test (Gauthier and Jamieson, 2008).

Because snow exists so close to its melting point, transitions from one grain type to another and attendant changes in snowpack stability may occur over the course of several hours or less. Metamorphism depends on a number of factors including snow density, crystal size and size distribution, crystal type, temperature and slope-normal temperature gradient (e.g. Sokratov, 2001) but is primarily a function of heat and water vapour transport. Heat transport through snow is accomplished through conduction, convection, release of latent

Table 1.1: *Properties recorded in a snow profile. Geographical location, slope angle and aspect, present weather and total snow depth are also recorded.*

Property	Abbrev.	Units	Notes
Layer depth	H	cm	Measured from ground for full profiles and from snow surface for partial (test) profiles
Temperature	T	°C	Measured at surface and each 10 cm thereafter and sometimes at layer boundaries
Layer density	ρ	kg m^{-3}	
Grain form	F	$\sim$	Symbols are detailed in Fierz et al. (2009)
Grain size (Extent)	E	mm	Often given as a range
Layer resistance	R	$\sim$	Varies from fist (softest) to ice (hardest). Also represented by horizontal bar graphs on the profile.
Liquid water content	θ	$\sim$	5 levels, plotted on snow profiles using vertical lines: from "dry" (no lines) to "slush" (4 lines).
Layer comments	$\sim$	$\sim$	May include date when layer was buried, which is used to track PWLs

heat by freezing water and radiation, though solar radiation is only significant close to the snow surface (Bakermans and Jamieson, 2009). Greene (2007) provides a brief review of studies regarding the importance of convection in the snowpack, most of which are in agreement that it is important only in porous snow in the presence of a strong temperature gradient. LaChapelle (1960) noted that the coefficient of diffusion of water vapour in snow was four to five times that of vapour in air. This emphasized the importance of what is now referred to as the 'hand to hand' process of mass transport between snow crystals. In field studies, the slope-normal temperature gradient is usually used as a proxy for heat and vapour flux. The measured slope-normal temperature gradient is sometimes referred to as the "bulk" temperature gradient to differentiate it from gradients that may occur on scales too small to measure with thermistors or thermocouples. Hereafter, the terms *slope-normal temperature gradient*,*vertical temperature gradient* and *temperature gradient* are used interchangeably.

Snowpack metamorphism is often classed as either Temperature Gradient or Equilibrium metamorphism based on the bulk slope-normal temperature gradient:

Temperature Gradient (TG) Metamorphism is assumed to occur when the slope-normal temperature gradient exceeds 10 $^{\circ}$C m^{-1}. This is a frequent occurrence near the surface of the snowpack due to relatively rapid fluctuations in the air temperature, and may occur throughout the full depth of shallow snowpacks. In this case, vapour transport through the snowpack arises from the bulk temperature gradient. The tendency is toward the formation of faceted crystals with flat faces, sharp edges and poor intragranular bonding. In the extreme case, very large edged or cupped crystals known as 'depth hoar' may result. Layers comprised of large facets or depth hoar are typically poorly bonded and weak and thus represent a potential failure layer for avalanches.

Equilibrium (EQ) metamorphism is assumed when the bulk temperature gradient is less than 10 $^{\circ}$C m^{-1}. In this case, vapour transfer is driven by a vapour pressure gradient arising from the differences in grain curvature within the snowpack, and not the bulk temperature

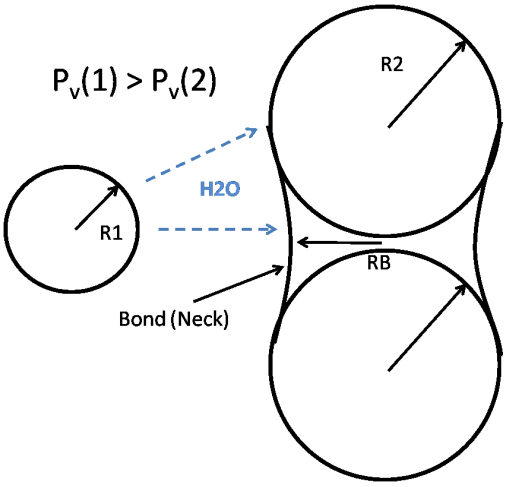

Figure 1.2: *Example of vapour transfer under low temperature gradients. Adapted from various figures in McClung and Schaerer (2006). The smaller grain with radius R1 will have a larger equilibrium vapour pressure P_v1 than the larger grain with radius R2. The gradient in vapour pressure will cause vapour transfer from the smaller grain to the larger grain. The same process will lead to grain growth at the neck between two grains.*

gradient (Colbeck, 1980; Flin et al., 2003). Small grains with a smaller radius of curvature will have a higher vapour pressure at the ice-air interface than will larger grains. This results in a transfer of mass from small or highly dendritic grains to large grains or necks between grains, as illustrated in Figure 1.2. This is traditionally assumed to be the dominant mechanism in the growth of rounded, well-bonded layers. A notable exception is when grains already have flat faces, which have a large radius of curvature: Although the edges, with a small radius of curvature, will round, the basic form will persist at low temperature gradients (Brown et al., 2001). These forms will be slower to round and form bonds with adjacent crystals, and indeed layers of faceted crystals tend to persist long after the strong temperature gradient disappears (Jamieson and Langevin, 2004). Dominé et al. (2003) and Legagneux et al. (2003) observed the formation of flat faces and edges during experiments in isothermal conditions. They hypothesize that these are due to structural dislocations within the snow crystal.

The terms "crust" or "melt-freeze crust" are used colloquially to refer to any layer that has been wetted and re-frozen. Crusts may form at any point during the winter through solar radiation, warm air temperature, rain, freezing rain or free water percolating through the

snowpack. Due to the variety of mechanisms of formation thickness varies from a few tenths of a millimetre to several centimetres and structure may also be dependent on elevation, aspect and slope angle. Crusts affect the seasonal snowpack in several ways: They may retard the flow of water or water vapour through snowpack and may also influence the local (grain-scale) temperature gradient due to their higher thermal conductivity; a thick crust may "bridge" weak layers below it, but stress may also concentrate at the upper boundary. Habermann et al. (2008) modeled shear stress concentration at crusts and found that thin crusts may concentrate stress in underlying weak layers, while the greatest stress concentration occurred when the crust was overlain by a weak layer and soft slab. Jamieson and Langevin (2004) summarizes the link between crusts and avalanches in the Columbia Mountains.

The influence of crusts on metamorphism of adjacent layers in the snowpack has been widely studied; Colbeck (1991) hypothesized that the higher thermal conductivity and lower permeability of a generic dense layer may cause faceting in the layer below. This was tested by Greene (2007), who found that a thin ice layer and a strong temperature gradient led to the growth of faceted crystals below the ice lens along with rounding and the loss of bonds in the layer above. Jamieson and van Herwijnen (2002) examined the formation of facets in a dry layer underlain by wetted snow and observed strong temperature gradients traditionally associated with TG metamorphism as well as the formation of facets soon after burial. Jamieson and Fierz (2004) modeled the experiments using the SNOWPACK model and found that it was able to simulate the observed temperature profile and metamorphism.

1.2 Research Goals

The role of melt-freeze crusts as potential avalanche bed surfaces and areas of shear stress concentration has been well studied and documented, and their role in the development of faceted layers at their upper boundaries during initial freezing is also well-understood. There have, however, been very few long-term systematic observations of metamorphism within

crusts after burial. Jamieson (2006) reported on observations of faceting within crusts in the absence of strong bulk temperature gradients. Buhler (2013) tracked structural properties of several crusts and reported one case where an apparent loss of hardness and increase in density occurred over time. With the exception of Buhler (2013), available data lack either regular observations at a study site or the precision of measurements that may be necessary to identify small-scale changes in crust microstructure.

Snowpack models are currently used in both research and, to a limited extent, in operational avalanche forecasting. They provide a valuable way of studying the formation and evolution of the seasonal snowpack, but still rely in part on empirical formulae to fill gaps in existing knowledge. In the case of melt-freeze forms, such formulae are often derived from small or mixed data sets. SNOWPACK (Lehning et al., 2002a) is one such model that remains in active development, and validation of the model using new observations provides an avenue for future improvements in the model.

The goals of this study are to:

- Track thermal and microstructural properties of melt-freeze crusts at fixed study sites from formation through to the onset of melt in the spring, as well as in a cold lab
- Employ and evaluate new techniques to observe properties and temporal evolution in melt-freeze crusts
- Evaluate the ability of a snowpack model to replicate formation and observed metamorphism

The data collected during this study will add to the body of knowledge concerning snowpack metamorphism, and help to fill a gap in knowledge regarding structure and temporal evolution of melt-freeze crusts. Measurements of thermal conductivity and SSA (introduced in Section 1.3) have not previously been used to track changes in buried melt-freeze crusts

and will complement existing data. Modeling of crusts tracked during this study will provide the opportunity to validate and improve existing empirical equations governing the evolution of crust properties.

1.3 Research Methods

The data-gathering portion of this study took place in Glacier National Park, in the Columbia Mountains of British Columbia, Canada, during three winters from 2007-08 through 2009-10. Data were gathered from from both natural crusts in the field, and from natural crusts brought into a cold lab. A total of nine natural crusts were tracked from formation until the end of the field season in mid-April. A tenth crust was tracked during the winter of 2007-08 (Smith et al., 2008) but due to spatial variability and an absence of measurements for the first month after formation it is not included in this study.

The study areas were in permanent public closures at Mount Fidelity and Rogers Pass, as well as one crust in Beaver Valley at the East end of Glacier National Park. More detail on the study areas is provided in Appendix A.

Natural crust sites were visited weekly and a test profile (CAA, 2007) was recorded at each visit. Thermistors or thermocouples, calibrated annually in ice baths, were placed above and below crusts shortly after burial. This follows reports from experienced field workers (e.g. Jamieson, 2006) that some crusts lose strength over time even under low temperature gradients. A typical arrangement of thermistors and thermocouples is shown in Figure 1.3. Digital photographs of the snow profile and disaggregated crystals from the crust were also recorded at each site visit.

Due to the destructive nature of all methods used in this study, snow pits were excavated in a linear manner starting from the edge of a flat study plot, or low on the slope at inclined study plots with subsequent observations proceeding uphill. Each new snow pit was excavated a minimum of 1.5 m back from the previous pit to eliminate the effects of a horizontal

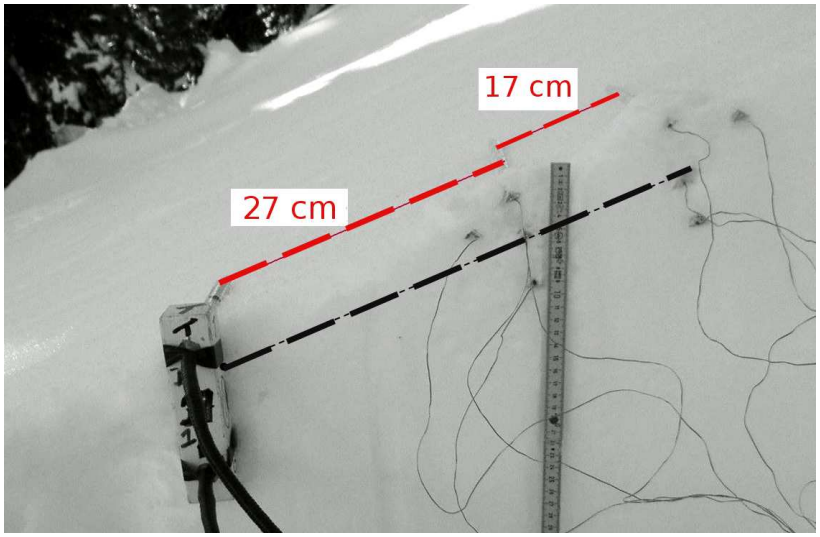

Figure 1.3: *Example of thermistor (left) and thermocouple (right) placement around a melt-freeze crust. The bottom of the crust is indicated by the black dashed line while the snow snow surface is indicated by a dashed red line. The along-slope distance between thermistors and thermocouples is also indicated.*

temperature gradient. This technique is widely used in avalanche studies when a study area must be used for an entire winter season. For non-destructive sampling or single-day studies of spatial variability Schweizer et al. (2008) summarizes a number of spatial sampling techniques that are more statistically rigorous than methods employed in this study.

Four natural crusts were brought into a cold lab and subjected to varying temperature gradients for periods ranging from twelve hours to four days during spring 2010. Samples were placed in an insulated box with an open top. The observation wall was cut back for each observation and re-covered with insulation once observations were complete. Digital photographs of the observation wall as well as disaggregated crystals were collected at the time of each observation.

Initial research methods included shear frames (Jamieson and Johnston, 2001), compression tests (CAA, 2007) and propagation saw tests (Gauthier and Jamieson, 2008; Ross, 2010) to monitor development of weak layers above, below or within crusts. Valid shear frame data proved to very difficult to obtain on the rough upper boundaries of most crusts while PST and CT results were largely invalid for the same reasons. These tests were discontinued

during the winter of 2009-10 when all study sites but one were flat, and also lacked the space required to conduct the tests. A thermal infrared camera was used to track snow temperature and gradients in cold lab experiments (e.g. Buhler, 2013) but the data were only used qualitatively due to the numerous sources of error and uncertainty (Schirmer and Jamieson, 2014).

Quantifying crust properties using traditional methods can be difficult: "Grain size" in traditional field observations is not well-defined due to strong bonding and poor definition of grain boundaries in most crusts, and density can be difficult to measure in a brittle crust, which will often fracture when attempting to extract a sample of known volume for density calculation. Unlike other grain types melt-freeze crusts may form by a number of methods including solar radiation, warm air temperatures, rain, freezing rain or percolation of meltwater through the snowpack. Crusts formed by different mechanisms tend to have varying properties of thickness, grain size, bond size and spatial variability. Although revised recording standards (Fierz et al., 2009) do classify crusts according to the mechanism of formation, older data do not follow these conventions. For this reason two relatively new observation techniques were used for the present study.

Beginning in winter 2008-09, digital photography was supplemented by near-infrared photography (NIR). Matzl and Schneebeli (2006) developed a method to derive the specific surface area (SSA) from the near-infrared reflectivity captured using a modified digital camera, with Spectralon diffuse reflectance standards (Labsphere, 2013) used to provide a calibrated reference near infrared (NIR) reflectivity. The SSA of snow can be defined as the ratio of surface area to volume, and evolution of the SSA can be used as a proxy for metamorphism that may not be evident from traditional snowpack observations and can also provide a more objective measure of snowpack characteristics.

A number of studies (Legagneux et al., 2003; Dominé et al., 2007) have found that SSA decreases over time, especially for new snow, and Dominé et al. (2009) cites one case where

the SSA of a melt-freeze crust increased over time in the presence of a strong temperature gradient. In addition to the method of Matzl and Schneebeli (2006), the SSA of snow may be measured using methane absorption (Legagneux et al., 2002), microtomography (Matzl and Schneebeli, 2006) or other instruments making use of NIR techniques (Picard et al., 2009). NIR methods and results are presented in Chapter 3.

Just as the temperature gradient is an important indicator of the type of metamorphism that can be expected in the snowpack, the thermal conductivity determines how the heat flows through the snowpack. The thermal conductivity may be defined as a proportionality constant that relates the temperature gradient to the heat flow, and is described in the 1D Fourier equation:

$$q = -k\frac{dT}{dz} \tag{1.1}$$

where q is the rate of energy transfer, k is the thermal conductivity and dT/dz is a temperature gradient. For the winter of 2009-10 a TP02 thermal conductivity probe (Hukseflux, 2003) was used to track the thermal conductivity of crusts as well as the layers above and below. Since the total heat flow is dependent on the ice lattice, water vapour and air within the snowpack, what is actually measured is the effective thermal conductivity k_{eff}. Much like the temperature gradient, the convention of "bulk" thermal conductivity is used to distinguish the sample size measured by the probe (approximately 10 cm in length by several millimetres in diameter) from scales used in modeling or microtomography studies. The thermal conductivity of melt-freeze crusts has been examined in past studies (e.g. Sturm et al., 1997) but sample sizes tend to be small and efforts at developing empirical or prognostic equations based on measurable parameters such as age or density have been unsuccessful. Thermal conductivity of crusts from 2009-10 is examined in Chapter 2.

The Swiss SNOWPACK model (Fierz and Lehning, 2001; Lehning et al., 2002a,b) is a physically-based single-column (1-dimensional) snowpack model that simulates accumulation

and metamorphism of snow. Simulations may be driven by measured or modeled (e.g. Bellaire et al., 2011) meteorological data and may be initialized either while the ground is bare or using an observed snow profile. Snow erosion and transport are included through the option to simulate slopes and the model has been used operationally or tested by avalanche forecasters in Switzerland, Canada and Japan (Hirashima et al., 2008). Due to its single-column nature it is not suitable for simulating layers that are spatially variable on the scale of a single slope (Smith et al., 2008). SNOWPACK version 3.2, released in February 2014, was used to simulate natural crusts in the Mount Fidelity permanent closure area of Glacier National Park. Output data were compared to observations of layer depth, hardness, temperature, SSA and, for winter 2009-10, thermal conductivity measurements. The model, methods and results are given in Chapter 4.

Field observations were collected over the course of three winters at fixed study plots in Glacier National Park, in the Columbia Mountains of British Columbia, Canada. Methods were specified by the author and were carried out by the author and other members of the The Applied Snow and Avalanche Research group at the University of Calgary (ASARC) research team, with the author present at all but one site visit. Methods such as the snow profile conformed to standards specified in CAA (2007) with more detail within and around target crusts. NIR photography was adapted from methods described by Matzl and Schneebeli (2006), and thermal conductivity measurements were done in accordance with manufacturer's recommendations (Hukseflux, 2003) modified slightly after testing to determine appropriate methods and power sources for use in the field. Methods for cold lab experiments were adapted from those described in Jamieson and van Herwijnen (2002), with varied measurement intervals and experiment lengths to account for the limited number of observations that could be taken from the insulated sample box.

NIR photographs were examined weekly to ensure that the camera equipment was functioning properly, as well as to check for contamination of the Spectralon standards. Thermal

conductivity data were processed weekly and checked for consistency in heating power of the TP02 and validity of sample data. All post-season processing and analysis were done by the author.

SNOWPACK simulations were designed and run by the author following recommendations by the model's developers as well as by other members of the ASARC research team. Input meteorological data were quality-controlled from ASARC and Parks Canada instrumentation at Mount Fidelity study area. In the cases where simulations were not started with bare ground, input snow files were built by the author using ASARC and Parks Canada profiles as sources. Snow profile data used for validation of model output were recorded by ASARC and Parks Canada. All analysis of model output was conducted by the author.

Results from Chapters 2-4 are synthesized in Chapter 5 and recommendations for future research are given in Chapter 6. A glossary is included in Appendix B as an easy reference for some terms used in this study.

Chapter 2

Thermal Conductivity

In this chapter the property of thermal conductivity is introduced along with how it may be used to describe the structure of a snow sample. For the winter of 2009-2010 a heated needle thermal conductivity probe was used to monitor changes in six natural crusts and five crusts in the cold lab. It was also used to measure the spatial variability of thermal conductivity at a crust site from the winter of 2008-09.

Students in professional avalanche courses in Canada are introduced to a document called "Observational Guidelines and Recording Standards", or OGRS for short (CAA, 2007). OGRS describes in detail procedures for collecting and recording snowpack observations. It is well written, succinct and extremely useful for communication observations amongst the hundreds of avalanche professionals in Canada. Unfortunately there is no such document for snow scientists who have long realized that describing the texture of snow, should they be lucky enough to find a perfectly homogeneous layer, is exceedingly difficult when the goal is to illuminate the relationships between structure and physical properties and processes.

The point of the preceding paragraph is to introduce the difficulty of describing snowpack structure precisely, accurately and consistently. This becomes even more difficult when attempting to quantify changes over time in the field and with multiple observers. At present thermal conductivity is used exclusively for research, and not operational avalanche forecasting purposes. Chapter 3 describes the use of near-infrared photography to objectively describe the structure and spatial variation of the specific surface area of layers exposed on a pit wall.

Overall these measurements were found to be quick and easy to conduct in both field and lab-based studies. Some problems with free water and melting of samples were encountered

when the snowpack temperature was close to 0 °C and in layers with large icy inclusions.

2.1 Non-steady-state thermal conductivity theory

Thermal conductivity has long been recognized as an important physical parameter of the seasonal snow as it directly influences changes in crystal habit, size and bonding and thus affects everything from snowpack stability to heat exchange within climate models (e.g. Cook et al., 2008). Thermal conductivity is most simply described by the 1D Fourier equation,

$$q = -k\frac{dT}{dz} \tag{2.1}$$

where k is the thermal conductivity. Put into words, the thermal conductivity is a proportionality constant that relates a gradient (in this case the vertical temperature gradient) to the heat flow. The vertical temperature gradient is used here as it is traditionally measured by avalanche practitioners and it is usually much stronger than the gradient in the horizontal directions. The convention used in this paper is that negative gradients mean colder temperatures toward the snow's surface. For scales of 10 cm to 1 m Equation 2.1 is probably a reasonable approximation to the bulk heat transport, but at the polycrystalline or grain scale things are not so simple due to the unequal distribution of pore space and effects of thermal pathways (tortuosity) through the ice lattice. To further complicate the matter, only in the thermal conductivity due to the ice lattice (k_{latt}) or perhaps due to the water vapour (k_{vap}) may be of interest. In practice the two often cannot be measured sseparately and instead the *effective* thermal conductivity, k_{eff} is measured. A semantic distinction must be adopted here to avoid confusion: Unless otherwise specified, the terms *thermal conductivity*, *bulk thermal conductivity* and *effective thermal conductivity* will be used synonymously throughout this text. 'Bulk' is used here to emphasize that samples are taken at the macro scale, on the order of 10 centimetres. A number of studies introduced in this chapter discuss thermal conductivity on the micro-scale, that is on the scale of microns

to millimetres. This distinction should further illustrate that thermal conductivity samples are a complex function of the structure and bonding of the ice lattice, the temperature of all three phases of water (if present), vapour pressure and time.

Sturm et al. (1997) divides thermal measurement conductivity techniques into 3 classes: Fourier-type, steady-state and transient-flow, or non-steady-state (NSS). Fourier-type analyses measure the thermal diffusivity and then determine the thermal conductivity through monitoring of the phase shift of temperatures at different points throughout the sample period. In this case the thermal diffusivity is the ratio of the thermal conductivity to the density times the specific heat capacity.

Steady state techniques apply heat across a sample, but require that it come into thermal equilibrium before a measurement is made. The guarded hot plate (e.g. Riche and Schneebeli, 2010) is an example of a steady state technique. Although accurate, it is cumbersome for field use.

NSS techniques apply a temperature gradient to a sample but do not require thermal equilibrium. The advantage of these techniques is the time and equipment required are reduced compared to steady state techniques. The most common technique involves the use of a heating wire which is treated as a perfect line heat source. Blackwell (1956) introduced an equation for the relative error in making such an assumption and found that a solid heated needle with a length/diameter ratio of 30 would give a maximum error of about 0.12%.

NSS techniques may be further classified into short-time (Britsow et al., 1994) and long time approximations to the analytical solution. In the short-time case the contact resistance between the probe and medium must be known. Riche and Schneebeli (2010) found that contact resistance was strongly affected by the insertion of the needle probe and resulted in thermal conductivities of 2-3 times less than those measured using a guarded hot plate apparatus. In the long-time case after a certain transient period the rate of temperature increase becomes constant and no longer depends on the probe's thermal properties and

the contact resistance. In this case the thermal conductivity (λ) may be found using the equation:

$$\lambda = \frac{Q}{4\pi\Delta T} ln \left(\frac{t_2}{t_1}\right) \tag{2.2}$$

where:

Q = heating power in W/m

t_1, t_2 = time [s] between end of the transient period and end of the measurement

Δ T = change in sample temperature [°C] between t_1 and t_2

Although the relative error as found by Blackwell (1956) may be small, the measurement is still affected by the stability of the power source, the accuracy of the instrument, the thermal equilibrium of the sample and, in the case of snow, melting during the measurement and unintended movement of the probe in low density snow. Sturm et al. (1997) noted that an offset in thermal conductivity between their new dataset and a grouped historical dataset was likely due at least in part to differences in the snowpack temperature.

Under certain conditions convection may also contribute to the measured effective thermal conductivity. Sturm and Johnson (1991) found that natural convection is relatively common in permeable shallow subarctic snowpacks which are often subjected to strong vertical temperature gradients. They also found that convection was potentially important even when the Rayleigh Number was less than the Critical Rayleigh Number that had been used in past studies to diagnose the presence or absence of convection (e.g. Brun and Touvier, 1987). The authors note that both high permeability and high temperature gradient are likely necessary conditions for measurable convection to take place.

2.2 Past Measurements

Studies dating to at least 1886 (Sturm et al., 1997) have attempted to measure the thermal conductivity of snow. The techniques and accuracy are varied but in general most efforts prior to 1950 employed some form of Fourier analysis to derive the thermal conductivity of a bulk sample. In recent years advances in instrumentation have simplified the task of collecting thermal conductivity measurements in the field, with most recent field studies making use of heated needle probes.

Sturm et al. (1997) summarize 26 studies conducted between 1886 and 1991 in what remains the definitive compilation of snow thermal conductivity data. Mean values in their data set ranged from 0.131 W $m^{-1}K^{-1}$ for samples with a mean density of 222 Kgm^{-3} to 0.810 W $m^{-1}K^{-1}$ for samples with a mean density 496 Kgm^{-3}. They note that although many studies have published relationships between density and thermal conductivity, the combined historical dataset shows no such relationship. Furthermore, the relationship between temperature and thermal conductivity was generally ignored in most studies. They and others (Arons, 1994) also emphasize the temperature dependence of the effective thermal conductivity of snow which, at least according to theory, becomes pronounced between -20 $^{\circ}C$ to 0 $^{\circ}C$.

The same paper introduced a new set of measurements which added to the the authors' previous work (see Sturm and Johnson, 1992). All thermal conductivity data were collected using an instrument similar to that described in Section 2.4. This is the first dataset where samples are described by their International Classification for Seasonal Snow on the Ground (Colbeck et al., 1992; Fierz et al., 2009), allowing a more direct comparison with the crusts which are the target of the present study: Samples of refrozen grains had thermal conductivities of 0.095 W $m^{-1}K^{-1}$ to 0.250 W $m^{-1}K^{-1}$ for densities ranging from 314 Kgm^{-3} to 496 Kgm^{-3} though this group also had the largest standard deviation in thermal conductivity of all grain types.

Relationships between density and thermal conductivity based on grain type were also introduced: For "density independent" snow types (depth hoar and other faceted types), the use of a single mean value was found to give the best fit to the measurements. For other types, both quadratic fits and maximum likelihood estimator were proposed. A follow-up study by Sturm et al. (2002) found good agreement with the above regressions when used to predict the thermal conductivity of layers classified by hand hardness and density.

Riche and Schneebeli (2010), in addition to evaluating the accuracy of short-time heated needle probes, used a guarded heat plate to measure thermal conductivities between 0.151 ($\rho = 213\ Kgm^{-3}$) and 0.185 W $m^{-1}K^{-1}$ ($\rho = 239\ Kgm^{-3}$) for rounded grains.

Schneebeli and Sokratov (2004) applied vertical temperature gradients to sieved snow samples and used microtomography to track structural changes as they underwent metamorphism. They observed an initial sharp increase in thermal conductivity from approximately 0.35 to 0.55 W $m^{-1}K^{-1}$ for samples with a constant density of 500 Kgm^{-3} while lower density samples tended to remain constant around their initial value of 0.11 W $m^{-1}K^{-1}$.

Satyawali et al. (2008) applied high vertical temperature gradients (28 $^{\circ}C\ m^{-1}$) to sifted natural snow samples and monitored microstructural and thermophysical changes over a period of 4 weeks. They noted that the thermal conductivity in samples with an initial density of $\rho = 180\ Kgm^{-3}$ increased more quickly during the 4 weeks and to ultimately higher values than another sample with initial density $\rho = 320\ Kgm^{-3}$. The pore intercept length also increased more quickly in the low density sample. This increase in thermal conductivity coupled with only a small increase in density implies that the ice skeleton in low density snow may rearrange itself into effective pathways for heat conduction faster than similar snow of higher density. A similar conclusion was drawn by Sturm and Johnson (1992) with respect to depth hoar in a shallow, highly faceted snowpack. This relationship between initial density and rate of change of thermal conductivity is opposite that observed by Schneebeli and Sokratov (2004) and may be due to similar factors that led Sturm et al.

Table 2.1: *A summary of published values of snow thermal conductivity since 1997. The grains in Satyawali 2008 were subjected to a high temperature gradient, but started as rounded grains (RG).*

Study	λ [$\mathbf{W}m^{-1}K^{-1}$]	**Grain**	ρ [Kgm^{-3}]	**Tmean** [$^{\circ}C$]
Sturm 1997	0.095-0.445	MFcl	314-496	-10.8
Sturm 1997	0.099-0.218	FCxr/RGxf	280-416	-12.1
Sturm 1997	0.021-0.142	DHch	154-369	-14.4
Sturm 1997	0.051-0.632	RGsr	170-340	-12.9
Schneebeli 2004	0.10-0.12	RG	260-300	-8
Satyawali 2008	$\tilde{0}$.10-0.12	RG (initial)	320	-7.2
Satyawali 2008	$\tilde{0}$.09-0.17	RG (initial)	180-200	-7.3
Riche 2010	0.073,0.061	RG	213,239	-15
Courville 2007	0.29 (mean)	RGwp	$\tilde{4}$00	-25 to -40
Courville 2007	0.15 (mean)	FC (firn)	400-500	-25 to -40
Sturm 1997	$\tilde{0}$.022 - 0.024	Air	1	-20 to 0
Sturm 1997	$\tilde{2}$.2 - 0.0	Ice	917	-20 to 0
Singh 2009	$\tilde{0}$.3 - 0.4	MF	480	-30 to -5

(1997) to conclude that density is not a good predictor for thermal conductivity in faceted grain types. Calonne et al. (2011) and Greene (2007) also observed the formation of highly faceted grain types with no attendant change in density.

A summary of published values of thermal conductivity is shown in Table 2.1. Grain types are those defined in Fierz et al. (2009).

2.3 Modeling

Many efforts at modelling prior to the late 1990s were hindered by the absence of information on the true microstructure of a snow sample. Although stereology could be used to estimate parameters such as connectivity and intercept length there was no way of simulating heat transport through the true structure of a snow sample. Modelers were thus constrained to using combinations of idealized shapes to simulate heat transfer through the lattice. Colbeck (1983) achieved some success in modelling crystal growth rates in dry snow but concluded the "the fact that we had to assume a distribution [for a geometrical enhancement factor]

points out the need for stereographic work on snow at various stages of metamorphism.". Arons and Colbeck (1995) summarized a number of efforts at physically-based snowpack modeling and reached a similar conclusion to Colbeck, while emphasizing the importance of texture, anisotropy and scale to heat transport in snow.

Adams and Sato (1993) developed a 1-D analytic model for the effective thermal conductivity of an isotropic snow sample represented by a collection of spheres, where heat was allowed to travel through either pore space, ice or pore space and ice in series. They found that the thermal conductivity was dominated by the ratio of bond radius to grain radius as well as the coordination number (degree of interconnectedness) and explained qualitatively a potential feedback mechanism for the growth of depth hoar.

The model of Adams and Sato (1993) was incorporated into the 1-dimensional SNOWPACK model (Bartelt and Lehning, 2002). SNOWPACK is a physically based model for metamorphism in the seasonal snow. See Chapter 4 for more detail on the model. The thermal conductivity in SNOWPACK is solved at discrete timesteps based on a layer's physical and microstructural properties. Fierz and Lehning (2001) found good qualitative agreement between SNOWPACK and measured thermal conductivities while at the same time concluding that the single adjustable parameter of neck to bond radius, even when combined with density is not adequate for the variety of textures that may be found in snow of similar densities. A study by Greene (2007) showed that while SNOWPACK consistently predicted thermal conductivity to within 10% of its measured value, it did not satisfy the criteria for 'model skill' outlined by Pielke (2002), that the standard deviation of modeled values be approximately equal to the standard deviation of the observed values and; the root mean squared error (RMSE) and RMSE with constant bias removed be smaller than the standard deviation of the observed values. Jamieson and Fierz (2004) used the model to approximate freezing times in a buried wet layer and found good agreement with measured data although thermal conductivity was not explicitly evaluated.

Bartelt et al. (2004) modified the model of Adams and Sato (1993) with the addition of a radiative transfer term to the ice thermal conductivity equation, though it was still confined to one dimension and a single neck to bond ratio for each layer. The new model was used in a modified formulation of the SNOWPACK model that allowed ice and pore space to be out of thermal equilibrium. Simulations showed that heat transfer through the ice/pore interface is potentially important, and that physical models should account for this by treating ice and air phases separately when calculating the bulk thermal conductivity. The utility of this new non-equilibrium model lies as much in distancing physically based models from empirical formulations as it does in calculating point values of thermal conductivity.

Satyawali and Singh (2008) explored the role of grain shape in explaining the the wide scatter apparent in previous measurements of thermal conductivity versus density. Their model results assumed constant thermal conductivity for ice and showed a clear dependence of bulk thermal conductivity on shape, with the highest conductivities found in layers with good bonding and spherical shapes and the lowest for cubic shapes with poor bonding. Their approach offers a promising compromise between having complete 3-D microstructural information and usability given the current state of knowledge.

Singh and Wasankar (2009) used the contiguity of snow (the fraction of a given phase in contact with another phase) to define the contact between adjacent phases, along with dendricity and sphericity, which together can be used to define the degree of metamorphism from new snow to either rounded or faceted forms. Their model showed relatively good agreement with thermal conductivity measurements from a high density melt-freeze crusts whose microstructural parameters were defined using image analysis software. A more comprehensive comparison is not possible as their microstructural parameters were not published.

Kaempfer et al. (2005) used computed X-ray micro-tomography to study heat transport in snow. A snow sample was subjected to a temperature gradient and was simultaneously imaged for use in a finite element model. Simulations neglecting any heat flow through pore

space resulted in thermal conductivity values that were approximately 80% of measured values implying that most heat flow is through the ice lattice. Similar to Bartelt et al. (2004), their simulations found high temperature gradients concentrated in small grain-scale regions. Consideration of the sample's tortuosity shows that idealized samples consisting of spheres and with tortuosities of 2.0-2.1 don't alter the path of heat flow relative to the axis of vapor diffusion, whereas a real snow sample with a tortuosity of 4.4 ± 0.3 forces it to travel along a much more sinuous path which, given the relatively higher conductivity of the ice lattice, may lead to localized high temperature gradients at scales not measurable by conventional methods.

Shertzter et al. (2010) introduced a 3-dimensional contact tensor to model the the change in thermal conductivity through the ice skeleton as an isotropic snow sample subjected to a vertical temperature gradient becomes anisotropic, with preferential bonding and increased thermal conductivity developing in the direction of gradient. As with Kaempfer et al. (2005), the contributions of conduction through air, convection and latent heat are ignored. The model as presented was limited by its assumption of stationarity of all microstructural properties except for the contact tensor and could not be used to effectively model changes over long periods but represents a promising start to incorporating more realistic microstructure into snowpack models. Riche and Schneebeli (2013) studied the anisotropy of thermal conductivity using heated needle probes and numerical simulations and found that, depending on grain type, the effective thermal conductivity measured only in the horizontal plane can lead to errors of up to 25%.

Kaempfer and Plapp (2007) and Kaempfer et al. (2009) built on previous μ-CT modelling efforts by using a phase field to represent the air-ice interface. Models of heat flow in two dimensions showed clearly the preferred pathways through oriented bonds but also allowed the contribution of air and water vapour, though convection was still neglected. Some simplifications were required in order to reduce computational time and no quantitative results

were obtained; however, the method shows qualitatively how heat flow and snow metamorphism may effectively be modeled using physical laws and real microstructure. Calonne et al. (2011) modeled the thermal conductivity of snow samples in three dimensions using μ-CT images and found significant anisotropy between the vertical and horizontal planes, though their model only considered conduction through the ice lattice and interstitial air.

Finally, although they are not explicitly applicable to the present study, much larger-scale models also depend on accurate characterization of snow's thermal conductivity. Cook et al. (2008) studied the sensitivity of a model to a range of conductivities and found measurable differences in heat exchange with the lower atmosphere as well as soil temperatures and permafrost dynamics.

Although there is a growing body of research regarding the thermal conductivity of natural snow there has been very little research devoted to an understanding of changes over time of specific snowpack layers, especially melt-freeze forms. Part of the goal of the current study is to fill this gap in the knowledge and synthesize results with concurrent observations of structure, density, temperature, grain form and specific surface area. The remainder of this chapter deals exclusively with observations of thermal conductivity. Results from this and other chapters are summarized together in Chapter 5.

2.4 Equipment

A Hukseflux TP02 thermal non-steady-state thermal conductivity probe (Hukseflux, 2003) was used for all measurements in this study. The probe, shown schematically in Figure 2.1, is designed to be used with the long-time approximation given in Equation 2.2. This means that incidences of poor contact between the probe and the sample will simply take longer to transition out of the zone of transient temperature increase. The power to the heating wire was controlled by a resistor in series from the 12 V power source and was measured with the use of a 10 Ohm 0.1% resistor. A thermistor in the base of the probe

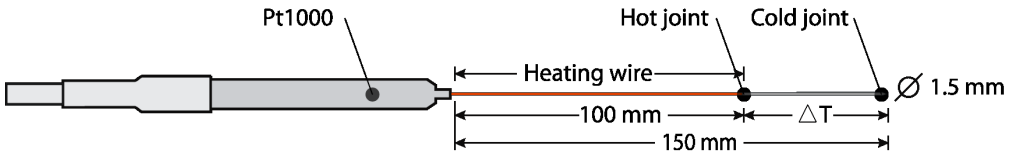

Figure 2.1: *Schematic of the Hukseflux TP02 thermal conductivity probe. Adapted from Figure 1 in Hukseflux (2003)*

gives a reference temperature and enables a direct calculation of the thermal conductivity. The manufacturer's stated accuracy at 20°C is ± (3% + 0.02) W $m^{-1}K^{-1}$. A correction during post-processing limits the error due to temperature to ± 0.02%, but measurements of low thermal conductivity will still have relatively high uncertainty due to the instrument's accuracy. Morin et al. (2010) modeled heat flow around the TP02 and found that the area sampled extends approximately 3 cm radially from the probe.

The TP02 was paired with a Campbell Scientific CR10X datalogger. Several 12 V power sources were tested including 6 V lantern batteries in series, 1.5 V AA batteries in series and an AC-to-12 V inverter. Ultimately the most stable power source was from the AA batteries and these were used for the majority of measurements in the field. All data were recorded at 1 second intervals for quality control during post-processing. The logger program also had several built-in warnings for unstable sample temperature heater power for real-time evaluation of measurement quality. An Ipaq 3950 hand-held computer and Campbell Scientific PConnectCE software were used to trigger TP02 measurements and monitor values as the measurement progressed.

The TP02 probe was new at the beginning of the 2009 - 2010 and came factory calibrated. No further calibrations were performed. Prior to use in the field all connections and resistances in the probe were verified to be within tolerances specified by Hukseflux. Connections with the CR10X datalogger were checked before each use.

2.5 Field Methods

The majority of TP02 data were gathered in the field simultaneously with other snowpack measurements. A test snow profile was used to describe qualitatively the crust structure and spatial variability over the scale of the pit wall (approximately 1 m horizontally). Near-infrared photography (Chapter 3) was used to record quantitative information on structure and variability.

Once the complementary measurements were completed, the TP02 was inserted into the layer of interest for several minutes to allow it to reach thermal equilibrium with the surrounding snowpack. This was checked by comparing the TP02's thermistor temperature with the layer temperature previously measured as part of the snow profile.

Once the measurement was triggered the probe temperature was allowed to stabilize for an additional 100 seconds before starting a 100-second heating cycle. Similar procedures were used by Morin et al. (2010) and Domine et al. (2012). The probe tip temperature was monitored to ensure that the temperature increase did not exceed 1.0 °C. Occasional problems were encountered at low temperatures when the stiff probe cable made it difficult to prevent the probe from shifting out of the sample area. These measurements were always discarded. Excepting cases where the crust was too warm, a minimum of two valid measurements were attempted for each layer. Typically the layer above (samples 1 and 2 in Figure 2.2, layer below (samples 5 and 6) and one or more layers within the crust itself (samples 3, 4, 7 and 8) were sampled. A final NIR image was then taken to record the position of each sample. NIR images were found to be superior to visible images for resolving layers and variability within the wall of a snow pit. An example is shown in Figure 2.2

In addition to field measurements, five cold lab experiments, similar to those conducted by Jamieson and Fierz (2004), were conducted to observe changes in and around a wet crust as it froze. Thermal conductivity measurements followed a similar procedure as for field measurements except that measurements were taken vertically through the crust. Care was

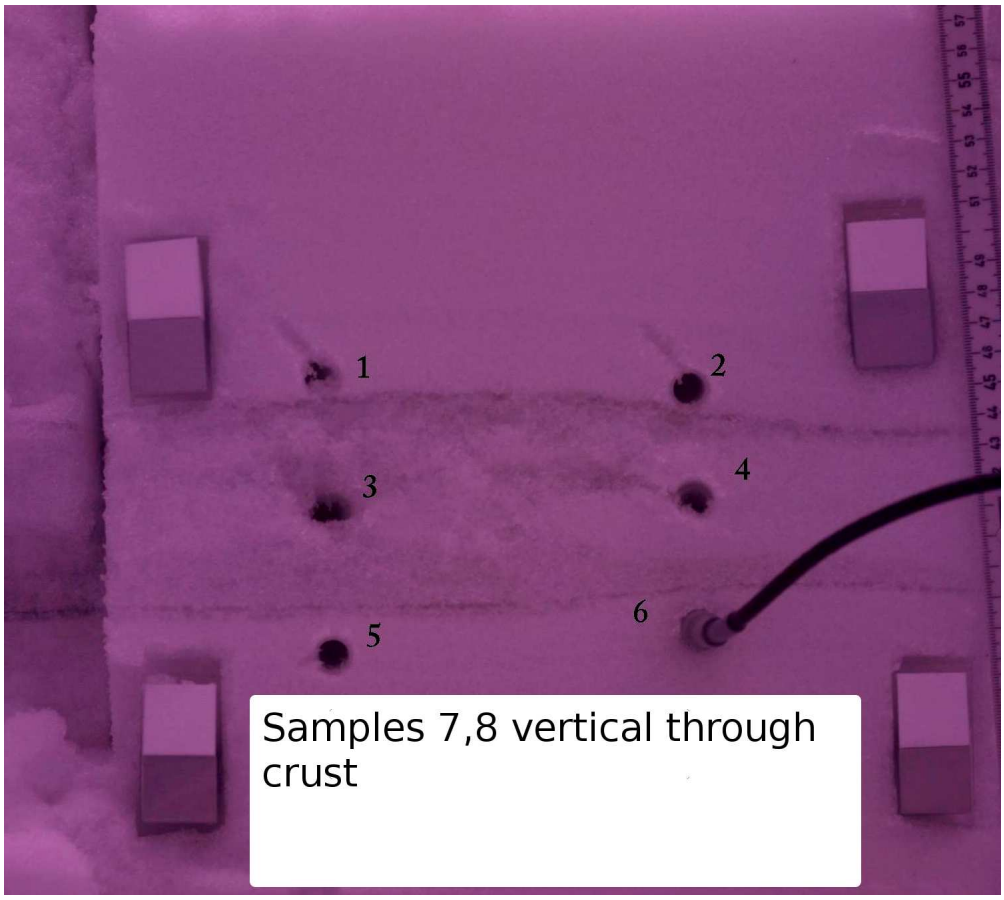

Figure 2.2: *Annotated NIR photograph of TP02 sampling locations. Layer boundaries and sampling locations are more easily discerned in this NIR photo than in photographs taken with a conventional digital camera in the visual spectrum. Similar images were used to complement field notes regarding depth of sampled layers and layer homogeneity.*

taken to ensure that the thermistor, thermocouples and heating portion of the wire were always positioned the same relative to the the layers of interest. Cold lab crusts all had thickness greater than 10 cm thus ensuring that no portion of the probe was sampling an adjacent layer.

Although the majority of measurements were successful there were a number of challenges encountered. The winter of 2009 - 2010 was abnormally warm and dry (see Appendix A) and as a consequence layers were often very close to 0 °C. Very faceted and disaggregated layers also proved difficult to sample due to large voids or extreme variability. Crusts were occasionally difficult to penetrate with the probe due to icy inclusions.

Power presented a minor challenge as the TP02 requires a stable source of 12 VDC power. Analysis of initial results found that nine 1.5 V rechargeable batteries were more stable, even at cooler temperatures, than two 6 V lantern batteries in series. Somewhat surprisingly, the AC power available in the Rogers Pass cold lab was the least stable of all power sources and was not used after the initial cold lab experiment on March 12, 2010.

2.6 Results and Analysis

A total of 261 successful thermal conductivity measurements were recorded in the field and in the lab during the study period. Although melt-freeze crusts were of greatest interest the layers above and below were also sampled. Table 2.2 summarizes the thermal conductivity measurements for each study site and cold lab experiment. Refer to Appendix A for locations and summaries of crust formation.

The analysis in this section is divided into several parts: In Section 2.6.1 thermal conductivity by grain type is summarized and compared with previous studies; in Section 2.6.2 links between thermal conductivity and physical characteristics of the sampled layers are investigated. This is similar to analyses performed in the past by Sturm et al. (1997), Sturm and Johnson (1992) and Kaempfer et al. (2005) and to the author's knowledge is the first

Table 2.2: *Observation period and number of thermal conductivity measurements during winter 2009-10. Crusts are named by geographical location and month/day of initial burial. BV: Beaver Valley; FI: Mt Fidelity; SR: South Run; RP: Rogers Pass study plot; LAB: Rogers Pass cold lab.*

Crust Name	**Start**	**End**	**Num. site visits**	**Approx. interval**
BV0112	01/31	03/23	7	weekly
FI0109	01/10	04/14	14	weekly
FI0308	03/15	04/14	5	weekly
RP0112	01/19	04/06	11	weekly
SR0131	02/03	04/07	10	weekly
SR0210	02/03	04/07	9	weekly
SR09	02/05	02/05	11 spatial samples	Once
LAB0312	03/12 12:00	03/13 15:10	7	30 min
LAB0330	03/30 09:30	03/30 12:05	3	hourly
LAB0409	04/09 13:00	04/10 14:30	5	6 hours
LAB0410	04/10 19:15	04/13 09:35	6	twice daily
LAB0413	04/13	04/18	6	daily

performed in a transitional snow climate. In Section 2.6.3 changes over time in thermal conductivity are examined along with its relationship to rates of change in other physical parameters. These are compared with a number of past studies that have either tracked physical changes or modeled changes over time. Section 2.6.4 gives a brief look at some of the difficulties in selecting a site for tracking temporal changes in buried layers.

All thermal conductivity measurements, both successful and unsuccessful, are given in Appendix C. The high incidence of bad measurements late in the season was due primarily to the layer of interest being at or near 0 °C.

Determination of the quality of each measurement was done manually in Microsoft Excel. Although the CR10X program included automated checks for quality, they frequently failed to identify bad measurements and incorrectly flagged good measurements. An ideal measurement will begin with a short period of transient heating before the rate of temperature

increase becomes constant. For a constant heating power Q, Equation 2.2 becomes:

$$\lambda = \frac{Constant}{\Delta T} ln\left(\frac{t_2}{t_1}\right) \tag{2.3}$$

where t_1 is the time, in seconds, at which the rate of increase of the sample temperature becomes constant, t_2 is the end of the measurement period and ΔT is the nominal rise in temperature between the two points. The term 'nominal' is used because the increase in temperature is relative to the temperature of a thermocouple at the base of the TP02, which serves to compensate of any changes in the layer temperature during measurement. This zone of constant temperature increase is linear when plotted using the natural logarithm of the ratio of t_1 and t_2 and is thus well suited for graphical analysis. Figure 2.3 shows a typical plot of nominal temperature rise versus ln(t). The value of λ is found by taking the inverse of the slope of the best-fit dashed line.

Concerns regarding the accuracy of heated needle probes were raised by Riche and Schneebeli (2010), who found that the needle is potentially in contact with only a small number of grains along its length. This concern was addressed by Morin et al. (2010) who modeled these effects and found that the only consequence would be a slight delay in the measurement reaching a rate of constant temperature increase.

Upper and lower limits for plausible values of λ may be estimated by using the thermal conductivities of pure ice and air. Ashton (1986) gives the following equation for pure ice valid from -40 to -0.1 °C.

$$\lambda = 2.21 - 0.011T \tag{2.4}$$

The majority of measurements were taken at temperatures warmer than -10 °C so following Equation 2.4 our limits for plausible thermal conductivity of snow and ice become $0.025 \leq \lambda \leq 2.32\ Wm^{-1}K^{-1}$, where the lower limit is the approximate thermal conductivity of air and the upper limit is the thermal conductivity of pure ice.

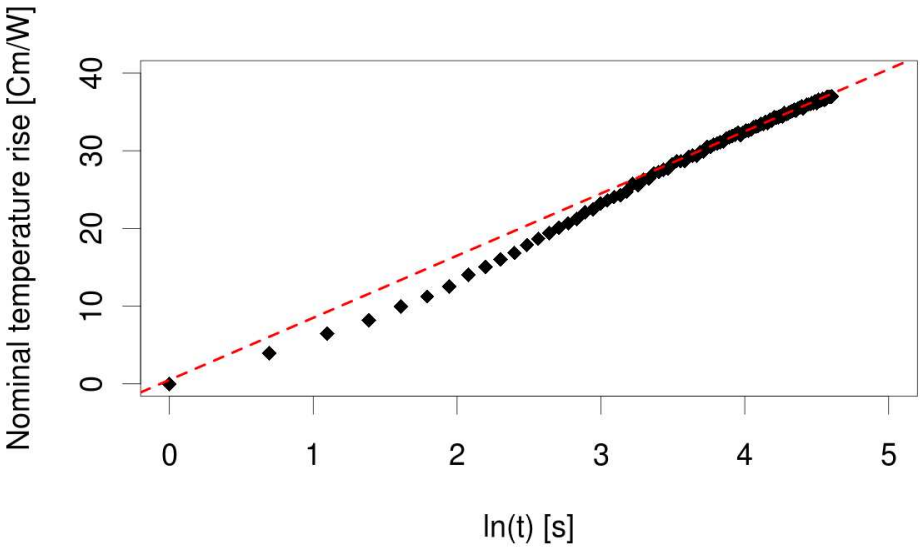

Figure 2.3: *A typical plot of ln(t) versus the nominal rise in temperature. The thermal conductivity is the inverse of the slope. In this plot the slope is 8, so* λ *is approximately 0.125* $[Wm^{-1}K^{-1}]$

2.6.1 Thermal conductivity by grain type

Table 2.3 shows the summary statistics for thermal conductivity measurements by grain type. There were enough instances of mixed faceted (FC) and melt-form (MF) layers that a new classification denoted 'MFFC' was created from the MF subset of grains. These layers were often spatially variable on the scale of the needle probe and multiple grain types were likely included in each thermal conductivity measurement. This decision may be tested using a Mann-Whitney U-test: With no removal of outliers the null hypothesis (at $p \leq 0.10$) that the distributions of thermal conductivity for MF and MFFC are the same is rejected.

The range of valid measurements is very similar to the theoretical limits calculated using Equation 2.4. The two subgroups of melt forms have substantially different mean thermal conductivity and density suggesting that this discrimination is worthwhile. As might be expected, ice forms (IF) have the highest mean thermal conductivity while precipitation particles (PP) have the smallest values.

Table 2.3: *Thermal conductivity and density by grain type. Units for thermal conductivity are* $[Wm^{-1}K^{-1}]$. *MF* and MFFC denote two subgroups of melt-forms (MF)*

Grain	# **Valid**	$\overline{\lambda}$	σ_λ	λ_{MAX}	λ_{MIN}	$\overline{\rho}$ $[Kgm^{-3}]$	# **Valid** ρ
ALL	261	0.205	0.200	2.103	0.022	279	190
MF	112	0.203	0.216	2.103	0.025	289	58
MF*	103	0.210	0.224	2.103	0.025	304	49
MFFC	9	0.127	0.052	0.236	0.064	210	9
FC	96	0.204	0.206	1.727	0.044	285	95
PP	5	0.068	0.028	0.108	0.040	89	6
RG	26	0.213	0.115	0.553	0.042	299	26
IF	10	0.317	0.196	0.843	0.175	NA	0
DF	6	0.090	0.036	0.122	0.090	145	6

Distributions for each grain type were tested for normality using the Shapiro-Wilk Normality test. The null hypothesis of normality for all grain types was rejected based on the presence of a small number of outliers in each data set. A series of kernel density plots showed large right-hand tails for most grain types due to a relatively small number of high values. Density plots for each grain type reveal similar tails except for types with few samples (MFFC and PP) and rounded grains (RG) which hints at a mixed-mode distribution. Further investigation reveals that two samples from a relatively high-density layer late in the season are likely responsible.

Given the probable presence of outliers, there is value in probing further into measurements that may not be representative of the larger population. The definition of what exactly constitutes an outlier is subject to debate and depends on a number of factors including *a priori* knowledge of the expected distribution. Outliers are defined here as any values further than 1.5 times the interquartile range from the upper and lower quartiles.

Figure 2.4 shows a box-whisker plot of all thermal conductivity measurements by grain type. The labels 'MFFC' and 'MF' correspond to the summary stats for groups MF* and MFFC in Table 2.3. Outliers are circled in red. MF* and FC have the greatest number of outliers while MFFC and PP have none.

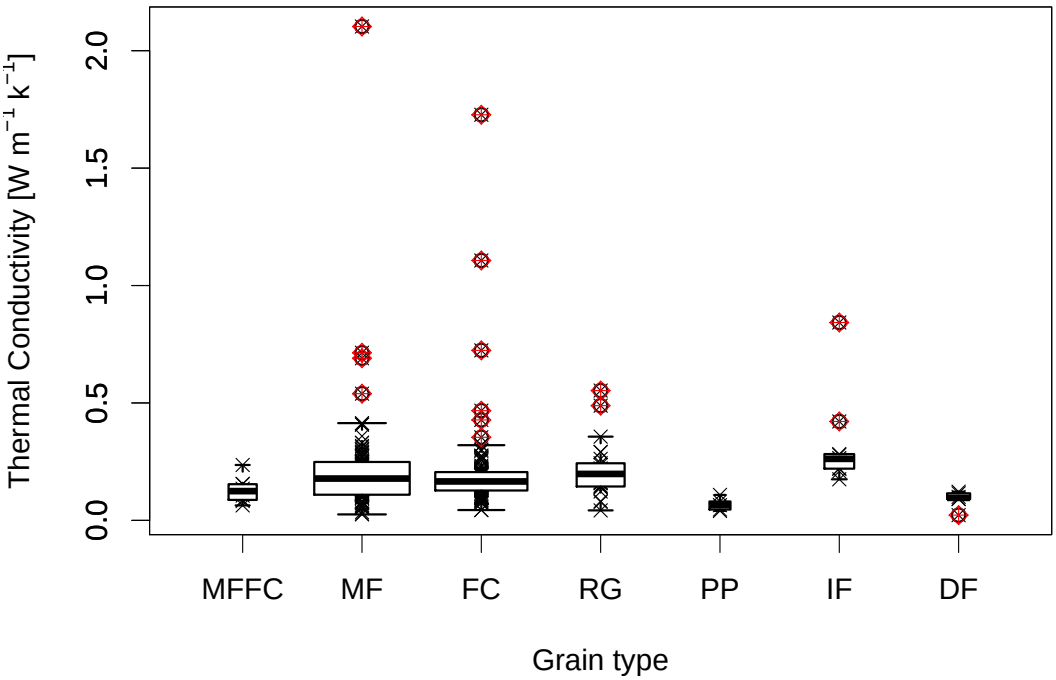

Figure 2.4: *Box Whisker plot of thermal conductivity by grain type for all samples. The box limits are the first and third quartiles and the band in the middle of each box is the median. Whiskers extend 1.5 times the interquartile range from the first and third quartiles. Outliers are circled in red.*

Old and new sample means are shown in Table 2.4. With outliers removed, the sample mean for most grain types is reduced as is the sample standard deviation. The differences in mean thermal conductivity are also smaller, and grain type alone does not appear to be adequate for estimation of thermal conductivity. This may however justify simple formulations of thermal conductivity in climate models, where grain types are sometimes differentiated by "new snow" and "old snow".

Mean values of λ reported by Sturm et al. (1997) are also given in Table 2.4. The mean for MF* and Sturm's 'melt grain clusters' are similar while the mean for MF lies between those of their 'rounded melt grains' and 'melt grain clusters'. This discrepancy is likely due to a combination of the somewhat subjective nature of grain classification and the fact that the present data set contained numerous moist layers and, with the exception of cold lab

Table 2.4: *Thermal conductivity by grain type with and without outliers, compared with those reported by Sturm et al. (1997).*

Grain	$\overline{\lambda}$	$\overline{\lambda}$ outliers removed	# outliers	$\overline{\lambda}$ Sturm	Sturm97 grain
ALL	0.204	0.170	13		
MF	0.203	0.173	4	0.188	rounded melt grains
MF*	0.210	0.177	4	0.250	melt grain clusters
MFFC	0.127	0.127	0		
FC	0.204	0.165	6	0.153	mixed forms
RG	0.213	0.187	2	0.169	small rounded grains
PP	0.068	0.068	0	0.070	new snow
IF	0.317	0.239	2		
DF	0.076	0.094	1	0.128	recent snow

crusts all samples were taken at much warmer temperatures. Referring back to Tables 2.3 and 2.1, the values published by Singh and Wasankar (2009) for MF are slightly greater than our mean λ but were also taken from layers with a higher density. The mean value for RG is larger than Sturm's and much greater than those published by Schneebeli and Sokratov (2004), Satyawali and Singh (2008) and Riche and Schneebeli (2010) for layers of similar density; however, the range of measurements is similar to Sturm's.

The three largest values for FC come from three different sites and all layers were recorded as being moist. Pure water has a thermal conductivity of approximately 0.563 $Wm^{-1}K^{-1}$ at 0 °C and it's likely that the presence of free water in the ice lattice affects λ, although without knowing precisely the water content it is not possible to quantify the contribution.

Given the heterogeneous structure of many crusts, the observation of some high thermal conductivities in MF forms is not surprising. The four outliers come from three different sites: Two were vertical measurements through the crust and two were measured parallel to the layer plane. None of the subjective observations (hand hardness, moisture content) or quantitative (layer temperature, density) set them apart from other samples.

Outliers aside, the distribution of MF observations does not appear normal and it is worth searching for any trends in seasonality or site. No trends in seasonality were found,

Table 2.5: *Thermal conductivity for crust samples (MF) by site. Units for thermal conductivity are* $[Wm^{-1}K^{-1}]$. *The final column gives the mean with outliers removed.*

Site	**# Valid**	$\overline{\lambda}$	$\tilde{\lambda}$	λ_{MAX}	λ_{MIN}	σ_λ	*# outliers*	$\overline{\lambda}^*$
BV0112	10	0.181	0.193	0.317	0.062	0.085	0	0.181
FI0308	16	0.324	0.184	2.100	0.055	0.486	3	0.191
FI0110	12	0.298	0.240	0.843	0.175	0.183	2	0.232
RP0112	25	0.142	0.135	0.239	0.059	0.0534	0	0.142
SR0131	8	0.226	0.153	0.714	0.055	0.210	1	0.156
SR0210	7	0.126	0.134	0.225	0.028	0.073	0	0.126
LAB0312	5	0.259	0.142	0.648	0.089	0.228	1	0.162
LAB0330	9	0.170	0.193	0.285	0.035	0.092	0	0.170
LAB0409	7	0.262	0.252	0.690	0.072	0.206	1	0.191
LAB0410	11	0.213	0.246	0.409	0.025	0.117	0	0.213
LAB0413	10	0.244	0.251	0.414	0.081	0.100	0	0.244

however individual sites did differ. Table 2.5 shows summary statistics for MF crusts at each site. Several sites stand out as having appreciably greater means than others. These are explained at least in part by high outlying values for sites FI0308 and RP0112, but even with the removal of outliers the cold lab experiments appear to have higher mean values than the field sites. There are two possible reasons for this: The final three cold lab experiments used crusts harvested from the same spot so it may be that this crust simply has a greater thermal conductivity. A second possibility is the method used to measure the thermal conductivity. Due to space constraints in the cold lab, the physical size of the harvested crusts had to be small and thermal conductivity was measured vertically through the crust rather than horizontally.

We use the Mann-Whitney U-test twice: Once to test whether field and lab thermal conductivities come from different distributions and once to test the vertical and horizontal measurements. In both cases the null hypothesis that the distributions are the same at the p ≤ 0.05 significance level is rejected. Unfortunately there is not a single site with concurrent vertical and horizontal measurements throughout the entire season and no conclusions may be drawn beyond the fact that the distributions are different.

Subsection 2.6.1 Summary In this section the relationship between thermal conductivity and grain type has been examined. The majority of samples in this study were comprised of either melt-freeze crusts or facets. Melt-freeze types were further divided into layers containing transitional grain forms and those comprised purely of melt-freeze forms. Model distributions for all grain types would have been approximately normal except for their large right-hand tails. Removal of outliers gave the expected result of lower mean thermal conductivities and standard deviations within each sample set, but also reduced the differences between grain types.

The subset of MF samples was further analyzed to find temporal trends or differences between sites. The cold lab experiments, with the exception of LAB0330, were found to have different means than the field sites. This was due to either the fact that cold lab crusts were harvested from the same location, or that thermal conductivity was measured vertically through the crusts and parallel to the temperature gradient, while field sites were primarily sampled parallel to the layer.

Thermal conductivity by grain type was compared to other published values where density and temperature information were available. When outliers were removed (in essence removing most of the moist samples) the means for most grain types were similar to those published by Sturm et al. (1997). Since many of the outliers were from moist layers this highlights a potentially important distinction. When available, the ranges for λ for each grain type were also similar across many of the studies.

The large range of measurements for each grain and the correspondingly large standard deviations serve to reinforce the conclusion the grain type alone is not a sufficient predictor of thermal conductivity. Given that many of the outliers were from layers identified as 'moist' or with temperatures near 0 °C, the qualitative measure of moisture content, commonly used in test profiles and snow pits, does appear to be a useful distinction for any predicted value of thermal conductivity even if no statistically significant relationships are found. The next

section explores the correlations between thermal conductivity, layer moisture, density and layer temperature.

2.6.2 Thermal conductivity and physical parameters

The previous subsection examined the relationship between thermal conductivity and grain type, including the distribution of measurements and the identification of possible outliers. Results indicated that with the possible exception of coarse weather and climate models, grain type alone should not be used to predict thermal conductivity. In this section the relationship between thermal conductivity and density and layer temperature is analysed.

Figure 2.5 shows a scatter plot of λ and density for all grain types given in Table 2.3 except for ice forms (IF) which lacked density measurements. Thermal conductivity generally increases with increasing density, but so does the heteroscedasticity. Outliers, circled in red, are identified using the quantile method discussed in the previous section. The majority of outliers are from samples that were moist. The empirical quadratic fit from Equation 4 in Sturm et al. (1997):

$$\begin{aligned} \lambda &= 0.138 - 1.01\rho + 3.233\rho^2 \quad (0.156 \leq \rho \leq 0.6) \\ \lambda &= 0.023 + 0.234\rho \quad (\rho < 0.156) \end{aligned} \tag{2.5}$$

and logarithmic fit with a maximum likelihood estimator (MLE) correction given from Sturm et al. (1997) Equation 7:

$$\lambda = 10^{(2.650\rho - 1.652)} \quad (\rho \leq 0.6) \tag{2.6}$$

are plotted on each figure (where ρ has units of g cm^{-3}), along with the quadratic fit from Calonne et al. (2011):

$$\lambda = 2.5e^{-6}\rho^2 - 1.23e^{-4}\rho + 0.024 \tag{2.7}$$

where ρ has units of kg m^{-3}. Both equations were fit to data gathered using similar equipment and methods to this study, albeit at colder temperatures. Both equations fit relatively well to the trends in this study's data but tend to underestimate the values. One possible reason for this discrepancy is that the new data were collected at much warmer temperatures and, as outlined in Section 2.1, warmer snow will have higher thermal conductivity.

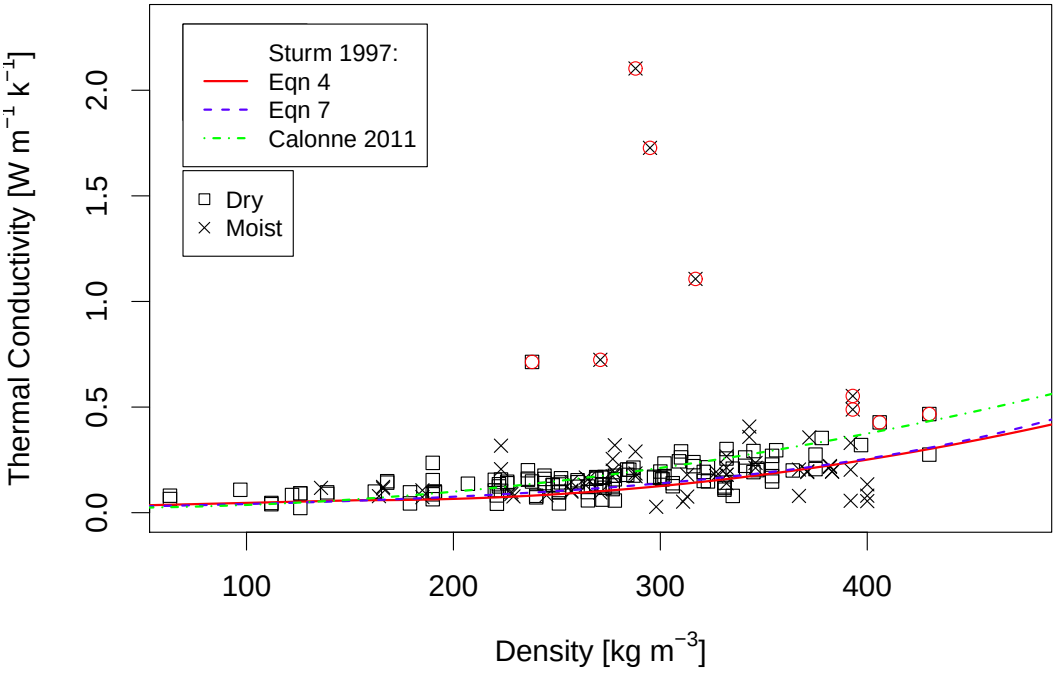

Figure 2.5: *Thermal conductivity versus density for all samples. Outliers are circled in red. Equations (4) and (7) from Sturm et al. (1997) and Equation (12) from Calonne et al. (2011) are plotted for reference.*

Table 2.6: *Significant correlations between thermal conductivity and density.*

Grain	Pearson R	P-value	Spearman ρ	p-value	outliers rem.	# **Valid**
All	0.521	6e-14	0.553	5e-16	Y (19)	242
FC	0.707	10e-15	0.768	2e-18	Y (6)	90
RG	0.777	3e-6	0.823	2e-7	N	26

Table 2.6 shows the Pearson and Spearman correlations for all samples together as well as by grain type. Only correlations with p $\leq$ 0.05 are shown. Even with outliers removed,

the relationship between density and λ for ALL grains is only weakly linear and monotonic. When considering each grain type separately some stronger relationships emerge: Faceted forms (FC), shown in Figure 2.6 with outliers removed, have a moderate positive linear monotonic relationship between ρ and λ. The equations from Sturm et al. (1997) and Calonne et al. (2011) are also plotted. The measurements in the present study are generally higher than the equations from Sturm while the empirical Equation from Calonne offers a slightly better fit. The same general relationship is evident for the sample of rounded grains (RG), shown in Figure 2.7. Attempts at linear and quadratic curve fitting did not result in any statistically significant equations, but there is some evidence that consideration of layer temperature along with density could result in an improved prediction of thermal conductivity.

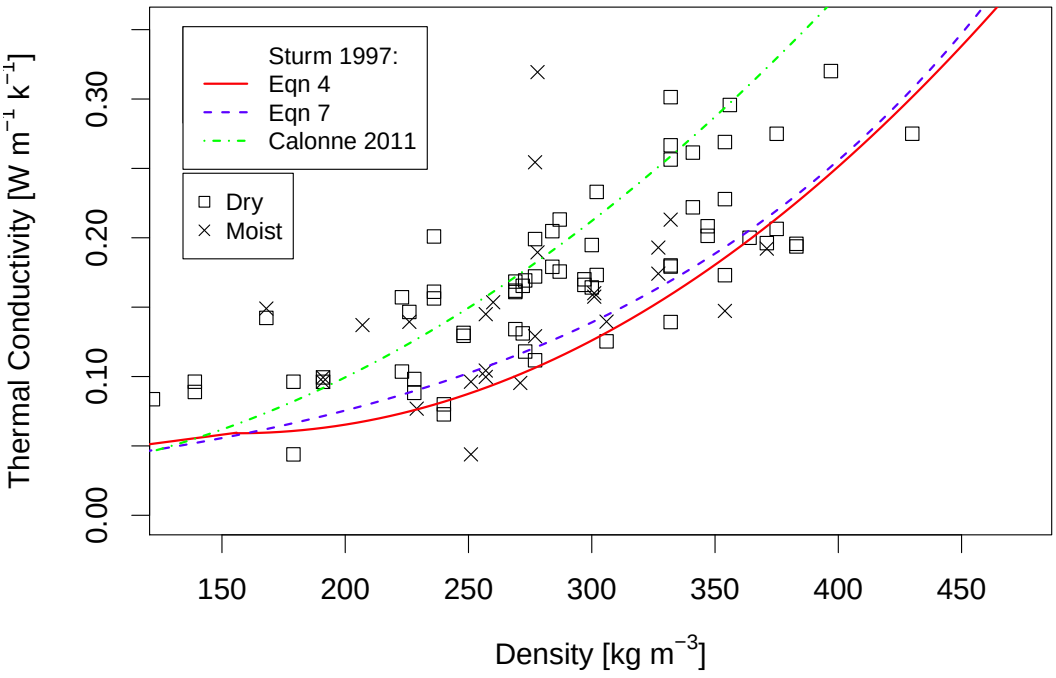

Figure 2.6: *λ versus density for faceted (FC) grain types with outliers removed. Equations (4) and (7) from Sturm et al. (1997) and Equation (12) from Calonne et al. (2011) are plotted for reference.*

Figure 2.8 shows a scatter plot of all layer temperatures and thermal conductivity. As

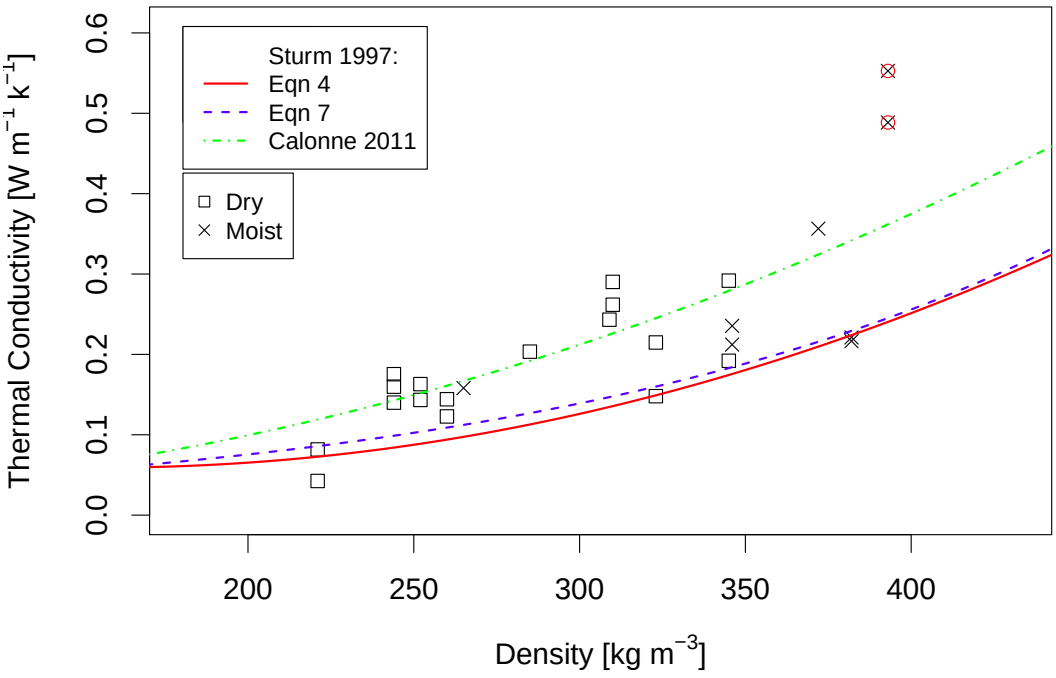

Figure 2.7: *λ versus density for rounded (RG) grain types. Equations (4) and (7) from Sturm et al. (1997) and Equation (12) from Calonne et al. (2011) are plotted for reference. Outliers are circled in red.*

was the case with density there are a number of outliers, most of which were sampled from moist layers. Table 2.7 shows significant correlations between temperature and thermal conductivity. FC have a weakly positive linear monotonic relationship while melt-freeze (MF) and the subset MF* have weakly negative linear relationships. The latter result, shown in Figure 2.9, is somewhat surprising given the theoretically positive relationship between temperature and thermal conductivity. There are several possible explanations: The measurements at colder temperatures all come from a single crust, so it is possible that this skews the results and represents a shortcoming in the visual classification of grain types. A second possibility is that some of the lower values of thermal conductivity come from crusts with high tortuosity or low coordination numbers. Sturm et al. (1997) concluded that the thermal conductivity of melt-freeze forms is best predicted using a mean value rather than accounting for density or temperature.

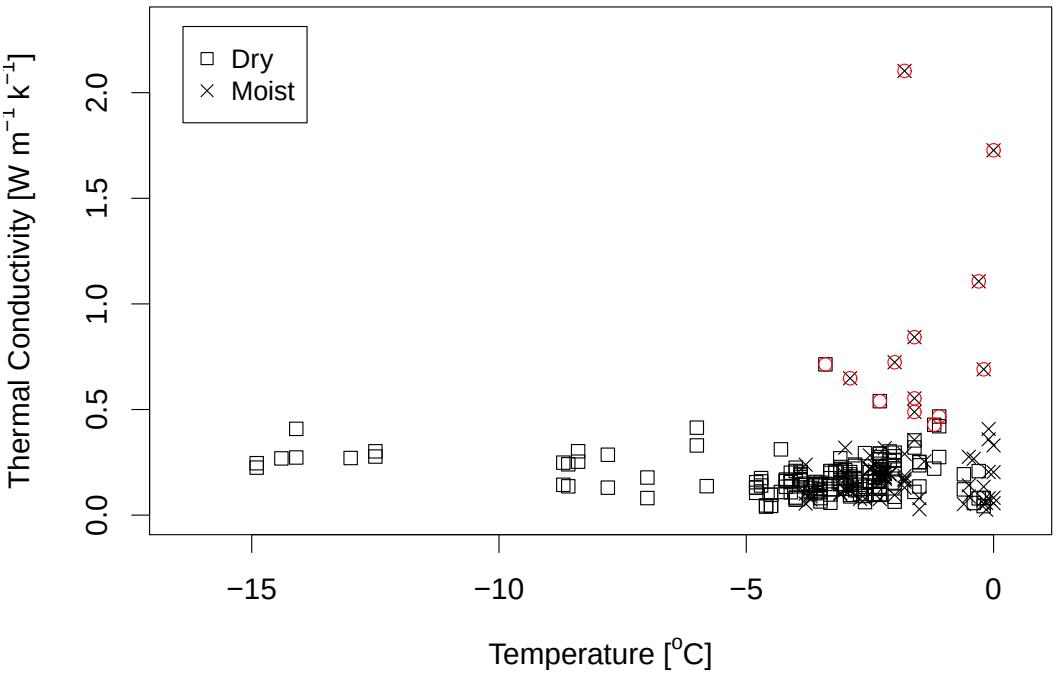

Figure 2.8: λ *versus temperature for all samples. Outliers are circled in red.*

Table 2.7: *Significant correlations between thermal conductivity and layer temperature.*

Grain	Pearson R	P-value	Spearman ρ	P-value	outliers rem.	# **Valid**
FC	0.548	8e-9	0.539	1e-8	N	96
MF*	-0.401	4e-5	-0.324	0.001	Y (4)	99
MF	-0.403	2e-5	-0.324	0.001	Y (4)	108

Many outliers shown in Figure 2.8 were from moist layers. Table 2.8 shows significant correlations between thermal conductivity and layer temperature when moist and dry layers are treated separately. Moist FC and RG both have moderate positive correlations; dry FC have a weak positive correlation and dry MF has a weak negative correlation.

A multivariate solution for thermal conductivity may be achieved in several ways: First, by considering all grain types that have positive monotonic relationships between λ and both density and temperature. We may further subdivide these by dry and moist layers. Correlation analysis has already shown that density and layer temperature are correlated

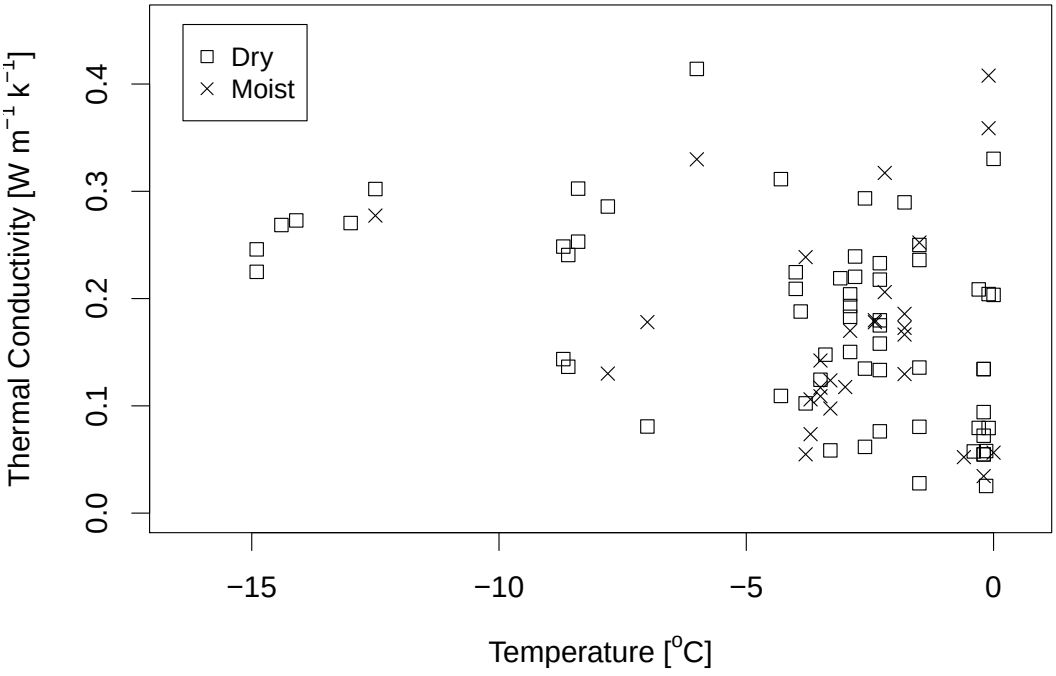

Figure 2.9: λ *versus temperature for melt-freeze (MF) forms.*

with thermal conductivity, at least for some grain types. Based on the scatter plots in this study as well as the results of Sturm et al. (1997) linear or quadratic models would be expected to provide the best fit.

Potential models were investigated using the linear model fitting 'lm' function in the statistical software suite R (R Core Team, 2013). A backwards stepwise regression was performed against λ to see whether a multivariate model actually offers a better solution than

Table 2.8: *Correlations between thermal conductivity and layer temperature by treating dry and moist layers separately.*

Grain Type	Pearson R	P-value	Spearman ρ	P-value	outliers rem.	# **Valid**
FC moist	0.71	5e-5	0.662	2.33e-4	N	26
FC dry	0.596	5e-8	0.458	6.63e-5	N	70
RG moist	0.768	0.016	0.735	0.024	N	9
MF dry	-0.490	5e-5	-0.399	0.001	Y (2)	62

a single variable model. Density, temperature and time-averaged slope-normal temperature gradient were all considered as potential independent variables. Based on the results already presented, melt-freeze and non-melt-freeze grains were treated separately. All sets were tested with and without statistical outliers.

The subset of dry non-MF grains yielded the following equation, which was constrained to equal the thermal conductivity of air when the density is zero:

$$\lambda = 1.562e^{-6}\rho^2 + 8.094e^{-5}\rho + 0.024 \tag{2.8}$$

with adjusted $R^2 = 0.94$, where λ has units of W m^{-1} K^{-1}. This has a similar form to Equation (12) from Calonne et al. (2011). Figure 2.10 shows the grains plotted against density. When extrapolated to the density of pure ice ($\approx$ 917 Kg/m^3) Equation 2.8 predicts $\lambda = 1.41$ W m^{-1} K^{-1}, well below its true value of ≈ 2.2 W m^{-1} K^{-1}.

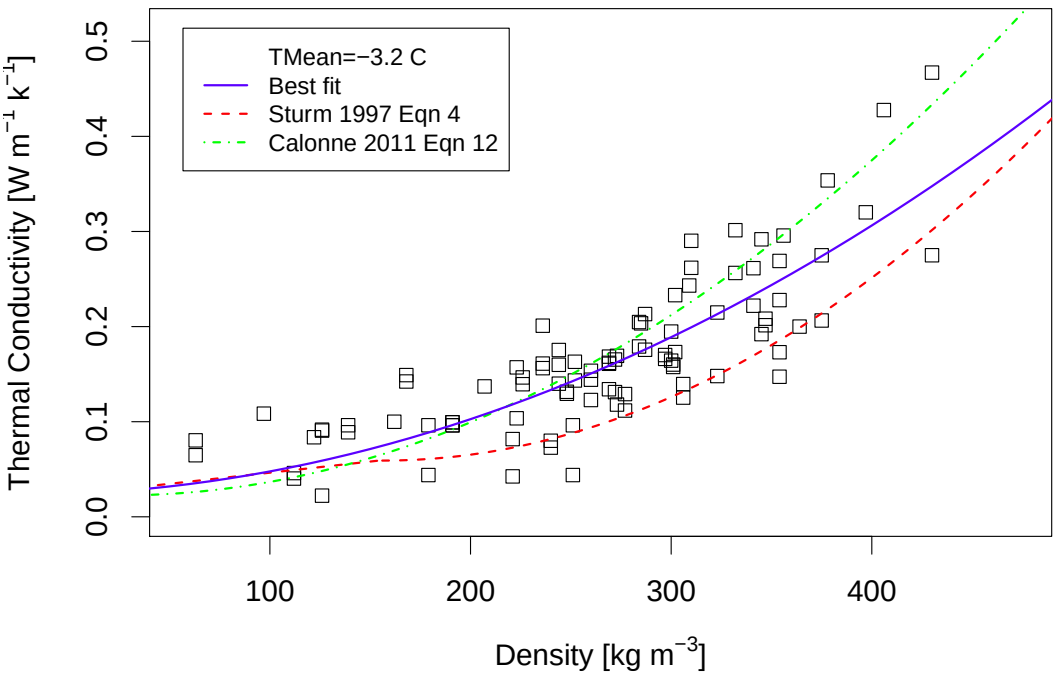

Figure 2.10: *Quadratic model fit for all dry non-melt-freeze samples of λ. Equation (4) from Sturm et al. (1997) and Equation (12) from Calonne et al. (2011) are included for reference. All referenced equations are included in Figure 2.5*

Although Equation 2.8 fits the measured data relatively well, it is likely less accurate for snow with very low or very high densities. When compared to the best-fit equation from Sturm et al. (1997) the disparity between their data set and ours becomes evident. There are several possible reasons but the most likely is that our mean temperature was almost 10 °C warmer than the majority of their samples. Unfortunately temperature did not emerge as a significant variable for this subset of data. For the subset of moist non-melt-freeze grains layer temperature did emerge as a significant ($p \leq 0.05$) predictor as part of a linear model of the form $\lambda = a + b\rho + cT$, but extrapolations beyond the relatively narrow range of temperatures yielded unrealistic values of λ. It should be noted that although moist grains should, by definition, exist only at 0.0 °C layers were sometimes classified as such even though the measured temperature was colder. Possible reasons for this discrepancy include strong insolation on many of the study days and the relatively crude nature of the 'glove test' (CAA, 2007). Temperature was also a significant predictor for the subset of dry MF grains while density was not. The equation,

$$\lambda = 0.140 - 0.010T \tag{2.9}$$

gives an adjusted $R^2 = 0.24$. The independence of thermal conductivity from density in MF layers has already been discussed; however, the decreasing values with warmer layer temperatures does not intuitively make sense. Although this result cannot be dismissed outright it seems more likely that it is due to the character of the cold lab crusts, which were from a single site and make up all measurements below -10 °C.

Subsection 2.6.2 Summary

This section probed for statistically significant relationships between physical parameters of the snowpack and measured thermal conductivity. Parameters were restricted to those commonly measured in the field, that is density, layer temperature, temperature gradient, moisture and grain type. As with previous studies, density was typically the single best

predictor of thermal conductivity for all grain types except for melt-freeze crusts. When compared with the empirical equations of Sturm et al. (1997) our data show similar trends but our values of thermal conductivity were typically higher. There is very likely a temperature dependence as the majority of our measurements were made at warmer snowpack temperatures but layer temperature did not emerge as a significant predictor variable. These findings are similar to those published by Sturm et al. (1997) with the possible exception that for our samples density was a good predictor for thermal conductivity in samples that had undergone kinetic (temperature gradient) metamorphism. This difference is likely one of semantics as their data included samples of depth hoar and highly faceted grains, while our 'facets' were typically transitional forms, barely differentiable from rounded grains.

Although field methods do not permit the level of precision offered by a model there are some worthwhile avenues to explore in future studies: 1) Dry and moist layers should be treated separately during analysis due to the increased presence of free water. In reality the change in actual water content is gradual but this distinction appears to be sufficient if precise measurements are not possible; 2) Grain type may be broadly treated as 'MF' or 'non-MF'. Our data set did not include depth hoar but based on work by Sturm and Johnson (1991) they should also be treated as a separate grain type; 3) Empirical equations based on density alone do illuminate trends but they are not sufficient on their own as predictive equations. Other parameters, likely temperature, need to be incorporated but our data did not include enough measurements over a wide enough range to accomplish this.

2.6.3 Thermal conductivity by site

The main goals of measuring crust thermal conductivity were to document rates of change and to identify significant correlations with other measured parameters. This knowledge is primarily useful for use in physical models such as SNOWPACK (Bartelt and Lehning, 2002) but also in mesoscale and climate weather models (e.g. Cook et al., 2008) that depend on parameterizations to model physical characteristics of ground cover including snow. This

section examines temporal changes in individual crusts.

Detailed information regarding the study sites and narratives of crust formation and evolution are included in Appendix A and all measurements are given in Appendix C. Measurement intervals for each crust are outlined in Table 2.2. Measurements were taken above, below and within the crust each field site except for SR09. Measurements of vertical thermal conductivity were taken at some field sites and for all cold lab experiments. Temperature and vertical temperature gradient were monitored with thermistors at some field sites and throughout all but one cold lab experiment. Temperature profiles were also measured manually at field sites during each visit as part of a standard test profile. It is worth reiterating that the convention used througout this paper is that a negative temperature gradient means colder temperatures closer to the snow surface.

Study sites FI0109 and FI0308 were both located at the Mount Fidelity study plot adjacent to the weather station. More information on this and other study is included in Appendix A and in Figure A.4. FI0109 formed as a thin ice lens in early January 2010. Thermal conductivity was tracked within the crust when possible as well as in the layers above and below throughout the remainder of the season. The layers at this site were buried relatively quickly and thus remained viable for sampling throughout the remainder of the season, through April 14. Figure 2.11 shows the evolution over time of thermal conductivity in the layer immediately above the crust and Figure 2.12 shows the layer below. The error bars represent the instrument error published by Hukseflux, the manufacturer of the TP02 instrument (Hukseflux, 2003). Grains in both layers progressed over time from precipitation particles (PP) to mixed forms (either RGxf or FCxr).

Thermal conductivity increases over time in both layers, with increased variability evident by early March. The thermal conductivity was positively correlated with density in both layers which is to be expected given the relationship already reported in the previous section. Both layers also had a moderately strong positive relationship between thermal conductivity

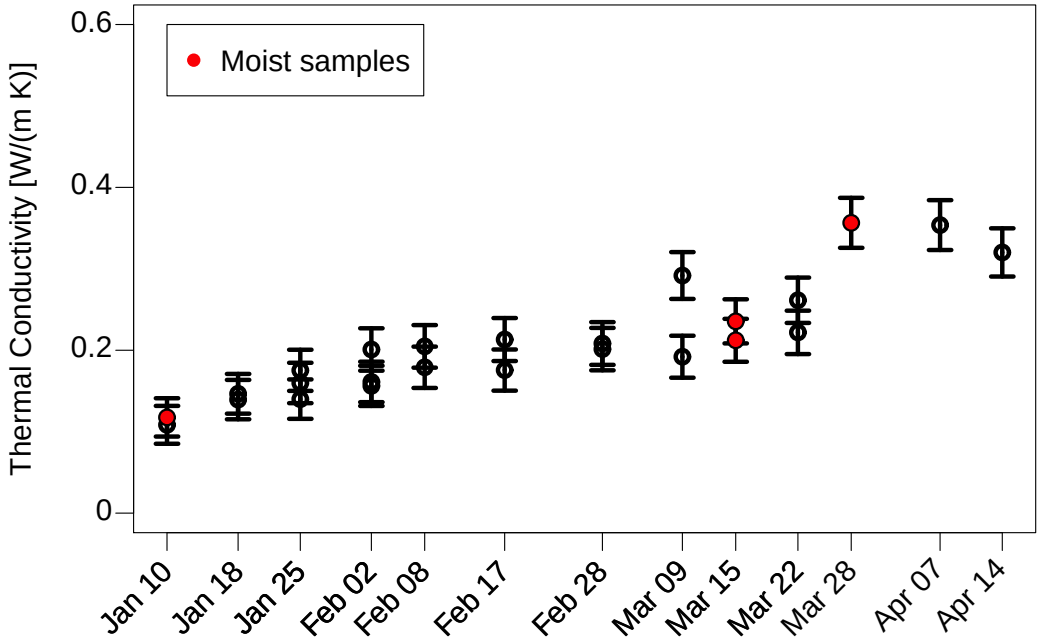

Figure 2.11: *Time series of thermal conductivity measurements in the layer above the FI0109 crust. Error bars denote range of possible values based on the thermal conductivity probe manufacturer's stated accuracy. Two measurements were attempted during each site visit but some were invalid.*

and layer temperature, as shown in Table 2.9.

Removing the moist layers from the correlation calculation did not affect the correlations between λ and layer temperature in either case, which runs counter to what was found in the previous section and may hint that this effect was more a function of specific layers in the dataset than it was a function of free water in each layer. Although calibrated thermistors and thermocouples were deployed at this site, they were inserted immediately above and

Table 2.9: *Pearson correlations between λ, density (ρ) and layer temperature (T) for layers above and below the FI0109 crust. All correlations are significant to $p \leq 0.01$.*

Layer	ρ	ρ range [kg m^{-3}]	T	T range (°C)	Grains	# **Valid**
Above	0.83	97-397	0.78	-4.7,-1.6	PP,FCxr/RGxf	25
Below	0.79	112-430	0.80	-4.8,-1.1	PP,FCxr/RGxf	27

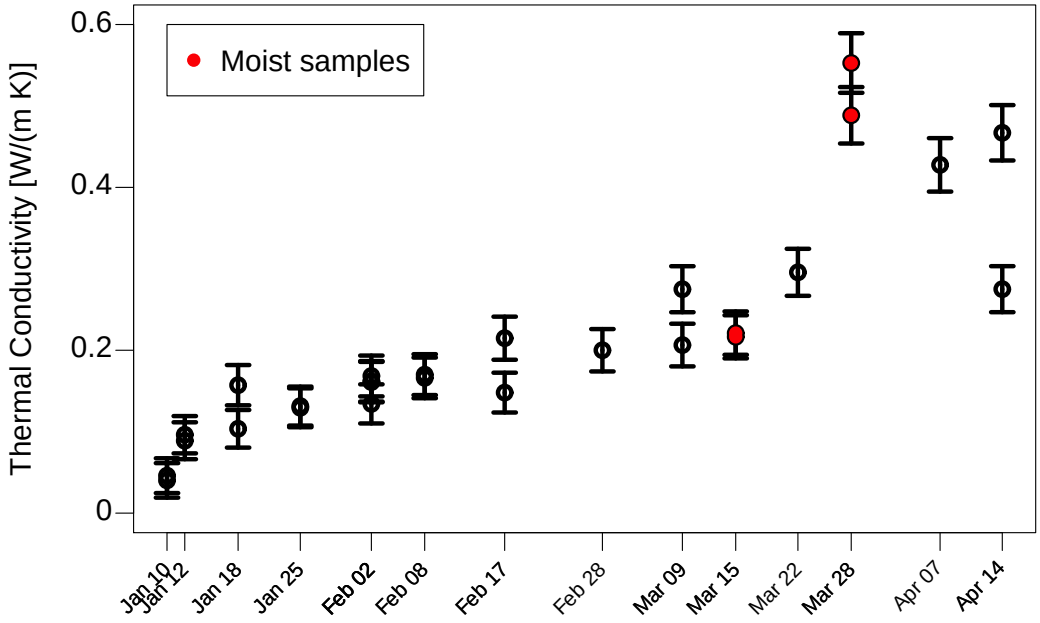

Figure 2.12: *Time series of thermal conductivity measurements in the layer below the FI0109 crust at Mt Fidelity study plot.*

below the crust so no analysis could be performed on rates of change of λ with respect to the vertical temperature gradient. Test profiles did note several very modest temperature gradients, on the order of 0.1 °C 10 cm^{-1} both above and below the crust.

Crust FI0308 formed during a period of warm weather and intense insolation in early March 2010. Unlike FI0109 it was thick enough to sample with the TP02 probe, however there were no identifiable temporal trends. Figures 2.13 and 2.14 show the time series for the layers above and below the FI0308 crust. As was the case with the layers above and below FI0109 the strongest correlations are between thermal conductivity and density. The correlation between layer temperature and λ was only statistically significant for the layer below the crust, and was improved when the moist samples were removed from the data set. This result is not included in Table 2.10 due to the small sample size.

The final natural crust presented here is RP0112. It formed in the study plot at Rogers

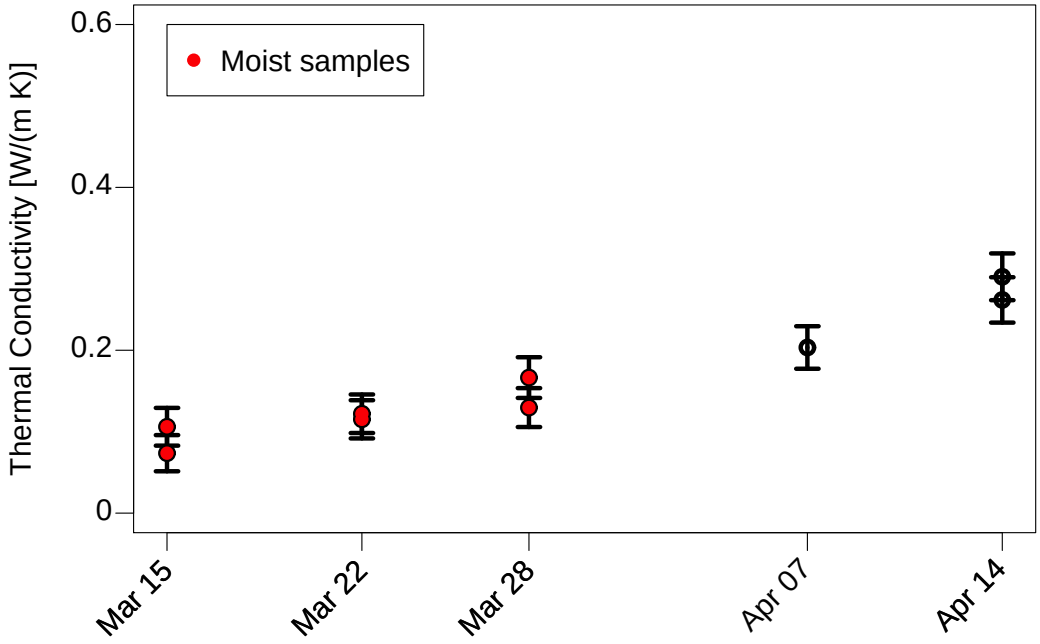

Figure 2.13: *Time series of thermal conductivity measurements in the layer above the FI0308 crust.*

Table 2.10: *Pearson correlations between λ, density (ρ) and layer temperature (T) for layers above and below the FI0308 crust. All correlations are significant to p ≤ 0.05.*

Layer	ρ	ρ range [kg m^{-3}]	T	T range (°C)	Grains	# **Valid**
Above	0.87	166-310	∼	-3.7,-1.8	DF,MF,RG	9
Below	0.98	228-332	0.78	-3.7,-1.8	FCxr,RGxf	8

Pass at the same time as BV0112 but was not subject to the continuous insolation and warm temperatures as the latter was due to its slightly higher elevation and shaded location. Time series plots of the layers above and below are shown in Figures 2.15 and 2.16. While both layers do appear to undergo a moderate increase in thermal conductivity, much of the week-to-week variability is within the bounds of the measurement error of the TP02. The layer above the crust has a moderately strong positive correlation between λ and density (R = 0.79, p $\leq$ 0.01) but that is the only correlation. The crust itself was noted to have many

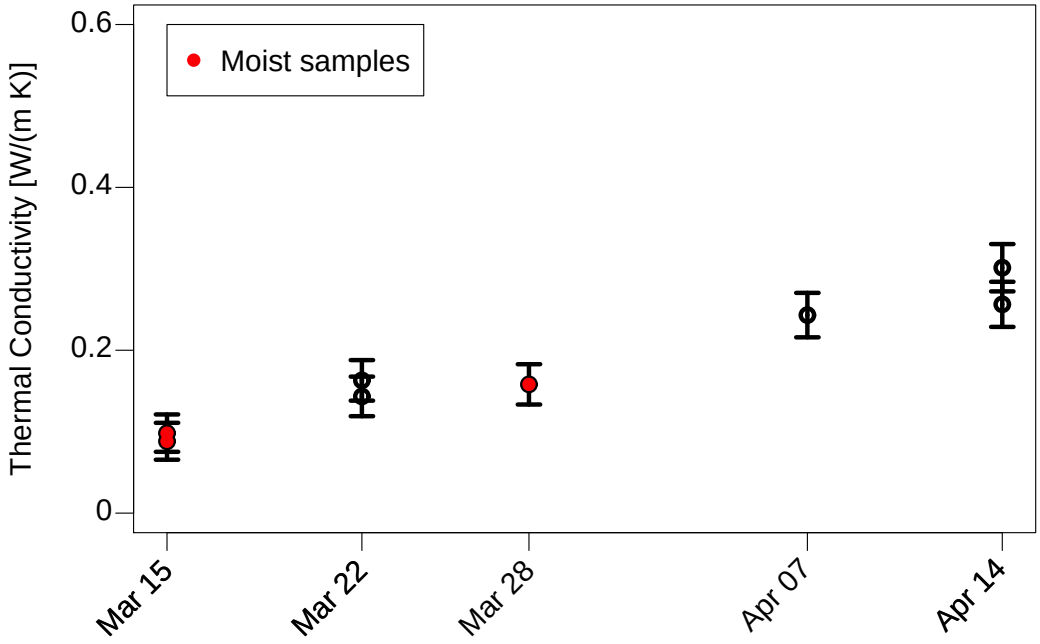

Figure 2.14: *Time series of thermal conductivity measurements in the layer below the FI0308 crust.*

icy inclusions and showed no visually or statistically identifiable trends or correlations.

The first attempts at cold lab experiments used sifted snow and manual wetting to create a uniform crust. These attempts were largely unsuccessful and usually resulted in percolation channels and inhomogeneous ice layers within the sifted snow. Later attempts at compacting the snow before wetting were also unsuccessful in creating a homogeneous crust. As a result natural crusts were harvested into an insulated box (shown in Figure 2.17) from a flat area near the residences at Rogers Pass and brought into the lab, where thermistors mounted on wood blocks 10 cm apart were inserted into the sample. A strong temperature gradient was induced by harvesting the crusts during the daytime and placing the uncovered box into the cold lab. The insulated base and size ensured that lower portions of the sample remained warm, at least initially, while upper portions of the crust quickly cooled. The size of the box limited the total number samples to around six and the measurement intervals were lengthened for each experiment to try and determine the time scale of changes in thermal

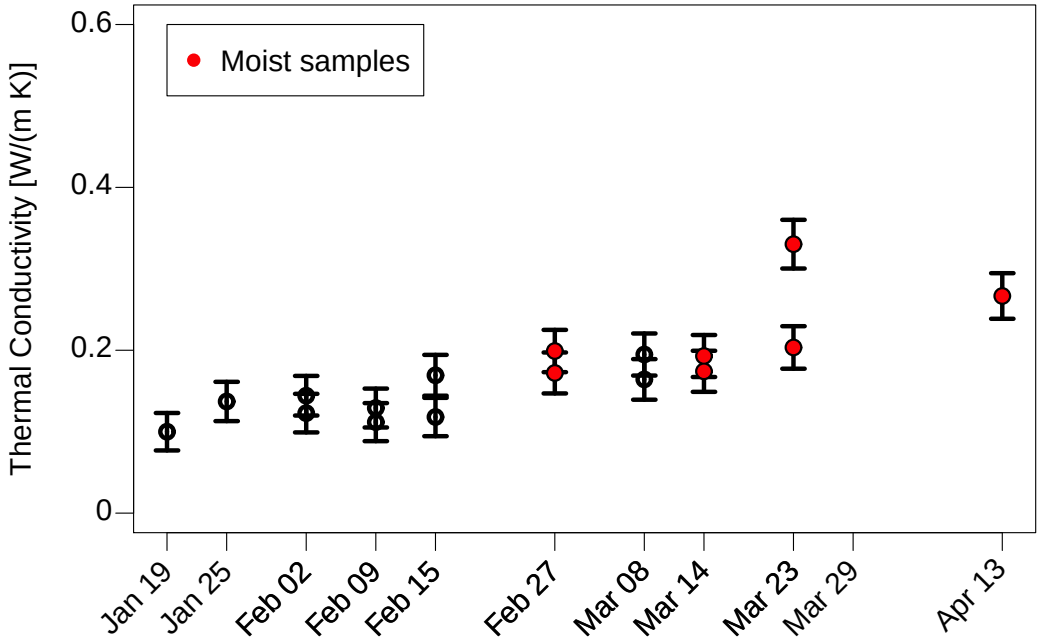

Figure 2.15: *Time series of thermal conductivity measurements in the layer above the RP0112 crust.*

conductivity under high temperature gradients. Table 2.2 summarizes the total duration of each experiment as well as the measurement intervals.

The majority of the cold lab experiments did not show any definite trends, however the final two, LAB0410 and LAB0413 are worth exploring further. Figure 2.18 shows the full time series of vertical measurements through the crust for LAB0410. The vertical dashed line denotes the time at which the crust froze according to the thermistors. The first set of measurements were taken outside, just before the crust was placed into the sample box and brought into the lab. There is a sharp increase over the first 24 hours, followed by a gradual decrease over the next 24 hours another increase at the final measurement.

The crust had an average density of 385 Kg m^{-3} when it was harvested, but could not be reliably sampled once it froze so the correlation between λ and ρ could not be tested, however if the results from field crusts are any indication, density would not be a reliable predictor. The vertical temperature gradient peaked about 9 hours after the crust was placed in the

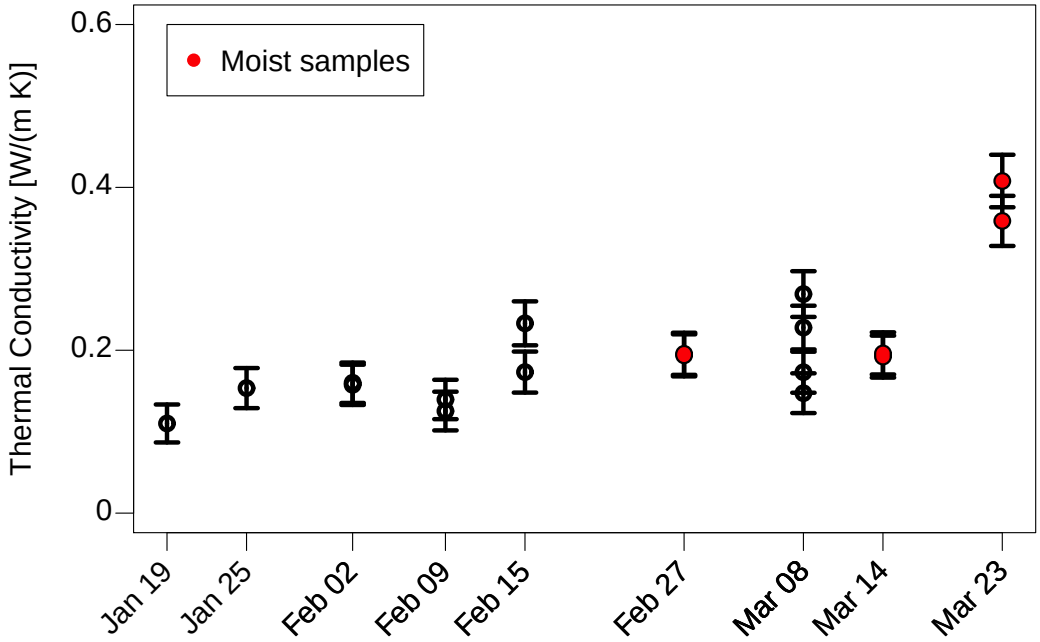

Figure 2.16: *Time series of thermal conductivity measurements in the layer below the RP0112 crust.*

cold lab, just about the time that it became fully frozen. The crust temperature ranged from -0.1 °C at the start of the experiment to -15.1 °C at the end, while the average vertical temperature gradient between observations varied from -2.96 °C 10 cm^{-1} to -0.06 °C 10 cm^{-1} at the conclusion of the experiment.

In this crust there were likely two competing processes affecting the thermal conductivity: As the moist layer froze new bonds were formed enabling more efficient transport of heat through the grain matrix. At the same time, a strong vertical temperature gradient would favour formation of vertically oriented bonds, but would also result in at least some faceting, which would increase the tortuosity and decrease the number of thermal pathways. Other studies have observed the preferential formation of vertical bonds when a sample of natural snow was subjected to continuous strong vertical temperature gradients in the lab (Greene, 2007) and the same mechanism has been hypothesized for natural depth hoar (Sturm and Johnson, 1992).

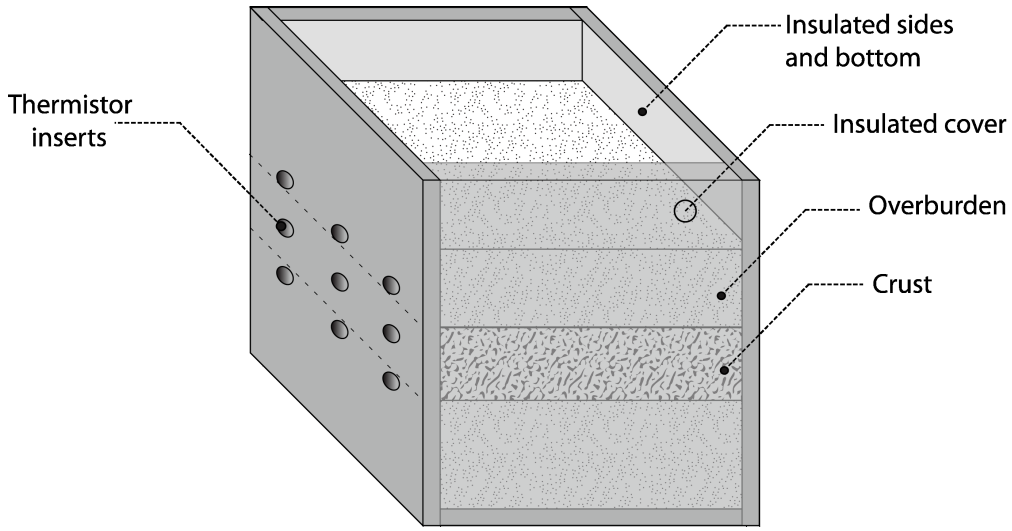

Figure 2.17: *Schematic of the insulated box used for cold lab experiments. The front and sides are insulated with foam while the top is left uncovered.*

There were no significant ($p \leq 0.05$) correlations between the rate of change of λ and average temperature, temperature gradient or time. It is possible that the relatively small sample size precludes the identification of any statistically significant correlations, or that a combination of factors is responsible for the observed changes.

The LAB0413 time-series is shown in 2.19. Sampling was done daily over a period of 5 days at intervals of approximately 24 hours each. As was the case with other cold lab experiments, a density sample was only obtained during the initial sampling before the crust was brought into the cold lab. This 40 cm thick sample averaged 385 Kg m^{-3} before it was placed into the insulated box. No settlement was observed during the course of the experiment. The trend in thermal conductivity closely mirrors that seen in LAB0410, with an initial increase over the first 48 hours. Unlike LAB0410 a weak trend of decreasing thermal conductivity continues through the end of the experiment.

Figure 2.20 shows the corresponding time series of average layer temperature and temperature gradient for the crust. Initially the upper portions of the crust are warmer but by 12 hours into the experiment the gradient reverses and remains equal or greater to 1 °C 10 cm^{-1} until approximately the third day. Table 2.11 shows the correlations between changes

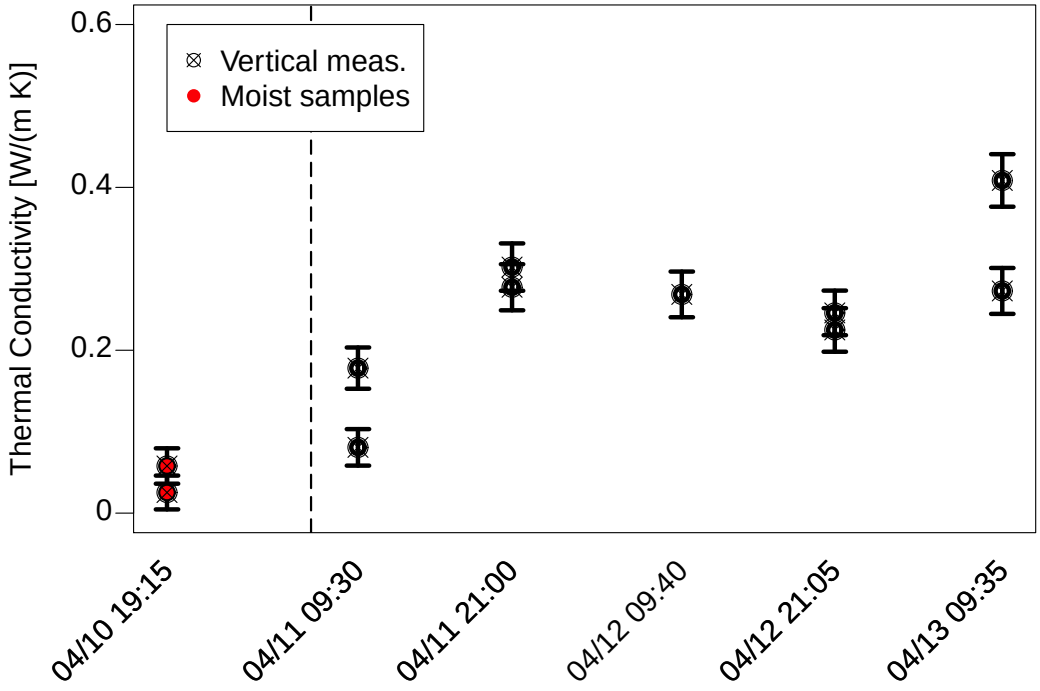

Figure 2.18: *Time series of thermal conductivity measurements for LAB0410. The vertical dashed line denotes the time at which the crust froze.*

over time in λ and both layer temperature and temperature gradient for this crust. The rate of change of thermal conductivity between measurements is strongly correlated in this case with the average temperature between measurements. Taken together with the correlation with the average temperature gradient a plausible physical explanation is that the initial sharp increase in thermal conductivity is due to bonds freezing, followed by the preferential formation of vertical bonds as the temperature gradient reaches a maximum. The link with the observed decrease in thermal conductivity over the final seventy-two hours is less clear, but may be related to continued faceting in the crust. This interpretation could be tested by conducting a similar experiment where the crust is cooled and then re-warmed over a similar time period.

Figure 2.21 shows a time series of thermal IR images taken immediately after a new crust face was exposed at each observation time. The image in the upper left was taken

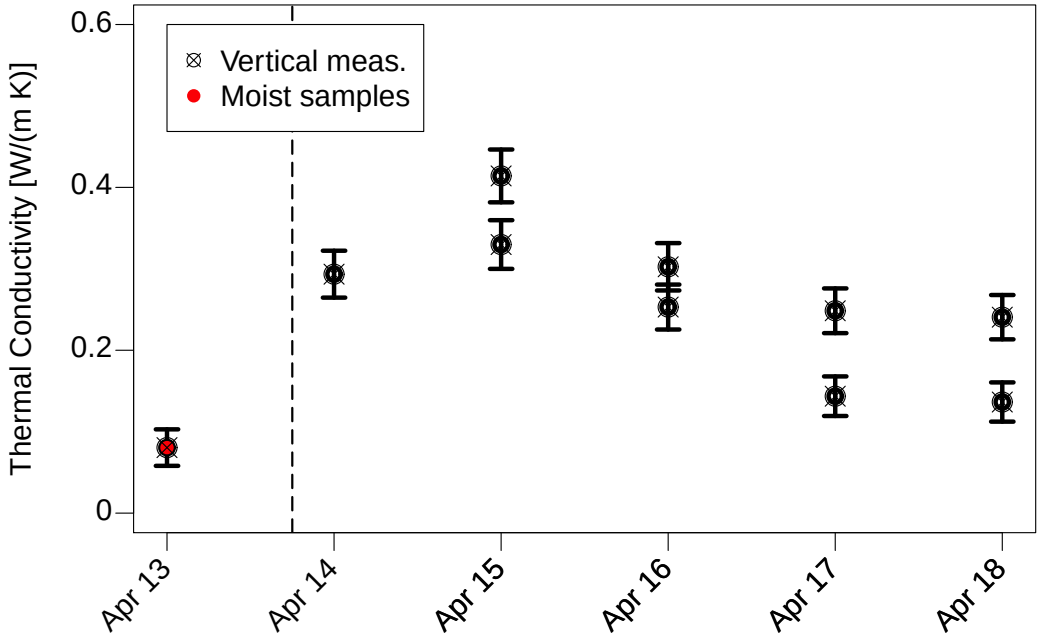

Figure 2.19: *Time series of thermal conductivity measurements for LAB0413.*

just after the crust was brought into the cold lab. The area of uniform temperature has just been exposed and the strips to each side had already had the chance to cool for several minutes. The overburden layer has cooled substantially by the next observation and the effects of imperfect insulation from the walls of the box are evident as only a small area of the lower crust remains near freezing while the sides have frozen. By the second observation at 50 hours this effect is still evident, though less pronounced and by 73 hours the crust's

Table 2.11: *Pearson correlations between rates of change of λ, average layer temperature (column 6) and average temperature gradient (column 7) for the LAB0413 crust. All correlations are significant to $p \leq 0.05$.*

Crust	λ range	T range	TG range	# Valid meas.	$\Delta\lambda$ Tavg between meas. $\lambda \sim$Tavg	$\Delta\lambda$ TGavg $\lambda \sim$TGavg
LAB0413	0.08-0.41	-1.5,-8.6	-0.1,-2.5	10	0.86	-0.68

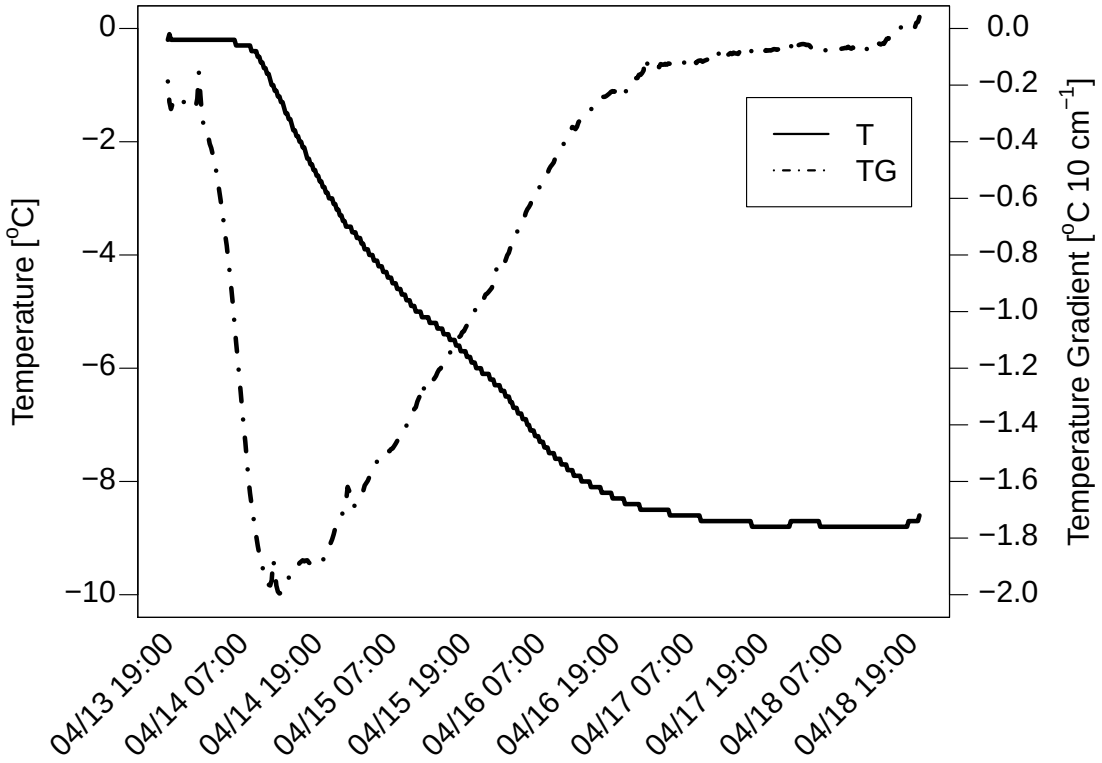

Figure 2.20: *Time series of average layer temperature and vertical temperature gradient for the crust in LAB0413.*

temperature is mostly uniform.

Figure 2.22 shows the crust at 99 hours with a reduced temperature scale. Relatively small variations in crust temperature can still be seen, and would not likely be identified using conventional thermometers or thermistors. This series of images shows the complexities of thermal pathways even in a relatively simple 2-dimensional environment. It is important to note that some recent research (Schirmer and Jamieson, 2014) indicates that a combination of inhomogeneous snow surfaces and sharp contrasts between snow and air temperature may result in false temperature gradients in thermal IR photography and video. The use of thermal IR methods for qualitative or illustrative purposes as it is done here is likely safe.

As with LAB0410 the change in thermal conductivity was affected by the competing processes of freezing during the initial part of the experiment and faceting as a sharp vertical

temperature gradient developed. This is evident both in the time series of thermal infrared images as well as the moderate correlation between rates of change of λ and the average temperature gradient.

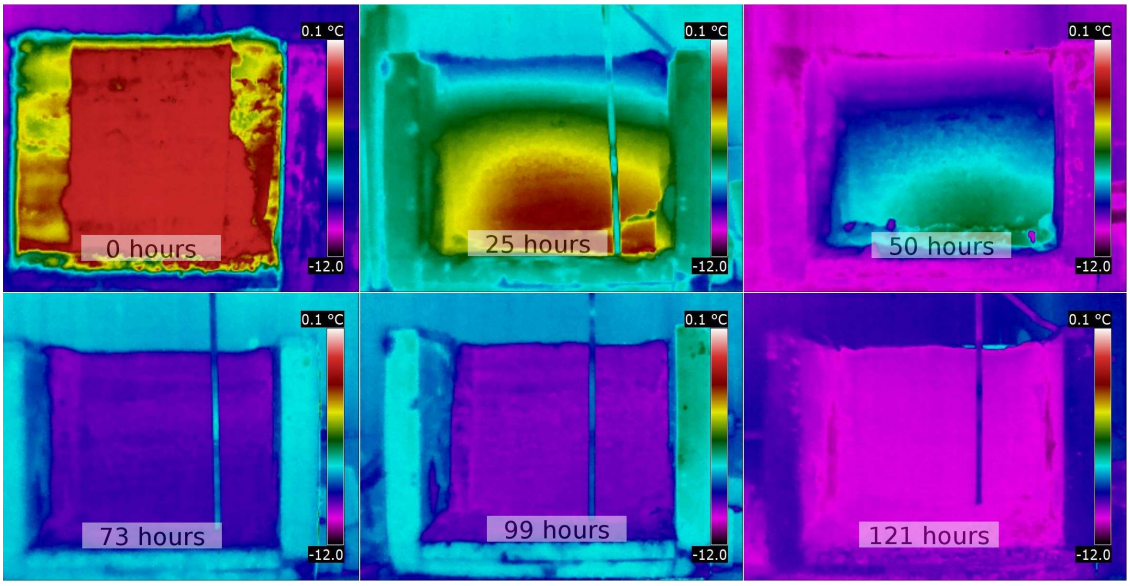

Figure 2.21: *Montage of thermal IR images of crust LAB0413 as it was cut back and exposed for each observation. The ruler is visible in most images as a vertical discontinuity.*

Samples from the South Run (SR) and Beaver Valley (BV) sites did not show any temporal trends or correlation with other measured physical parameters such as density, layer temperature or average vertical temperature gradient. Snow at these sites was subject to both strong insolation (South Run) and persistent warm air temperatures due to low elevation (Beaver Valley) and layers remained moist for extended periods at both sites.

Subsection 2.6.3 Summary

This section presented a summary of time series measurements of natural layers in the field and in a cold lab. Most crusts did not yield any statistically significant correlations with regards to thermal conductivity or rates of change of thermal conductivity. The exception was the final cold lab crust, LAB0413 where the rate of change of λ was correlated with both the layer temperature and the average vertical temperature gradient. A number of non-MF layers did have significant correlations between λ and density. Taken together with results

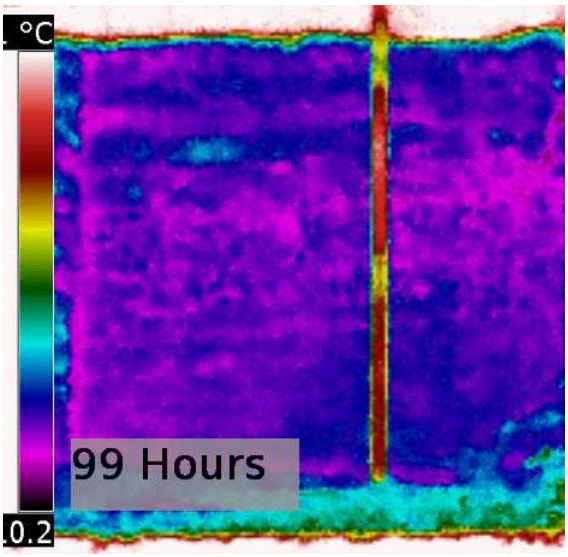

Figure 2.22: *Thermal IR image at 99 hours, scaled to show small variations in temperature.*

from the previous section, the evolution of thermal conductivity can be predicted, with some error, without precise knowledge of the grain form as long as it is not highly faceted.

The data set had a number of shortcomings, some due to the experimental design and others due to the relatively warm winter of 2009-10: 1) Crust samples in the cold lab experiment were too small and often too brittle once frozen to accurately measure density, even if it likely does not correlate well with thermal conductivity; 2) With the exception of cold lab crusts, the small range of temperatures in all tracked layers made correction for temperature virtually impossible; 3) Temperature and temperature gradient were not tracked in layers above and below natural crusts, negating an opportunity to link them to rates of change of λ; 4) The thermal IR camera was only available for short periods and it is likely that the presence of small temperature gradients was missed, especially at crust boundaries.

Given these results, future experiments should focus on measuring thermal conductivity under measurable and controllable conditions in a cold lab. The most interesting results were from LAB0413, where the thermal conductivity peaked just after the entire crust froze, then gradually diminished through the end of the experiment. These observations are consistent with results published by Kaempfer et al. (2005) as well as the theoretical pathways proposed

by Kaempfer and Schneebeli (2007), Kaempfer et al. (2009) and Shertzter et al. (2010). Structural changes identified by Near IR photography are covered in Chapter 3.

2.6.4 Spatial variability of thermal conductivity

A significant assumption when tracking changes over time is that a given layer began with uniform physical properties and all changes occurred uniformly within a study plot on the order of several metres square . As many studies (e.g. Campbell and Jamieson, 2007; Landry, 2002; Schweizer et al., 2008; Buhler and Jamieson, 2012) have found, this can be a problematic assumption when applied to snowpack stability and thus presumably to the structure of a given layer. This may be a reasonable assumption if the site is relatively small and if the meteorological conditions contributing to the layer formation are known. This can become complicated for melt-freeze crusts due to how they are formed: A rain crust will almost certainly have percolation channels and icy inclusions while crusts formed due to above-freezing temperatures and/or direct insolation may be more uniform depending on the duration and intensity of the heating.

Since measurements of thermal conductivity in buried layers are necessarily destructive it is not possible to measure the initial spatial variability for the field sites described in this chapter. This uncertainty is offset somewhat by selecting sheltered sites and by taking multiple measurements of thermal conductivity during each site visit. It is also possible to test these assumptions to a certain extent by taking spatial measurements across a site that should be uniform.

Figure 2.23 shows a planar south-facing slope on the "South Run" area of Mt. Fidelity on February 5, 2010. In late January a melt-freeze crust formed here due to solar radiation and was buried January 31. Thermal conductivity was measured at 2 m intervals across an area 20 m^2. The sample area was planar with sparse mature timber adjacent on either side. Due to the low angle of the sun in January as well as blocking by surrounding topography, the entire sample area received approximately uniform insolation during the period of crust

Figure 2.23: *South-facing site used to evaluate spatial variability.*

formation. The crust was of uniform visual appearance and thickness across all sample sites.

Figure 2.24 shows the measured thermal conductivity (in red) and the layer temperature (in black) at each sample location. The right transect has a slightly lower mean thermal conductivity, possibly due to shading from the single tree visible in Figure 2.23. There are no clear trends in the upslope direction, nor is there a relationship between layer temperature and thermal conductivity in this sample. Near-infrared photographs taken at each sample site showed qualitatively similar profiles of specific surface area and are discussed further in Chapter 3.

The results in this section illustrate that great care must be taken in selecting study sites for tracking changes in thermal conductivity. It is likely that the conditions under which a layer is formed and before it is buried are important in determining its initial spatial variability. This does not imply that, for example, rain crusts cannot be tracked over time, but that during analysis care must be taken to separate temporal trends from spatial trends.

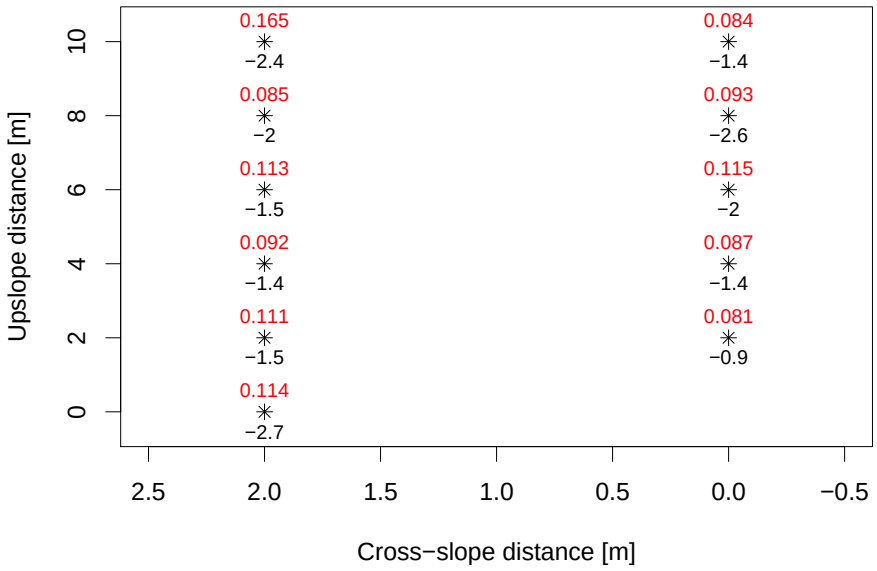

Figure 2.24: *Thermal conductivity measurements on a planar south-facing slope. Numbers in red are thermal conductivity and numbers in black are layer temperature, both recorded concurrently.*

Evidence for the former may be supported by measurements of density, temperature and temperature gradient or by visual observations of structure. Potential study sites should also be carefully evaluated for any factors such as vegetation, slope, aspect or exposure to wind that may increase the spatial variability.

2.7 Chapter Summary

Thermal conductivity was measured over time in five natural crusts and five crusts in the cold lab. For natural crusts the thermal conductivity of layers above and below the crust was also monitored. The Hukseflux TP02 thermal conductivity probe was found to be an effective instrument for both field-based and lab-based studies. A number of difficulties were encountered, most having to do with the warm temperatures and low snowfall during the winter of 2009-10 in southwestern British Columbia.

Thermal conductivity measurements were grouped according to grain type and compared with previous studies including the data published in Sturm et al. (1997). Distributions for each grain type were tested for normality using the Shapiro-Wilk Normality test. It should be noted that the Shapiro-Wilk implementation in R uses an extension (Royston, 1995) of the original test which is valid for samples up to n = 5000. The null hypothesis of normality for all grain types was rejected based on the presence of a small number of outliers in each data set. This was especially prevalent in layers that had been classified as moist. When outliers were removed, then mean thermal conductivity of non-MF grains were similar to those published by Sturm et al. (1997).

The subset of melt-freeze (MF) grains was especially varied with the highest and lowest measured values approaching those of pure ice and air respectively. Two new subsets were created; pure MF (MF*) and MF containing aggregates of faceted forms (MFFC). The mean thermal conductivity of the former was similar to the mean for 'melt grain clusters' reported by Sturm et al. (1997).

Correlations were computed between λ and easily measurable physical parameters such as layer temperature and density. The influence of outliers and of layer moisture was also checked. The strongest correlations between density and λ were found for FC and RG grain types. The correlation between ρ and λ runs counter to conclusions published by Sturm et al. (1997) and illustrates a difficulty in using grain type classifications; it is very likely that the FC in the present study were less faceted, and had settled and bonded to a greater degree than those measured by Sturm. Though not directly applicable to MF grain types, the observations of Calonne et al. (2011) and Greene (2007) that faceting is not necessarily accompanied by changes in density may be relevant, in that the MF classification encompasses a wide variety of structures from poorly-bonded clusters to uniform well-bonded layers.

Empirical equations from Sturm et al. (1997) matched the general trend of increasing λ with increasing density but actual predicted values of λ were consistently lower than measured values from the present study. Attempts were made to formulate a new empirical equation but layer temperature did not emerge as a significant predictor. A polynomial equation with a similar form to Sturm's was produced for the set of all dry non-MF forms. Like Sturm's it is likely of limited value outside of the range of temperature from the dataset from which it was derived. If the data from Sturm's study, which were measured at much colder temperatures, were combined with those of the present study it is possible that layer temperature could be incorporated as a statistically significant predictor in a more generalized empirical equation.

Time series of individual layers were examined for trends in thermal conductivity and correlation with layer temperature, density and temperature gradient. In this case several layers showed good correlations between λ and both density and layer temperature suggesting that the characteristics of the individual layer are as important as the grain type for non-MF forms.

Two cold lab crusts, LAB0410 and LAB0413 showed similar trends in thermal conductivity. Both showed increases in λ until some time after the crust was frozen, then a slow decrease. A potential explanation for these observations is the formation of oriented bonds as the layer slowly freezes thus increasing λ, followed by faceting due to the unequal cooling of the crust from the top down. A series of thermal infrared images taken during the LAB0413 experiment confirms that sharp vertical temperature gradients were present well after the crust was frozen.

The results from this chapter offer several avenues for future research: 1) The results from the present study should be combined with those of Sturm to examine more thoroughly the effects of layer temperature on thermal conductivity. Their data were gathered at much colder temperatures while ours, with the exception of cold lab crusts, were often just below freezing. Should that attempt be successful the role of moisture may also become more evident; 2) Further cold lab studies should be conducted with melt-freeze crusts. The results from LAB0410 and LAB0413 match hypotheses proposed by Kaempfer and Schneebeli (2007) and Kaempfer et al. (2009) regarding increased tortuosity and changes in thermal pathways under strong temperature gradients. These studies should include the sampling of temperature as well as both vertical and horizontal measurements of thermal conductivity. Temperature measurements should be supplemented with thermal IR photography as the detail offered by embedded thermistors or thermocouples does not offer sufficient spatial resolution to identify small and transient temperature gradients.

Chapter 3

Near Infrared Photography

continuous process rather than a set of discrete steps it is easy to miss gradual transitions. In recent years the use of optical methods to quantify snowpack morphology, rather than size and shape, has seen increased use. Snow morphology influences the spectral albedo of snow (e.g. Wiscombe and Warren, 1980; Warren and Wiscombe, 1981) and has important implications in many fields of study outside of avalanche research, including remote sensing (e.g. Toure et al., 2008), climate modeling (e.g. Flanner and Zender, 2006) and snow chemistry (Douglas et al., 2008).

This chapter introduces the theory behind NIR and SSA and summarizes the results of studies by other authors. The equipment, field techniques and methods of analysis are summarized and results from this study from the winters of 2008-09 and 2009-10 are presented. It is important to note that the NIR portion of the solar spectrum is defined here as wavelengths between 700 nm and 2000 nm, and the meaning of the term varies somewhat across disciplines.

3.1 Specific surface area (SSA) theory and past studies using optical methods

specific surface area (SSA) is defined as the ratio of surface area to volume of a given sample of snow or ice crystals, with units of mm^{-1}. In some cases it is reported as the ratio of the surface area to volume times the density of ice and has units of $m^2\ kg^{-1}$. It generally decreases over time (Legagneux et al., 2003), and at accelerated rates at warmer temperatures (Taillandier et al., 2007) as new snow transitions from dendritic to rounded forms, though Dominé et al. (2009) record three instances where it increased. Various empirical (e.g. Dominé et al., 2007)

and prognostic (e.g. Jacobi et al., 2010) equations based on grain type or density have been proposed but there has been little practical validation for melt-freeze layers.

Prior to the late 1990s the only option for measurement of SSA was to use stereological methods. This required that samples either be cultivated in, or transported to a cold lab as well as access to specialized equipment. Aside from the difficulties in preserving natural snow samples, stereological techniques are time-consuming and may only measure small samples. In the past 15 years new imaging techniques have emerged, allowing sampling to be done relatively quickly and, as importantly, directly at field sites. Haddon et al. (1998) first published an experimental algorithm for the analysis of near infrared (NIR) images of snow profiles. Matzl and Schneebeli (2006) modified a digital camera with an 830 nm filter and correlated *in-situ* NIR photographs with SSA measured using stereological techniques. Calibrated NIR photographs could be mapped to measured SSA using an empirical equation with a correlation of 90%. This technique was found to be valid for layers as thin as 1 mm although results may be susceptible skewed by light leaking from adjacent layers (Matzl and Schneebeli, 2010). The importance of this light leakage when observing buried layers is debatable as radiation at NIR wavelengths does not penetrate far into the snowpack, with estimates ranging from 3.5 cm (Gallet et al., 2009) to 1-5 cm (Kokhanovsky and Rozanov, 2012), depending on the precise wavelength and grain geometry. The NIR spectrum above 900 nm has the additional property of weak sensitivity to impurities within the snow sample (Grenfell et al., 1981).

Toure et al. (2008) used techniques similar to those of Matzl and Schneebeli (2006) to derive the correlation length from the calculated SSA, while Tape et al. (2010) used similar equipment and techniques to quantify lateral variability in a sub-arctic snowpack, but did not calculate the SSA. Langlois et al. (2010) used a modified digital camera similar to that used by Matzl and Schneebeli (2006) but used a 750 nm filter and added 840 nm and 1000 nm filters in successive steps. The authors found that the geometric diameter, defined as

the average of the major and minor axis diameters, was weakly correlated with NIR, and that a stronger correlation might have been possible with an instrument sensitive to longer wavelengths. The reclassification of grain types into broad classes of 'large', 'medium' and 'small' spheres, and by assuming a shape factor for each (Kokhanovsky and Zege, 2004), it was also possible to retrieve the optical grain diameter from NIR photographs.

Gallet et al. (2009), and later Morin et al. (2010) used an active laser diode-equipped instrument known at DUFISSS to measure the reflectance of snow, then converted it to reflectance and SSA. The advantage of this instrument is that it emits at a single wavelength (1310 nm) and allow results to be integrated into radiative transfer models with greater ease.

Despite numerous field and modeling studies, there has been little research into SSA of melt-freeze crusts. These layers present particular difficulties as traditional assumptions regarding metamorphism are not always applicable: Although several studies have examined the formation of weak layers at the boundaries of crusts or buried wet layers under relatively high temperature gradients (e.g. Greene, 2007; Jamieson and Fierz, 2004), a number of experienced practitioners have also reported the development of facets and laminations in buried crusts even when the temperature gradient as measured by traditional means would imply such such weakening should not take place (John Hetherington, *pers. comm. 2009*).

The advent of models such as CROCUS (Brun et al., 1992) and SNOWPACK (Bartelt and Lehning, 2002; Lehning et al., 2002a,b) promise to mitigate some of these challenges; however many processes at the microstructural level are not well-understood and consequently not always well-modeled. Jacobi et al. (2010) tested both empirical and prognostic equations for SSA in the CROCUS model and found that both tended to overestimate the values. Morin et al. (2010) performed a field validation of SSA in the same model and concluded that although the model performed well, there was ample room for improvement.

NIR photography was used in the present study with the goal of tracking changes over time of SSA in melt-freeze crusts, both in the field and in the cold lab where conditions may

be better controlled. The equipment and techniques introduced by Matzl and Schneebeli (2006) were chosen for their relatively low cost and ease of use in the field environment.

3.2 Equipment and Field Methods

When tracking temporal changes in a type of snow known to be spatially variable (e.g. Schweizer et al., 2008) it is critical to gather as much information as possible about the initial structure. By careful selection of study sites and by monitoring the meteorological conditions during crust formation some assumptions about the scale of the variability could be made: Many of the crusts tracked during this study formed over several days on uniform slopes during periods of warm temperature or strong insolation and little to no precipitation. By selecting study plots with uniform sky view and which were also sheltered from the wind, many potential sources of variability were reduced.

Of four study sites, three were situated in or near Glacier National Park study plots (see Appendix A), allowing for accurate measurement of meteorological conditions during formation. Each site was visited weekly from the time of initial burial until mid-April, at which time the snowpack was usually moist or wet. The observation wall was cut back by a minimum of 1 m from the previous week's pit and a standard test profile was recorded along with push tests (e.g. Seligman, 1936) and thermal conductivity measurements (Chapter 2). A three megapixel Canon D30 digital SLR camera, modified by Life Pixel (www.lifepixel.com), was used for all NIR photography. The hot mirror filter over the CMOS sensor, which reflects near-infrared radiation, was replaced with a 'deep infrared' filter, equivalent to an 830 nm filter. The precise upper limit of the CMOS spectral sensitivity is not known, but is approximately 1050 nm (Langlois et al., 2010). This method offers advantages over simply using a lens-mounted filter as much more light is transmitted to the sensor enabling photographs to be taken in ambient light without the need for long exposures. The lens used for all photographs was a manually focused 90 mm f2.8 1:1 macro. This lens offered the

advantage of very little barrel distortion so that image correction during post-processing was minimal. Distortion was tested by photographing a snow crystal screen with 1 mm squares from distances ranging from 30 cm to 2 m and evaluating distortion at each. No measurable distortion was found at any distance. Most camera lenses do not transmit light uniformly to the digital sensor on a camera and corrections must be made during post-processing to equalize the images and remove any artifacts. Reference correction images were created by photographing the interior of a Lambertian integrating sphere, which is simply a hollow sphere coated with a material that reflects light isotropically and provides a uniform source of diffuse radiation at surface of the camera lens. The resultant images may then be examined for any artifacts introduced by the lens and used for correction during post-processing. More details on correction and post-processing are given in Section 3.3.

Labsphere Spectralon diffuse reflectance standards (Labsphere, 2013) of 99% and 50% were used for calibration of all NIR photographs. The standards are Lambertian in the range 250 - 2500 nm and are thus well suited for calibration in the NIR spectrum. Four targets calibration targets were constructed with the 99% and 50% standards side-by-side on each one. An adjustable steel frame, painted white to minimize heating, allowed the calibration targets to be mounted with magnets around the target layers and flush with the snow surface.

The methods developed by Matzl and Schneebeli (2006) require uniform diffuse lighting at the snow pit wall. When possible, NIR photography was done when the sky was obscured by cloud cover. A white vinyl shower curtain with sleeves sewn in each side was set up to shade the study site, and a white flat field target was constructed with the same white vinyl material and placed over the target area for later correction of any remaining inhomogeneous lighting. All photographs were taken either cross-slope or on flat ground to reduce the risk of sampling adjacent layers. In cases where the observation wall was back-lit by the sun, the snow surface was shaded at least 1.5 m back from the wall.

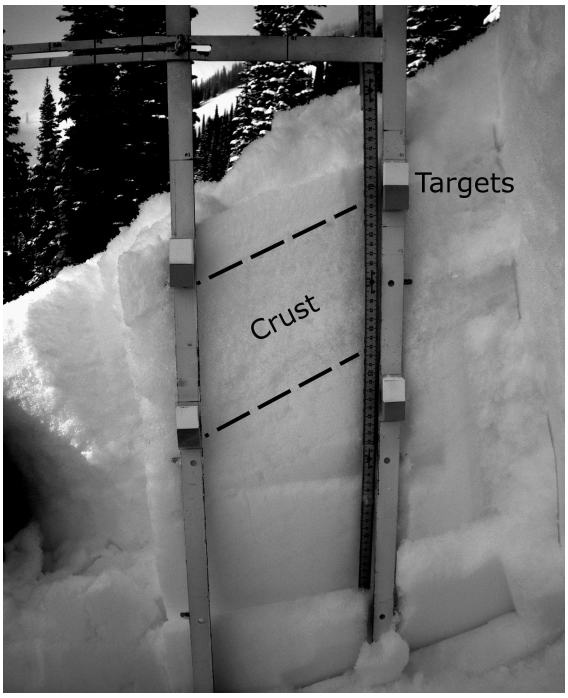

Figure 3.1: *Typical setup for near-infrared photography. Spectralon reference standards are mounted on an adjustable frame surrounding the target area and a ruler is included for reference. The shower curtain used to ensure diffuse lighting is not present in this image.*

Figure 3.1 shows a typical setup for NIR photography. The metal frame is adjusted and placed around the target area and the Spectralon targets are mounted just above and below the target area. A field ruler is placed adjacent to the frame for easy reference during post-processing. The camera was mounted on a tripod approximately 1.5 m back from the pit wall giving a resolution of approximately 0.1 mm.

Photographic equipment was set up prior to the snow pit wall being cut back by 1 m to minimize any warming of the observation wall. A metal cutting plate was used to create a smooth pit wall, ensuring that data were not influenced by scrapes or voids in the image. This was not always possible due to fracturing of brittle crusts, but such areas were identified and discarded during subsequent processing. The pit wall was photographed three times using JPG and later RAW format in winter 2008-09 and RAW format exclusively in winter 2009-10. The RAW format avoids artifacts due to de-mosaicing (Wikipedia, 2013), which is the

process by which individual photo-sensors are blended so that each pixel on the resultant image has a red, green and blue component. In RAW format de-mosaicing is not done and the actual data from the CMOS sensor are saved to the camera's memory card. This approach has the added advantage of being able to process the red, green and blue channels of the image separately and assess each for artifacts or signal noise. An additional three images of the flat field target were then captured. The distance from the lens to the pit wall was recorded and additional visible spectrum photographs were captured for later reference. Following the photographs standard observations of grain form and size, hardness, density, temperature and layer thickness were recorded.

NIR photography was found to be simple both in the field and in the cold lab. Equipment generally required under ten minutes to set up, and the photography itself required only 1-2 minutes. A complete set of observations including NIR photographs and a test profile including density could be completed in 90 minutes by a single trained observer. Transportation of equipment to field sites was simple with the exception of the metal frame which was not used for the latter half of winter 2009-10. The metal target frame was found to influence calibrated reflectivity around the edges of the pit wall, reducing the useful sample size in the processed images, and its use was discontinued midway through the 2009-10 season. Spectralon targets were instead placed directly into the pit wall surrounding the crust.

As is the case with many field studies, weather presented the biggest challenge. Sunny days with little or no cloud cover usually resulted in at least some inhomogeneity of the lighting on the pit wall and those samples generally had noisier signals even after flat field correction. Gauging proper exposure was also challenging and some images had to be discarded due to over or underexposure. Camera focus was done manually while looking through the viewfinder and presented minor challenges given that the camera's LCD screen was inadequate for verifying that each image was focused properly. Ambient air temperature also presented a significant challenge as the winter of 2009-10 was especially warm with many

days near 0 °C. Sampling at some sites had to be suspended or discontinued due to free water in the sample profile. A worn ball mount on the camera tripod allowed for some movement between images and as a result several days only had one, rather than three, usable NIR images.

3.3 Analysis Methods

Methods for image analysis were closely modeled after those developed by Matzl and Schneebeli (2006). RAW images were converted to 16-bit TIFF prior to analysis. The 90 mm macro lens used for all photographs was tested for barrel distortion at various distances using a standard snow crystal card. No distortion was found and no image correction was applied during subsequent analysis.

All post-processing was done using Exelis IDL software (ITT Visual Information Solutions, 2010) due to its strength in dealing with large arrays and its suite of interactive visualization tools. Prior to any analysis all images had to be corrected for inhomogeneous lighting on the pit wall as well 'bright spots' due to the camera lens and any irregularities or dead pixels due to the camera's CMOS sensor. This process is outlined in Figure 3.2. For each crust observation, the sets of three pit wall images were first averaged. Lens effects and hot pixels (pixels which are unnaturally bright due to current leakage and excitation) from the CMOS were removed by subtracting a dark field image and normalizing over the value of an integrating sphere image. If flat field images were available they were then averaged and corrected in same manner; if they were not available or if the flat field had been contaminated with dirt, a flat field was generated by linear interpolation between the grey Spectralon targets using IDL functions Triangulate and Trigrid. Finally the effects of inhomogeneous lighting were corrected:

$$I_{corr} = \frac{I - C_{dark}}{C_{flat}} * \overline{C_{flat}} \tag{3.1}$$

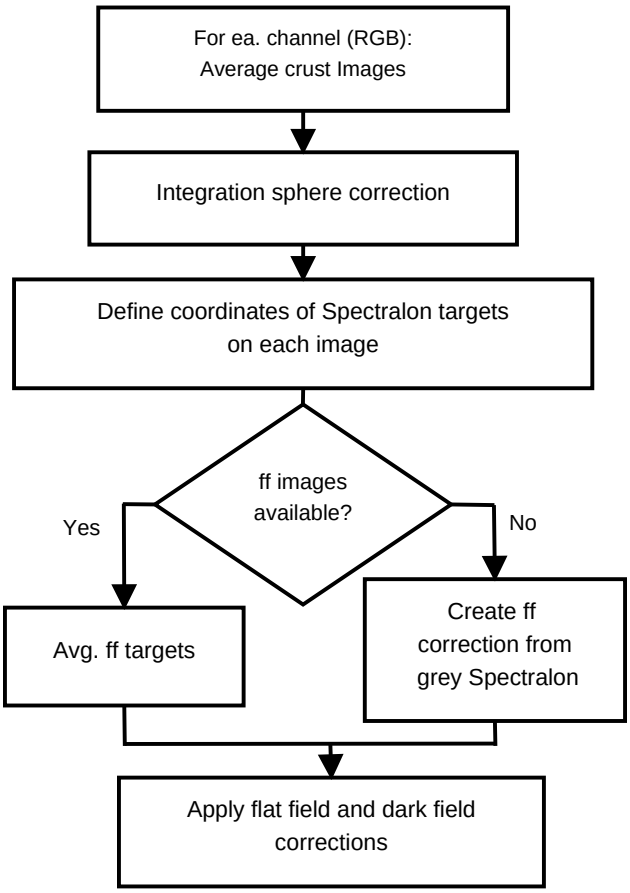

Figure 3.2: *Flow chart for flat field (ff) correction of NIR images.*

Where I_{corr} is the corrected crust image, C_{dark} is the dark field correction, C_{flat} is the flat field correction and $\overline{C_{flat}}$ is the mean value of the flat field correction. This process was repeated for each of the red, green and blue bands and a single channel was selected for time series analysis based on a combination of best fit in the calibrated near-infrared reflectivity (NIR) image and adequate contrast. For cold lab crusts the red channel was the only one with sufficient intensity to produce clear images due to the incandescent bulbs used to illuminate the cold lab.

The calibrated NIR reflectance then was obtained by deriving a linear best-fit equation between measured intensity and ideal reflectivity at the Spectralon targets. The coefficient of variation (CV) of each target was tracked to ensure that no contamination or physical damage such as pitting or scratching affected results. Although the CV was generally less

than 1%, one contaminated target was identified and removed from further processing steps in 2010. The R^2 value of the linear best-fit exceeded 0.98 for all calibrated image sets, indicating that contaminants on the targets and inhomogeneous lightning were properly corrected before further analysis.

The calibrated reflectance images were then used to calculate the SSA using the equation introduced by Matzl and Schneebeli (2006):

$$SSA = Ae^{r/t} \tag{3.2}$$

Where r is the calibrated reflectance, A = 0.017 ± 0.009 mm^{-1}, t = 12.222 ± 0.842 (R^2 = 0.908) and SSA has units of mm^{-1}. The processing steps from image correction, to NIR calibration and calculation of SSA each introduce variability into the image array. This may be quantified by calculating the CV for three regions of interest as an image array is processed, shown in Figure 3.3. This is not inherently problematic, but suggests that simply using calibrated NIR images may be more appropriate if the goal is simply to track structural changes visually, or to obtain greater detail of snowpack layering than is possible with traditional visible photographs.

Although the image resolution from the CMOS is approximately 0.1 mm, Matzl and Schneebeli (2010) have shown that results using these techniques should not be extended to the sub-millimetre scale due to concerns about light leakage between layers and subsequent biased reflectivity measurements. Image correction and generation of NIR and SSA images for one observation date could be accomplished in 5-10 minutes up to this point, with the bulk of the time spent manually outlining the Spectralon targets and checking for any anomalies in target coefficient of variation (CV).

At the conclusion of the field season and once all images for a given crust were processed, the time series as a whole was examined for any apparent trends in morphology or variability. Further analysis required that specific regions of interest (ROIs) be defined within each image. Automated edge detection methods were tested in the hopes of reducing the manual input

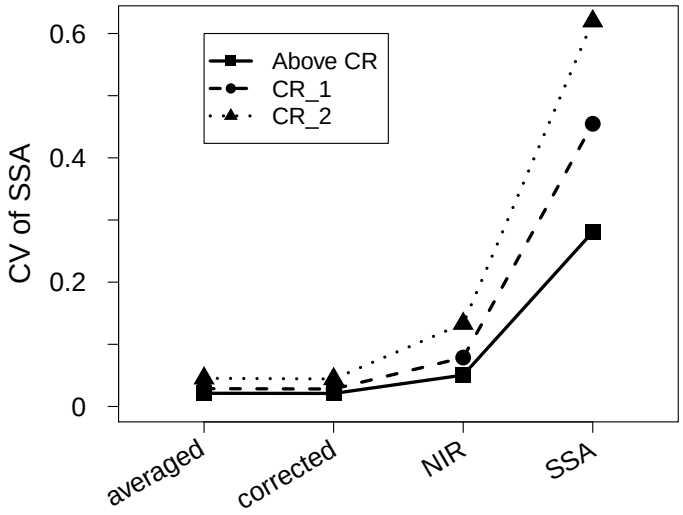

Figure 3.3: *Increase in the coefficient of variation (CV) of SSA for 3 regions of interest at various points in the post-processing. The regions of interest (ROIs) include an area above the crust and two areas within the crust.*

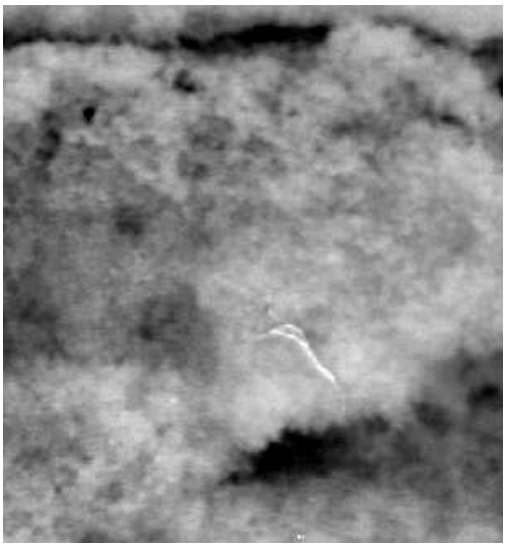

Figure 3.4: *Example of a rejection portion of a calibrated reflectance image due to large voids in the brittle crust as well as a gouge in the flat field correction material.*

required, but were found to be impractical due to the occurrence of voids such as those shown in Figure 3.4, where exposed crust surface is uneven due to crumbling when the pit wall was cut back. The IDL *iimage* utility was used to graphically define ROIs in each image using two different approaches. First, separate ROIs were defined for the crust and layers directly above and below. Summary statistics including mean, standard deviation, range and CV were calculated for each region of interest (ROI). The area could also be calculated by creating a line of reference length along the snow study ruler that was included in each NIR image. A final ROI included the crust and adjacent layers above and below. SSA values were averaged horizontally across this ROI to create vertical profiles of SSA and variability.

The analysis of NIR imagery was refined during the summer of 2010 and crusts from 2008-09 were subsequently re-processed using the new methods. Profiles containing moist or wet layers were problematic as Equation 3.2 was not calibrated using moist or wet snow and free water content was only recorded as per OGRS standards (CAA, 2007) so no corrections could be applied. Images from such days were not used in time series analyses.

3.4 Results and Discussion

Each crust was analyzed individually for temporal trends in structure and variability of SSA as well as correlations with other characteristics such as density, grain size, average temperature and slope-normal temperature gradient. Prior to analysing specific crusts, it is useful to compare some representative values to those obtained during similar studies. Matzl and Schneebeli (2006) used stereological methods to determine SSA, including six samples classified as either 'crust' or 'frozen wet grains'. Those samples yielded SSA ranging from 5 mm^{-1} to 20 mm^{-1}. Dominé et al. (2007) measured layers consisting of melt forms (6cl, 6mf, 8il, 9mfc per Colbeck et al. (1992)) which correspond roughly to MF and IF grain types (from Fierz et al. (2009)) and recommended using an average value of 0.86 mm^{-1}. Areal averages taken from ROIs in the present study yielded values ranging from approximately 2.5

mm^{-1} to 20 mm^{-1}, with the lowest values occurring in crusts that had undergone repeated freeze- thaw cycles and which were comprised primarily of large clustered grains.

3.4.1 2008-09 Crusts

Three crusts were tracked during the first winter of NIR observations, all at the south-facing same site on the South Run area of the Mt. Fidelity permanent closure. Appendix A gives further details on the physical characteristics of the site as well as the weather contributing to the formation of the crusts.

Figure 3.5 shows the times series of SSA for crust SR090127 as well as the layers immediately above and below. As outlined in the previous section, an areal average SSA was calculated by defining an ROI for each layer of interest for each observation date. This crust was initially composed of two identifiable layers, with a well-bonded melt-freeze crust overlying smaller clustered grains. The SSA of the crust is characterised by a rapid rise during the first week of observations followed by a slow and gradual decrease until the final observation on 11 April 2009. Thermistor data are missing during the period of the initial increase but surface temperatures warmed to near 0 °C at the Mt. Fidelity weather station and a new crust had formed on the surface at the South Run study site, so it is likely that strong vertical temperature gradients were induced across the crust. Some weak faceting was observed in upper portions of the crust where grains were 2-3 mm in diameter. From 10 February through 6 April the vertical temperature gradient remained weaker than 1 °C 10 cm^{-1} and the crust temperature was below freezing. From 6 April to 11 April the crust temperature was within 0.1 °C of freezing, the density decreased (Appendix C) and the layer was classified as 'moist', indicative of some free water. The slight increase on 11 April is likely at least partly attributable to free water in the snowpack.

No statistically significant ($p \leq 0.05$) correlations were found between rates of change of SSA and other measured parameters; however, a qualitative link appears to exist between decreasing hand hardness and decreasing SSA.

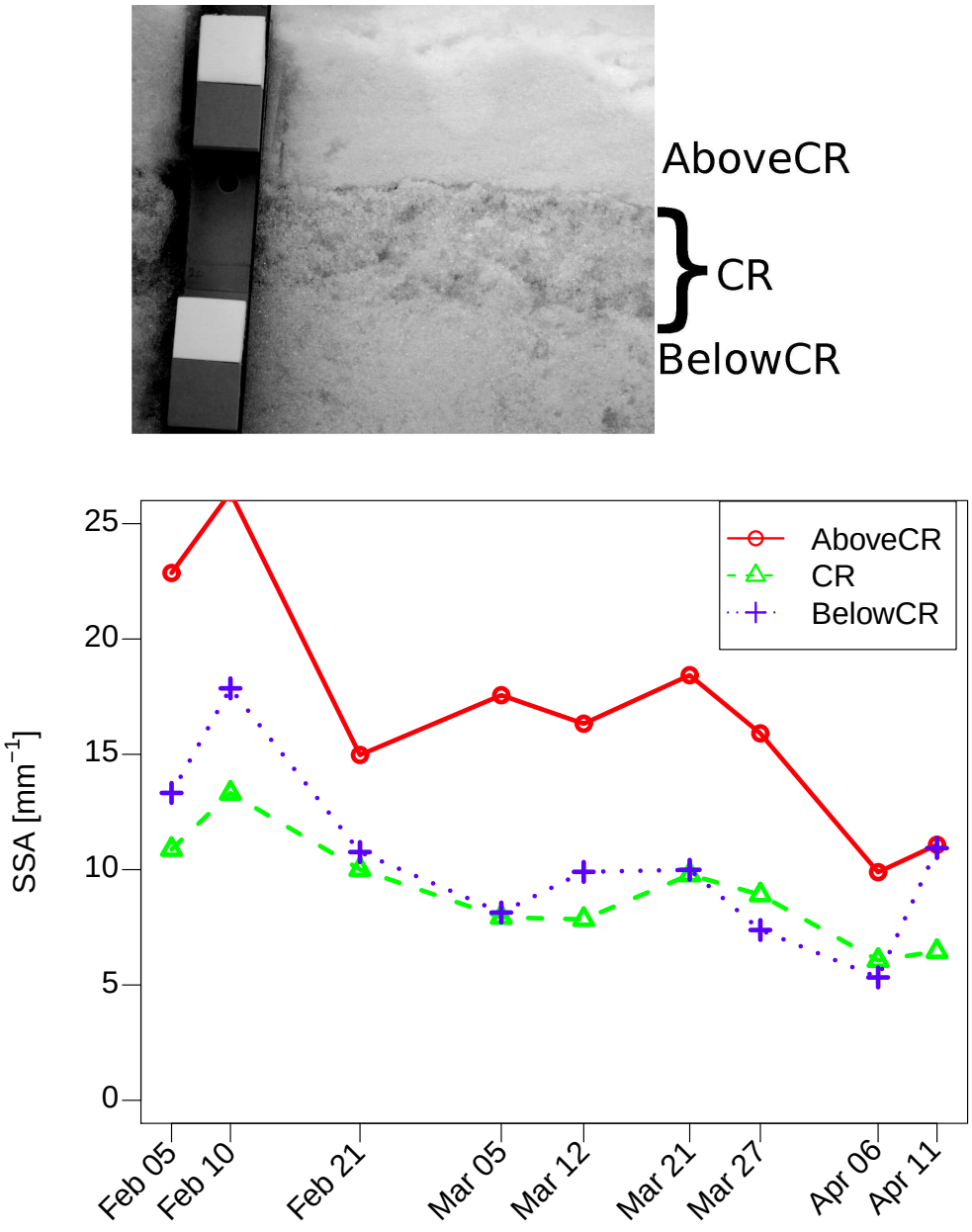

Figure 3.5: *NIR image (top) and SSA time series for crust SR090127 and adjacent layers.*

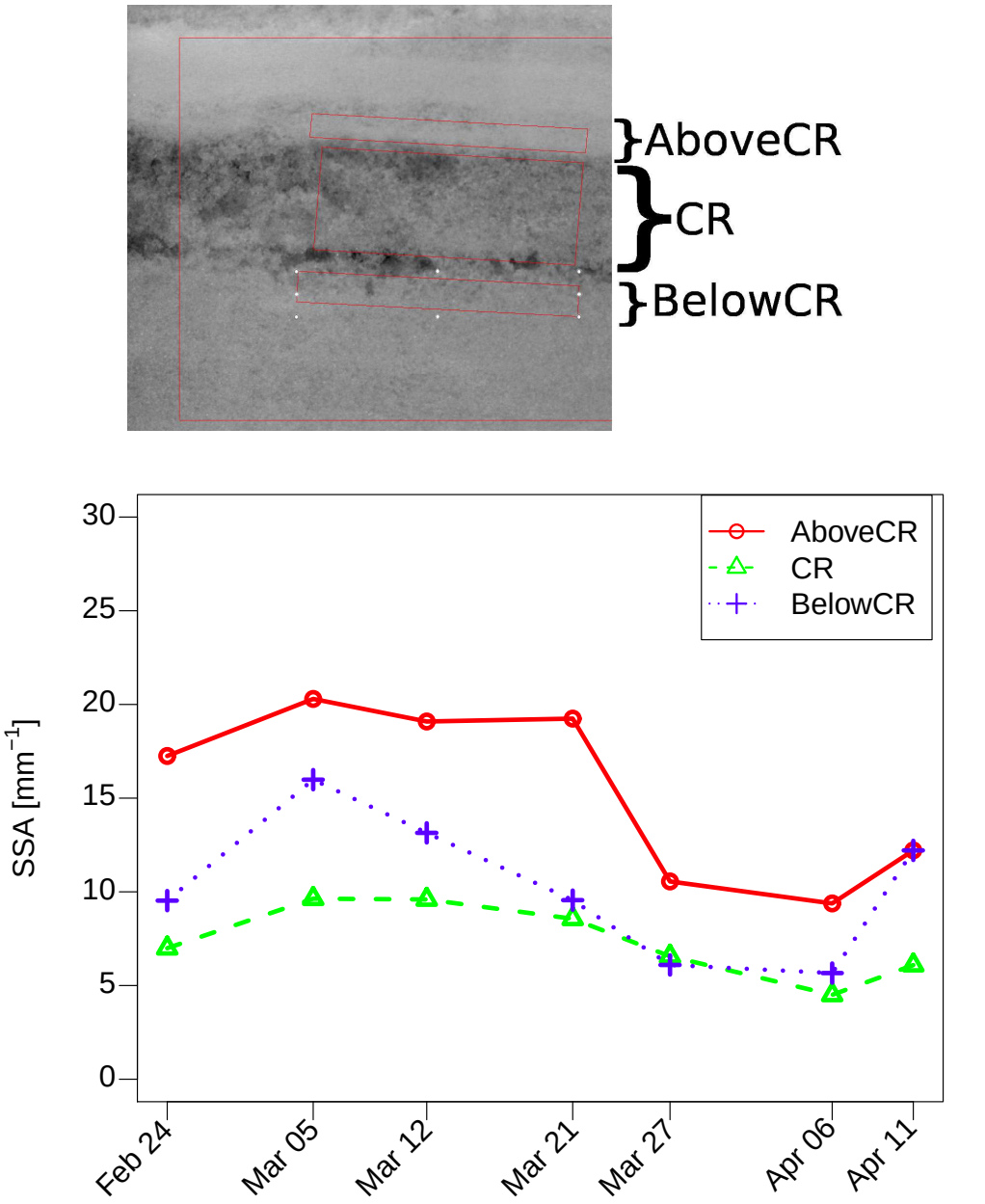

Figure 3.6: *NIR image (top) and SSA time series for crust SR090222 and adjacent layers. The ROIs used for determination of sample mean SSA are also illustrated. The largest ROI is used to calculated mean vertical profiles of SSA.*

Crust SR090222 formed during a warm dry period in early February and was finally buried on 22 February. Thermistors were inserted above and below the crust just after burial and were removed at the time of the final observation on April 11. Figure 3.6 shows the time series of mean areal SSA within the crust and in adjacent layers above and below. The crust was initially uniform in appearance and physical characteristics, with strong bonds that made obtaining a smooth pit wall relatively difficult. The crust remained within 50 cm of the snow surface through mid-March and vertical temperature gradients frequently approached, though did not exceed, 1 °C 10 cm^{-1}. The only apparent signal from this period of stronger gradients was a slight increased in horizontal variability of SSA across the same area on 5 March and some edges (indicative of faceting) on 12 March, but hand hardness remained consistent until 6 April when the layer temperature approached 0 °C. As with CR090127 the increase in SSA on 11 April is likely at least partly attributable to free water in the snow. Strong significant ($p \leq 0.05$) correlations were found between SSA and the vertical temperature gradient, but these are misleading as the actual temperature gradient did not vary beyond the measurement accuracy of the thermocouples (0.1 °C) for most of the season.

Evolution in SSA of CR090301 over one month of observations is shown in Figure 3.7. The vertical temperature gradient underwent strong diurnal fluctuations during the first week of March before stabilizing as the crust was buried. The increase in mean SSA from 21 March to 27 March is related to increased SSA in the lower part of the crust and a corresponding increase in vertical CV and reduction in hand hardness. Solar insolation had been strong for the week prior and the vertical temperature gradient had approached 1 °C 10 cm^{-1}. By 6 April the crust temperature had warmed to near 0 °C and a strong diurnal cycle in temperature continued until the final observation on 11 April. The large drop in SSA on 11 April is consistent with the observation that the crust structure had changed from well bonded MFcr to large refrozen polycrystals, but may also be affected by free water in the

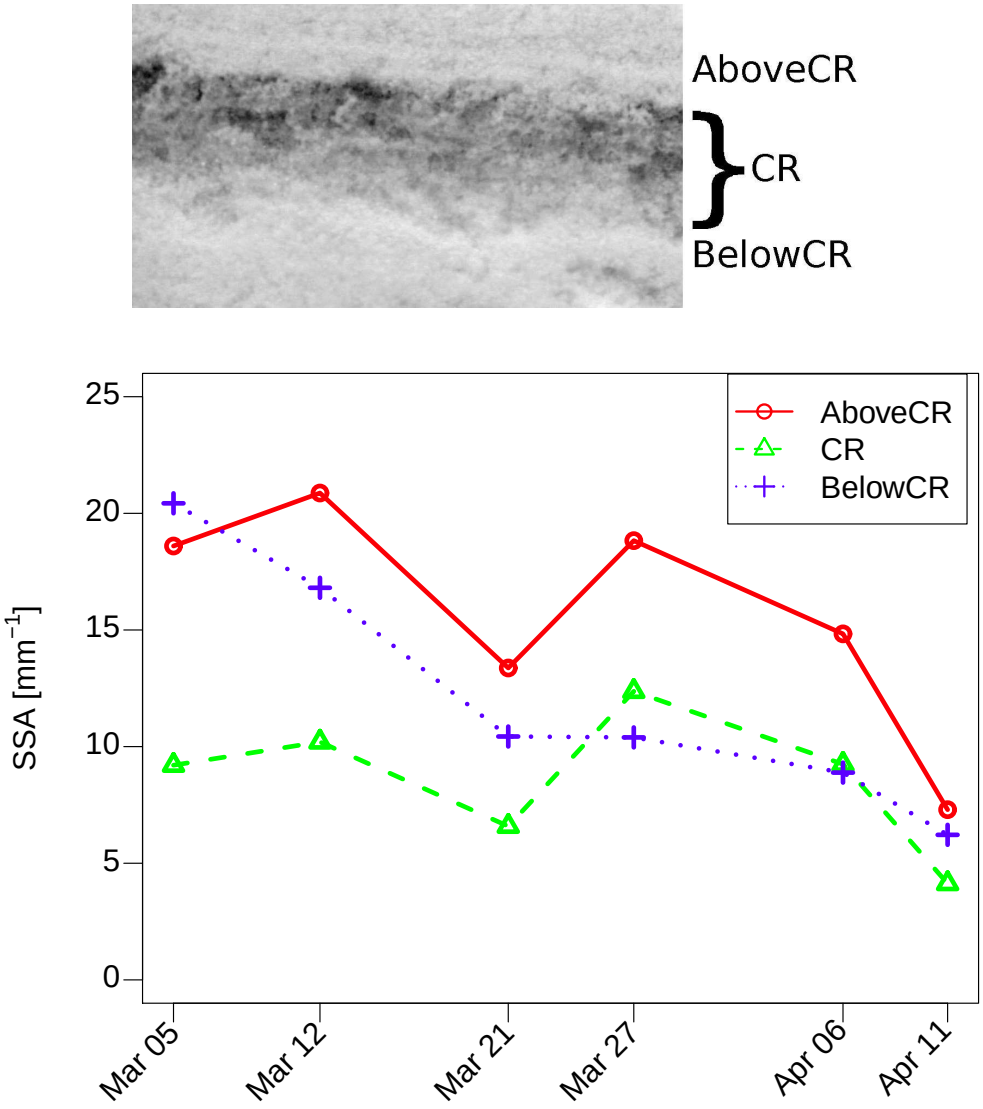

Figure 3.7: *NIR image (top) and SSA time series for crust SR090301 and adjacent layers.*

Table 3.1: *Correlations of Specific Surface Area (SSA) and Near-Infrared Reflectivity (NIR) with other crust properties. TG is the vertical temperature gradient and TG96 is the 96-hour averaged vertical temperature gradient. TG* denotes the omission of CR090301.*

Variable	Correlation	p	n
SSA-TG	0.69	0.001	19
SSA-TG*	0.79	0.0005	15
SSA-TG96	0.61	0.05	19
SSA-ρ	-0.46	0.04	19
NIR-Gsz	-0.37	0.08	23

layer.

Given that all three crusts formed under similar meteorological conditions and were tracked at the same site, it is worthwhile to analyze them as a group. For reference, crust properties are tabulated in Appendix C. Table 3.4.1 shows the correlations between SSA, NIR and other measured variables. The moderate correlation between SSA and slope-normal temperature gradient improves somewhat if CR090301 is excluded but instantaneous temperature gradient is not likely a causal factor for any trends in SSA. Lagged and average temperature gradients were tested for correlation with SSA and rates of change and the only statistically significant result was between the average absolute gradient over the previous 96 hours (TG96) and SSA. The negative correlation between density and SSA was also found by Dominé et al. (2007) for a range of crystal types that included crusts. The negative correlation between NIR and grain size is expected due to the dependence of reflectivity on grain size and the weakness is due at least in part to the difficulty in defining an 'average' grain size for melt-freeze layers.

A range of other physical and stability factors such as overburden mass, shear strength at the upper boundary, compression test result and failure type and propagation saw test (Gauthier and Jamieson, 2008) were also tested for correlation with NIR and SSA but no significant ($p \leq 0.05$) results were found.

Discussion: 2008-09 Natural Crusts

The first season of SSA observations included three natural melt-freeze crusts at a single planar south-facing study site. All three crusts formed due to a combination of warm air temperature and strong insolation, and were tracked from formation until mid-April when all crusts because moist and bonds began to weaken (Appendix C). A number of parameters were tested for correlation with both SSA and rates of change of SSA but few statistically significant relationships were found. Given that the vertical, or slope-normal temperature gradient is the primary driving force behind snowpack metamorphism a stronger correlation with an averaged temperature gradient or a time-lagged averaged temperature gradient might be expected. The relatively warm winter from January - April 2009 may be one factor, as all three crusts remained within 5 °C, and often within 1-2 °C of freezing during the observation period. This prevented the occurrence of strong temperature gradients that would drive the formation of facets in the interior or at the boundaries of crusts. Diurnal temperature gradients were evident by early April but several authors (e.g. Pinzer and Schneebeli, 2009) note that diurnal gradients do not necessarily lead to faceting. The most significant structural changes occurred at the end of the season as the crusts warmed to 0 °C and bonds began to weaken, but that change was only weakly reflected in plots of areal average SSA.

Other links between SSA and physical qualities for these crusts were largely qualitative, such as an increase in vertical variability concurrent with the weakening of bonds in portions of the crust. The decreasing trend of SSA and weakening bonds in CR090127 may provide some evidence for the importance of isothermal sintering processes (e.g Kaempfer and Schneebeli, 2007) in melt-freeze crusts but this cannot be quantified based on the data collected during this study.

3.4.2 2009-10 Crusts: Field

During the winter of 2009-10 six natural crusts were tracked from time of burial until mid-April and four natural crusts were harvested, transported to a cold lab and subjected to

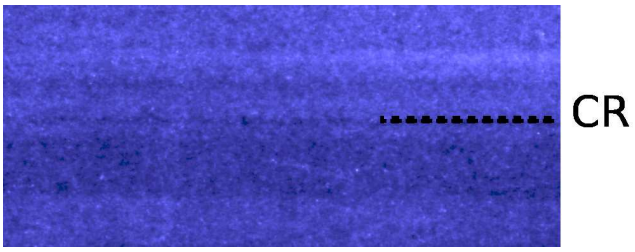

Figure 3.8: *SSA image of CR100109. The crust is labeled and marked by a dashed line on the right hand side of the image.*

strong temperature gradient conditions. The earliest crust, FI100109, is shown in Figure 3.8 and formed during a light freezing rain event in early January 2010. Although NIR photography and subsequent derivation of SSA were useful for visual tracking of the crust and surrounding layers, graphical analysis did not produce adequate discrimination from surrounding layers to permit tracking of temporal changes. Two crusts, SR100131 and SR100210, were tracked near the South Run site used for the winter 2008-09 crusts. Low snowfall, strong insolation and warm temperatures caused this crust to quickly blend with surrounding layers and tracking the original layer became difficult. The frequency of moist or wet layers at this site also reduced confidence that SSA derived from NIR photographs could be used for tracking temporal changes of crust structure.

Crusts RP100112 and BV100112 both formed during a rain/wet snow precipitation event in mid-January 2010 (see Figure A.11 in Appendix A). RP100112 was quickly buried but remained within 30-40 cm of the surface until a storm in mid-March. The crust composition was variable from the time of formation, with mixed sections of refrozen polycrystals and pockets of small rounding facets bounded above and below by solid melt-freeze layers with some areas of solid ice. Figure 3.9 shows the evolution of the mean vertical SSA profile from 25 January to 29 March, at which point free water in the snow reduced the confidence in the SSA measurements. The upper and lower boundaries of the crust are evident as persistent areas of low SSA. The SSA in the interior of the crust is highly variable throughout the

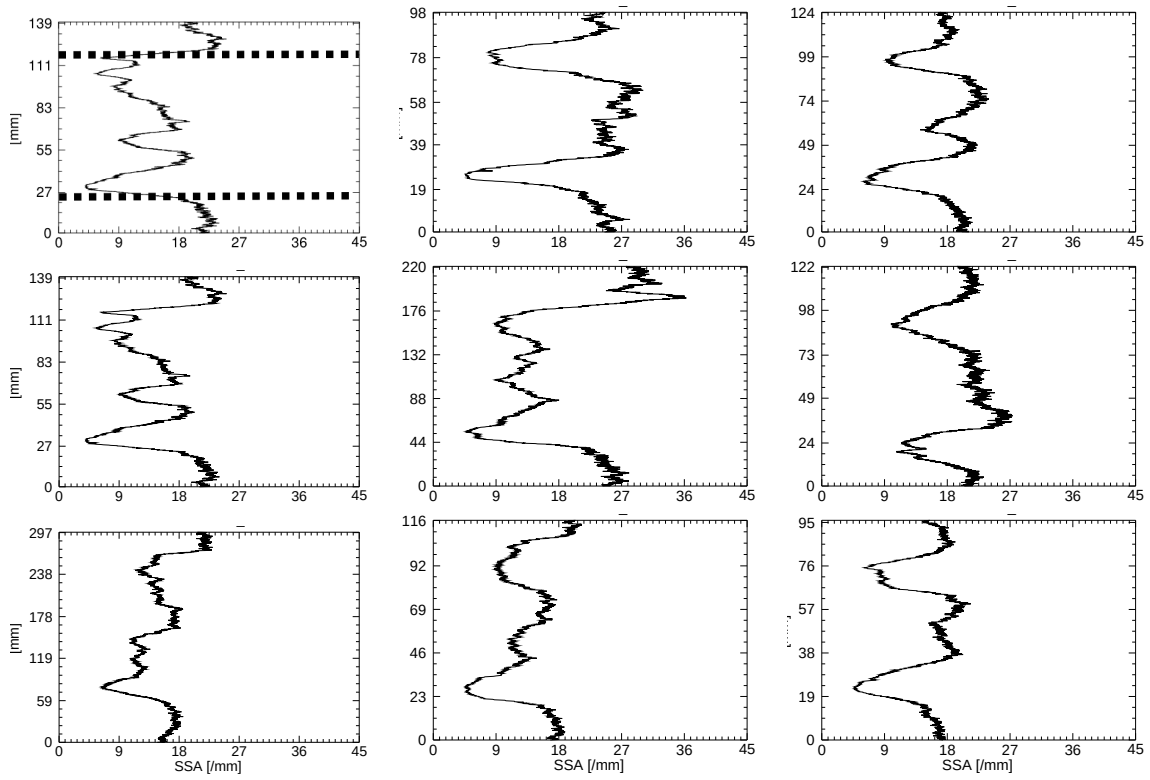

Figure 3.9: *Weekly vertical SSA profiles for crust RP100112, 25 January - 29 March, 2010. Order of evolution is left to right, top to bottom. The upper and lower boundaries of the crust are indicated by dashed lines on the first image in the series and are visible throughout as spikes of low SSA. Scale was calibrated by the inclusion of a ruler in near-infrared images. Note also that the vertical scale varies by image as regions of interest used to create the vertical profiles had to be defined manually for each set of images and were not always consistent in their upper and lower extent.*

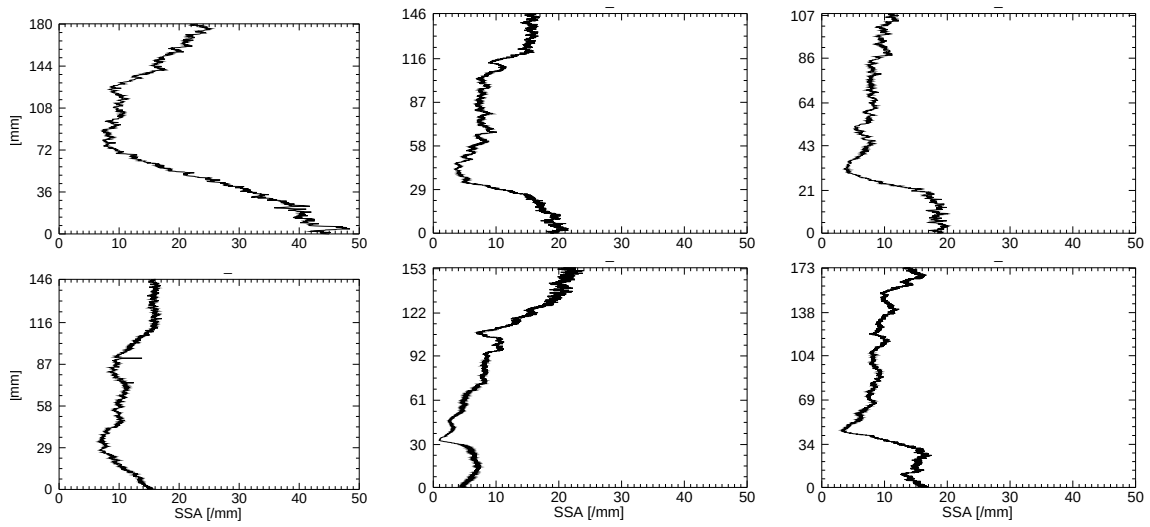

Figure 3.10: *Weekly vertical SSA profiles for crust BV100112, 31 January - 14 March, 2010. Order of evolution is left to right, top to bottom.*

time series, which is due at least in part to the spatially variable nature of the crust. Due to the shallow burial the vertical temperature gradient was sensitive to large changes in air temperature and approached, though did not exceed, 1 °C 10 cm^{-1} several times throughout the season. A trend of decreasing SSA in the crust's interior is reversed on 8 March (2^{nd} row, 3^{rd} image) when it briefly increases, then falls again over the next three weeks. There is no evidence to support widespread interior faceting and this is likely a function of initial spatial variation moreso than temporal change.

Crust BV100112 at the Beaver Valley study site was similar to RP100112 in terms of horizontal variability at the study plot scale (1- 2 m). It likely received more liquid precipitation during formation due to its lower elevation and remained relatively warm and shallow throughout the entire observation period. Weekly site visits continued until 23 March at which point the entire snowpack was isothermal and abundant free water was evident. Figure 3.10 shows weekly vertical profiles of SSA from 31 January through 14 March, 2010. The spatial variability of the crust is evident in that there is only a single consistent structure with low SSA that persists throughout the whole time series. The gradual disappearance of

any areas of SSA greater than 15-20 mm^{-1} is supported by the disappearance of any non-melt-forms in the test profiles that were recorded concurrent with the NIR imagery, but as with RP100112 most of the apparent change throughout the time series is likely attributable to a high degree of spatial variation upon the crust's formation.

Crust FI100308 was the only natural crust from winter 2009-10 that formed in a nearly uniform manner and was buried relatively quickly. That, and the flat aspect of the study plot at Mt. Fidelity, allows for a high degree of confidence that any observed changes were temporal rather than due to spatial variability. Figure 3.11 shows the time series of mean SSA for the crust and adjacent layers including a thin ice lens at the lower crust boundary. Figure 3.12 shows vertical profiles through the crust as well as a buried surface hoar layer from 15 March through 14 April. The profile from 9 March is not included as bright sunlight through low density snow contaminated much of the image. The ice lens was observed on 14 April but was barely distinguishable on the vertical profile of SSA. The first profile in the latter image is superimposed over a NIR image and illustrates one of the dangers of relying on fully automated image processing: a drop in SSA between the crust and surface hoar layer is caused by icy inclusions on the pit wall and, as can be seen in the following vertical profiles, is not a consistent feature of the snowpack at the study site location.

The layer temperature of FI100308 remained between -2.5°C and -5°C throughout the observation period; however, a vertical temperature gradient of approximately -1.5°C 10 cm^{-1} was induced in the third week of March by the onset of colder air temperatures (Figure A.9). This gradient persisted through to the end of observations on 14 April in both thermocouple and manual temperature measurements. Despite the gradient there was no evidence of the structural changes that might be expected, such as faceting within the crust or at its boundaries. Nor were there any discernible increases in the areal averaged SSA or the vertical profiles that would be indicative of faceting.

Some evidence of relative change in SSA between the crust and adjacent layers can be

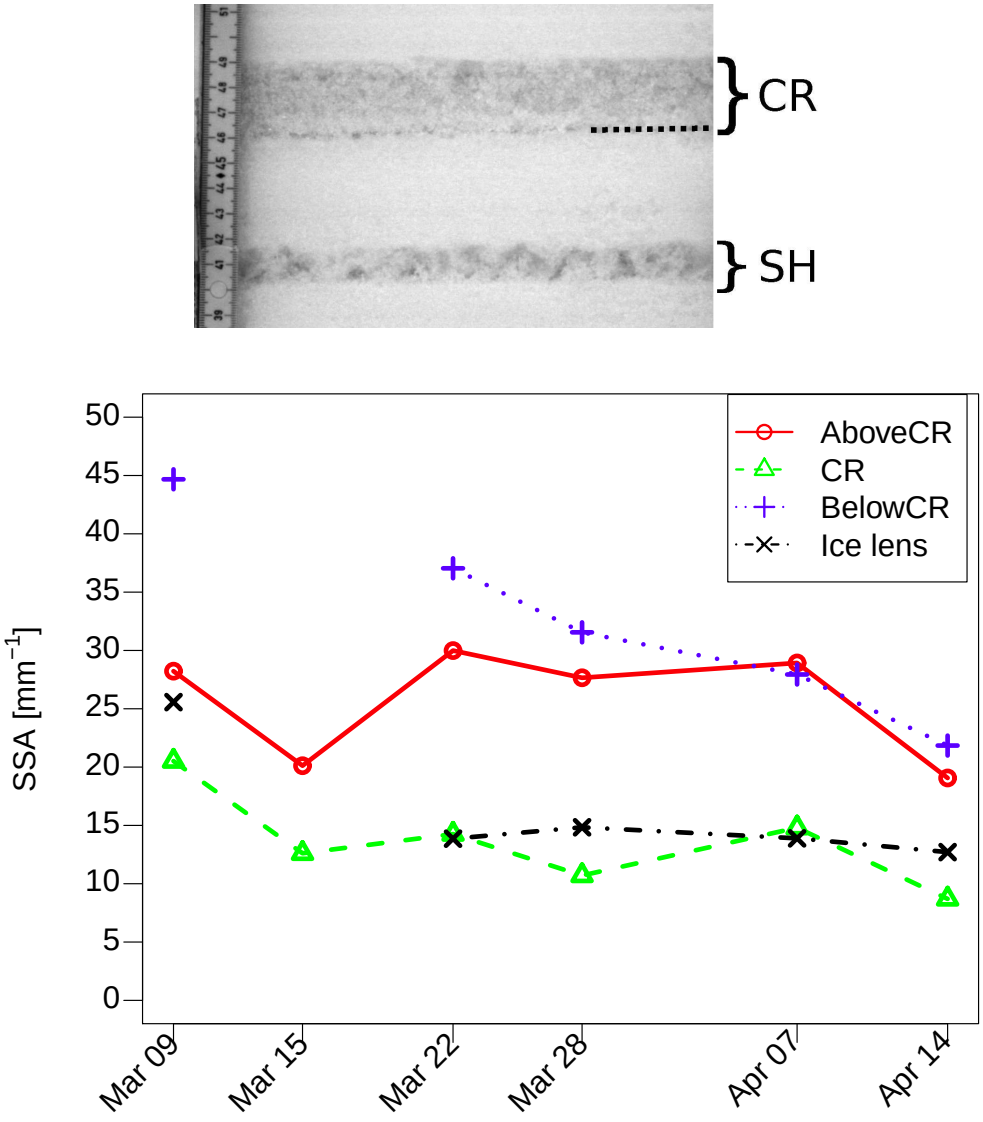

Figure 3.11: *NIR image (top) and SSA time series for crust FI100308 and adjacent layers including a layer of buried surface hoar (SH). An ice lens at the lower crust boundary is marked by a dashed line.*

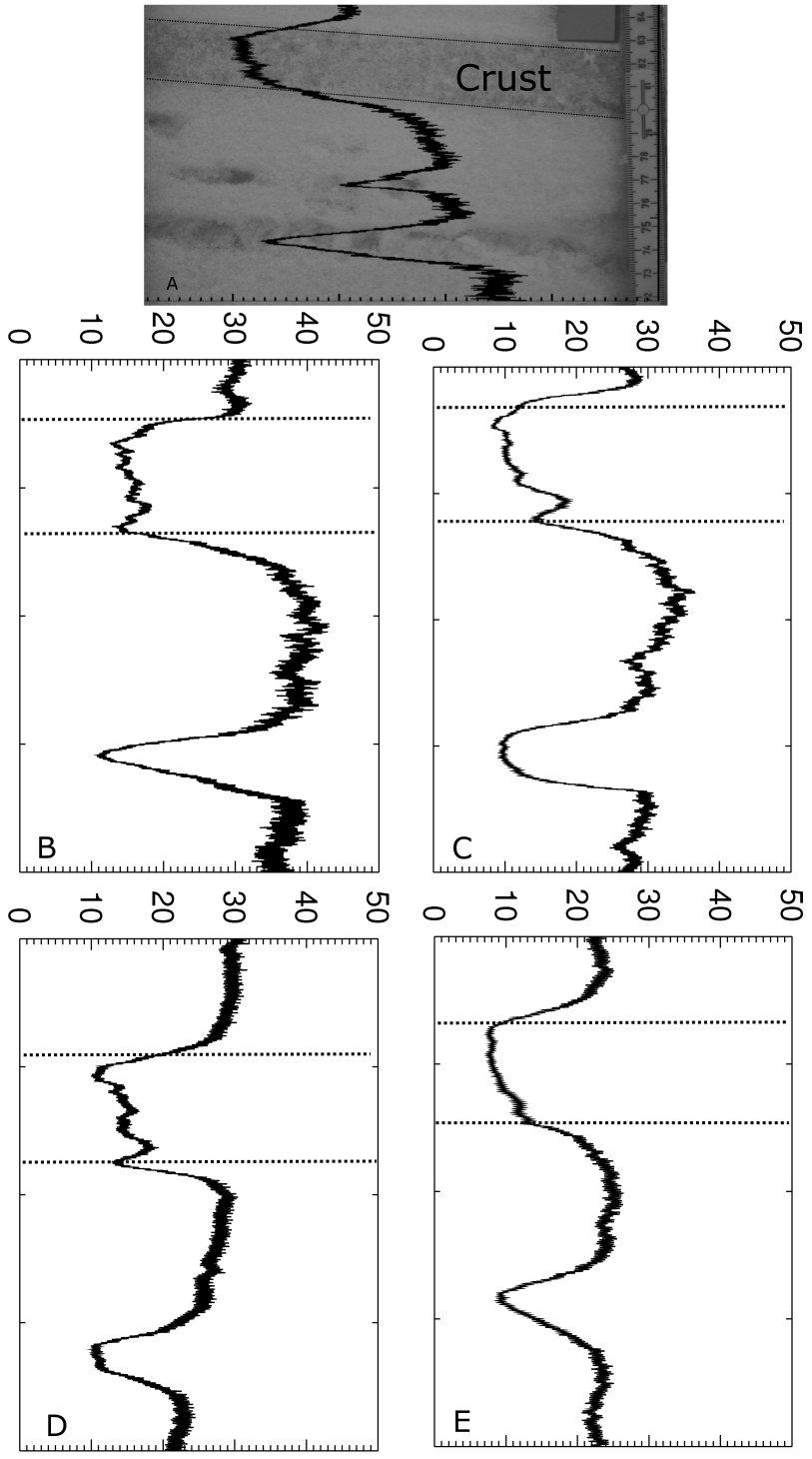

Figure 3.12: *Weekly measurements of mean vertical SSA for crust FI100308 over one month from March 15 (A) through April 14 (E). Image A shows the SSA superimposed over an image of the crust and surface hoar. The crust is outlined by dashed lines in images B - E.*

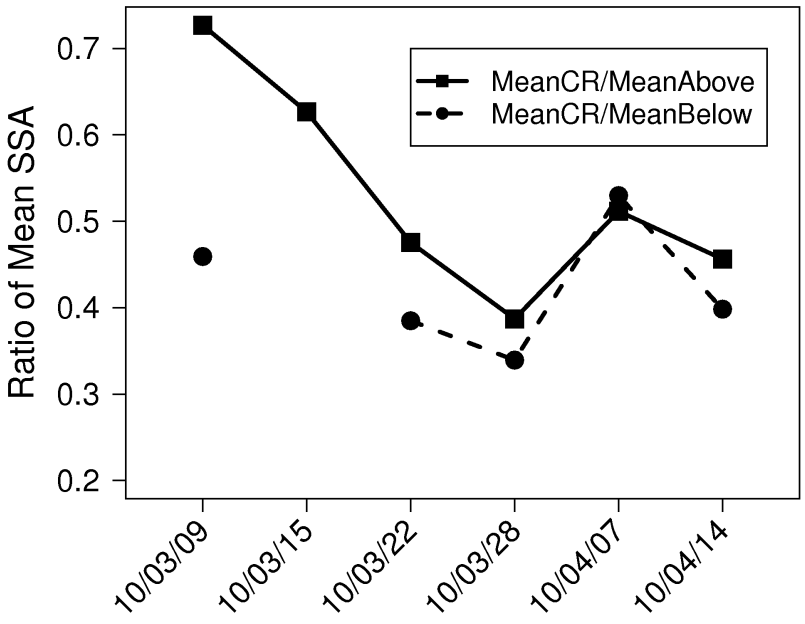

Figure 3.13: *Change in the ratio of areal averaged SSA of FI100308 to layers above and below.*

seen by calculating the ratio of areal averages, shown in Figure 3.13. The average SSA of FI100308 falls relative to the layers above and below from 9 March through 28 March, hinting at either a rounding process (lower SSA) within the crust or, more likely, some slight faceting within the layers above and below. This process reverses sharply on 7 April before the ratios fall again on 14 April.

Stability and shear tests were not performed at Fidelity or Rogers Pass Study plots due to space limitations, nor were they attempted at the South Run site once the two crusts became indistinguishable from one another. Compression tests were attempted at the Beaver Valley site but the shallow, often moist snowpack led to a high number of failures during isolation on basal weak layers.

Discussion: 2009-10 Natural Crusts

Six natural crusts were tracked during the winter of 2009-10. The time-series observations from two of these crusts (SR100131 and SR100210) were discarded due to the inability to

distinguish the crusts from one another as both remained shallow and subject to continuous melt-freeze cycles throughout late February. A third crust, FI100109 was a very thin ice lens and image analysis techniques used here were not adequate for tracking changes in crust SSA, although they were effective in discriminating the thin layer from adjacent layers in the snowpack.

Two crusts formed during a rain/wet snow event in early January and were tracked through mid-April: RP100112 was comprised of three distinct structures that were easily tracked in plots of vertical SSA, but were not suited to analysis using larger areas of mean SSA as was done for the 2008-09 crusts due to internal variability even at the scale of the pit wall. BV100112 was likewise variable upon formation. The difference in elevation and temperature was likely the main reason for the difference in initial structure between the two crusts and also to their variability at the scale of the study plot. Both crusts remained near the surface but with enough of an insulation layer of snow cover to prevent the occurrence of diurnal vertical temperature gradients. The warm air temperature in January, February and the first half of March likewise prevented any strong vertical temperature gradients across the crusts. Given these conditions the only changes in SSA that might be expected would be a trend to lower SSA from melting and re-freezing into larger polycrystals. Although this appears to be the case with BV100112, it is difficult to determine from the data whether this is the case, or whether temporal changes were eclipsed by the initial spatial variation.

Crust FI100308 may be compared more directly with crusts SR090127 and SR090222 in that it formed at the surface during a period of warm air temperature and strong solar insolation, then was quickly buried. Spatial variability at the snow pit scale was much less than in BV100112 and RP100112 as would be expected from the method of formation. Unlike other crusts from 2009-10, FI100308 remained mostly dry through mid-April and was subjected to a weak vertical temperature gradient through the final three weeks of observations. The slight increase in crust SSA from 28 March to 7 April may be a consequence

of some faceting within the crust's interior; however no edges or faceting were found in visual observations and the decrease from 7 April to 14 April is the opposite of what would be observed during formation of facets. The ratio of areal mean SSA is a useful method of quantifying relative changes in SSA between a spatially uniform crust and adjacent layers. The increased ratio on 7 April, in conjunction with the cooling trend over the previous week and the observation that all layers were dry, gives strength to the hypothesis that some faceting in the crust did occur in early April.

3.4.3 2009-10 Crusts: Cold Lab

The natural crusts used in the Rogers Pass cold lab were all harvested from the same location between 30 March and 13 April, 2010. Test profiles, NIR photography and thermal conductivity were all recorded before the crust was removed in an insulated box and transported to the cold lab. The primary motivation was to track changes in physical properties of crusts over relatively short periods under controlled conditions. The number of observations was limited by the size of the insulated snow sample box shown in Figure 3.14. The cold lab experiments were all conducted with similar ambient temperatures in the cold lab, while varying the intervals between observations in each experiment.

Experiment LAB100330 was conducted over the course of 22 hours with a total of six observations including one *in situ* before transport to the cold lab. The entire sample was moist before it was brought into the cold lab, where the air temperature was set to -13°C. The crust froze slowly from the top down and was completely frozen after approximately 12 hours. Figure 3.15 shows the time series of areal average SSA of four ROIs within the crust. The first two observations at 09:30 and 12:05 are of dubious utility as all portions of the crust contained free water. The 'Lower' ROI at 14:12 is also suspect as it was not yet frozen and some drainage of free water had occurred from upper layers.

All ROIs show similar trends in SSA, with the 'Upper' sample reaching its peak four hours prior to the low layers. This is consistent with what would be expected given that

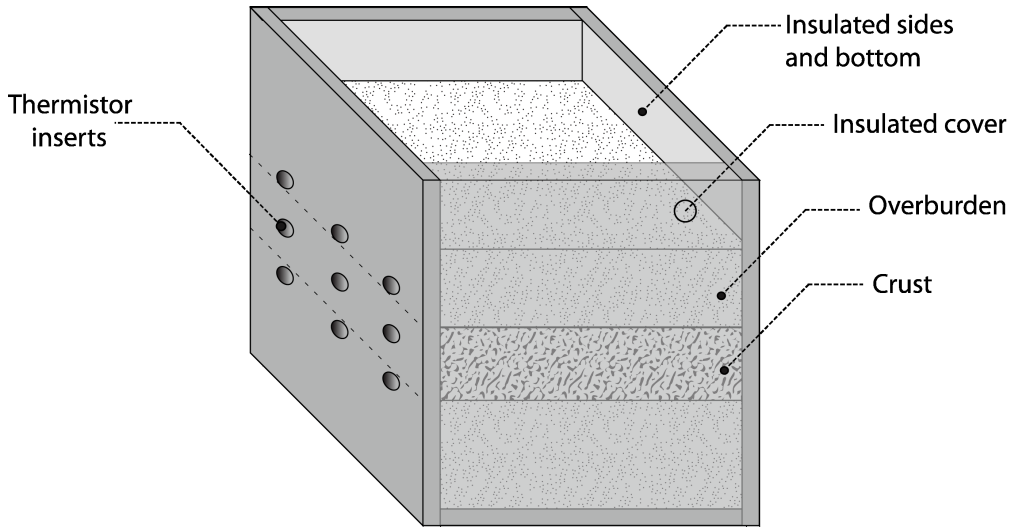

Figure 3.14: *Schematic of the insulated box used for cold lab experiments. The front ('Insulated Cover') and sides are insulated with foam while the top is left uncovered.*

upper layers were subject to strong vertical temperature gradients as soon as the sample was brought into the lab, while deeper layers were insulated to a degree and were subject to a less-intense and longer-lasting gradient. Thermocouples were not used during this experiment but thermal IR images were captured at each time step immediately after the crust face was cut back (and subsequently covered with insulation once observations were finished). These images show that even once frozen at 21:50 the interior of the crust within 0.4 °C of freezing. A recent paper by Schirmer and Jamieson (2014) has questioned the validity of using thermal imaging for snow pit temperatures, but in this case the thermal IR imagery is used only for qualitative evaluations of temperature and not in the identification of small-scale variations or gradients. The SSA of all ROIs decreased between 16:55 and 21:50, then remained approximately constant with the exception of the 'Upper' ROI which continued to decrease slightly until the end of the experiment.

Experiment LAB100409 was conducted in a similar manner to LAB100330 and the cold lab air temperature was once again set to -13°C, but observations were evenly-spaced at approximately 6-hour intervals and thermistors were inserted into the site of the insulated cold lab box. Figure 3.16 shows the areal averaged SSA for ROIs in the upper, middle and

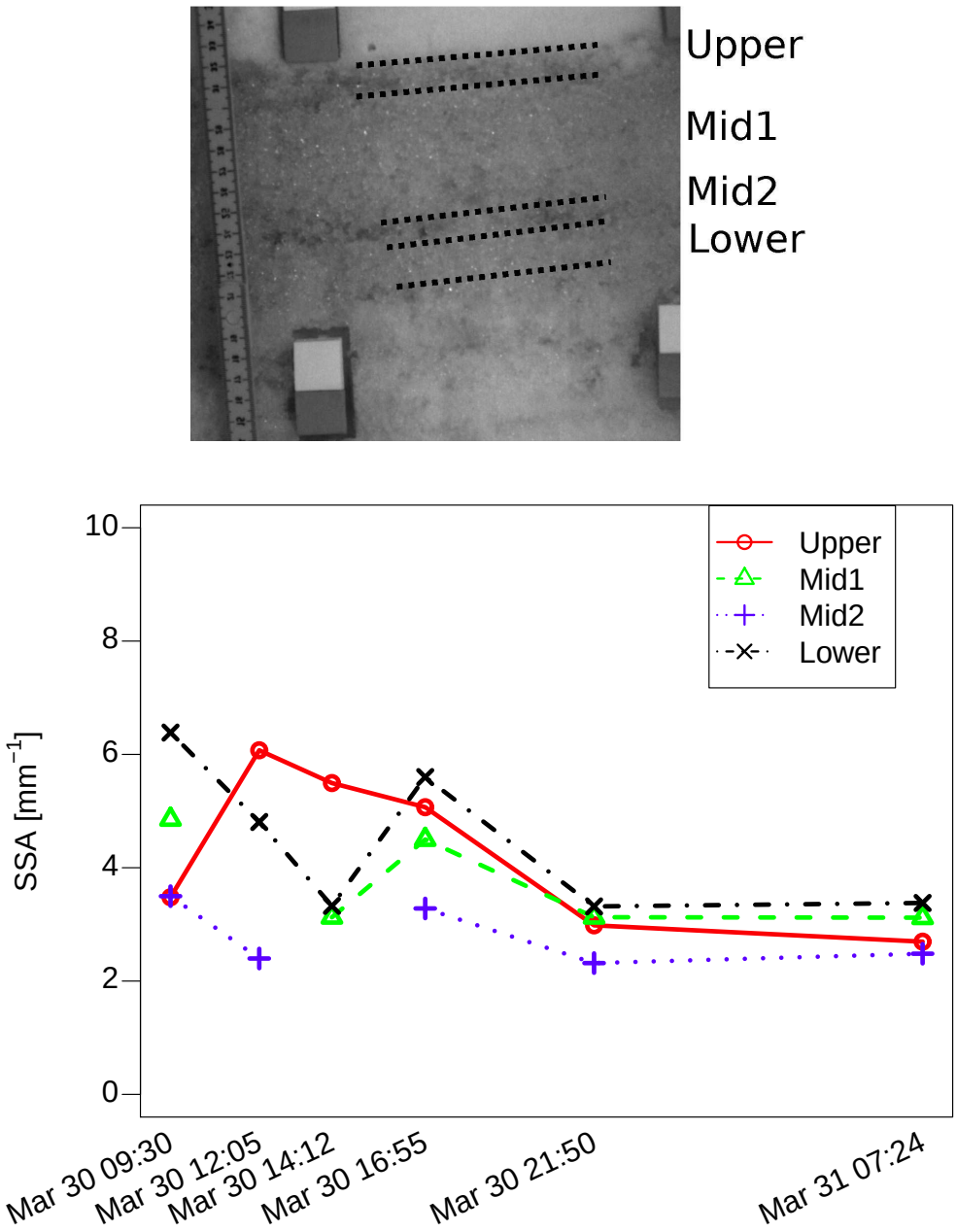

Figure 3.15: *NIR image (top) and SSA time series for crust LAB100330. The Upper and Mid2 ROIs are visible as slightly darker areas at the top of the crust and in the middle of the crust, respectively.*

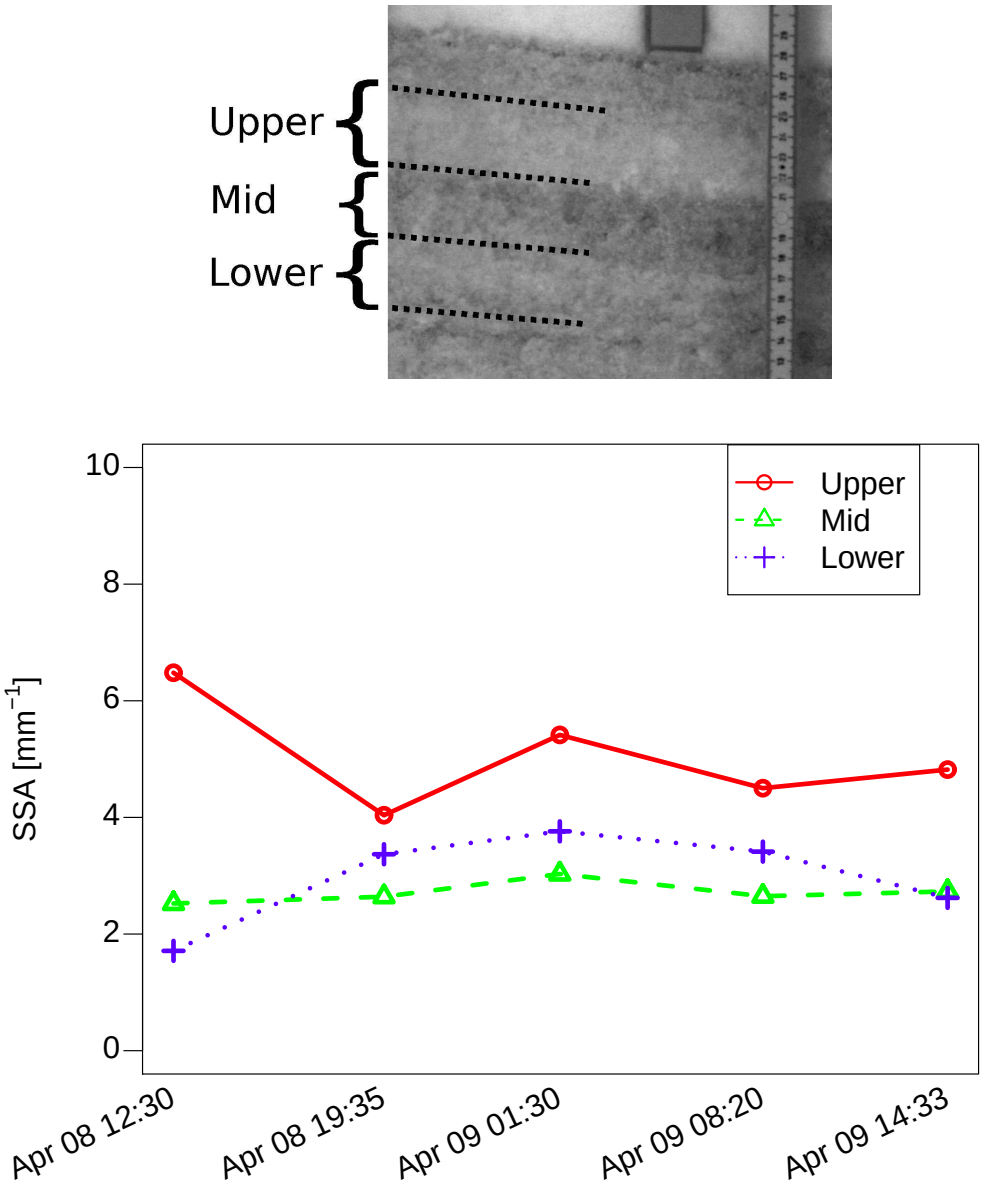

Figure 3.16: *NIR image (top) and SSA time series for crust LAB100409. Portions of the crust above the layer marked 'Upper' contained too many voids to ascertain the SSA with any confidence.*

lower portions of the crust. The initial observations on 8 April at 12:30 were taken prior to transporting the crust into the cold lab and all layers were either moist or wet.

The lowest portions of the crust froze by 23:00 but lower and middle portions continued to cool slowly and did not reach equilibrium with the air temperature and vertical temperature gradients greater than 1°C 10 cm^{-1} persisted until the conclusion of the experiment. If the initial observations with moist layers at 12:30 are ignored, the ROIs show a similar trend to those in LAB100330 and all reach maximum SSA after approximately 12 hours. The SSA of upper portion of the upper and middle portions of the crust both remain stable while the lower portion decreases slowly over the final 12 hours.

The interval between observations was extended to 12 hours for experiment LAB100410 and all other methods including the cold lab temperature were left unchanged. The time series of areal averaged SSA for five identifiable ROIs are shown in Figure 3.17. As with previous cold lab experiments, the upper portion of the crust experienced strong vertical temperature gradients immediately upon placement in the cold lab and froze first, with the gradient dropping to below 0.1°C 10 cm^{-1} 14 hours after being placed in the cold lab. Lower portions of the crust maintained a vertical temperature gradient in excess 1°C 10 cm^{-1} for 24 hours and did not reach equilibrium with the cold lab air temperature until 36 hours. Unlike the first two cold lab experiments, none of the ROIs reach a peak, and in fact the SSA continues to decrease until the 24-hour point, remains approximately stable through 36 hours (at which point all temperature gradients were near 0 °C) then increased through the next 12 hours before finally dropping again during the final observation 13 April at 09:35.

The final cold lab experiment extended the observation interval to 24 hours and the total experiment duration to 120 hours. The cold lab temperature was set to -9°C to slow the freezing time and extend the duration of strong temperature gradients. The entire crust was frozen after approximately 36 hours and the temperature of all ROIs was equalized with the cold lab air temperature after 66 hours. Temperatures gradients greater than 1°C 10 cm^{-1}

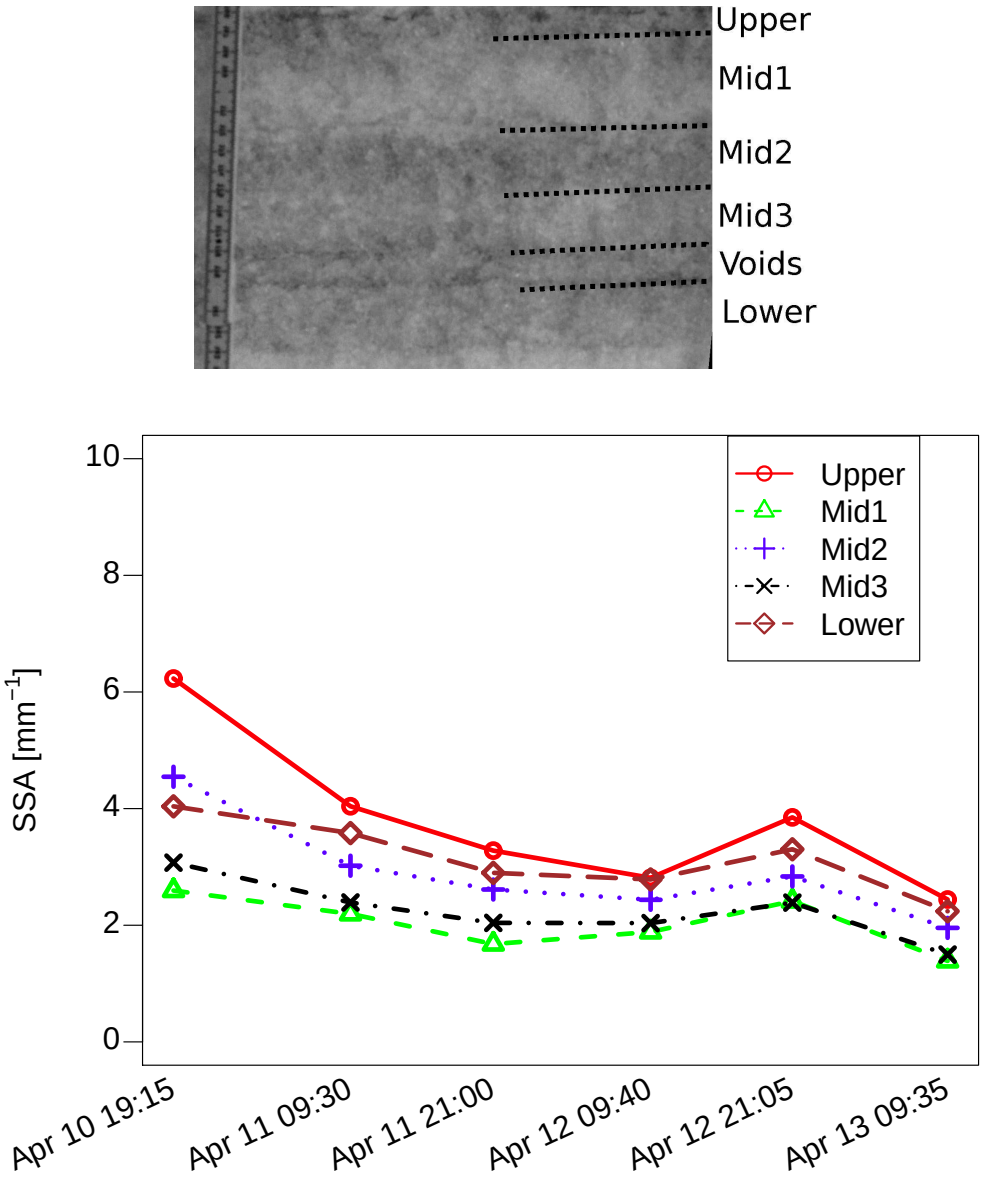

Figure 3.17: *NIR image (top) and SSA time series for crust LAB100410. The first observation 10 April at 19:15 was taken outdoors before the crust was brought into the cold lab. The area marked 'Voids' crumbled easily and the SSA could not be determined.*

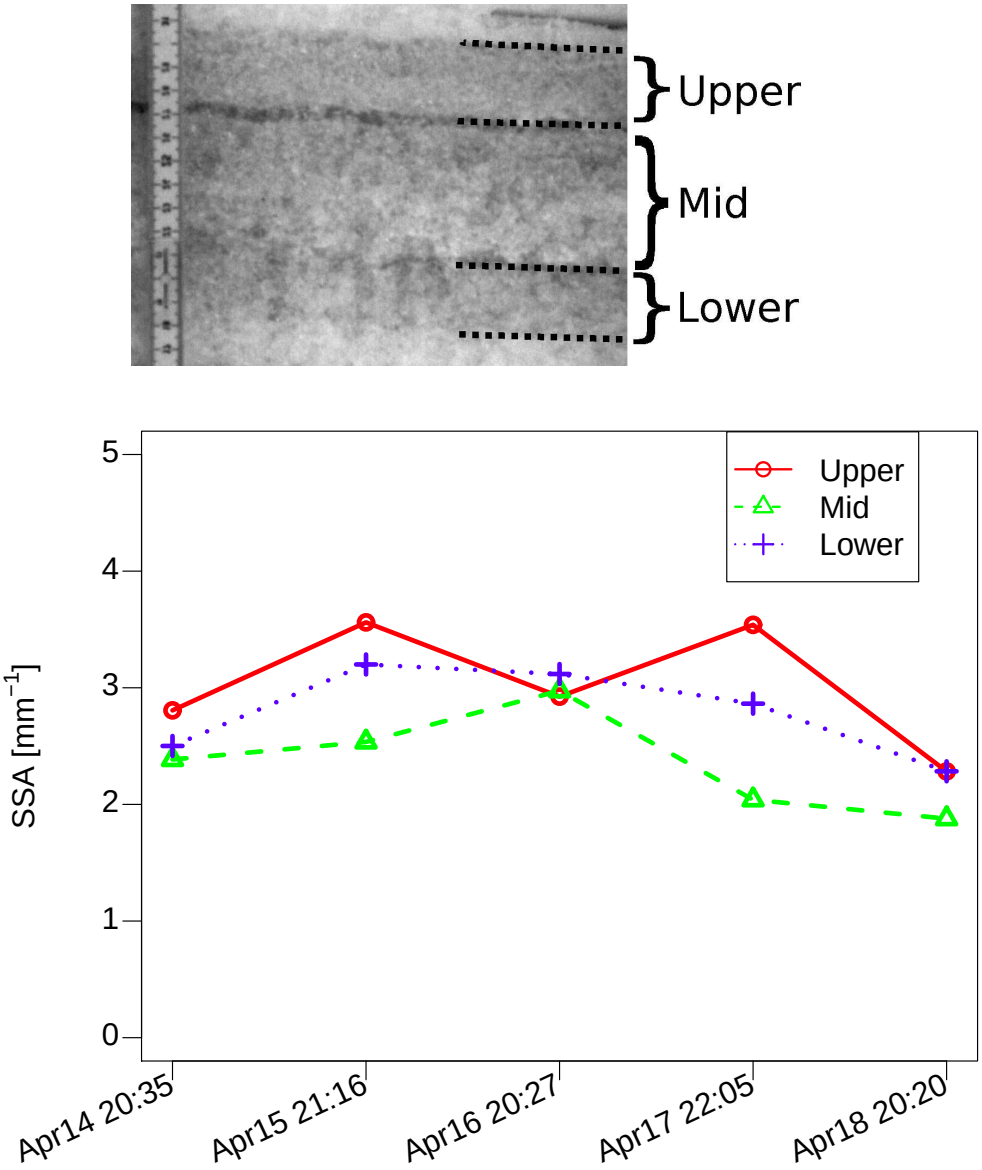

Figure 3.18: *NIR image (top) and SSA time series for crust LAB100413.*

persisted in lower and mid-portions of the crust for 48 hours.

Areal average SSA for LAB100413 are shown in Figure 3.18 with the backyard observations excluded. The first observation shown is for 14 April, after 24 hours in the cold lab. The SSA of the lower ROI is a slight parabolic curve, similar to that observed over a shorter period in the lower portion of LAB100409. The mid and lower ROIs both reach peaks at 72 hours into the experiment then decrease through the remainder. Some small developing facets in the mid and lower ROIs were observed under a microscope on 16 April but no observed structural changes could account for the subsequent decrease in SSA.

Discussion: 2009-10 Cold Lab Crusts

A series of four cold lab experiments were conducted at the Rogers Pass cold lab using natural crusts harvested from the same area. All samples were moist or wet before being brought into the cold lab and, as with other natural crusts, the validity of including SSA measurements in time series analysis is questionable. At minimum, samples with observable free water ('moist' or 'wet') should not likely be compared with dry or fully frozen samples if SSA is being used as a proxy for structural change in the crust.

Three of four crusts had initial increases in SSA in upper portions which were exposed to a strong vertical temperature gradient as soon as they were placed in the cold lab. Some development of facets and an corresponding increase in SSA would normally be expected with melt-freeze grain types which tend to be composed of clusters of large semi-spherical grains even when the temperature gradient is of relatively short duration (e.g. Jamieson and Fierz, 2004). LAB100410 was the sole experiment where this was not observed. Even discounting the first observation 10 April when the crust was moist or wet, the SSA of the upper ROI exhibits a decreasing trend. One possible explanation is that free water within this upper layer froze in the interstitial portions of the upper ROI leading to a lower areal SSA. The continued decrease throughout the remainder of the experiment may be attributable to the sintering process hypothesized by Kaempfer and Schneebeli (2007).

LAB100410 is also anomalous due to the uniform increase of SSA in all ROIs 48 hours into the experiment once the crust temperature was nearly equalized with the cold lab temperature. There was no change in lighting source, diffusion of light at this time step, nor was any shadowing evident in the NIR or visible photographs. There were also no apparent changes in the crust structure visible under a microscope and it seems likely that the increase due to some factor in the observational technique, but no specific reason is immediately apparent.

It is apparent from trends in all crusts that vertical temperature gradient alone is not reliable predictor for trends in SSA. This could be due to a number of factors including magnitude and duration of the temperature gradients as well as the structural characteristics of the crusts themselves, which tend to have large grains resistant to metamorphism, high thermal conductivities and lack barriers to vertical heat transport, the opposite of what was observed by Greene (2007).

The decrease in SSA under weak temperature gradients for LAB100413 is similar to what was observed in the 2008-09 South Run crusts, but once again no other observations offer a clue as to the mechanism responsible. The most likely explanation is that the natural crusts were subject to episodic temperature gradients due to the strong diurnal cycles in the air temperature and had already developed some internal faceting. This would be missed by NIR photography due to the free water and then masked as the free water either refroze or drained to lower layers and the temperature gradient disappeared as the crust reached equilibrium with the cold lab temperature. If this hypothesis is correct, the changes are too subtle to be tracked visually or with the aid of microscopes.

NIR photography appears to be a valid tool to track changes in crusts under artificial conditions of the cold lab, but it is apparent that allowances have to be made for differences in moisture content as samples are moved from a relatively warm outdoor environment into the lab. Although various authors (e.g. Morin et al., 2010) have used NIR on layers with

abundant free water it is likely that including these data in any time series analyses will lead to erroneous conclusions based both on the influence of free water on the derived SSA and the unequal distribution of free water in a given sample.

3.4.4 Spatial variation of SSA on a planar slope

The site used for observations of the three crusts during winter 2008-09 was revisited on 5 February 2010 in the hopes of quantifying the variability of SSA in a natural crust at that site. Crust SR100131 formed under similar meteorological conditions to those tracked during the previous winter and was buried approximately 10 cm below the surface. Sample methods and a site picture are provided with more detail in Chapter 2.

Figure 3.19 shows the values for areal averaged SSA at 11 points that were laid out on a 2 m by 10 m planar grid. Each grid point shows the SSA for a 1 cm thick layer directly above the crust (top), the crust (middle, red text) and a 1 cm layer directly below the crust (bottom). Sky conditions were overcast during the sampling and all samples were recorded over the course of approximately 45 minutes.

The SSA allows for easy differentiation of the three layers at all but three sample locations, but each is variable within the 20 m^2 sample site. The reason for at least some of the variability in the mean SSA for the crust can be seen by examining the vertical profiles in Figure 3.20. The sample lowest on the slope from the left-hand transect is excluded for the sake of space, and the plots are arranged as they were on the slope. The crust's two highest mean values of 15 mm^{-1} and 16 mm^{-1} in the left-hand transect are associated with small areas of high SSA in the vertical profile. This is true to a lesser extent for the mean value of 13 mm^{-1} in the right-hand transect. No linear trends were found in the mean SSA in the upslope direction, but Figure 3.20 illustrates the pitfalls of relying on mean values alone.

Figure 3.21 shows vertical profiles of CV at the sample sites, with the lower left sample excluded for space. The regions of greatest CV coincide with the crust and also with the highest mean values of crust SSA. The layers immediately above and below have higher SSA

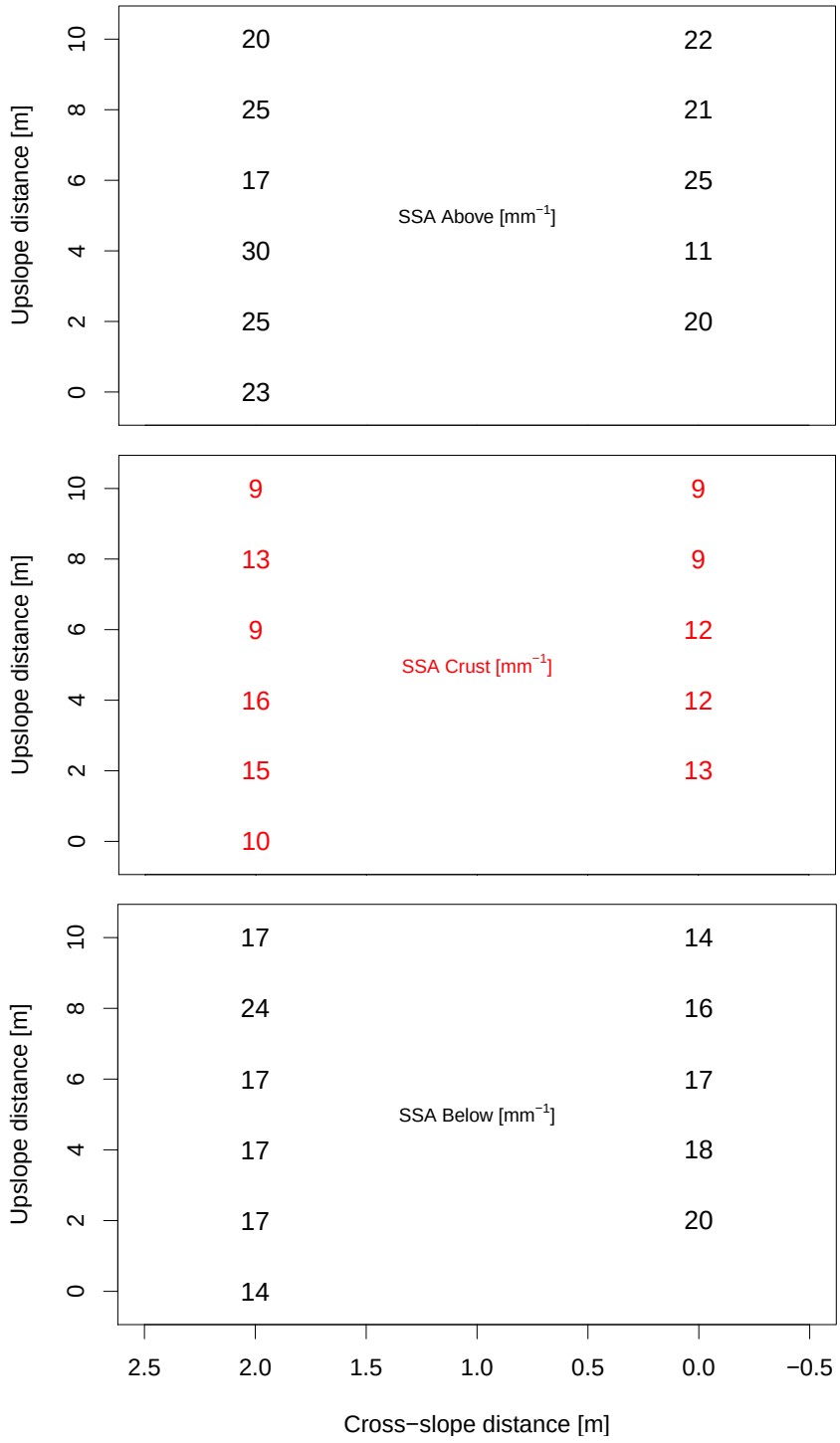

Figure 3.19: *Areal SSA measurements at the planar, south-facing slope used for 2008-09 crusts. The three values at each point on the slope are from a 1 cm layer above the crust, the crust (red text) and a 1 cm layer below the crust.*

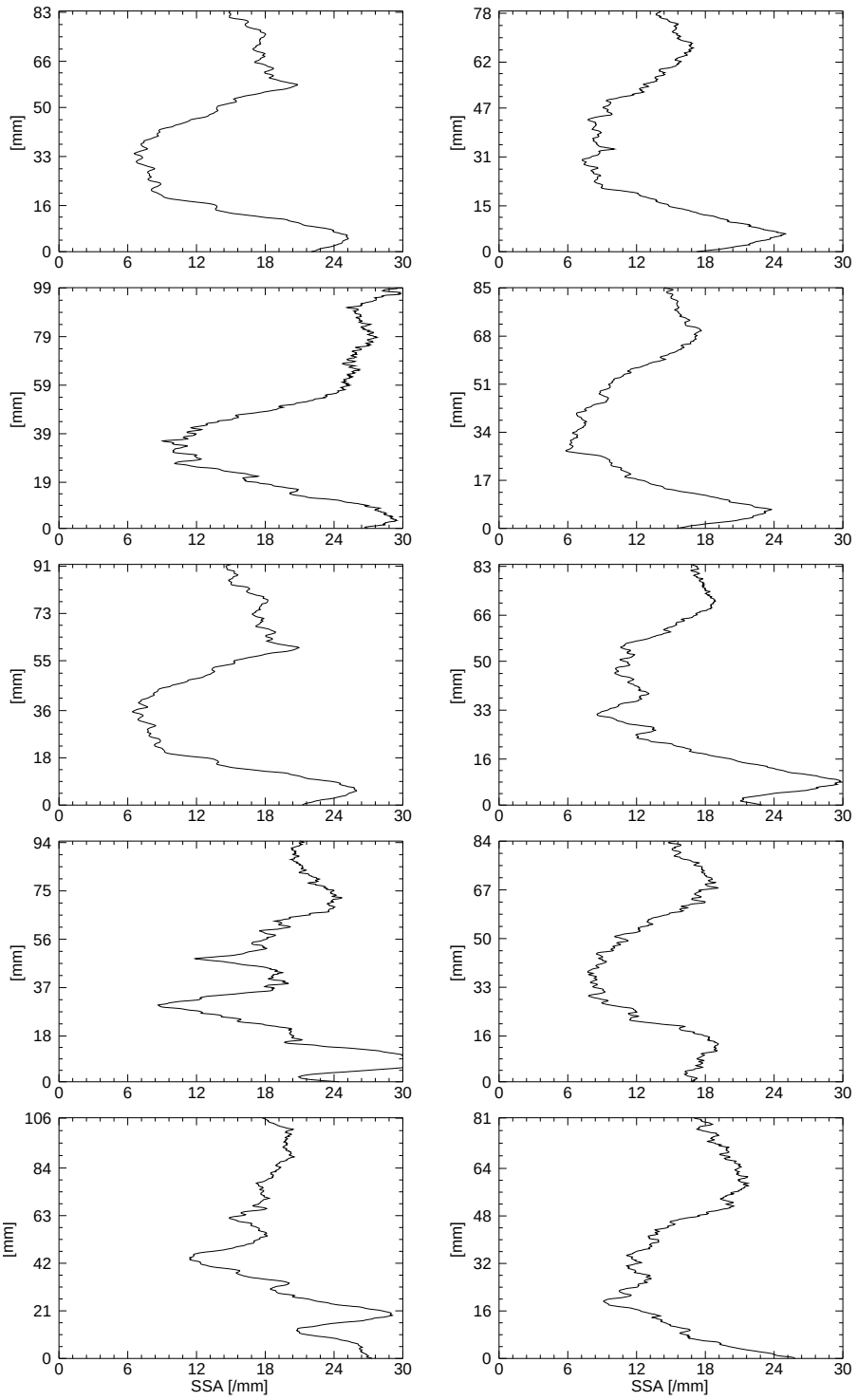

Figure 3.20: *Spatial variability of vertical profiles of SSA at the site used for tracking 2008-09 crusts. The left column corresponds to the left-hand transect and the right column to the right-hand transect.*

(Figure 3.19) but lower variability.

Discussion: Spatial variation of SSA

The site used for tracking of changes during the winter of 2008-09 was revisited in 2010 with the goal of quantifying spatial variation in a natural crust on a uniform slope. The meteorological conditions of formation were solar insolation and warm air temperatures and did not include any form of precipitation, so the crust might be assumed to be uniform on a planar slope with no shading from vegetation. Figure 3.19 illustrates the utility in using NIR photography for discrimination of adjacent layers, but also shows that mean SSA may vary substantially over short distances even on uniform slopes. Figures 3.20 and 3.21 illustrate how alternative analyses techniques may complement the areal average SSA and uncover the reasons behind spatial variation in SSA.

As was shown with crust FI100308 the appropriate method of analysis for a given crust will vary based on its structural characteristics. Even apparently uniform crusts may show some variation and it is important to select a study site that will not contribute to this variability. Each crust should be analyzed not only by its areal mean SSA but also by vertical profiles of SSA and CV. This section illustrates the importance of considering all methods of analysis: If only Figure 3.19 was used, the crust would seem to be more spatially variable than it is. Once Figure 3.20 and 3.21 are considered, the reason for some of this variation can be assigned to small areas of high SSA which of course result in a greater mean areal SSA.

Of course some crusts such as those formed during rain-on-snow events are not well suited for tracking of temporal changes using NIR photography due to their inherent spatial variability. As used here, NIR photography only samples a small section and temporal changes will likely be masked by the larger spatial variability. In these cases structural changes should be tracked by methods using a combination of greater extent and support (e.g.l Schweizer et al., 2008).

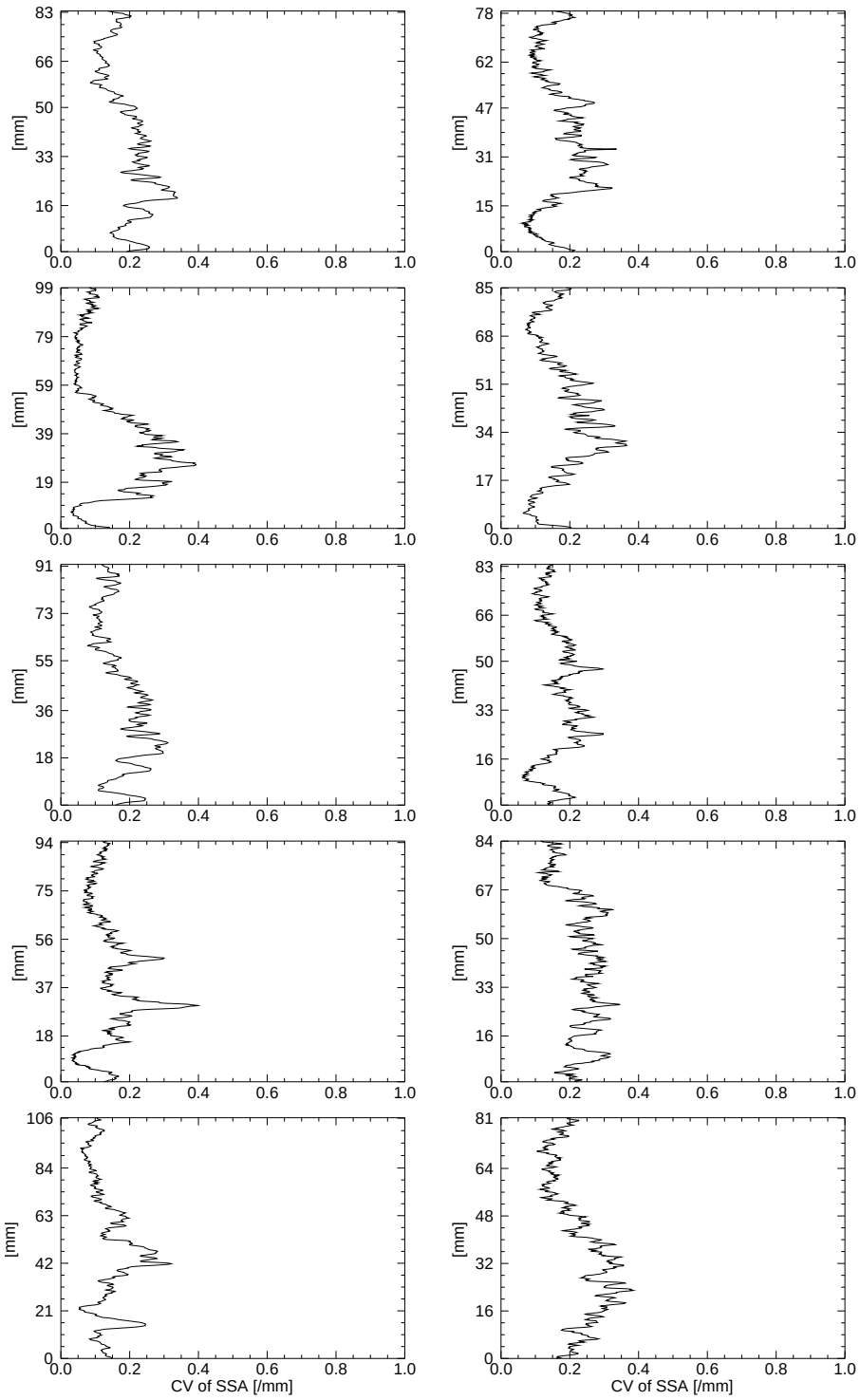

Figure 3.21: *Spatial variability of vertical profiles of CV of SSA at the site used for tracking 2008-09 crusts. The left column corresponds to the left-hand transect and the right column to the right-hand transect.*

3.5 Chapter Summary

NIR photography was used derive areal mean and vertical profiles of SSA in melt-freeze crusts over the course of two winter seasons at Rogers Pass. A total of nine natural crusts were tracked from formation until mid-April. Four cold lab experiments were conducted by transporting samples of natural crust into a cold lab, which was maintained at a constant temperature for periods ranging from 12 to 120 hours. NIR observations were supplemented with continuous temperature measurements using thermistors and thermocouples as well as standard test profiles, which recorded grain type and size, density, hardness and temperature.

Some difficulties were encountered due to shallow crusts and anomalously warm temperatures during the winter of 2009-10, otherwise NIR photography techniques were found to be simple and efficient after minimal practice. Graphical analysis of imagery proved to be time-consuming as images had to be checked manually for pitting or scrapes along the pit wall to ensure that they were excluded from the data set. Although imagery of adjacent non-crust layers were captured they were not analysed during the present study.

Values and trends of SSA were compared with other observed crust properties for the identification of any correlations or similar trends. In most cases data sets were too small to obtain meaningful or significant correlations, but the aggregate of the three 2008-09 crusts, all of which were formed by similar processes, revealed a moderate correlation between the slope-normal temperature gradient and areal SSA as well as a weak correlation between NIR reflectivity and grain size. A link between temperature gradient and SSA is expected as the former is a major driver for snowpack metamorphism, but no correlation was found between time-lagged or averaged temperature gradient and rates of change of SSA in either natural crusts or cold lab crusts where the interval between observations was shorter. The link between NIR and grain size is likewise expected due to the strong dependence of NIR on grain size and shape. The fact that it is weak in this study is likely due to the difficulty in defining 'grain size' in a well-bonded melt freeze crust.

No significant correlations between SSA and other crust properties were found in the 2009-10 data set; however, several apparently contradictory observations raise some questions which may be appropriate for future research. Three of four cold lab experiments as well as one natural crust had SSA that remained consistent or decreased despite the presence of a vertical temperature gradient greater than 1°C 10 cm^{-1}, which would normally be associated with faceting and an increase in SSA. Several observations of decreasing SSA over time despite no observable changes in crust strength or structure hint at the importance of microscale processes, and perhaps of destruction of weak bonds in favour of strong bonds due to curvature effects. The presence of free water (moist or wet layers) on some dates was problematic for analysis of time series data. The SSA equations were not validated with this application in mind and the influence of varying percentages of free water cannot be qualified or discounted.

An attempt was made to track the horizontal and vertical variability of SSA over time in each crust. In some cases this proved to be successful, with trends of increasing or decreasing variability identified, usually near the upper or lower crust boundary. In most cases this was of limited value due to the small sample size obtained.

Finally, although well-suited for ease of operation and tracking of layers, the use of a DSLR camera for NIR photography does present limitations in the data that may be derived. Chief amongst those is the fact that the camera is sensitive to a broad spectrum and results cannot be used for precise calculation of parameters such as optical diameter and by extension cannot be used directly in radiative transfer models. Langlois et al. (2010) employed a slightly modified technique in an attempt to overcome this limitation. Newer methods of portable SSA measurement employed by authors such as Gallet et al. (2009) offer more flexibility in this regard.

3.6 Recommendations for future studies

Results from the present study suggest improvements for future studies. NIR photography was found to be useful both in tracking structural changes over time and in discriminating crust layers from adjacent layers, but difficulties were encountered when layers contained free water (classified as 'moist' or 'wet'). Free water in the NIR image will affect the reflectivity and by extension the derived SSA. There is no way to quantify the effects of free water with the current set of observations and future studies should include quantitative measurements of moisture content.

Temperatures in natural crusts did not vary much nor were there many instances of strong vertical temperature gradients. Although a gradient of 1°C 10 cm^{-1} is accepted as the approximate point at which temperature gradient metamorphism becomes significant it is likely that crusts, with high thermal conductivity, large grains and thick bonds, are more resilient to change and require either stronger or more persistent gradients before interior faceting occurs. For crusts that are spatially variable from time of formation there may be utility in developing an index to quantify degree of faceting over time. It is likely that such an index would also require larger sample sizes than were used in the present study.

Spatial variability in a relatively uniform crust is presented in Section 3.4.4. By analysing areal average SSA and vertical profiles of SSA and CV of the SSA an accurate picture of spatial variability may be obtained, but as outlined by Schweizer et al. (2008) tests using only small sample areas ('support') may not get an accurate picture of the true variability in a layer. Future studies should include more rigorous tests of spatial variability of a variety of crusts including those formed from solar/air temperature effects versus those formed due to wet snow or rain events. Such studies will by necessity be time and labor intensive due to the destructive nature of most snowpack observations. Methods such as those used by Tape et al. (2010) offer a good starting point for studies of spatial variability.

Analytical methods for treatment of NIR photography could be refined beyond what

was used in the present study. As was shown in Section 3.4.4, the mean SSA may vary substantially across a small study plot, but relative temporal change in relation to adjacent layers may offer valuable insight to structural changes in crusts, especially at the upper and lower boundaries when strong vertical temperature gradients are present.

Finally, the processing of NIR imagery could likely be automated beyond what was done in the present study. More effort in ensuring diffuse lighting and proper exposure in the field may enable increased automation during post-processing and analysis. This was attempted in the present study but was unsuccessful due to over or underexposure in some samples. The most time-consuming portion of analysis involved the manual definition of specific ROIs for each crust for each observation date.

Chapter 4

Snowpack Modeling

Chapter 2 and 3 introduced two relatively new methods for tracking temporal changes in melt-freeze crusts. These measurements as well as more traditional observations of grain type, temperature and density may be simulated using a variety of snowpack models of varying complexity. This chapter provides a brief introduction to two physically based models; the French CROCUS and the Swiss SNOWPACK. Five natural melt-freeze crusts from the winters of 2008-09 and 2009-10 are simulated using the SNOWPACK model and results are discussed along with potential improvements and recommendations for future studies.

4.1 Literature Review

Two snowpack models are presently used in operational avalanche forecasting: SNOWPACK (Lehning et al., 2002a,b; Bartelt and Lehning, 2002) and CROCUS (Brun et al., 1992) are both single-column (1D) physically based models that allow evolution of microstructural and mechanical properties of discrete layers (often referred to as 'nodes') of the snowpack. The use of some empirical parameterizations is unavoidable due to limitations in scale and gaps in knowledge. One such case is the flux of water vapor under varying vertical (slope-normal) temperature gradients: Metamorphism under weak macroscopic temperature gradients (equitemperature, or 'radius of curvature' metamorphism (Colbeck, 1980)) is dependent largely grain size and shape, ratios of grain to bond size (Brown et al., 2001; Miller et al., 2003) and curvature. At some point when the slope-normal temperature gradient becomes strong enough (typically around 10 °C m^{-1}) curvature effects become dominated by temperature gradient effects (Baunach et al., 2001; Kaempfer et al., 2009). To further complicate matters

Sturm et al. (1997) found that vapor flux is related to grain growth rates, but they are not directly coupled. Pinzer et al. (2012) showed that in seasonal snow subjected to high temperature gradients of 50 °C m^{-1} the total lifetime of individual grains was on the order of 100 hours, with longer residence times for larger or vertically oriented structures. The same authors (Pinzer and Schneebeli, 2009) showed that alternating the direction of a strong temperature gradient led to high recrystallization rates but not necessarily to the development of faceted forms. The state of knowledge on metamorphism at the micro or grain scale has advanced rapidly in recent years but such scales are smaller than what can currently be resolved in snowpack models and metamorphism under weak or strong gradients must be treated as discrete processes.

There has been little validation of snowpack models specifically dealing with melt-freeze forms, though some studies have examined their influence on adjacent layers. Colbeck and Jamieson (2001) proposed a mechanism for the formation of facets above crusts. Jamieson and Fierz (2004) performed cold lab experiments with dry snow overlying wet snow, and SNOWPACK was successful in reproducing the observed faceting at interface of the two layers. Jamieson (2006) summarized the current state of knowledge regarding buried crusts, formation of weak layers and their roles in persistent slab avalanches. Greene (2007) used ice layers of varying thicknesses in a cold lab to test the effects of barriers to vapor flow under high temperature gradients. Stereological analysis allowed for the retrieval of SSA and effective bulk thermal conductivity. SNOWPACK was used to simulate the experiments and close agreement was found between modeled and observed temperature profiles, while the bulk thermal conductivity was generally overestimated. Smith et al. (2008) modeled the formation and evolution of a rain-on-snow crust (CR071205) and found that the model was unable to reproduce the formation based on meteorological inputs from a nearby weather station. Re-initializing using an observed snow profile yielded small overestimations of temperature and density until spring, when temperature and grain size were poorly modeled. This was likely

due at least in part to how the crust was initialized in the model. Rutter et al. (2009) compared thirty-three snow cover models during simulated winter season runs using North American Regional Reanalysis data as meteorological input, and found that such warming events and associated drainage of free water through the snowpack were the major cause of divergence between models.

The evaluation of model simulation of SSA and thermal conductivity is of particular interest for this study. The temporal evolution of SSA in CROCUS may be described by either prognostic equations based on snow age and temperature gradient (Taillandier et al., 2007) or diagnostic equations based on either snow type and density (Dominé et al., 2007) or dendricity, grain size and sphericity (Morin et al., 2013). In the prognostic equation of Dominé et al. (2007) melt forms are assigned a constant SSA of 4.5 mm^{-1}. Recent validation studies (Jacobi et al., 2010; Morin et al., 2013) indicate that both routines perform relatively well, with diagnostic equation being slightly worse due to its dependence on density. The effective thermal conductivity is that derived by Yen et al. (1981) and is entirely a function of density.

In SNOWPACK the optical equivalent radius is calculated as part of grain growth routines, from which the SSA may be calculated. The thermal conductivity is diagnosed as a function of relative fractions of air, ice and water in a given layer. The conductivities of water and ice are both dependent on temperature and an enhancement for water vapor is applied for wet snow. Convection is not allowed, but is not likely relevant in the present study due to the absence of long-lived sharp temperature gradients and the large voids characteristic well developed depth hoar (Sturm and Johnson, 1992). Fierz and Lehning (2001) describe the initial steps involved in tuning and validating grain growth and thermal conductivity against observed values and noted that they closely followed the density-dependent equation proposed by Sturm et al. (1997).

4.2 The SNOWPACK model

SNOWPACK may be driven by either measured or simulated (e.g. Bellaire et al., 2011) meteorological data. For cold lab studies (Greene, 2007; Jamieson and Fierz, 2004) variables such as wind and precipitation may simply be set to 0, incoming long and shortwave radiation may be set to constants appropriate to the lab conditions and Dirichlet boundary conditions are imposed by measured surface and basal temperatures. The minimal meteorological inputs are air temperature, relative humidity, wind speed and direction, incoming long and shortwave (solar) radiation and precipitation (either liquid equivalent or snow depth). The model can also be constrained by measured surface and basal temperatures, snow depth and measured surface albedo.

Simulations may be started before there is snow on the ground, with layers allowed to form within the model, or the model may be initialized with a full snow profile recorded once there is already snow on the ground. Lower boundary conditions may be set to a constant, or the model may derive these based on meteorological inputs and ground cover (soil, grass or snow). Rather than use IACS classifications for snow type (Fierz et al., 2009) the model defines individual layer elements by a combination of density, grain radius, bond radius, dendricity and sphericity. The latter two terms vary between 0 and 1, with new snow having a dendricity of 1 and sphericity of 0, perfect rounded grains a dendricity of 0 and sphericity of 1 and transitional (facets become rounded or vice-versa) grains a dendricity of 0. New snow is assigned a default initial grain radius (by default 0.15 mm) and no grain growth occurs until dendricity reaches 0. If initializing a simulation with an observed snow profile, some trial and error is often necessary when deciding on these parameters for each existing layer.

Figure 4.1 shows one of several matrices that are used for converting from IACS grain types observed in snow profiles (Fierz et al., 2009) to the dendricity, sphericity and grain size needed by SNOWPACK. Similar matrices exist for grains that have already reached

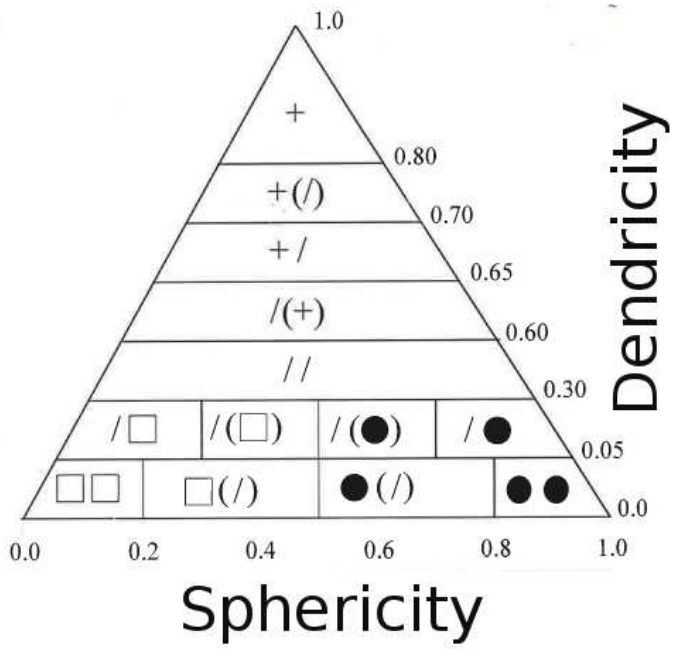

Figure 4.1: *Matrix for converting IACS grain types to SNOWPACK grain types. Similar matrices exist for grain types with dendricity of 0 and grains that have undergone melting and re-freezing. From SNOWPACK documentation.*

a dendricity of 0, in which case the grain in SNOWPACK is initialized using sphericity and grain size. For layers that have undergone melting and/or refreezing the grain size and sphericity are supplemented by a grain type marker. Markers and typical values of sphericity, dendricity and grain size used to initialize SNOWPACK are shown in Table 4.1.

As outlined in the previous section, SNOWPACK outputs are a mixture of prognosed and diagnosed physical properties. The former (grain and bond radius, layer density and temperature) are physically based and are allowed to evolve throughout the course of the simulation according the physical laws in the model. The density of new snow is based on empirical equations and may depend on air and surface temperature, wind speed, relative humidity and elevation, depending on the parameterization chosen by the user. Layer temperature evolves based on boundary conditions in conjunction with heat transport through adjacent layers in the snowpack. Metamorphism and density both depend on grain and bond

Table 4.1: *Typical parameters used to initialize SNOWPACK from an observed snow profile. Abbreviations follow IACS classifications (Fierz et al., 2009). A layer of moist rounded grains (RG) would have a marker of 12, and once refrozen would have a marker of 22.*

Grain Type	Dendricity	Sphericity	Grain Size	Marker
PP	0.65-1	0-0.2	any	0
DF	0.3-0.65	0-0.8	any	0
FC	0	0-0.4	0-1.5	1
DH	0	0-0.5	$\geq$1.5	1
RG	0-0.1	0.5-1	0-0.7	2
RGxf/FCxr	0	0.2-0.8	0-1	2
SH	0	0	any	3
Moist or Wet	0	0-1	any	+10
Refrozen (MF)	0	0-1	any	+10

radii, dendricity, sphericity, microstructure marker, coordination number, thermal conductivity and viscosity. The transition between equitemperature (EQ) and temperature gradient (TG) metamorphism is defined explicitly in terms of the vapour pressure gradient and is by default 5 hPa m^{-1}.

Other parameters such as optical equivalent grain size, effective thermal conductivity, layer hardness are diagnosed at each time step after metamorphism has occurred. Some, such as hardness, are calculated only for evaluation purposes while others such as thermal conductivity and optical radius are carried forward to the next time step for use in thermal and metamorphic routines.

Version 3.2 of SNOWPACK, used in this study, incorporates a number of recent formulations for thermal conductivity, equivalent optical diameter and water transport (e.g. Hirashima et al., 2008, 2010). This latest version was selected due to the relative abundance of recent research that has been incorporated from snow climates around the world, whereas older versions had often been validated primarily in the Swiss Alps.

The optical equivalent diameter in the near-infrared band in SNOWPACK is derived by

an empirical equation published in Vionnet et al. (2012) where for non-dendritic forms,

$$d_{opt} = 2 * (0.5 * (2 * r_g * s + (1 - s) * max(0.4, r_g)) \tag{4.1}$$

where d_{opt} has units of mm, r_g is the model grain radius and $0 < s < 1$ is the model sphericity, which varies from 0.0 for new snow to 1.0 for perfectly rounded crystals. For grains with a sphericity of 1.0 the optical diameter is equal to the physical diameter. To compare with field measurements of SSA, the transform published by Matzl and Schneebeli (2006) may be used;

$$d_{opt} = \frac{6}{SSA} \tag{4.2}$$

where d_{opt} has units of mm and SSA has units of mm^{-1}. Due to the uncertainty in spectral response of the camera used to capture NIR images in this study as well as well as in the equation used to determine the SSA (Chapter 3) this is not an exact relationship but will still give a relative measure of model performance.

Thermal conductivity for very high or very low density snow is defined as a linear combination of thermal conductivity of the volumetric fractions of ice, air and water for each layer. For snow of intermediate density a more complex empirical equation is used which incorporates wind pumping, water vapor in pore spaces and temperature dependence of thermal conductivities of ice and water fractions.

For hand hardness, SNOWPACK has three available parameterizations for hand hardness, all of which output a hardness index from 1 - 6 per the International Classification of Seasonal Snow on the Ground (Fierz et al., 2009). The default configuration (MONTI) assigns a hardness based on grain type and density with lower index values with increasing water content. Fully frozen melt-freeze forms are assigned a constant value of 5; the Swiss parameterization depends only on grain size and density except in the case of melt forms, when the index is reduced with increasing water content; the ASARC parameterization is based on a regression on the ASARC database from 2002 and depends on grain type

and density for new snow and surface hoar. Grain size is incorporated for other forms as well as water content for melt forms. The hardness may be converted to Swiss Ramsonde penetration resistance for output using the formula

$$R_N = 19.3 * R_{index}^{2.4} \tag{4.3}$$

where R_N is in units of Newtons. Calibrated vertical penetration resistance should not be directly compared to the horizontal resistance recorded in test profiles following the standards in CAA (2007) but the two are likely monotonically related.

SNOWPACK may be used to simulate multiple aspects starting either from bare ground or by initializing the model using both a flat-field profile and profiles from each aspect to be simulated. In this case the snow cover is allowed to evolve independently on each aspect based on meteorological data from the flat-field weather station, and snow transport by wind may also be simulated from one aspect to another.

4.3 SNOWPACK Simulations

Five natural crusts from winters 2008-09 and 2009-10 were simulated using SNOWPACK version 3.2, which was released in February 2014 and incorporated significant changes from past versions including an improved water transport scheme (Hirashima et al., 2010). Two of these were natural crusts at Mount Fidelity study plot and the remaining three were from the South Run area of Mount Fidelity closure. The crusts were chosen due to their relative homogeneity as being more suitable to simulation by a single column model that by its nature cannot incorporate spatial variability over the scale of a study plot. A rain crust from December 2007 that was simulated with an older version of SNOWPACK (Smith et al., 2008) was not revisited due to its spatial variability and the conclusion that formation could not be simulated using only surface meteorological measurements. Several crusts from winter 2009-10 were not simulated due to a lack of input meteorological data (RP100112, BV100112) and

difficulty in tracking the crusts due to constant melting and merging (SR100131, SR100210).

Model data were extracted from SNOWPACK output files and plotted alongside observations of layer depth, density, temperature, SSA and, for 2010, thermal conductivity. Evaluation of a thin rain crust (FI100109) was limited to qualitative evaluation of formation and thickness as the layer was too thin for reliable measurements of SSA, density and thermal conductivity.

4.3.1 SNOWPACK configuration

Meteorological data from Mount Fidelity station, described in Appendix A, were used to drive simulations for all natural crusts. Hourly data at the station were supplied by a ventilated incoming pyranometer and incoming longwave radiometer, wind speed and direction, air temperature, relative humidity and a precipitation accumulator with resolution of 0.1 mm. Hourly measurements of new snow accumulation on a 24-hr snow board, cleared approximately daily, were used by Bellaire et al. (2011) but were not used to constrain model snow depth in these simulations. Data were logged on a Campbell CR10X datalogger powered by batteries, which typically ran down over the summer so data were not available until the first site visit of the winter season in late November or early December.

Simulations were initialized using full depth profiles (CAA, 2007) observed by Parks Canada avalanche technicians or from ASARC researchers. All model runs were configured with neutral atmospheric stability, Neumann boundary conditions and with the canopy model disabled as all study sites were in open areas. Default model parameterizations were used for surface albedo, new snow density and layer hardness. Some other options were modified to provide better agreement between modeled output and observations; these are detailed in the next section.

4.3.2 South Run 2009 Crusts

Three natural melt-freeze crusts (SR090127, SR090222 and SR090301) were tracked at the South Run area of the Mount Fidelity study area during the winter of 2008-09. The study plot is approximately 700 m from the Fidelity weather station on a south-southeast aspect. As outlined in Appendix A, a failure of the Fidelity datalogger led to a loss of radiation data from 20 February - 5 March so simulation of a complete winter's snowpack was not possible. Specific Surface Area measurements are described more completely in Chapter 3 and thermal conductivity data were not collected during the winter of 2008-09.

Simulations of the South Run crusts were initialized using a Parks Canada full profile at Mount Fidelity from 2 March and ASARC test profiles at Fidelity and South Run from 5 March. The South Run test profile extended to 20 cm below SR090127 and the remainder of the profile was artificially populated with rounded grains. The two profiles at Fidelity were merged into a synthetic 'full profile'. The developers of SNOWPACK note that this approach is less ideal than allowing all layers to form naturally. The initialization of melt-freeze crusts presents some unique difficulties since grain and bond size are not well-defined or easily measured.

Snow erosion and snow distribution routines were enabled, the canopy model was disabled and other parameterizations were left at their default configurations for the initial run with a 60 minute timestep. This first configuration led to a lack of convergence in the temperature subroutines, possibly due to strong insolation and warming. The timestep was subsequently reduced to 15 minutes with meteorological data resampled from the original 60 minute intervals. Resampling is done automatically by the MeteoIO library, which is used to process input data for SNOWPACK version 3.2. The three simulations run for these crusts are summarized in Table 4.2.

Evolution of grain type and snow depth from this first simulation SR20090305-1, are shown in Figure 4.2. A period of accumulation from early to late March followed by rapid

Table 4.2: *SNOWPACK iterations for SR20090305.*

Run Name	**Parameters modified**	**Modified value**
SR20090305-1	none	model defaults
SR20090305-2	crust grain size	optical diameter from SSA
SR20090305-3	water transport	NIED

warming and settling is evident, as is the rapid warming of the upper snowpack by April 11, denoted by a region of solid red. The three crusts of interest exist at the start of the run shortly after SR090301 was first buried.

The simulated and observed depth of the top of each crust is shown in Figure 4.3. SNOWPACK's simulated depths are very close to measured depths with the exception of 21 March, when the simulated depth is 10-20 cm shallower than observed depth for all crusts. Referring to Figure 4.2 it appears that actual snow accumulation exceeded simulated accumulation. The simulated depth for SR090127 on 27 March is greater than was observed indicating insufficient settling in upper midpack layers.

Figure 4.4 shows simulated and measured density and temperature for crust SR090127. Minimum and maximum values from SNOWPACK are due to the the model treating layers as multiple discrete nodes so there is often a range of physical properties that correspond to a single 'layer' in an observed snow profile. There is a marked negative temperature bias in the simulation until the snow becomes isothermal on 11 April. The simulated density tracks closely with observations until 27 March when the observed density spikes. The observed temperature on March 27 was -0.8 °C and although the crust was classified as 'dry' it is likely that the increased density was related to these warmer temperatures which were not replicated by SNOWPACK.

Figure 4.5 shows the simulated and observed SSA for SR090127, where the simulated SSA are derived from the model optical diameter using Equation 4.2. There are multiple sources of error in the measurements including errors in the SSA parameterization, spatial

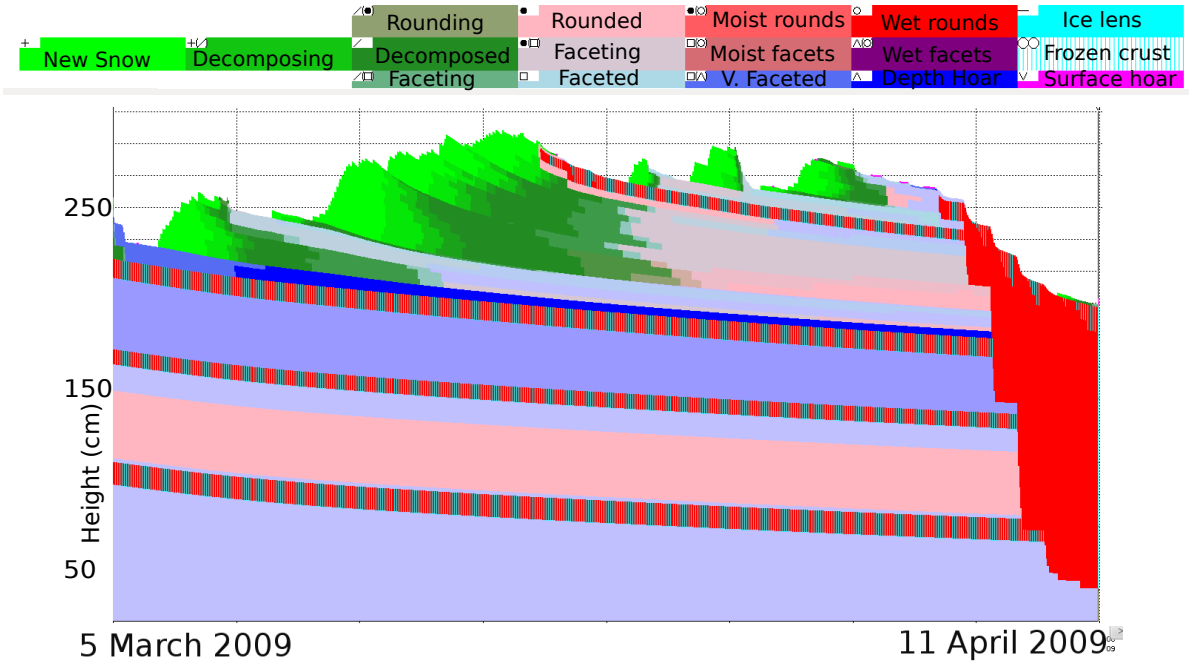

Figure 4.2: *Evolution of snow depth (cm) and grain type for simulation SR20090305-1 run from 5 March - 11 April, 2010. Melt-freeze crusts are denoted by red with vertical cyan lines and moist or wet layers by solid red shading. New snow is shaded green and rounded grains are shaded pink.*

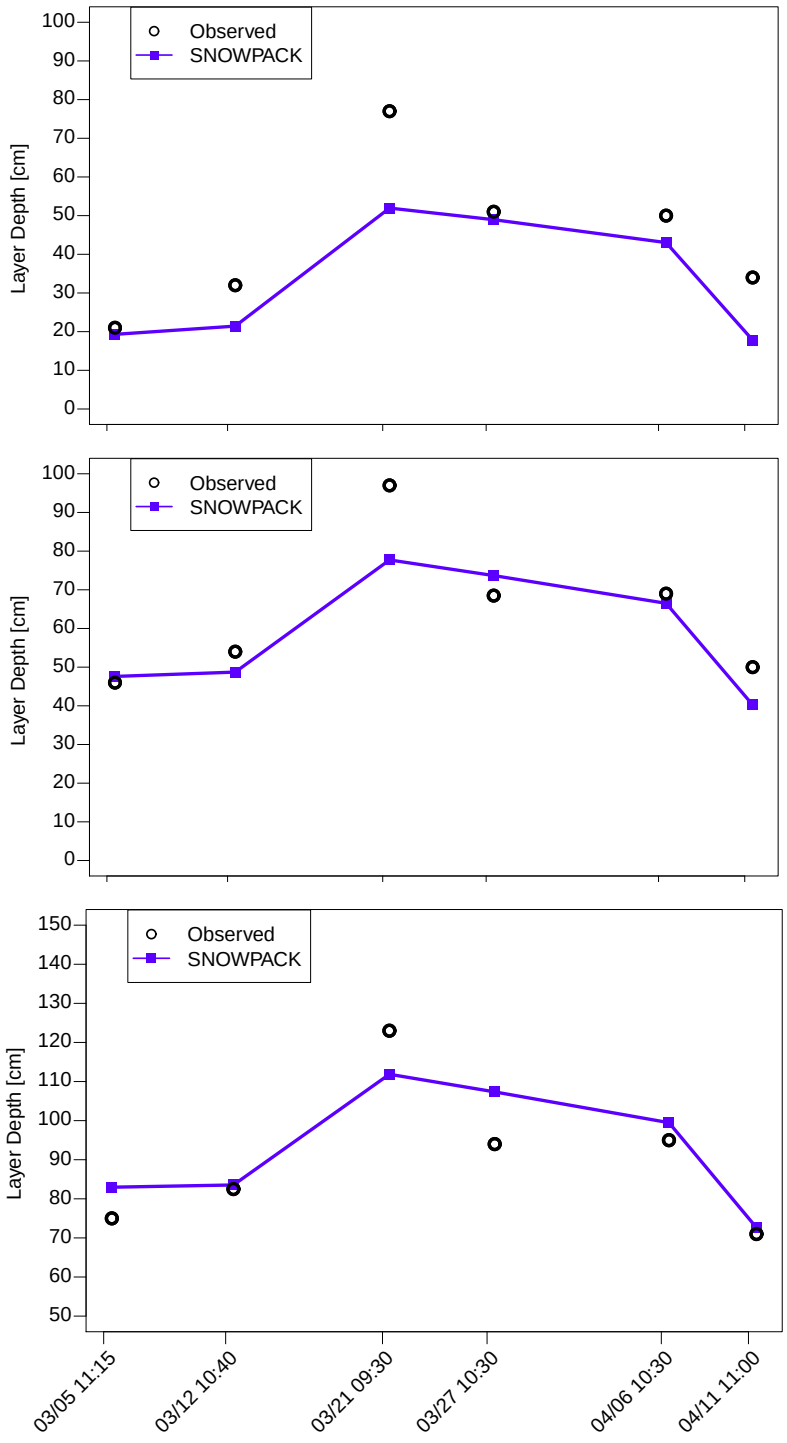

Figure 4.3: *Modeled versus observed layer depth for SR090301 (top), SR090222 (middle) and SR090127 (bottom) from run SR20090305-1.*

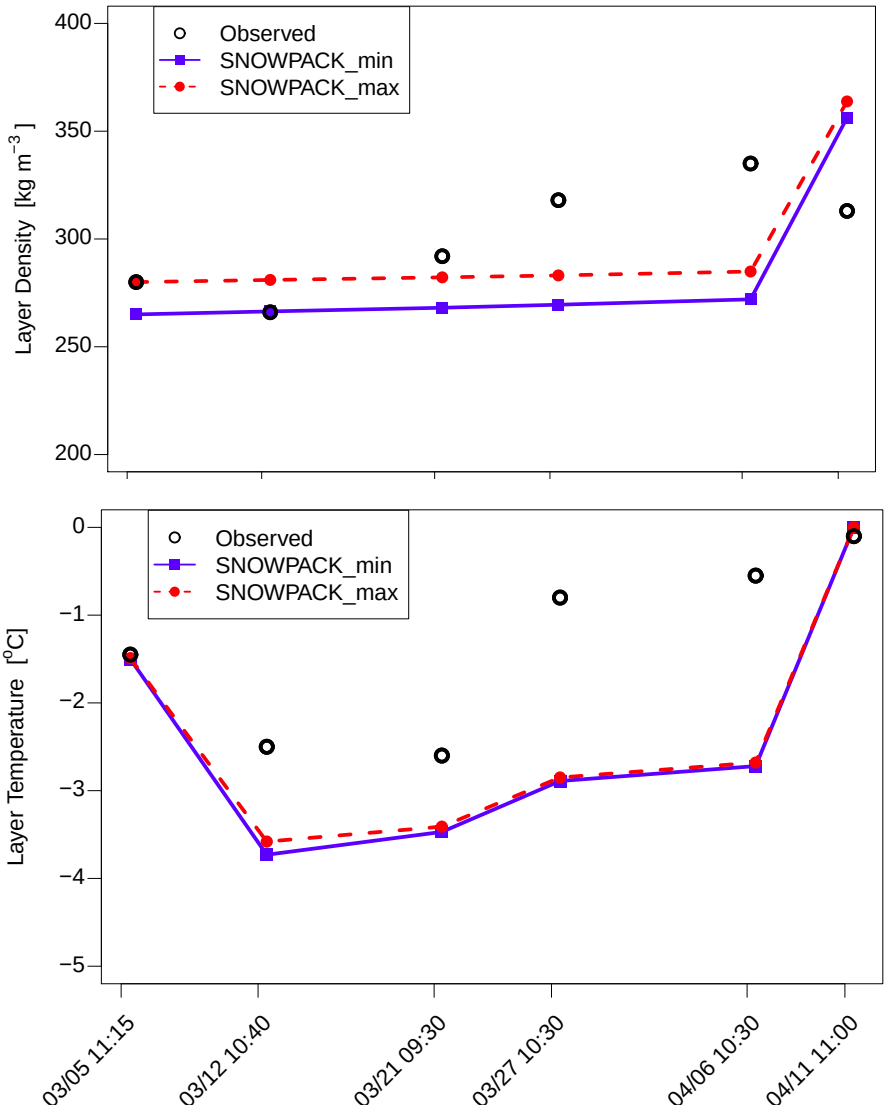

Figure 4.4: *Measured versus simulated layer density (top) and layer temperature (bottom) for SR090127 from run SR20090305-1.*

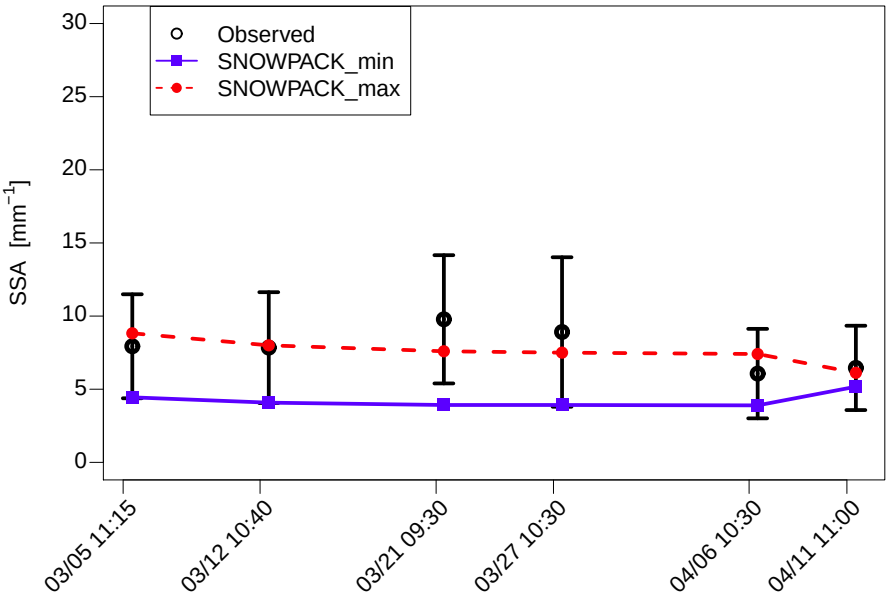

Figure 4.5: *Measured versus simulated specific surface area for SR090127 from run SR20090305-1.*

variation over the sample area and voids or pitting in the pit wall. In this case the standard deviation of the SSA over the sample area was used for the error bars; although it cannot capture all potential sources of uncertainty it does provide some measure with which to compare the simulated values. SNOWPACK was somewhat constrained since the crust had already formed before the beginning of the simulation and input parameters of grain size and bond radius had to be defined based on observations. With the exception of 21 March and 27 March all observations fall between the maximum and minimum simulated values. As outlined in Chapter 3 the temperature gradient across the crust was very weak during this period and no physical explanation was found for this small observed increase. The crust became moist, then wet by early April and observations of decreasing SSA (larger optical diameter) are matched by simulated values.

Measured and simulated density and temperature for SR090222 are shown in Figure 4.6. The same negative model temperature bias from SR090127 is also evident here but the observed density remains within the range of simulated density and an increase on 11

April is accurately modeled. A comparison of SSA is given in Figure 4.7. There is a large difference even at the start of the simulation, reflecting the difference between observed grain size and SNOWPACK's treatment of grain size for melt-freeze crusts. Despite this, observations converge with simulated SSA by 6 April when the crust became moist and grain size increased.

Measured and simulated density and temperature for SR090301 are shown in Figure 4.8 and SSA in Figure 4.9. The observed density is generally within the bounds of simulated density for the layer except for 6 April, where the observed density increased sooner than the simulated density. The simulated layer temperature is once again colder than observations until isothermal conditions were reached by 11 April. Like SR090127, the simulated SSA tracks closely with the observations and accurately captures the decrease once the layer became moist and then wet in April.

Simulation SR20090305-2 was identical to SR20090305-1 except that all three crusts were initialized using the optical diameter derived from the observed SSA on 5 March rather than the observed grain size. The time series of simulated versus observed SSA for all three crusts is shown in Figure 4.10. The simulated SSA on 5 March does not exactly match observations because the crusts were assigned a sphericity of 0.9 so the physical diameter does not quite correspond to the optical diameter and SSA.

In the case of SR090301 the new initialization actually leads to a slightly greater spread in simulated SSA, with the same general trend in values and sharp decrease in April. The difference between the grain size from field observations and that derived from SSA on 5 March was small so this is not surprising. For SR090222 the difference in initialized grain size between the two simulations is large, and the new simulation tracks much closer to observations until late March, when the observed SSA decreased faster than simulated values. This could be an artifact of the cold temperature bias in the model.

SR090127 was initially composed of two identifiable layers, with an upper portion com-

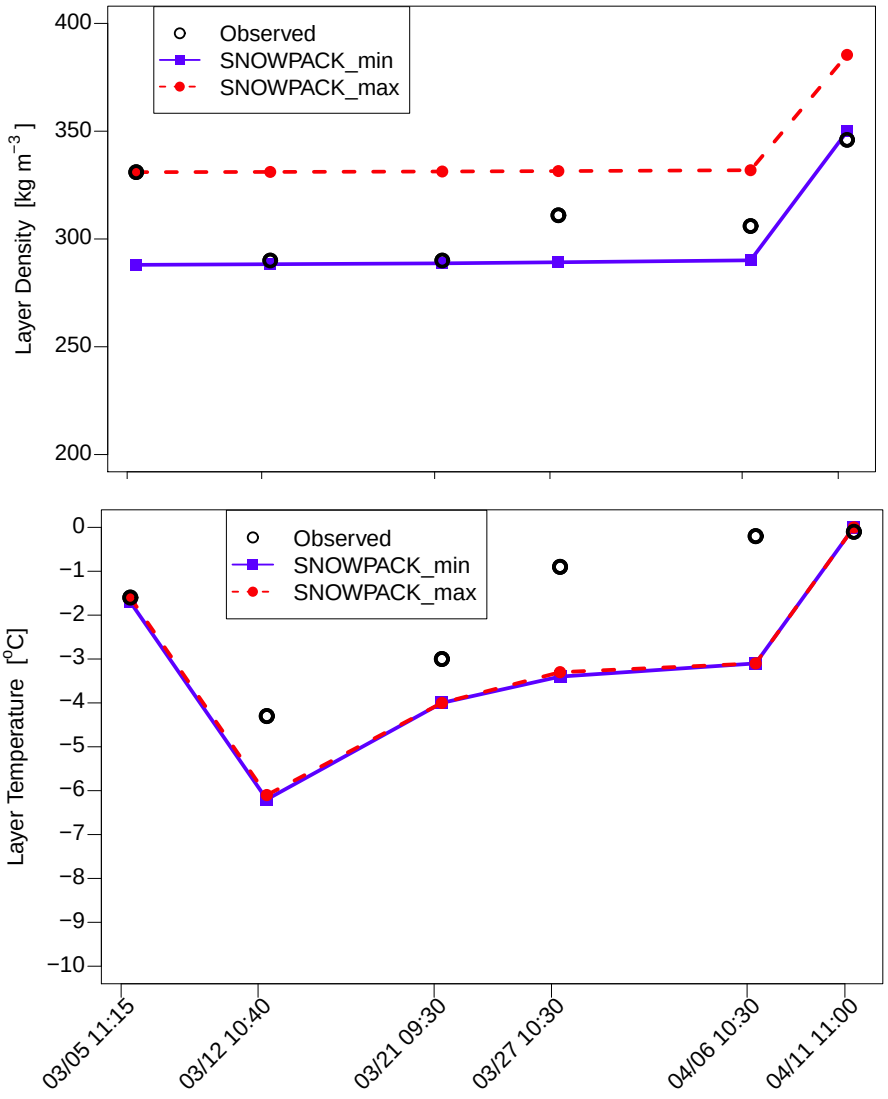

Figure 4.6: *Measured versus simulated layer density (top) and layer temperature (bottom) for SR090222 from run SR20090305-1.*

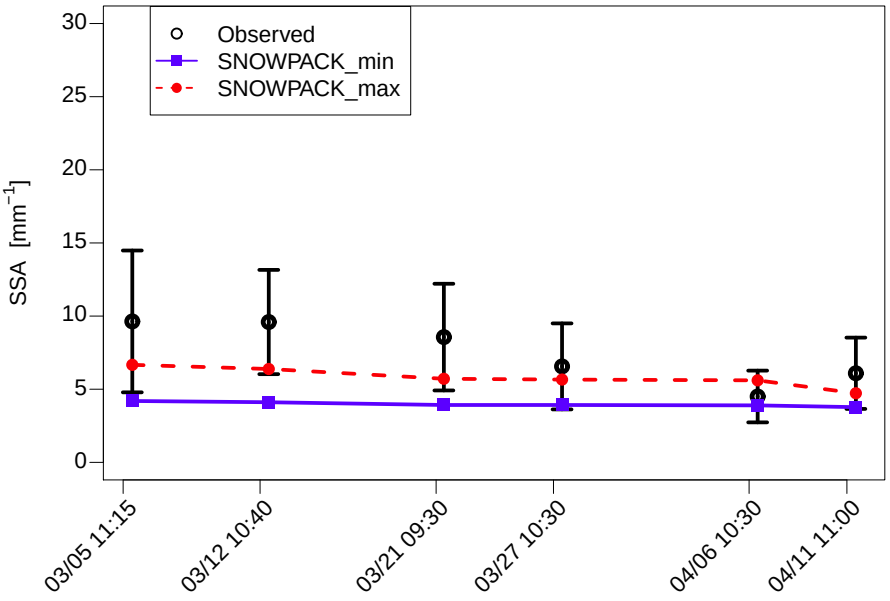

Figure 4.7: *Measured versus simulated specific surface area for SR090222 from run SR20090305-1.*

posed of smaller grains and the lower portion having larger grains. This was reflected in the results from SR20090305-1 where simulated SSA was based in initialization from observed grain size, but the use of observed SSA removes this distinction and as a result the spread in simulated values is very small until 11 April. The general trend in observations is well-modeled but observed SSA did decrease slightly earlier than simulated SSA.

The simulated temperature, layer depth and layer density did not change with the new initialization and are not shown here. The third simulation, SR20090305-3 used the same initialization as SR20090305-1 except that the Japanese NIED snow water transport model was used instead of the default Bucket model. In this case warming and layer wetting occurred much too soon, to a greater degree and extended much deeper than was observed. Since performance using this routine was poor, the results are not shown here.

The final parameter evaluated is the hand hardness. As explained in Section 4.2 the default routine in SNOWPACK sets the hardness of frozen melt forms to 5, with decreased hardness assigned with increasing water content while the ASARC routine incorporates den-

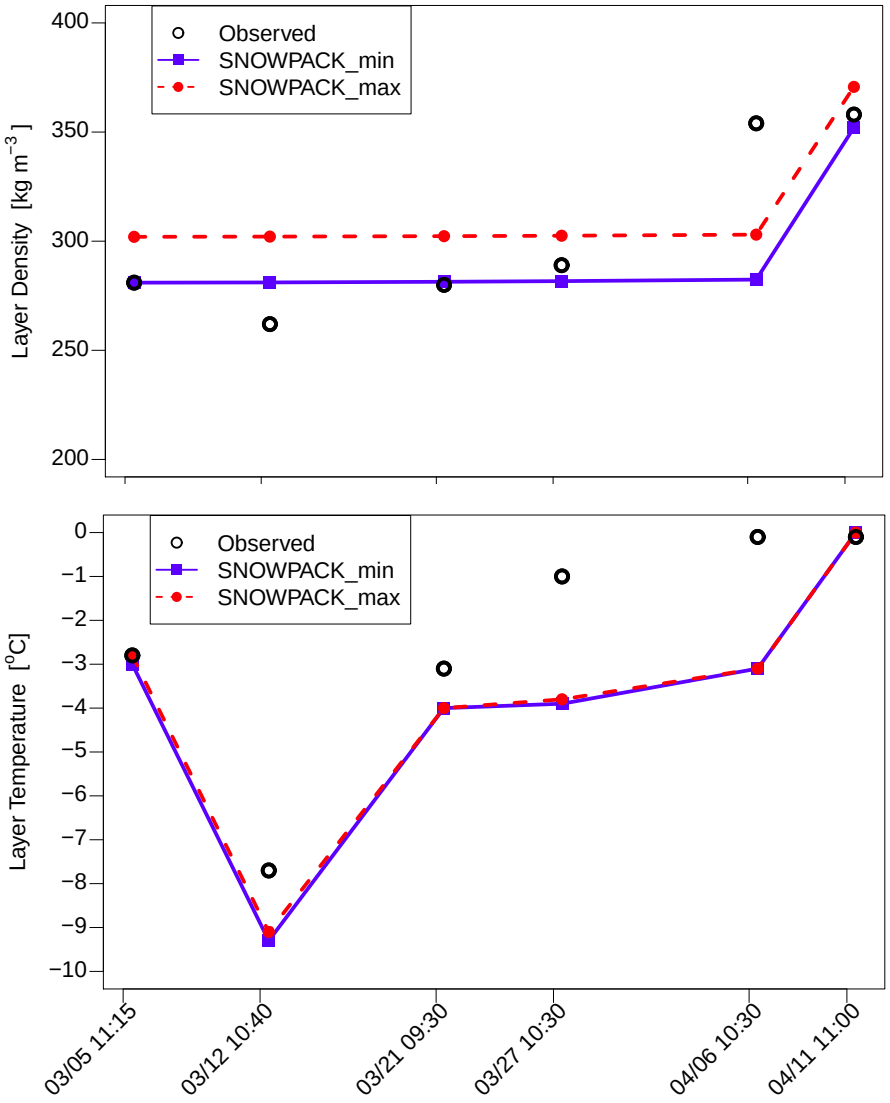

Figure 4.8: *Measured versus simulated layer density (top) and layer temperature (bottom) for SR090301 from run SR20090305-1.*

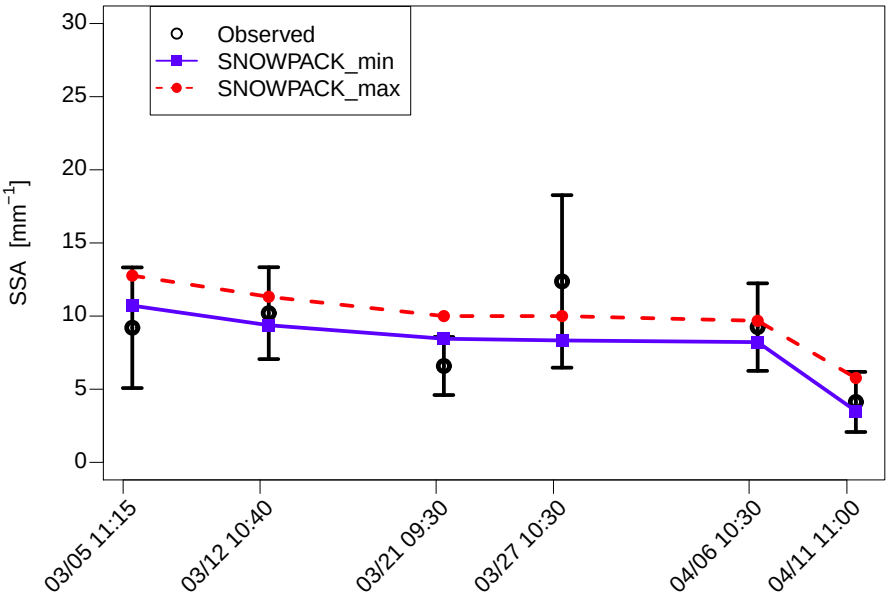

Figure 4.9: *Measured versus simulated specific surface area for SR090301 from run SR20090305-1.*

sity. Field observations of hand hardness were converted to index values using tabular data in Fierz et al. (2009). It should be emphasized that observations of hand hardness are subject to variability due both to differences between observers and the relatively imprecise methods used to record them. If a given layer is not isotropic then simulated values given in SNOWPACK may not correspond to those observed in the field.

Figure 4.11 shows the observed hand hardness compared with simulated values using the default MONTI routine as well as the ASARC routine. The ASARC routine underestimates hardness until the crusts became moist at which point it accurately captured both hardness and the decrease in hardness between 6 April and 11 April. The default MONTI parameterization was more accurate while the crusts remained frozen but grossly overestimated the decrease in hardness for SR090301 and SR090222 between 6 April and 11 April. The cold bias in the model seen for all three crusts was likely a factor as crusts became moist and lost strength sooner than they did in the simulations.

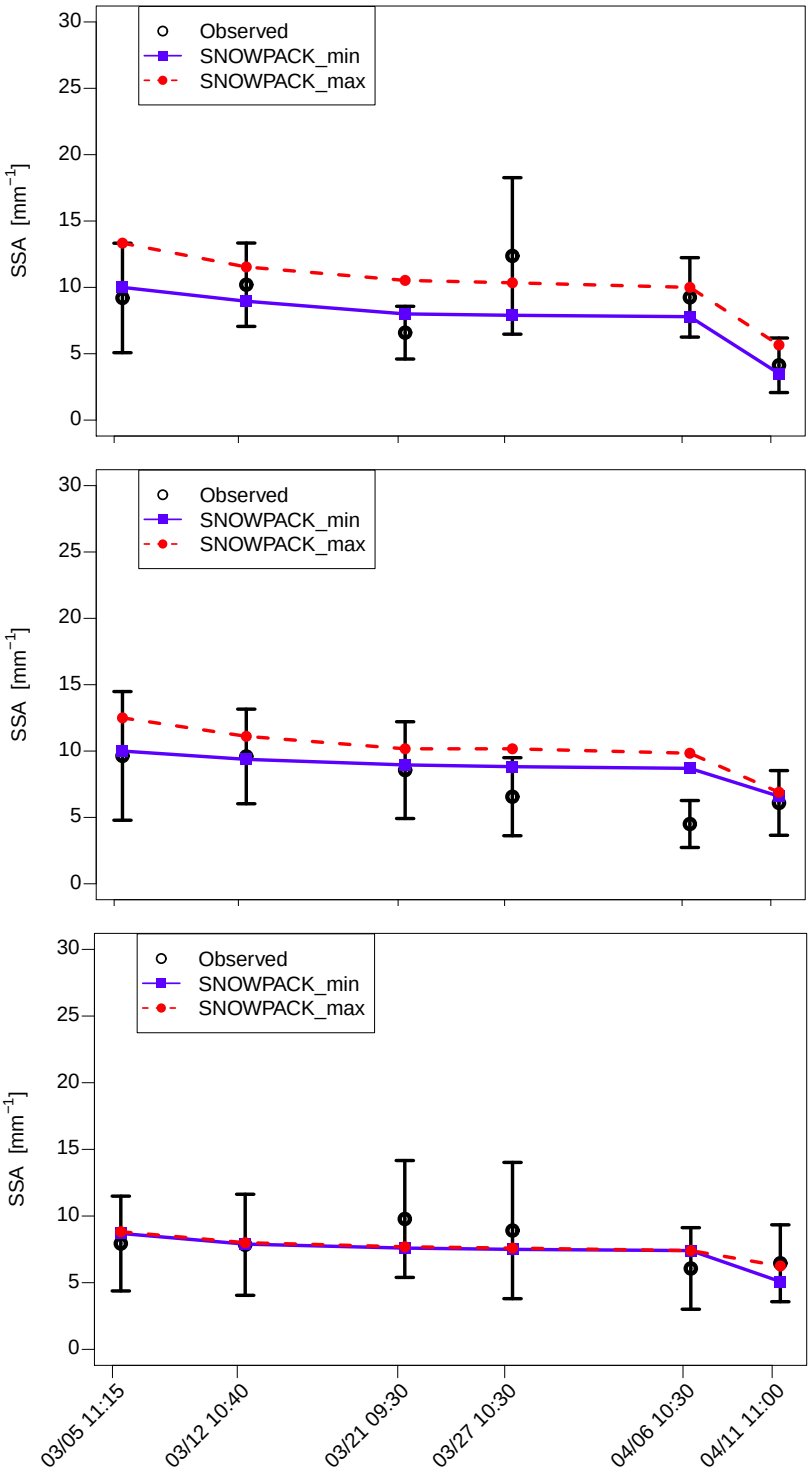

Figure 4.10: *Measured versus simulated specific surface area for SR090301 (top), SR090222 (middle) and SR090127 (bottom) from run SR20090305-2. Crust grain size was initialized using optical diameter derived from SSA measurements.*

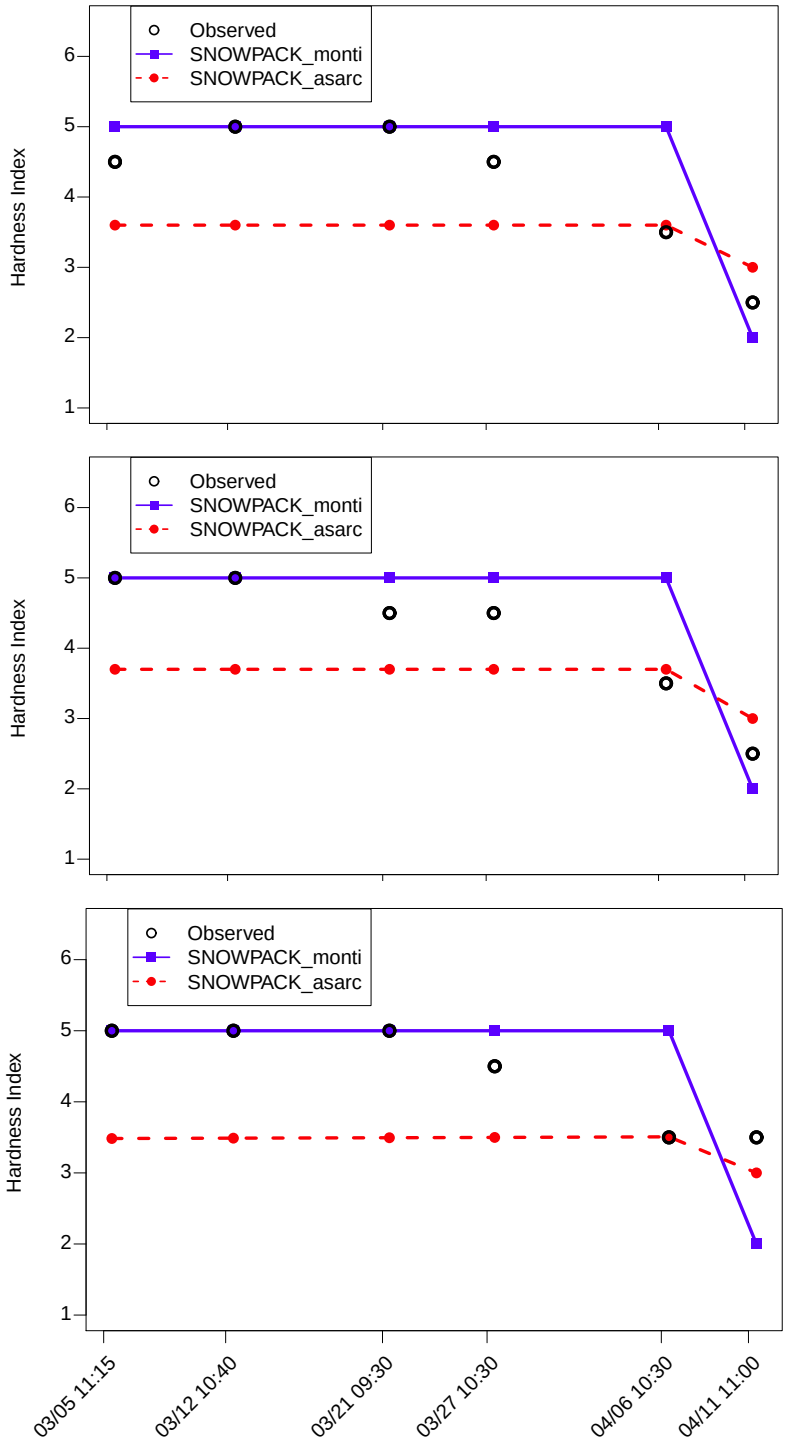

Figure 4.11: *Hardness index for SR090301 (top), SR090222 (middle) and SR090127 (bottom) from simulation SR20090305-1.*

4.3.3 South Run 2009 Crusts Discussion

SNOWPACK simulations of crusts SR090127, SR090222 and SR090301 on a simulated south-facing slope revealed a cold bias in the model that persisted until the final observation on 11 April when all three layers had become isothermal. This temperature bias was likely the most important contributing factor to errors in layer depth and for the lag between increases in observed and simulated density for SR090301 and SR090222. This lag was not observed in SR090222 but it also had generally higher densities than the other two crusts and may not be expected to increase in density quite as quickly with small increases in water content.

There are several possible reasons for the temperature bias, including model albedo being too high and overprediction of nighttime cooling. It is also possible that measured incoming solar radiation at Mount Fidelity was not representative of South Run. Although the two sites are separated by only 700 m, South Run faces the intersection of two large valleys while Fidelity lies just downstream of the convergence zone: when clouds formed due to orographic lift it was quite possible to have different sky conditions at the two sites.

Hand hardness was modeled relatively well using the default hardness routine in SNOWPACK, but not as well once layers became moist and lost strength. The cold bias in the model is likely at least a contributing factor to this discrepancy. The ASARC hardness routine, which incorporates density for frozen melt forms, underestimated hardness until the layers became moist or wet, at which point it became a better predictor of the actual hardness as well as the decrease in hardness due to layer wetting. It should be noted that the MONTI routine does include a density-dependent equation for hardness of dry or moist melt-freeze forms but it is not used in the present version of SNOWPACK.

The simulation of trends in SSA is generally good in SNOWPACK, especially as grain coarsening occurred with springtime wetting and diurnal melt-freeze cycles. The largest limitation was with the initialization of crusts using observed grain size, which is not well-defined for melt-freeze forms and does not necessarily correspond to how grain size and

bond radius are treated in SNOWPACK. In this case using an optical diameter derived from measured SSA gave better results. Some thought for other initialization parameters such as sphericity and bond radius is still required as they will affect the rate of grain growth and thermal conductivity. This approach was not tested for adjacent layers but it is possible that this approach could offer improvements for situations when simulations cannot be started with bare ground.

4.3.4 FI100308

The simulation for FI100308 was initialized from a full profile recorded by Parks Canada avalanche technicians on 8 December, 2009 and was run until the final ASARC profile on 14 April, 2010. The study site was immediately adjacent to the meteorological instrumentation on flat terrain, and was sheltered from all but North winds so was rarely subject to snow drifting. Exposure to solar radiation was uniform across the entire study plot. Unlike simulations for South Run crusts in 2008-09, meteorological data were available beginning in early December 2009 and both crusts of interest were allowed to form naturally rather than being explicitly defined.

Both FI100308 and FI100109 were of interest for this simulation, but simulations of the latter are only evaluated based on whether or not it forms. Table 4.3 summarizes the three simulations that were run. FI100109 did not form during FI20091208-1, but did once threshold temperature between rain and snow was increased from -0.5 °C to 0.9 °C for simulation FI20091208-2. This was likely a limitation due to lack of surface temperature measurements as the skin temperature must then be calculated using a combination of measured air temperature and incoming solar and longwave radiation. This is an important consideration for future work involving numerical weather models as their current ability to prognose skin temperature is relatively poor. For simulation FI20091208-3 the water transport parameterization was changed to the newer NIED formulation (Hirashima et al., 2010) but the timing and depth of wetting was much greater than what was observed. The

Table 4.3: *SNOWPACK iterations for FI20091208.*

Run Name	Parameters modified	Modified value
FI20091208-1	none	defaults
FI20091208-2	rain-snow threshold	increase by 1.4 °C
FI20091208-3	water transport	NIED

remainder of this section presents only results from FI20091208-2.

Evolution of grain type and accumulation of new snow for the entire simulation, from 8 December, 2009 to 14 April, 2010, is shown in Figure 4.12. Crust FI100109 can be seen to form and become quickly buried in early January, but this was achieved only by tuning the model threshold between rain and snow to observed air temperature and precipitation in the meteorological inputs. Had measurements of surface temperature been available this tuning may not have been necessary. Crust FI100308 is visible as the first thick crust to form, approximately two thirds of the way through the simulation. Like FI100109 it is quickly buried and does not become wetted by the end of the simulation.

Figure 4.13 shows the comparison between observed and simulated snow depth, layer depth and layer temperature beginning with the first observation of FI100308 on March 9, 2010. The simulation had been allowed to run for three months up to this point with no nudging of surface temperature or snow depth; new snow layers were created entirely by the snowpack model and based only on meteorological inputs. The simulated snow depth is remarkably close to observations, with a slight underprediction in early April when simulated new snow layers were slightly too dense and settlement occurred too quickly. The same pattern is evident in the depth of the top of FI100308. Both snow depth and layer depth were correct for the first observation on 9 March and the larger discrepancies are associated with increasing downwelling solar radiation and a week-long cold spell in late March and early April (see A for more detail on meteorological data).

Simulated layer temperatures exhibit a warm bias but are still within 1 °C. This is in

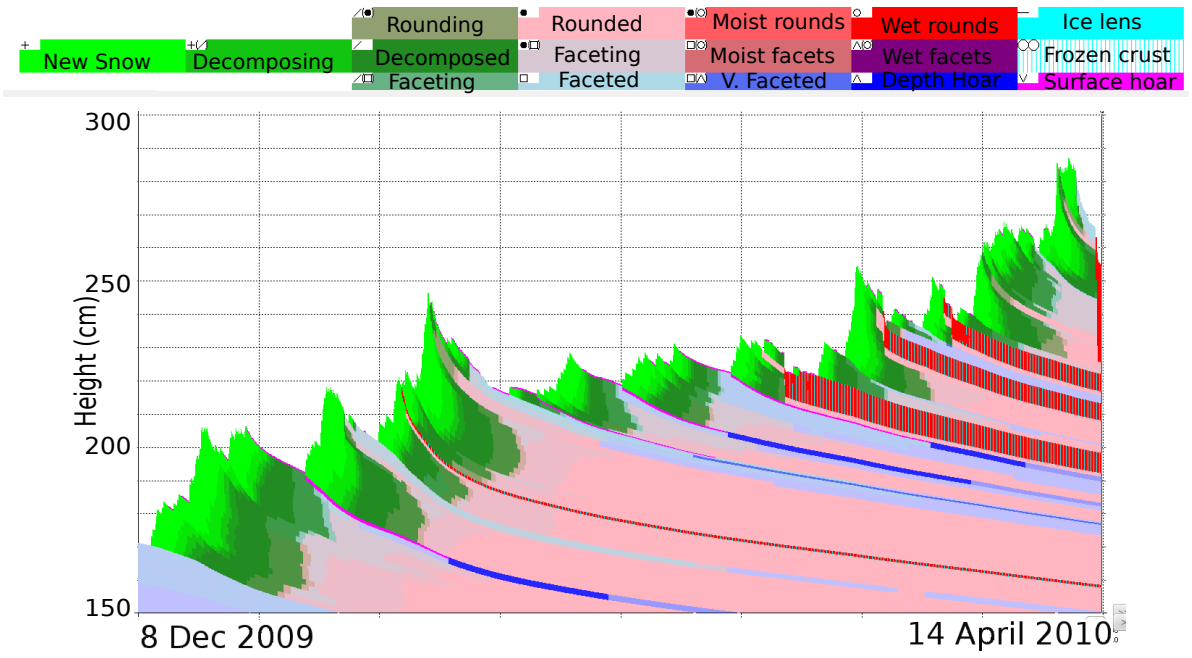

Figure 4.12: *Evolution in snow depth (cm) and grain type for simulation FI20091208-2 run from 8 December, 2009 to 14 April, 2010. Melt-freeze crusts are denoted by red with vertical cyan lines, moist or wet layer by solid red shading and new snow by green shading. Lower portions of the snowpack are omitted.*

sharp contrast to simulations from 2008-09, when simulations all had a cold bias. FI100308 was also buried quickly and remained well below the surface and below freezing for the duration of the simulation so there was no chance for the layer to become isothermal. The one point where model and observations coincide is on 15 March when the crust was observed to be moist.

Simulated and observed SSA are shown in Figure 4.14. The first observation on 9 March was discarded for analysis in Chapter 3 due to contamination of the image by sunlight through low density snow at the surface, but is included here for the sake of completeness. Simulated SSA is lower than observed values until the April 14, but the standard deviation of the observed SSA is also quite large. This is due at least in part to a thin ice lens that formed at the base of the crust, but did not form in the simulations. Since the lens had a very low SSA (see Chapter 3, Figure 3.12) this still would not reconcile the difference between observations and simulation here.

The simulated and observed thermal conductivity of FI100308 is shown in Figure 4.15. SNOWPACK must by its nature treat all layers as isotropic so simulated thermal conductivity is compared separately with horizontal and vertical measurements. Error bars are based on figures published by the thermal conductivity probe's manufacturer (Hukseflux, 2003). No significant ($p \leq 0.05$) temporal trends were found in either vertical or horizontal measurements, but the simulation does show a gradual increase from 9 March until 14 April. If the observed vertical thermal conductivity of 0.54 on 14 April is discarded as an outlier, the simulated thermal conductivity does match a very modest trend of increasing thermal conductivity in the observations. Even then, there is no significant ($p \leq 0.05$) correlation between the observed and simulated thermal conductivity for an admittedly small dataset. Calonne et al. (2011) found that melt freeze forms showed less anisotropy in thermal conductivity than other grain types but it is evident at least from this dataset that anisotropy is still present, even in crusts that are visually isotropic.

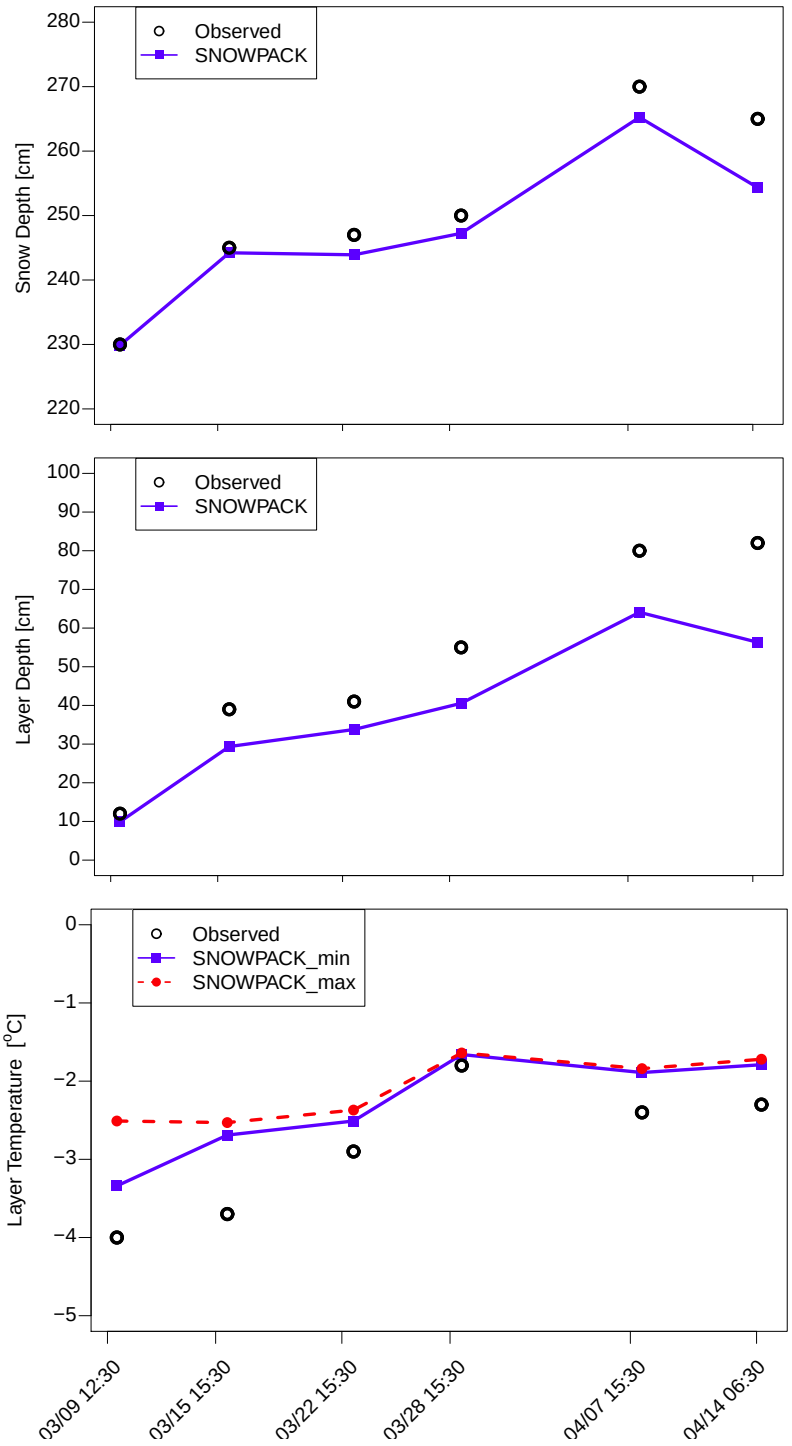

Figure 4.13: *Measured versus simulated snow depth, layer depth and layer temperature for crust FI100308 from simulation FI20091208-2.*

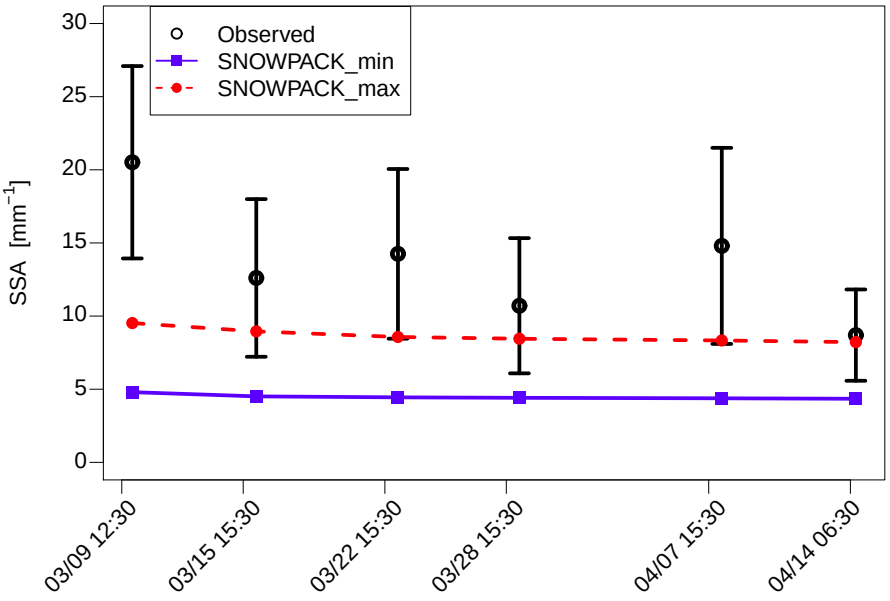

Figure 4.14: *Measured versus simulated specific surface area for FI100308 from simulation FI20091208-2.*

4.3.5 FI100308 Discussion

Two crusts from the winter of 2009-10 were simulated starting from 8 December and running until 14 April. The earlier crust, FI100109, did not form in the simulation using default model settings. When the model threshold was increased so that SNOWPACK produced rain rather than snow the layer did form, albeit thicker than was observed. It is possible that if surface temperature measurements were available that the crust would have formed as observed. This does illustrate the difficulty of diagnosing precipitation type using only surface observations, when above freezing layers may produce rain or freezing rain while the surface air temperature remains below 0 °C. A similar synoptic environment was present during the formation of thick rain crust in December 2007 and, lacking that information, SNOWPACK interpreted the precipitation as snow rather than rain.

Total snowpack height and depth of crust FI100308 were very well simulated especially considering that the first field observations occurred three months into the simulation. Simulated snowfall settled slightly too quickly from mid-March until early April with the largest

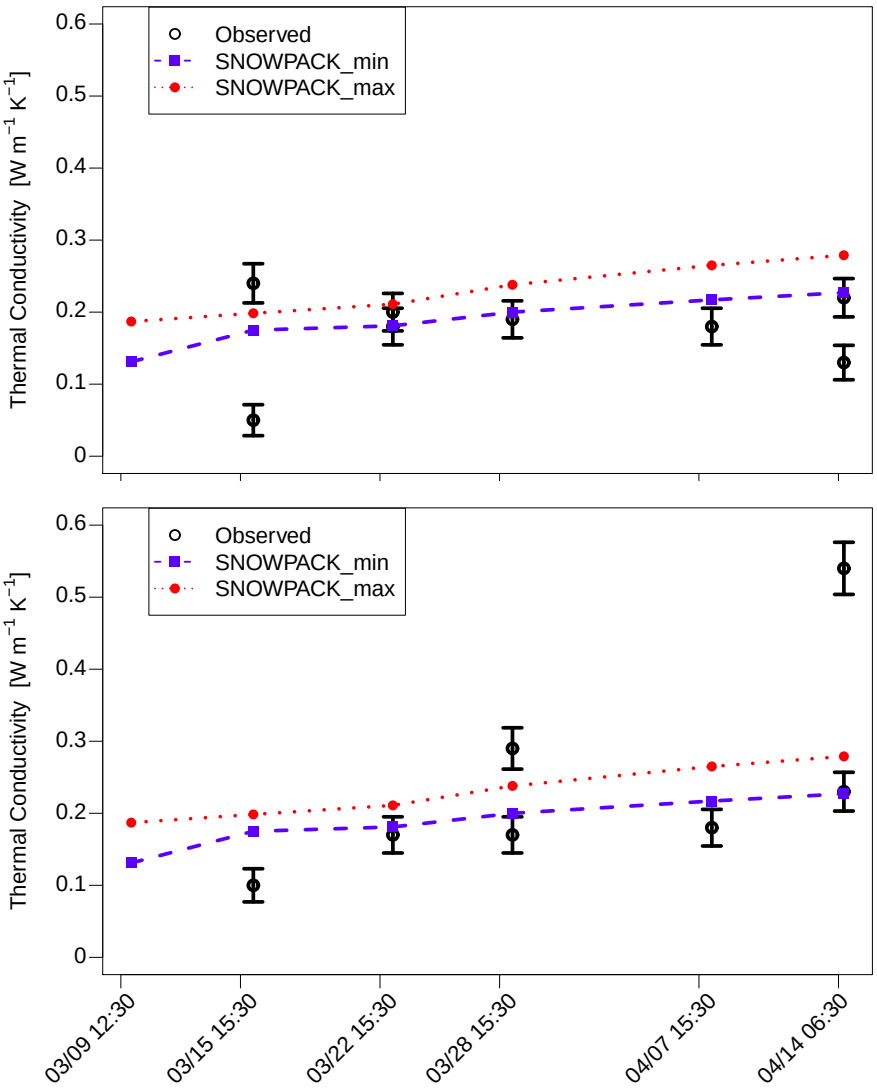

Figure 4.15: *Measured versus simulated horizontal (top) and vertical (bottom) thermal conductivity for FI100308 from simulation FI20091208-2. At least two measurements of horizontal and vertical thermal conductivity were attempted at each visit, but many measurements were discarded due to non-linear heating. See chapter 2 for more detail on measurements and post-processing.*

errors on 14 April once the snow depth began to decrease. SNOWPACK temperatures in FI100308 exhibited a slight warm bias throughout the period where observations were available. This is the opposite of what was found for the simulated south-facing slope used to model crusts from 2008-09. The lack of surface temperatures to constrain the model may be at fault here as well, as the simulated snowpack may cool too quickly. This effect would be greater in midwinter with shorter days but could also be responsible for the discrepancies in this case. Model albedo could also be the culprit if simulated albedo for new snow, which continued to accumulate from 9 March - 14 April, was too low.

Simulated SSA was substantially lower than observed areal mean SSA until the final observation on 14 April, indicating that model grain size was too large, that grains were too spherical or a combination of the two factors. Simulated sphericity was 1.0 for all nodes of FI100308 while observations noted some sharp edges within the crust, though there was no visible evidence of faceting. The most likely explanation is that grain coarsening during the initial wetting resulted in grains that were too large in the simulation.

Simulations of thermal conductivity showed a slight upward trend similar to measurements of vertical thermal conductivity in FI100308. The simulated trend was due to an increase in density, and was slightly offset due to rising temperatures as the thermal conductivity of ice decreases with increasing temperature. A correct simulation of vertical conductivity is likely more important since temperature gradients are typically larger in the vertical plane and correct simulation faceting or rounding processes will depend in part on this value. The slight anisotropy of FI100308 is evident by the difference between horizontal and vertical measurements.

4.4 Chapter Summary

Five natural crusts from two study plots were simulated using SNOWPACK version 3.2. A set of three crusts were simulated on a south-facing slope from just after formation of the last

crust until early April using meteorological data from Mount Fidelity station. The default model configuration gave better results than an alternate configuration using a new water transport model, which resulted in water percolating through the snowpack much sooner and deeper than was observed. Simulations exhibited a marked cold bias in all layers resulting in deviations in layer depth and density by late March. The discrepancy could be due to model error in surface albedo or outgoing longwave radiation, or by a genuine difference in incoming solar radiation between the two sites.

SSA simulation results were heavily dependent on the parameters chosen to initialize the crusts in the SNOWPACK. Grain size from test profiles on 5 March was initially used, but the definition of grain size for melt-freeze forms is ill-defined when all grains are well bonded. A subsequent simulation using grain sizes derived from SSA observations on 5 March yielded better results, though the choice of sphericity and bond size parameters still had some impact on results.

Simulations of hand hardness using the default routine were accurate while crusts remained frozen but larger errors were introduced once the snowpack began to warm and bonds lost strength. An alternate equation incorporating density and layer moisture, based on a fit to ASARC data, performed better in this case. Field observations of hand hardness are subject to a wide spread regardless, but differences in hardness between adjacent layers are important to the interpretation of snowpack stability due to stress concentration at the interfaces.

Two crusts were simulated from early December until mid-April at the flat Mount Fidelity study plot. The default model configuration was used initially, but a thin early January rain crust did not form in the simulation until the rain-show threshold temperature was adjusted upward to force rainfall. This represents a limitation of diagnosing precipitation type using only surface meteorological data and may possibly be overcome by incorporating input from a numerical weather model to produce hybrid meteorological inputs. A similar shortcoming

was found during the formation of a thick rain crust in December 2007 (Smith et al., 2008). The formation of the second crust was accurately simulated albeit slightly thicker than observed. Total snow depth and layer depth were simulated very well with slight negative biases and the greatest error in mid-April when the snow depth decreased. In contrast to the three south-facing crusts, the layer temperatures in the flat field crust exhibited a positive bias. Errors in simulated albedo or surface temperature may account for the bias.

Simulated SSA for the second crust was much lower than observations, possibly due to excessive simulated grain growth during initial wetting. Analysis in Chapter 3 found that the crust was subjected to a vertical temperature gradient on the order of -1.5°C 10 cm^{-1} in late March and may have led to some interior faceting. The vertical temperature gradient in simulations was an order of magnitude lower. Thermal conductivity increased slightly both in simulations and in observations though in the latter case the increase was barely larger than the range of instrument error and was not statistically significant. Simulated values corresponded more closely to measurements of vertical than horizontal thermal conductivity and both sets of observations show that anisotropy was present even in a visually uniform crust.

Most crust properties were simulated quite well using SNOWPACK, but temperature bias did consistently lead to some errors in other physical parameters. The available hardness parameterizations for melt-freeze crusts are relatively crude and will affect stability assessments due to misidentification of areas of possible stress concentration. It is also evident that the model does need to be tuned to a particular snow climate as the choice of the wrong parameterization may lead to very inaccurate results. This is not an unusual requirement and is widely used in meteorological models. The availability of a wide range of parameterizations for water transport, settling, grain growth and the ease with which they may be altered in the newer versions of SNOWPACK means that this is a relatively straightforward, though important, endeavor.

4.5 Recommendations for future studies

Based on results from this study there are a number of avenues that may yield data to improve SNOWPACK simulation of melt-freeze crusts. Although model results at the simulated south-facing slope were quite good overall, it appears that translation of meteorological variables from the flat-field site may have been responsible for some inaccurate modelling. Validation of surface, near-surface and air temperatures, incoming and reflected solar radiation (or albedo) and outgoing or net longwave radiation on adjacent slopes may lead to improvements in this area. For simulations of crusts at flat-field sites measurements of both incoming and reflected solar radiation as well as surface temperature would likely have reduced or eliminated the temperature bias observed during this study. Accuracy may also be increased by exploring the use of hybrid meteorological inputs combining numerical weather model output with actual surface meteorological data. Hybrid inputs may improve meteorological inputs from numerical weather models by 'nudging' them toward observed values, thereby minimizing input errors due to poor timing of precipitation or frontal passages.

Thermal conductivity measurements were reproduced quite well but outside of this study most existing data come from cold lab studies using physically small samples. Although past studies (e.g. Calonne et al., 2011) have found that anisotropy in melt freeze forms is less than in other grain types the results from this study make it clear that it is a factor and should be investigated further using natural crusts.

The SSA for the single crust that was allowed to form in SNOWPACK did not correspond very closely to observations and can be traced at least in part to excessive grain growth during initial wetting. Although availability of reflected solar radiation and surface temperature meteorological inputs may have improved model performance in this case, the magnitude of coarsening should be further investigated in cold lab experiments in conjunction with measurements of SSA.

Initializing existing layers using observed SSA appears to be a valid technique for melt-

freeze forms and could also be applied for other grain types where sphericity is close to 1.0. Using SSA to initialize grain size for large facets, surface hoar or depth hoar should done directly.

Hand hardness is important for slope stability evaluations only as a method of identifying areas of possible stress concentration. The default parameterization in SNOWPACK did not decrease hardness quickly enough once layers became moist while the alternative ASARC parameterization underestimated hardness while the crust was frozen and better than the default once wetting began. A hybrid of these two parameterizations may lead to better results and more accurate interpretations for avalanche forecasters and snow hydrologists.

Finally, driving SNOWPACK from numerical model data rather than from actual data has already been tested at the Mount Fidelity site by Bellaire et al. (2011), including the formation of the FI100308 crust. By filtering inputs from the Canadian GEM15 model the authors found that precipitation, new snowfall and air temperature closely matched observations from Mount Fidelity. Since that time the GEM15 model has been upgraded to a 10 km resolution version with further improvements planned in the near term. This approach is already used in Switzerland (SNOWPACK) and France (using the CROCUS model) and represents a promising avenue of research where spatial coverage will not be limited by the availability of meteorological stations. Further validation still needs to be undertaken with regards to virtual slopes and precipitation phase, but the data from this study are ideal for such an application. As already outlined, nudging of model data by surface data, or a hybrid of the two inputs, should also be considered.

Chapter 5

Conclusions

The results from Chapters 2 - 4 have given insight into tracking of microstructural and thermal properties of buried melt-freeze crusts, including measurements techniques that were applied for the first time to the temporal evolution of melt-freeze crusts.

5.1 Temporal trends of SSA and thermal conductivity

Temporal trends in crust specific surface area (SSA) were found for three natural crusts from the winter of 2008-09, but no statistically significant relationships were found between rates of change and temperature or temperature gradient, possibly due to the lack of strong temperature gradients and generally warm temperatures at the site. Diurnal temperature gradients did occur near the end of the winter but no faceting was observed within or at the boundaries of crusts, and past studies have found that a strong temperature gradient that switches direction diurnally will not necessarily lead to faceting. A qualitative link was found between the vertical variability of SSA and observations of weakening bonds in portions of the crusts, but no correlations or causal mechanisms could be identified.

Six natural crusts were tracked during the winter of 2009-10. One temperature-radiation crust on a flat aspect was tracked for five weeks from early March (formation) through mid-April, and remained dry with a weak slope-normal temperature gradient throughout the period. A small increase in mean SSA was thought to be due to faceting although no edged crystals could be found with an 8x loupe. A period of decreasing mean SSA near the end of the study period, and during the presence of stronger temperature gradients, is the opposite of what would be expected had faceting occurred. Vertical profiles of SSA revealed the disappearance of small structures with higher SSA within the crust during this

same period. Although no clear temporal trends were identified within this crust, the ratio of mean SSA between it and adjacent layers was found to be useful in identifying relative changes in structure.

No temporal trends in thermal conductivity were found in any of the natural crusts, but layers above and below the crusts, usually rounded (RG) or mixed forms (RGxf) did reveal trends that were well-correlated with layer density as in previous studies. SSA time series data were discarded for two shallow crusts on a south-facing slope as they became indistinguishable from one-another, and a thin rain crust could be distinguished in SSA imagery but the resolution of near infrared (NIR) methods was not sufficient to track temporal changes. Two thicker rain crusts were spatially variable and unsuitable for time series analyses, but NIR methods were successful in characterizing crust structure.

Four cold lab experiments were conducted in 2009-10, with natural crusts being brought into the lab in an insulated box and sampled at regular intervals that varied from hourly to daily. The two longest cold lab experiments showed similar trends of increasing thermal conductivity during freezing, then a slow decrease. Although thermal infrared imagery could not be used for qualitative analysis, it did indicate the presence of strong vertical temperature gradients well after the crust became frozen. The decrease could be explained by faceting within the crust due to the lingering temperature gradients, but there was no corresponding increase in mean SSA that might be expected. No temporal trends in thermal conductivity were found in the natural crusts at the study sites, but layers above and below generally showed trends of increasing thermal conductivity that were well correlated with increasing density, as in previous studies.

Few strong temperature gradients were observed in natural crusts, but were present in cold lab crusts during initial stages of each cold lab experiment. Temperature gradients were not found to be good predictors of trends in SSA possibly due to to the high thermal conductivity of such layers. Although this would appear to contradict what was observed by

Greene (2007), his experiments used an impermeable ice lens while crusts in this study were more permeable, and adjacent layers in his study were rounded grains with lower thermal conductivity while all layers in this study were composed of melt forms.

5.2 Modeling observations with SNOWPACK

Simulations of the three crusts by the SNOWPACK model, initialized post-formation, revealed a model cold bias that persisted until the layers became isothermal in mid-April. Corresponding biases in layer depth and densification were likely the result of this temperature bias. The cause could not be determined unambiguously but positively biased model surface albedo or outgoing longwave radiation are both possibilities. Hand hardness corresponded closely to observations before crust warming, but performed poorly once crusts warmed to near 0 °C and lost strength. Simulations of SSA were dependent on parameters chosen to initialize the crusts in SNOWPACK: When observed grain size was used, model SSA did not closely match observations. When measured SSA was used to derive an optical radius for use as "grain size" to initialize SNOWPACK, the results improved. To the best of the author's knowledge this technique of initialization has not previously been used with the SNOWPACK model.

SNOWPACK was allowed to simulate formation and evolution of the two crusts observed during winter 2009-10 at Mt. Fidelity. The thin rain crust, FI100109, did not form when default model settings were used, but did form once the model rain/snow threshold was adjusted. Had surface temperature observations been available it is possible that SNOWPACK could have correctly simulated formation without adjustment of parameters. Total snowpack height was modeled well throughout the simulation even though the model was unconstrained by a measured snow depth. Unlike simulations from 2008-09, the model exhibited a slight warm bias at Mt. Fidelity and consequently modeled settlement rates during early spring exceeded observed rates.

Modeled SSA for FI100308 was substantially higher than observations, with the likely cause being excessive modeled grain coarsening during initial wetting and crust formation. Once again, the availability of measured surface temperatures may have mitigated this error. Simulations of thermal conductivity matched the observed trend for measurements of vertical thermal conductivity through FI100308.

The SNOWPACK model is a promising tool for simulation and study of seasonal snow. In this study the majority of instances where the model validated poorly appeared to be related to meteorological inputs rather than to the model itself. The single exception was hand hardness of crusts, which is not an intrinsic property of layers within SNOWPACK and is calculated empirically at each time step.

5.3 Spatial variability of SSA and thermal conductivity

The spatial variability of thermal conductivity and SSA could not be determined at study sites due to the necessarily destructive nature of the observations, but a uniform planar south-facing slope was selected in an attempt to quantify the variability in a solar crust that would normally be assumed to be spatially uniform. Thermal conductivity varied substantially in both the upslope and cross-slope directions. Concurrent measurements of mean SSA revealed variability in the upslope and cross-slope directions but also showed the effects of various analysis techniques: While the mean SSA was variable across the study plot, vertical profiles of SSA and the CV of SSA revealed small areas of high SSA that skewed the mean. That level of resolution was not possible to measure using the thermal conductivity probe, but the effects of pit-scale variability may be mitigated by collecting multiple samples in both the slope-normal and slope-parallel directions.

5.4 Thermal conductivity, grain type, density and temperature

Chapter 2 summarized thermal conductivity measurements from five natural crusts, and five crusts brought into a cold lab from a study plot. Thermal conductivity data were first grouped by IACS grain type and compared to existing data sets. With measurements from moist or wet layers excluded, the mean thermal conductivity for non-melt-freeze grain types was similar to those measured from past studies. The sample size of melt-freeze forms from this study is larger than in any published study, and thermal conductivity measurements were found to vary considerably.

Correlations between thermal conductivity and other physical parameters were similar to past studies (e.g. Sturm et al., 1997) for rounded grain types but in opposition to the same studies for faceted grain types, with the likely cause being a lesser degree of faceting in samples from the present study. Empirical equations for the density-conductivity relationship from that same study matched the trend of data from this study but with a negative offset. A new polynomial equation was proposed which gives a good fit to observed data, but does not give realistic values for densities approaching that of ice. Like past studies, the range of layer temperatures is likely the dominant factor in the difference between various extant equations. Although significant correlations were found between layer temperature and thermal conductivity, the former did not emerge as statistically significant factor in attempts to fit the data. The same correlations were attempted for individual layers, where both density and temperature did emerge as predictors, suggesting that characteristics of individual layers are still variable even within a given grain type.

5.5 Use of SSA to quantify the structure of melt-freeze crusts

NIR photography was found to be a useful complement to traditional snowpack observations in the field and in the cold lab. While the photography could be conducted quickly, the image analysis was time consuming due in part to the need to screen all images for non-

planar areas (scratches or voids) in the pit wall, as these lead to misleading results. This was especially problematic with brittle crusts or layers with large polycrystals, both of which tend to crumble when a pit face is exposed. Free water in layers was also problematic as SSA from moist or wet layers cannot be used to track structural changes in time series analyses.

Field methods were adapted from those published by Matzl and Schneebeli (2006), and new methods were developed for tracking changes over time of the mean SSA of specific structures within the snowpack as well as vertical profiles of SSA across crust boundaries.

5.6 Use of a thermal conductivity probe in melt-freeze crusts

This study was the first to track changes in the thermal conductivity of natural melt-freeze crusts from formation. The use of a thermal conductivity probe in field and lab studies was found to be simple and efficient. Subsequent analysis was relatively time-consuming as each measurement had to be checked for uniform and linear rise in heating of the layer. Non-melt-freeze layers of moderate density tended to yield good measurements, while low-density snow and melt-freeze crusts had a higher proportion of erratic measurements that had to be discarded. Poor contact between the snow and voids in the crust interior and the likely reasons for these difficulties, and could be overcome by taking multiple measurements at each site visit.

The heated needle probe used in this study required a sample depth of approximately 5 cm, so slope-normal thermal conductivity could not be measured for thin samples and care was required for slope-parallel measurements of thin layers. The required size of the sample complicated direct comparison with SSA measurements and SNOWPACK model results.

5.7 Contributions to snow science

Time series of thermal conductivity measurements in melt-freeze crusts collected during this study have not been attempted previously and represent a contribution to the existing

body of knowledge. Thermal conductivity measurements in the crusts as well as adjacent layers complement existing data sets such as that of Sturm et al. (1997), and may be used to better study the influence of temperature on the effective thermal conductivity of snow. This study has also shown the pitfalls inherent in relying on grain type classification, especially in different snow climates and with multiple observers.

The NIR field methods used in this study closely followed those used by Matzl and Schneebeli (2006) but the subsequent analyses, examining not only areal mean SSA but also vertical profiles and sample variability has shown even visually uniform layers are variable at the snow pit scale and assumptions of uniformity should be made with caution. The SSA has also been shown to be useful in the initialization of models such as SNOWPACK, where traditional observations of grain size may not be sufficiently precise.

The SNOWPACK model has been widely used in research applications, but validations of crust formation and evolution performed during this study highlight some areas for future improvement of the model and should also be of use in forthcoming studies involving the use of numerical weather models to drive SNOWPACK. Although hand hardness is not an intrinsic property of layers within SNOWPACK it is widely used by avalanche forecasters, and this study has shown the need for improvement in the parameterization of hand hardness in melt-freeze crusts, especially during warming and wetting.

Chapter 6

Recommendations for Future Research

The results from this study offer some insight into structural and thermal properties of melt-freeze crusts, but also identify avenues for future research as well as refinements of experimental design.

6.1 Thermal Conductivity

The data collected during this study complement past thermal conductivity studies, specifically that of Sturm et al. (1997). Neither study was able to isolate an empirical relationship between layer temperature and thermal conductivity, but data from each study were gathered within a relatively narrow temperature range. By combining the data it is possible that a better understanding of the temperature-thermal conductivity relationship will be revealed.

Further cold lab studies should be conducted to further investigate the changes in thermal pathways under strong temperature gradients proposed by Kaempfer and Schneebeli (2007) and Kaempfer et al. (2009). The techniques used in this study may not be sufficient to identify any small scale changes in pathways, but changes in the anisotropy of thermal conductivity should be detectable. Improvements in thermal infrared camera techniques to account for shortcomings identified by Schirmer and Jamieson (2014) could help to overcome the difficulties of measuring sub-millimetre scale temperature gradients that are not detectable using thermistors or thermocouples.

The role of layer moisture presented difficulties in this study, as the only available measurement were the qualitative “dry”, “moist” or “wet”. Incorporating measurements of moisture content in future field campaigns may provide better insight into the role of layer

moisture in thermal conductivity.

6.2 Specific Surface Area

The field methods used to measure SSA, once refined, complemented the observations gathered from snow profiles and stability tests. As with thermal conductivity, the role of moisture in the snowpack presented some obstacles to quantifying temporal changes in crust structure and future studies should incorporate measurements of moisture content.

The analysis of spatial variability showed that even visually uniform crusts are variable on the slope scale. Further analysis of spatial variability on the slope scale should be undertaken to better quantify the variability of crusts on the pit and slope scales. Improved quantification of the spatial structure of melt-freeze crusts alongside measurements of thermal conductivity and propagation propensity may improve forecasts of deep slab avalanche potential. New tools such as the SnowMicroPen (WSL Institute for Snow and Avalanche Research SLF, 2014) would also complement the techniques used in this study, and provide the means to gather information on spatial variability without resorting to destructive profiles across a slope.

The SSA of crusts was examined using a variety of techniques in this study including areal averages, vertical profiles and ratios between adjacent layers. It is unclear from the data in this study which technique, if any, is optimal for diagnosing the formation or evolution of weak layers within and at the boundaries of crusts. Further studies incorporating shear frame tests and the thin blade hardness tests used by Buhler (2013) will help to clarify this question.

The time required for analysis of NIR imagery makes it prohibitive for use in any operational context. Further refinement and automation of techniques used in this study could allow NIR observations to be incorporated into the weekly snow profile observations conducted by avalanche professionals.

6.3 Modeling

The SNOWPACK model is a promising tool for avalanche research and forecasting but further validation is needed, especially in the formation of melt-freeze crusts. Validation against observations from this study showed that grain coarsening during snowpack wetting was not reproduced by the model, possibly due to the lack of surface temperature measurements. The modeling of grain coarsening during crust formation could be further validated through cold lab experimentation concurrent with SSA measurements.

A cold model temperature bias on the virtual south-facing slope may be due to poor translation of radiation measured at the reference flat-field site, and field validation of incoming and reflected radiation may identify the specific source of the error. The meteorological data used to drive the model simulations in this study did not include surface temperature or albedo, and adding these constraints would likely improve model performance.

Hand hardness is an important parameter used by avalanche professionals to identify potential failure layers in the snowpack. The parameterizations used for crust hand hardness in SNOWPACK did not validate well with observations. As the hand hardness itself is somewhat qualitative, further measurements and validation using density, moisture, hand hardness and thin blade resistance may yield improved model parameterizations for crusts.

Although SNOWPACK's developers recommend initializing the model while the ground is bare rather than from an observed profile, in some cases this is not possible. A single simulation using SSA rather than observed grain size to initialize a crust in SNOWPACK hints that this may be an effective and more accurate way of initializing layers composed of spherical, or nearly spherical grains.

Finally, driving SNOWPACK simulations with numerical weather model data shows promise for use in North American avalanche forecast operations, especially in areas with sparse weather and snowpack data. The use of hybrid inputs, where model data are constrained by nearby surface observations, should also be considered.

Bibliography

Adams, E. and A. Sato, 1993: Model for effective thermal conductivity of a dry snow cover composed of uniform ice spheres. *Annals of Glaciology*, **18**, 300–304.

Arons, E., 1994: *Dependance of snow thermal conductivity on microstructure.*. Ph.D. thesis, Dartmouth College.

Arons, E. and S. Colbeck, 1995: Geometry of heat and mass transfer in dry snow: A review of theory and experiment. *Rev. Geophy.*, **33**, 463–493.

Ashton, G., 1986: *River and lake ice engineering*. Water Resources Pubns.

Bakermans, L. and B. Jamieson, 2009: Swarm: A simple regression model to estimate near-surface snowpack warming for back-country avalanche forecasting. *Cold Reg. Sci. Tech.*, **59**, 133–142.

Bartelt, P., O. Buser, and S. A. Sokratov, 2004: A nonequilibrium treatment of heat and mass transfer in alpine snowcovers. *Cold Reg. Sci. Tech.*, **39**, 219–242.

Bartelt, P. and M. Lehning, 2002: A physical SNOWPACK model for the Swiss avalanche warning. part I: numerical model. *Cold Reg. Sci. Tech.*, **35**, 123–145.

Baunach, T., C. Fierz, P. Satyawali, and M. Schneebeli, 2001: A model for kinetic grain growth. *Ann. Glaciol.*, **32**, 1–6.

Bellaire, S., B. Jamieson, and C. Fierz, 2011: Forcing the snow-cover model snowpack with forecasted weather data. *The Cryosphere*, **5**, 1115–1125.
URL `http://www.the-cryosphere.net/5/1115/2011/tc-5-1115-2011.html`

Blackwell, J., 1956: The axial-flow error in the thermal conductivity probe. *Can. J. Phys.*, **4**, 412–417.

Blöschl, G. and M. Sivapalan, 1995: Scale issues in hydrological modelling: a review. *Hydrological processes*, **9**, 251–290.

Britsow, K., R. White, and G. Kluitenberg, 1994: Comparison of single and dual probes for measuring soil thermal properties with transient heating. *Austral. J. Soil Res.*, **32**, 447–464.

Brown, R., P. Satyawali, M. Lehning, and P. Bartelt, 2001: Modeling the changes in microstructure of snow during metamorphism. *Cold Reg. Sci. Tech.*, **33**, 91–101.

Brun, E., P. David, M. Sudul, and G. Brunot, 1992: A numerical model to simulate snow-cover stratigraphy for operational avalanche forecasting. *Journal of Glaciology*, **38**, 128.

Brun, E. and F. Touvier, 1987: Etude experimentale de la convection thermique dans la neige. *J. Phys. Paris*, **48**, 257–261.

Buhler, R., 2013: *Melt-Freeze Crust Formation and Evolution in the Columbia Mountains*. MSc thesis, University of Calgary, Calgary, Canada, 163 pp.

Buhler, R. and B. Jamieson, 2012: Tracking melt-freeze crust evolution. *International Snow Science Workshop*, Anchorage, Alaska, volume 1, 84–91.

CAA, 2007: Observational Guidelines and Recording Standards. Technical report, Canadian Avalanche Association, Revelstoke, BC.

— 2014: Annual trends in canadian avalanche fatalities. Technical report, Canadian Avalanche Association.
URL `http://www.avalanche.ca/cac/library/patterns-in-avalanche-accidents/fatalities/general-annual-trends`

Calonne, N., F. Flin, S. Morin, B. Lesaffre, S. R. du Roscoat, and C. Geindreau, 2011: Numerical and experimental investigations of the effective thermal conductivity of snow.

Geophysical Research Letters, **38**.

URL http://dx.doi.org/10.1029/2011GL049234

Campbell, C. and B. Jamieson, 2007: Spatial variability of slab stability and fracture characteristics within avalanche start zones. *Cold Regions Science and Technology*, **47**, 134–147.

Colbeck, S., 1980: Thermodynamics of snow metamorphism due to variations in curvature. *J. Glaciol*, **26**, 291–301.

— 1983: Theory of metamorphism of dry snow. *Journal of Geophysical Research*, **88**, 5475–5482.

— 1991: The layered character of snow covers. *Rev. Geophy.*, **29**, 81–96.

Colbeck, S. C., E. Akitaya, R. Armstrong, H. Gubler, J. Lafeuille, K. Lied, D. McClung, and E. Morris, 1992: The international classification for seasonal snow on the ground. Technical Report IASH Report MP 2794, The International Commission on Snow and Ice of the International Assoiation of Scientific Hydrology/International Gaciological Society/U.S. Army CRREL.

Colbeck, S. C. and B. Jamieson, 2001: The formation of faceted layers above crusts. *Cold Reg. Sci. Tech.*, **33**, 247–52.

Conlan, M. and B. Jamieson, 2012: Research to improve forecasting for deep slab avalanches. *The Avalanche Journal - The voice of Canada's Avalanche Community*, **100**, 70 – 72.

Cook, B. I., G. B. Bonan, S. Levis, and H. E. Epstein, 2008: The thermoinsulation effect of snow cover within a climate model. *Clim. Dyn.*, **31**, 107–124.

Domine, F., J.-C. Gallet, J. Bock, and S. Morin, 2012: Structure, specific surface area and thermal conductivity of the snowpack around Barrow, Alaska. *Journal of Geophysical Research: Atmospheres (1984–2012)*, **117**.

Dominé, F., T. Lauzier, A. Cabanes, L. Legagneux, W. Kuhs, K. Techmer, and T. Heinrichs, 2003: Snow metamorphism as revealed by scanning electron microscopy. *Microscopy Research and Technique*, **62**, 33–48.

Dominé, F., A. Taillandier, A. Cabanes, T. Douglas, and M. Sturm, 2009: Three examples where the specific surface area of snow increased over time. *The Cryosphere*, **3**, 31–39.

Dominé, F., A. Taillandier, and W. Simpson, 2007: A parameterization of the specific surface area of seasonal snow for field use and for models of snowpack evolution. *J. Geophys. Res.*, **112**.

Douglas, T., M. Sturm, W. Simpson, J. Blum, L. Alvarez-Aviles, G. Keeler, D. Perovich, A. Biswas, and K. Johnson, 2008: Influence of snow and ice crystal formation and accumulation on mercury deposition to the arctic. *Environ. Sci. Technol*, **42**, 1542–1551.

Fierz, C., R. Armstrong, Y. Durand, P. Etchevers, E. Greene, D. McClung, K. Nishimura, P. Satyawali, and S. Sokratov, 2009: The international classification for snow on the ground. Technical report, IACS, prepared by the ICSI-UCCS-IACS Working Group on Snow Classification.

Fierz, C. and M. Lehning, 2001: Assessment of the microstructure-based snow-cover model SNOWPACK: thermal and mechanical properties. *Cold Reg. Sci. Tech.*, **33**, 123–131.

Flanner, M. and C. Zender, 2006: Linking snowpack microphysics and albedo evolution. *J. Geophys. Res*, **111**, doi:10.1029/2005JD006834.

Flin, F., J. Brzoska, B. Lesaffre, C. Coleou, and R. Pieritz, 2003: Full three-dimensional modelling of curvature-dependent snow metamorphism: first results and comparison with experimental tomographic data. *Journal of Physics D-Applied Physics*, **36**, 49.

Gallet, J., F. Dominé, C. Zender, and G. Picard, 2009: Measurement of the specific surface

area of snow using infrared reflectance in an integrating sphere at 1310 and 1550 nm. *The Cryosphere*, **3**, 167–182.

Gauthier, D. and B. Jamieson, 2008: Evaluation of a prototype field test for fracture and failure propagation propensity in weak snowpack layers. *Cold Reg. Sci. Tech.*, **51**, 87–97.

Google, 2013: Google Maps. [Retrieved May 22, 2014].
URL `http://maps.google.ca`

— 2014: Google Earth, Province of British Columbia, Europa Technologies, Cnes/Spot Image. [Retrieved May 22, 2014].

Greene, E., 2007: *The thermophysical and microstructural effects of an artificial ice layer in natural snow under kinetic growth metamorphism.*. Ph.D. thesis, Colorado State University.

Grenfell, T., A. Perovich John, and K. Donald, 1981: Spectral albedos of an alpine snowpack. *Cold Reg. Sci. Tech.*, **4**, 121–127.

Habermann, M., J. Schweizer, and B. Jamieson, 2008: Influence of snowpack layering on human-triggered snow slab avalanche release. *Cold Regions Science and Technology*, **54**, 176–182.

Haddon, J. F., M. Schneebeli, and O. Buser, 1998: Automatic segmentation and classification using a co-occurrence based approach. *Imaging Technologies: Techniques and Applications in Civil Engineering. Second International Conference*.

Haegeli, P. and D. McClung, 2003: Avalanche characteristics of a transitional snow climate–columbia mountains, british columbia, canada. *Cold Reg. Sci. Tech.*, **37**, 255–276.

— 2007: Expanding the snow-climate classification with avalanche-relevant information: initial description of avalanche winter regimes for southwestern canada. *J. Glaciol.*, **53**, 266–276.

Heierli, J. and M. Zaiser, 2008: Failure initiation in snow stratifications containing weak layers: Nucleation of whumpfs and slab avalanches. *Cold Regions Science and Technology*, **52**, 385–400.

Hirashima, H., K. Nishimura, S. Yamaguchi, A. Sato, and M. Lehning, 2008: Avalanche forecasting in a heavy snowfall area using the snowpack model. *Cold Reg. Sci. Tech.*, **51**, 191–203.

Hirashima, H., S. Yamaguchi, A. Sato, and M. Lehning, 2010: Numerical modeling of liquid water movement through layered snow based on new measurements of the water retention curve. *Cold Regions Science and Technology*, **64**, 94–103.

Hukseflux, 2003: TP02 non-steady-state probe for thermal conductivity measurement. Technical report, Hukseflux.

ITT Visual Information Solutions, 2010: Using IDL. Technical report, Boulder, Colorado, USA, last checked July 18, 2013.

Jacobi, H.-W., F. Dominé, W. Simpson, T. Douglas, and M. Sturm, 2010: Simulation of the specific surface area of snow using a one-dimensional physical snowpack model: implementation and evaluation for subarctic snow in Alaska. *The Cryosphere*, **4**, 35–51.

Jamieson, B., 2004a: Between a slab and a hard layer: Part 1 – formation of poorly bonded crusts in the Columbia Mountains. *Avalanche News*, 48–54.

— 2004b: Between a slab and a hard layer: Part 2 – persistence of poorly bonded crusts in the Columbia Mountains. *Avalanche News*, 34–37.

— 2006: Formation of refrozen snowpack layers and their role in slab avalanche release. *Rev. Geophy.*, **44**.

Jamieson, B. and C. Fierz, 2004: Heat flow from wet to dry snowpack layers and associated faceting. *Ann. Glaciol.*, **38**, 187–194.

Jamieson, B. and T. Geldsetzer, 1996: *Avalanche Accidents in Canada, Volume 4, 1984-1996*. Canadian Avalanche Association, Revelstoke, BC, Canada, 202 pp.

Jamieson, B., P. Haegeli, and D. Gauthier, 2010: *Avalanche Accidents in Canada, Volume 4, 1996-2007*. Canadian Avalanche Association, Revelstoke, BC, Canada, 429 pp.

Jamieson, B. and C. Johnston, 2001: Evaluation of the shear frame test for weak snowpack layers. *Ann. Glaciol.*, **32**, 59–69.

Jamieson, B. and P. Langevin, 2004: Faceting above crust and associated slab avalanching in the Columbia Mountains. *ISSW 2004 Proceedings*, USDA Forest Service, Fort Collins, CO.

Jamieson, B. and A. van Herwijnen, 2002: Preliminary results from controlled experiments on the growth of faceted crystals above a wet snow layer. *Proceedings of the International Snow Science Workshop*, Penticton, B.C.

Kaempfer, T., B. Pinzer, J. Spiegel, and M. Schneebeli, 2009: Evolution of snow microstructure: New insights into properties and processes. *IAMAS, IAPSO, IACS Joint Assembly 2009.*, Montreal, PQ.

Kaempfer, T., M. Schneebeli, and S. Sokratov, 2005: A microstructural approach to model heat transfer in snow. *Geophys. Res. Lett*, **32**, 21.

Kaempfer, T. U. and M. Plapp, 2007: Modeling heat and mass transfer in snow at a microstructural level using a phase-field approach - first results. *64th Eastern Snow Conference, St. Johns, Newfoundland, Canada*.

Kaempfer, T. U. and M. Schneebeli, 2007: Observation of isothermal metamorphism of new snow and interpretation as a sintering process. *Journal of Geophysical Research: Atmospheres (1984–2012)*, **112**.

Kokhanovsky, A. and E. Zege, 2004: Scattering optics of snow. *Applied Optics*, **43**, 1589–1602.

Kokhanovsky, A. A. and V. V. Rozanov, 2012: The retrieval of snow characteristics from optical measurements. *Light Scattering Reviews, Vol. 6*, Springer, 289–331.

Labsphere, 2013: Technical guide, reflectance materials and coatings. Technical report, 231 Shaker Street, North Sutton, New Hamphshire USA, last checked July 11, 2013.
URL `http://www.labsphere.com/uploads/technical-guides/a-guide-to-reflectance-materials-and-coatings.pdf`

LaChapelle, E., 1960: Critique on heat and vapor transfer in snow. Technical report, U.S Department of Agriculture, Forest Service, Alta Avalanche Study Center.

Landry, C. C., 2002: *Spatial variations in snow stability on uniform slopes: Implications for extrapolation to surrounding terrain*. Master's thesis, Montana State University, Bozeman Montana.

Langlois, A., A. Royer, B. Montpetit, G. Picard, and L. Brucker, 2010: On the relationship between snow grain morphology and in-situ near infrared calibrated reflectance photographs. *Cold Reg. Sci. Tech.*, **61**, 34–42.

Legagneux, L., A. Cabanes, and F. Dominé, 2002: Measurement of the specific surface area of 176 snow samples using methane adsorption at 77 K. *J. Geophys. Res*, **107**.

Legagneux, L., T. Lauzier, F. Dominé, W. Kuhs, T. Heinrichs, and K. Techmer, 2003: Rate of decay of specific surface area of snow during isothermal experiments and morphological changes studied by scanning electron microscopy. *Canadian Journal of Physics*, **81**, 459–468.

Lehning, M., P. Bartelt, B. Brown, and C. Fierz, 2002a: A physical SNOWPACK model

for the Swiss avalanche warning. part II: Snow microstructure. *Cold Reg. Sci. Tech.*, **35**, 147–167.

— 2002b: A physical SNOWPACK model for the Swiss avalanche warning. part III: meteorological forcing, thin layer formation and evaluation. *Cold Reg. Sci. Tech.*, **35**, 169–184.

Matzl, M. and M. Schneebeli, 2006: Measuring specific surface area of snow by near-infrared photography. *Journal of Glaciology*, **52**, 558–564.

— 2010: Stereological measurement of the specific surface area of seasonal snow types: Comparison to other methods, and implications for mm-scale vertical profiling. *Cold Regions Science and Technology*, **64**, 1–8.

McClung, D. and P. Schaerer, 2006: *The Avalanche Handbook.*. The Mountaineers, Seattle,WA.

Miller, D., E. Adams, and R. Brown, 2003: A microstructural approach to predict dry snow metamorphism in generalized thermal conditions. *Cold Reg. Sci. Tech.*, **37**, 213–226.

Morin, S., F. Domine, L. Arnaud, and G. Picard, 2010: In-situ monitoring of the time evolution of the effective thermal conductivity of snow. *Cold Regions Science and Technology*, **64**, 73 – 80.
URL `http://www.sciencedirect.com/science/article/pii/S0165232X10000340`

Morin, S., F. Domine, A. Dufour, Y. Lejeune, B. Lesaffre, J.-M. Willemet, C. Carmagnola, and H.-W. Jacobi, 2013: Measurements and modeling of the vertical profile of specific surface area of an alpine snowpack. *Advances in Water Resources*, **55**, 111 – 120.
URL `http://www.sciencedirect.com/science/article/pii/S0309170812000206`

Natural Resources Canada, Earth Sciences Sector, Centre for Topographic Information, 2013: Canadian Digital Elevation Data. [Retrieved April 15, 2013].
URL `http://www.geobase.ca`

Picard, G., L. Arnaud, F. Dominé, and M. Fily, 2009: Determining snow specific surface area from near-infrared reflectance measurements: Numerical study of the influence of grain shape. *Cold Reg. Sci. Tech.*, **doi:10.1016/j.coldregions.2008.10.001**.

Pielke, R. A., 2002: *Mesoscale meteorological modeling*. Academic Press.

Pinzer, B. and M. Schneebeli, 2009: Snow metamorphism under alternating temperature gradients: Morphology and recrystallization in surface snow. *Geophysical Research Letters*, **36**.

Pinzer, B. R., M. Schneebeli, and T. U. Kaempfer, 2012: Vapor flux and recrystallization during dry snow metamorphism under a steady temperature gradient as observed by time-lapse micro-tomography. *The Cryosphere*, **6**, 1141–1155.
URL `http://www.the-cryosphere.net/6/1141/2012/`

R Core Team, 2013: *R: A Language and Environment for Statistical Computing*. R Foundation for Statistical Computing, Vienna, Austria.
URL `http://www.R-project.org`

Riche, F. and M. Schneebeli, 2010: Microstructural change around a needle probe to measure thermal conductivity of snow. *J. Glaciol.*, **56**, 871–876.

— 2013: Thermal conductivity of snow measured by three independent methods and anisotropy considerations. *The Cryosphere*, **7**, 217–227.
URL `http://www.the-cryosphere.net/7/217/2013/`

Ross, C., 2010: *Testing fracture propagation propensity for slab avalanche forecasting*. Master's thesis, University of Calgary, Calgary, AB, Canada.

Royston, P., 1995: Remark AS R94: A remark on algorithm AS 181: The W test for normality. *Applied Statistics*, **44**, 547–551.

Rutter, N., R. Essery, J. Pomeroy, N. Altimir, K. Andreadis, I. Baker, A. Barr, P. Bartlett, A. Boone, H. Deng, et al., 2009: Evaluation of forest snow processes models (SnowMIP2). *Journal of Geophysical Research: Atmospheres (1984–2012)*, **114**.

Satyawali, P. and A. Singh, 2008: Dependence of thermal conductivity of snow on microstructure. *Journal of Earth System Science*, **117**, 465–475.

Satyawali, P., A. Singh, S. Dewali, P. Kumar, and V. Kumar, 2008: Time dependence of snow microstructure and associated effective thermal conductivity. *Ann. Glaciol.*, **49**, 43.

Schirmer, M. and B. Jamieson, 2014: Limitations of using a thermal imager for snow pit temperatures. *The Cryosphere*, **8**, 387–394.

Schneebeli, M. and S. Sokratov, 2004: Tomography of temperature gradient metamorphism of snow and associated changes in heat conductivity. *Hydrological Processes*, **18**.

Schweizer, J., K. Kronholm, B. Jamieson, and K. W. Birkeland, 2008: Review of spatial variability of snowpack properties and its importance for avalanche formation. *Cold Reg. Sci. Tech.*, **51**, 253–272.

Seligman, G., 1936: *Snow Structure and Ski Fields*. Macmillan London.

Shertzter, R. H., E. E. Adamas, and M. Schneebeli, 2010: Characterizing microstructural arrangement and effective properties of dry snow: thermal conductivity. *Proceedings of the 2010 International Snow Science Workshop*, Squaw Valley, CA, USA.

Simenhois, R. and K. Birkeland, 2007: An update on the extended column test: New recording standards and additional data analyses. *The Avalanche Review*, **26**.

Singh, A. and K. Wasankar, 2009: Microstructure based model for effective thermal conductivity of snow. *Indian Journal of Pure I& Applied Physics*, **47**, 206–211.

Smith, M., B. Jamieson, and C. Fierz, 2008: Observation and modeling of a buried melt-freeze crust. *Proceedings of 2008 International Snow Science Workshop, Whistler, Canada, 21-27 September 2008*, C. Campbell, S. Conger, and P. Haegeli, eds., 170–178.

Sokratov, S. A., 2001: Parameters influencing the recrystalliation rate of snow. *Cold Reg. Sci. Tech.*, **33**, 263–274.

Sturm, M., J. Holmgren, M. König, and K. Morris, 1997: The thermal conductivity of seasonal snow. *Journal of Glaciology*, **43**, 26–41.

Sturm, M. and J. Johnson, 1991: Natural convection in the subarctic snow cover. *J. Geophys. Res.*, **96**, 11657–11671.

Sturm, M. and J. B. Johnson, 1992: Thermal conductivity measurements of depth hoar. *J. Geophys. Res.*, **97**, 2129–2139.

Sturm, M., D. K. Perovich, and J. Holmgren, 2002: Thermal conductivity and heat transfer through the snow on the ice of the Beaufort Sea. *J. Geophys. Res.*, **107**.

Taillandier, A., F. Dominé, W. Simpson, M. Sturm, and T. Douglas, 2007: Rate of decrease of the specific surface area of dry snow: Isothermal and temperature gradient conditions. *J. Geophys. Res*, **112**, doi:10.1029/2006JF000514.

Tape, K. D., N. Rutter, H.-P. Marshall, R. Essery, and M. Sturm, 2010: Recording microscale variations in snowpack layering using near-infrared photography. *J. Glaciol.*, **56**, 75–80.

Toure, A. M., K. Goïta, A. Royer, C. Mätzler, and M. Schneebeli, 2008: Near-infrared digital photography to estimate snow correlation length for microwave emission modeling. *Applied Optics*, **47**, 6723–6733.

Vionnet, V., E. Brun, S. Morin, A. Boone, S. Faroux, P. Le Moigne, E. Martin, J. Willemet, et al., 2012: The detailed snowpack scheme crocus and its implementation in surfex v7. 2. *Geoscientific Model Development*, **5**, 773–791.

Warren, S. and W. Wiscombe, 1981: A model for the spectral albedo of snow. II: Snow containing atmospheric aerosols. *J. Atmos. Sci*, **37**, 2734–2745.

Wikipedia, 2013: Demosaicing — wikipedia, the free encyclopedia. [Online; accessed 22-July-2013].
URL http://en.wikipedia.org/w/index.php?title=Demosaicing&oldid=545156799

Wiscombe, W. and S. Warren, 1980: A model for the spectral albedo of snow. i. pure snow. *J. Atmos. Sci*, **37**, 2712–2733.

WSL Institute for Snow and Avalanche Research SLF, 2014: The SnowMicroPen as a tool to integrate multiple scales in quantitative snow measurements.
URL http://www.slf.ch/ueber/organisation/schnee_permafrost/projekte/SnowMicroPen/index_EN

Yen, Y., C. R. Research, and E. L. (US), 1981: *Review of thermal properties of snow, ice and sea ice*. National Technical Information Service.

Appendix A

Description of study sites and narratives of crust formation and evolution

This appendix introduces the study areas and weather during formation of specific crusts referenced throughout the dissertation. The majority of data were collected at two main areas: Mt. Fidelity and Rogers Pass are both situated in the Columbia Mountains of central British Columbia, Canada. Both experience transitional snow climates (Haegeli and McClung, 2003, 2007), characterized by heavy snowfall, a moderating influence from maritime air and significant avalanche activity on persistent weak layers, notably surface hoar and early season facet-crust combinations.

Although they are separated by only 15 km, the influence of the surrounding topography and elevation differences can lead to substantial differences in local weather and snowpack. A synoptic view of southern British Columbia (Figure A.1) reveals several notable topographical features; An eastward-propagating storm will first encounter the Coast Mountains, then the interior plateau, the Columbia Mountains and finally the Rocky Mountains. The latter two are delineated by the Rocky Mountain trench. A closer look at the regional topography (see Figure A.2) reveals a more complex situation. Even in the case of a large winter storm, the orientation of valleys, the height of surrounding land and the availability of open water early in the season exert a strong influence on local snowpack characteristics.

Rogers Pass: Rogers Pass lies along the Trans-Canada Highway in Glacier National Park (Figure A.3). The highway elevation ranges from 835 m to 1330 m while the surrounding peaks may exceed 3000 m. The highway offers easy access to a number of drainages . Due to the area's popularity as a skiing destination, it is difficult to establish a site for long term monitoring of the snowpack - ski tracks have been found in many unlikely places after several

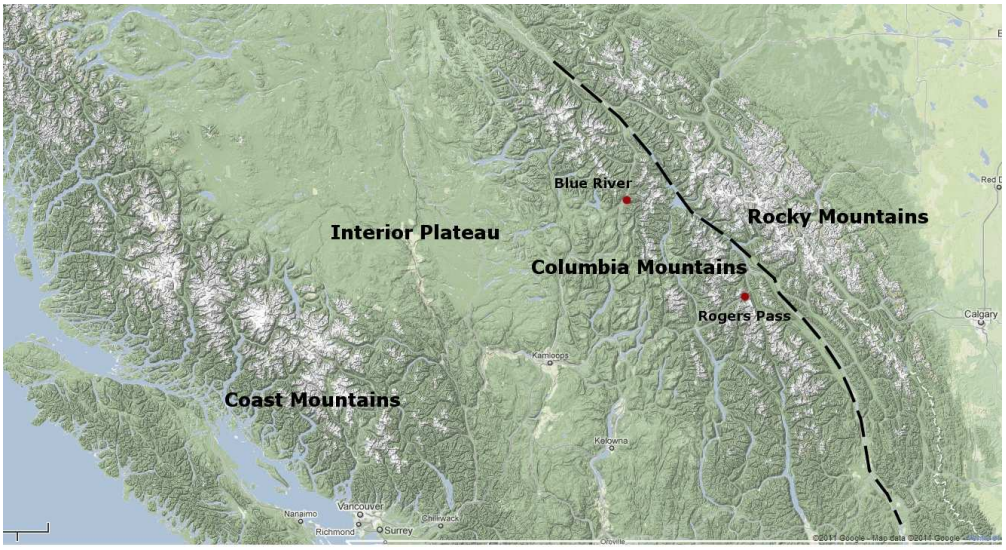

Figure A.1: *Mountains of Western British Columbia. Base image from Google Maps (Google, 2013).*

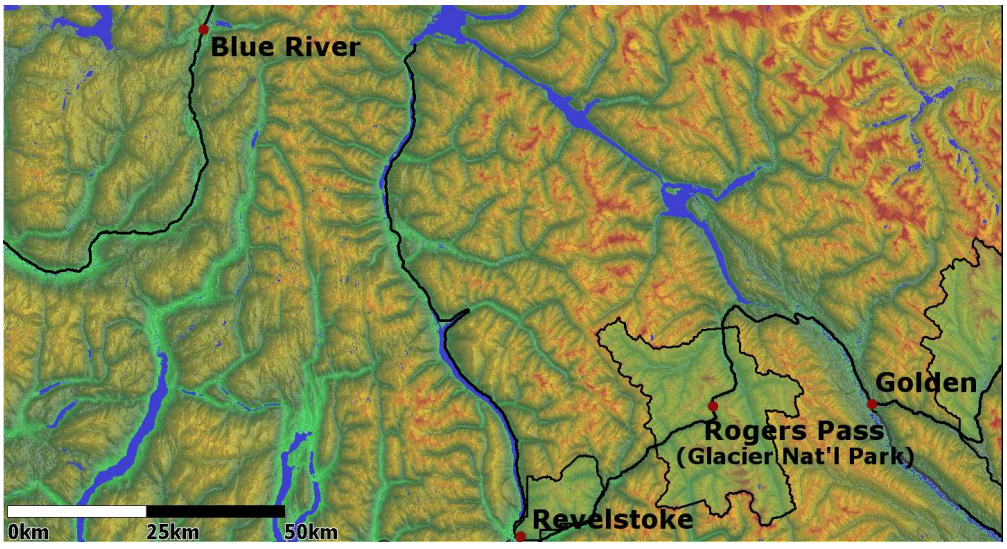

Figure A.2: *Topography and location around study areas referenced in this dissertation. Digital Elevation data from Geobase.ca (Natural Resources Canada, Earth Sciences Sector, Centre for Topographic Information, 2013).*

Table A.1: *Study Sites in Rogers Pass. Abbreviations used in crust identifiers are in parentheses.*

Name	**Elev.**	**Asp.**	**Veg.**	**Notes**
Fidelity Study Plot (FI)	1905 m	flat	TL	Met stn
Beaver Valley (BV)	870 m	flat	BTL	Old gravel pit
Rogers Pass Study Plot (RP)	1305 m	flat	BTL	Met stn
Fidelity South Run (SR)	1950 m	SE	BTL	Small open glade.
RP Study Slope (RP)	1890 m	ENE	BTL	Below Fidelity Met stn

hours of digging. For this reason all study sites were established either in areas closed to recreational use or with no open slopes for skiing. Table A.1 summarizes the topography and vegetation at each study site. Two sites, at the Mt. Fidelity and Rogers Pass study plots, were adjacent to meteorological instrumentation. Both are equipped with precipitation and temperature gauges while Fidelity is also equipped with long and shortwave radiometers. Along with the Fidelity study plot, the South Run and Study Slope sites were situated in an area closed to public access during the winter season. Figure A.4 shows the area surrounding the Mt. Fidelity station. Fidelity study plot is known as a site with little to no wind effect and a very uniform snowpack, making it ideal for tracking changes over time of specific layers.

This remainder of this appendix summarizes the general characteristics of each crust that was observed in the field along with crusts observed in the Rogers Pass cold lab. Each crust is named according to general location and date of first burial. This is consistent with the guidelines for naming persistent weak layers given in CAA (2007). Knowledge of the weather leading up to the formation of the crust and its subsequent burial can be useful for making inferences about the spatial variability and extent of a given crust; for instance the winter of 2009-2010 was notable for the persistent ridges of high pressure over much of interior British Columbia. Temperatures were mild and there was little precipitation. As a result, crusts formed by the end of January on all unshaded south-facing slopes. Structure and variability were dictated mostly by the slope and aspect as well as any shade provided

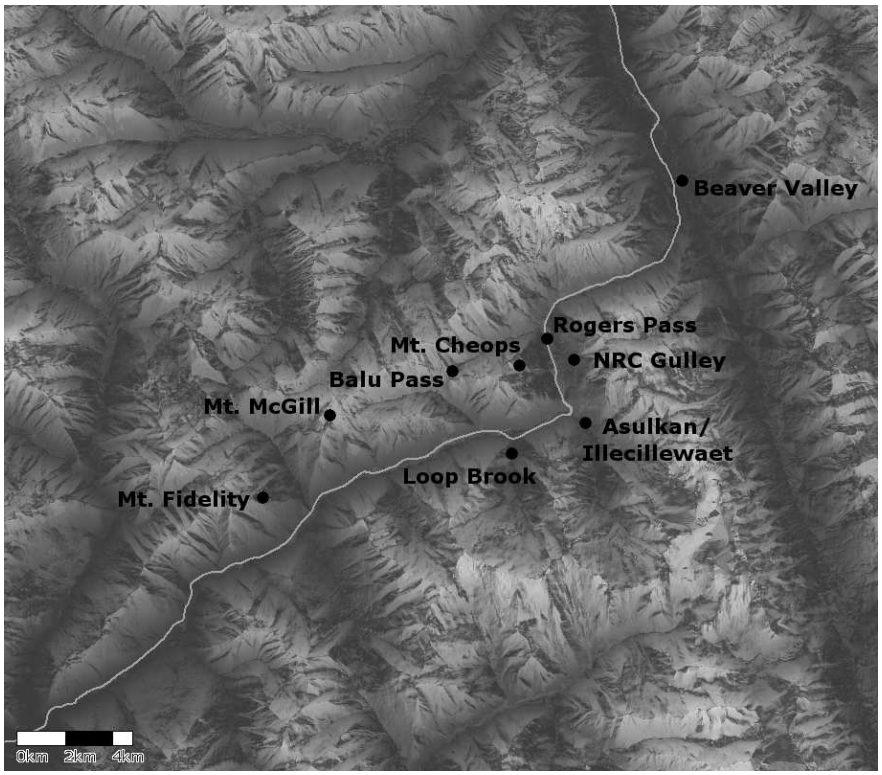

Figure A.3: *Topography and location of landmarks surrounding Rogers Pass in Glacier National Park. Digital elevation data from Geobase.ca (Natural Resources Canada, Earth Sciences Sector, Centre for Topographic Information, 2013)*

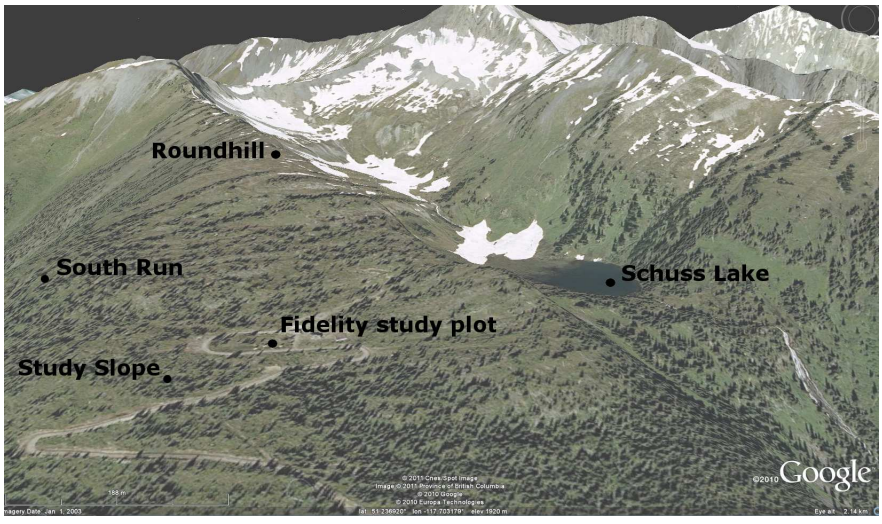

Figure A.4: *Area surrounding Mt. Fidelity study plot in Glacier National Park. Image from Google Earth (Google, 2014).*

by local vegetation.

A.1 2007-08 Crust

FI071205: This crust formed as the result of a warm, moist air mass ('Pineapple Express') that moved into British Columbia from the southwest in early December 2007. The system brought elevated freezing levels and rain or wet snow up to 2000 m in the North Columbia mountains. Cooler temperatures and snow followed throughout the next day and the crust was buried. The 'December 5^{th}' crust exhibited a large degree of variability at all spatial scales and included percolation channels, ice lenses and laminations. The crust was monitored at a fixed study site on the Mt. Fidelity study slope from 2 January – 29 March 2008. It was also observed and tested at a number of other sites in Glacier National Park, Blue River and Kicking Horse Mountain Resort . This crust is discussed further in Smith et al. (2008). This is one of only 2 crusts in the data set that formed as the result of precipitation; all others were due to incoming solar radiation, elevated air temperature or a combination of the two.

Figure A.5 shows the air temperature and liquid precipitation recorded at the Mt. Fidelity weather station. The temperature rose to above freezing from 03:00 PST 4 December and remained above freezing until 17:00. During this time 13 mm of precipitation fell, likely as a mixture of wet snow and rain. The air temperature then fell over the next 48 hours, with an additional 17 mm of precipitation falling as snow. This rapid transition from wet snow or rain to cooler temperatures and snowfall allowed for an extended period of conditions suitable to temperature gradient metamorphism within the wetted layer and at its boundaries as the liquid water froze.

Clear cold conditions continued until 11 December (Figure A.6), when another period of snowfall began and the crust was rapidly buried over 1 m deep in the snowpack. Weekly site visits commenced 2 January, 2008 and thermistors were in place within the crust and at its

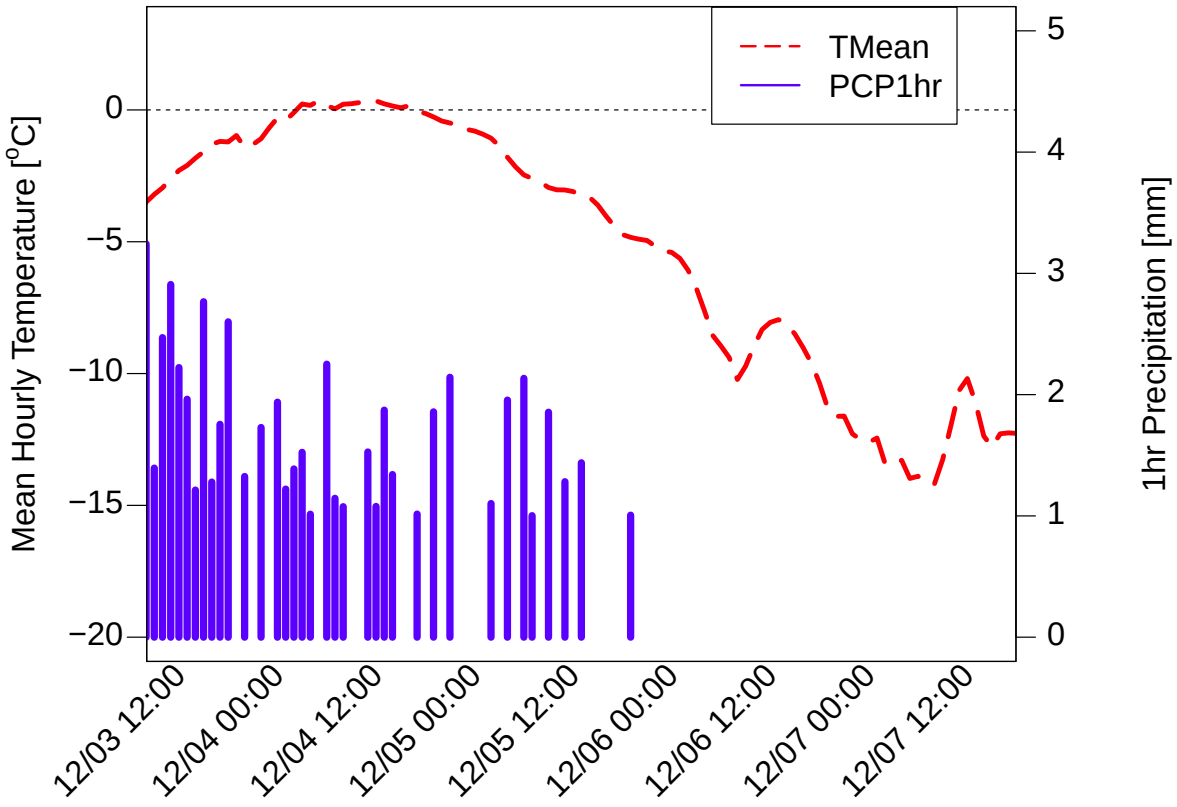

Figure A.5: *Hourly air temperature and precipitation at Mt. Fidelity weather station during the formation of crust CR071205.*

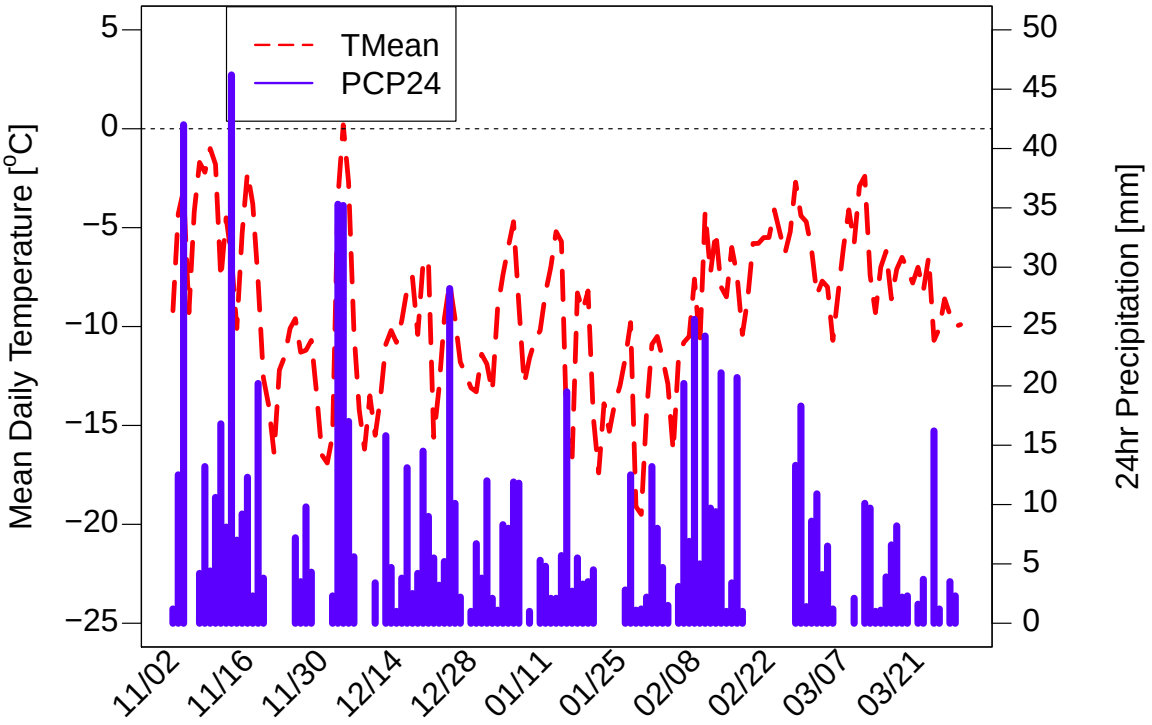

Figure A.6: *Air temperature and daily precipitation at Mt. Fidelity weather station, winter 2007-08*

boundaries from 14 January - 25 February. The crust was observed weekly at a fixed study plot at Mt. Fidelity and also at various sites and elevations in the Rogers Pass, Blue River and Kicking Horse Mountain Resort areas until the conclusion of the study season in mid-March. Standard observations at the fixed study plot included Propagation Saw Test (PST), shear frame tests and a test profile.

A.2 2008-09 Crusts

Unlike the previous winter which had very few clear sunny periods after early December, winter 2008-09 was marked by several clear sunny periods which allowed for the formation of thick sun crusts on south-facing slopes. Three crusts were tracked this winter, all located on the South Run area of the Mt. Fidelity closure. Figure A.7 shows the air temperature and liquid precipitation recorded at the Mt. Fidelity weather station from early January

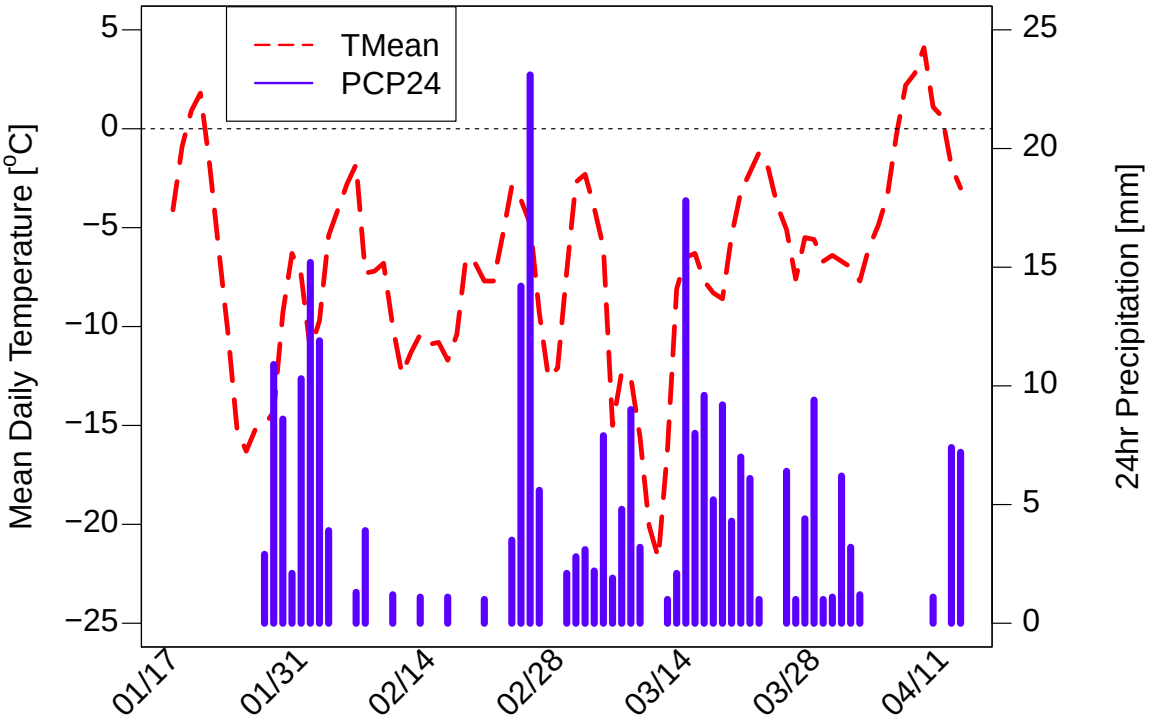

Figure A.7: *Air temperature and daily precipitation at Mt. Fidelity weather station, winter 2008-09.*

to early April 2009, while Figure A.8 shows the measured incoming solar and net longwave radiation. Radiation data were lost for a 2-week period in late February when a datalogger battery failed.

SR090127: This crust formed on south-facing slopes during a warm, sunny period in late January. Maximum temperatures reached 8.0 °C on 20 January, followed by a cooling trend through 27 January when the crust was buried. Thermistors were placed within the crust and at its upper and lower boundaries at a fixed study site on Mt. Fidelity South Run on 18 January and site visits continued weekly until 11 April at which point the crust was still 71 cm below the surface. Standard observations included NIR, PST, shear frames at the upper boundary and a test profile.

SR090222: The crust formed on south-facing slopes following a period of generally clear weather. Unlike the conditions preceding the formation of SR090127, air temperatures did not rise above 0 °C and melting of surface snow was due entirely to incoming solar radiation.

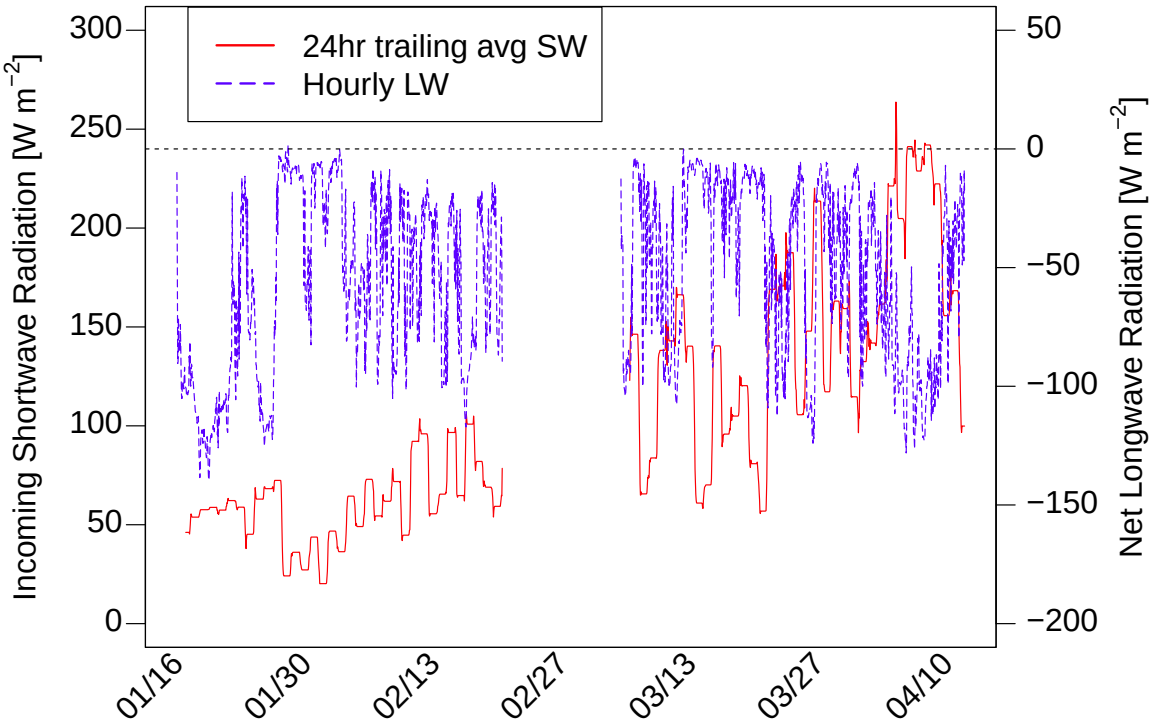

Figure A.8: *Incoming shortwave and net longwave radiation at Mt. Fidelity weather station, winter 2008-09. Data are missing from 20 February - 5 March due to the failure of the datalogger battery.*

The crust was buried late on 22 February and thermistors were placed within the crust and at its boundaries on 24 February. Weekly site visits continued until 11 April and thermistors were removed on 17 April. The crust was 50 cm below the surface at the time of the final observation. Standard weekly observations were the same as for SR090127.

SR090301: A short period of clear sunny skies in late February was responsible for the formation of this crust, which was quickly buried on 1 March and by the time of the first study plot visit on 5 March was 20 cm below the snow surface. Thermocouples were placed within and around the crust on 7 March. Weekly visits continued until 11 April and standard observations were the same as for SR090127 and SR090222.

A.3 2009-10 Crusts

The winter of 2009-10 was generally very warm, with the mean daily temperature rarely dropping below -7 °C at Mt. Fidelity weather station. The period from mid-January to mid-March was marked with alternating periods of clear weather and light precipitation at Mt. Fidelity and Rogers Pass, as shown in Figures A.9 and A.11, respectively. Incoming shortwave radiation and net longwave radiation at Mt. Fidelity are shown in Figure A.10. Periods of clear skies occurred when the net longwave is strongly negative and the amplitude of the incoming shortwave radiation is larger, for instance around 12 February.

Natural crusts were formed at Mt. Fidelity by freezing rain, incoming solar radiation and temperature. Rainfall and wet snow formed crusts at Rogers Pass and Beaver Valley but did not extend as high as Mt. Fidelity. Natural crusts were also harvested at Rogers Pass and studied in a cold lab. Thermal conductivity measurements were first used on crusts this season.

Fidel100109: This 2 mm thick crust was formed by a freezing rain event at Mt Fidelity on the evening of 9 January, 2010. Air Temperatures were well below 0 °C and the wetted snow was buried by 2 cm of snow several hours later. Thermocouples were placed above

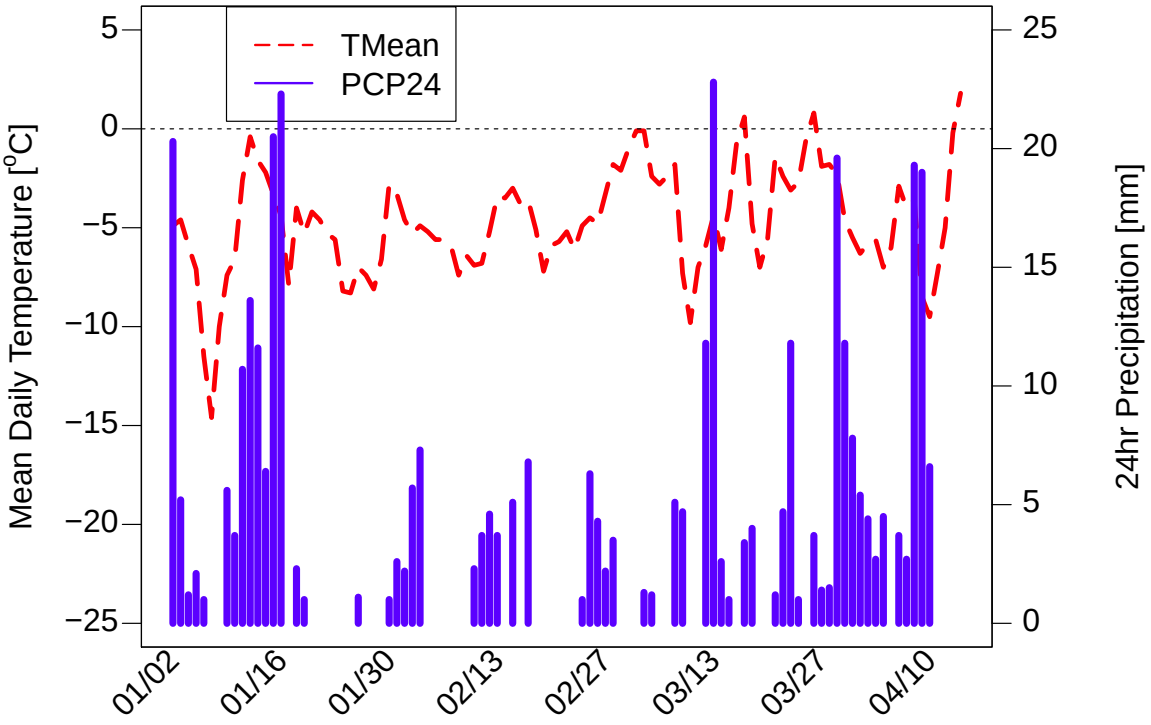

Figure A.9: *Air temperature and daily precipitation at Mt. Fidelity weather station, winter 2009-10*

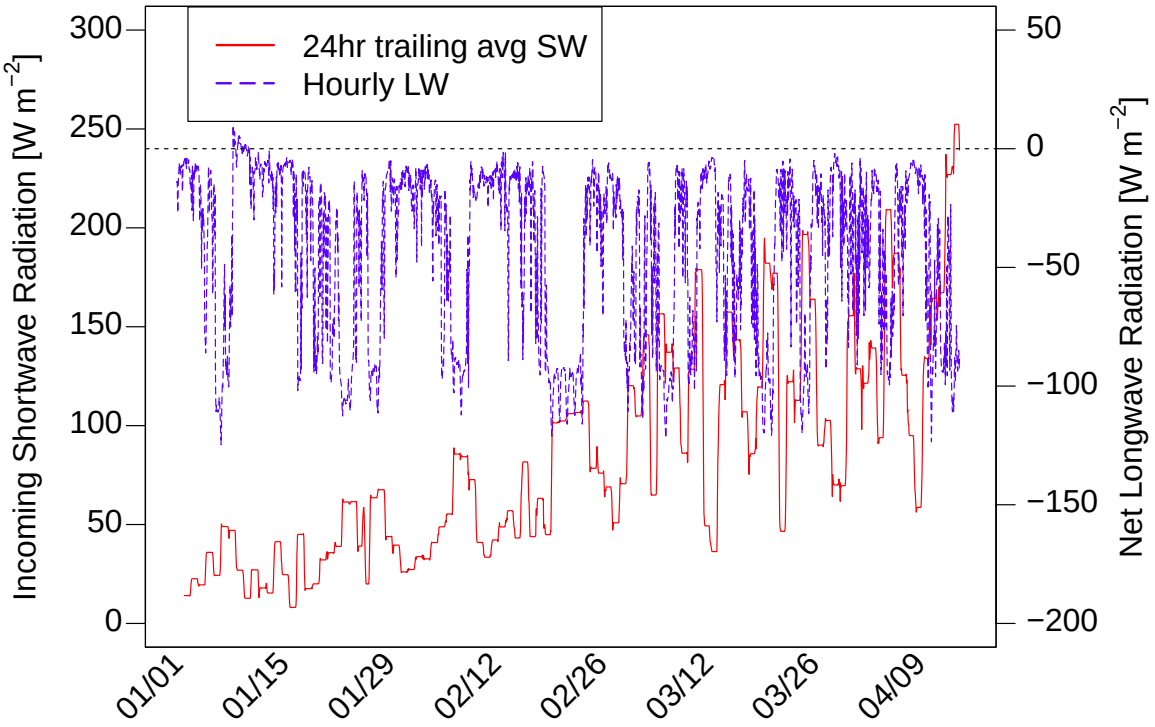

Figure A.10: *Incoming shortwave and net longwave radiation at Mt. Fidelity weather station, winter 2009-10*

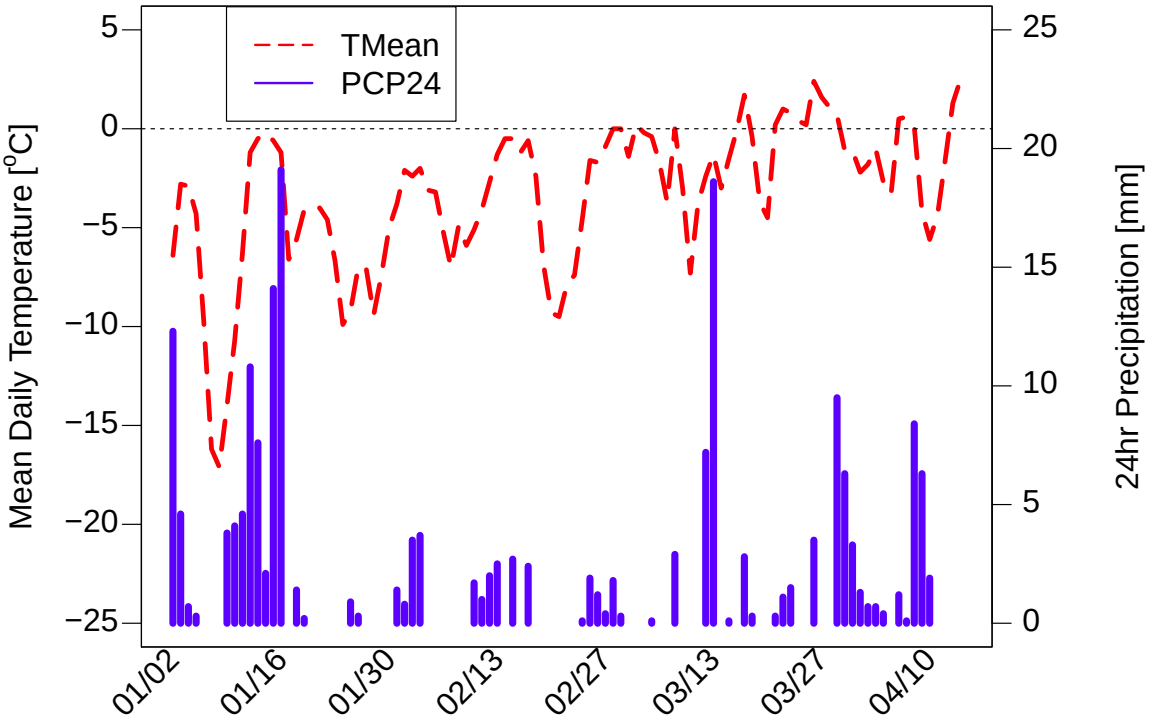

Figure A.11: *Air temperature and daily precipitation at Rogers Pass weather station, winter 2009-10*

and below the crust on 10 January and remained in place until the final observation on 14 April at which point the crust was approximately 140 cm below the snow surface. Standard observations included NIR photography, thermal conductivity measurements and a standard test profile (CAA, 2007). Stability tests were not performed due to space considerations.

RP100112: Formed during a wet snow/rain event that lasted several days, beginning on 12 January. Temperature and liquid precipitation are shown in Figure A.11. Thermistors were placed within and around the crust on 19 January and observations continued until 6 April. Warm temperatures and moist or wet layers caused difficulties with some observations especially during the latter half of March. Standard observations included NIR photography, thermal conductivity and a test profile. Stability tests were not performed due to space considerations.

BV100112: This crust was formed during the same weather event as RP100112 but there was likely more liquid precipitation as this site due to its lower elevation. The study plot

was established in an old gravel pit on 31 January and thermistors were placed above, below and within the crust to record the hourly temperature. Weekly observations continued until thermistors were removed on 27 March. As was the case with RP100112, persistent warm temperatures caused difficulties with observations during some site visits. Standard observations included NIR photography, thermal conductivity and a test profile.

SR100131,SR100210: These crusts formed on south-facing slopes in late January and early February during consecutive clear, sunny periods. Ambient air temperature at Mt. Fidelity, several hundred metres away at a similar elevation, averaged -5 °C during formation of both crusts. The study site was on Mt. Fidelity South Run, within the public closure area. Due to low snow and strong insolation during February and early March these two crusts became one and tracking specific features became difficult due to continued melting and percolation. Thermistors were placed in SR100131 on 3 February and in SR100210 on 10 February. Weekly observations continued until 7 April and included NIR photography, thermal conductivity above, below and within, and a test profile. The upper snowpack containing the crusts became isothermal in late March and remained so until the end of the season.

FI100308: Formation occurred during a series of warm and sunny days with minimal precipitation in early March. The study site was on flat terrain in the Mt. Fidelity study plot coincident with the study site for FI100109. The crust was first observed on 8 March and weekly observations continued until 14 April at which point the crust was approximately 85 cm below the surface. Standard observations included NIR photography, thermal conductivity above, below and within the crust and a standard test profile. Stability tests were not performed due to space considerations.

SR09site:A spatial variability study was performed on the SR100131 crust at the same site used for the 2009 crusts. Observations were spaced along two grid lines running upslope and included NIR photography, thermal conductivity and a test profile.

LAB: Crusts were harvested from an area adjacent to the Rogers Pass staff residence and transported in an insulated box to the cold lab approximately 100 m distant. The natural crust was formed by the same processes responsible for RP100112. Observations prior to harvesting included NIR photography, thermal conductivity within the crust and in adjacent layers, and a test profile. Five cold lab experiments were performed and conditions for each are described in more detail in Chapters 2, 3 and 4.

Appendix B

Glossary

This appendix includes definitions of some commonly-used terms and acronyms. References to further information are included where appropriate.

Bond: The region of ice lattice connecting two discrete snow particles.

Bridging: Refers to the ability of a stiff snow slab to reduce or spread the force transmitted to a buried weak layer.

Compression Test (*CT*): A test for ease of initiation of a weak layer in the seasonal snow pack. A layer of interest does not need to be identified beforehand. A column 30 cm x 30 cm is isolated to a depth of up to 1 – 1.5 m and increasing loading is applied to the top of the column with a snow shovel. Interpretation is dependent on the number of 'taps' on the shovel required before the weak layer fails as well as the manner in which it fails. Described by CAA (2007).

Coordination Number: The number of bonds per snow grain; influences heat transfer and snowpack settling. Often an intrinsic property of layers in snowpack models.

Correlation Length: The distance beyond which variations of the dialectric constant in one region of space become uncorrelated with those in another region (Toure et al., 2008). In the context of the present study, the correlation length is proportional to optical grain size and inversely proportional to SSA.

Disaggregated: In the context of a crust, refers to an area where bonds are extremely weak or broken. When referring to crystal photography, the bonds are broken manually in order to examine individual crystals.

Equilibrium Metamorphism *(see also: Temperature Gradient Metamorphism)***:** Snow grain metamorphism that is driven by localized curvature-dependent gradients in vapour

pressure rather than a temperature gradient. The equilibrium vapour pressure is higher over grains with a smaller radius of curvature, and such grains will tend to lose mass while grains with a larger radius of curvature gain mass. Typically results in well-bonded snow comprised of rounded grains.

Extended Column Test (*ECT*): A test of the ease of initiation and propagation propensity of a weak layer, though the weak layer does not need to be identified beforehand. Techniques and recording standards introduced by Simenhois and Birkeland (2007). Similar to the Compression Test, except that the column is isolated 90 cm across the slope instead of 30 cm.

Faceting: The metamorphism of snow grains from either fresh or rounded forms to forms exhibiting sharp edges and flat faces. Usually associated with a slope-normal temperature gradient greater than 1 °C 10 cm^{-1}.

Grain size: Typically describes the average diameter, or sometimes size range, in a representative sample of snow crystals. A somewhat fuzzy concept when attempting to quantify physical characteristics if there is no clear delineation between grain and bond.

Grain Type: Grain type for seasonal snow is classified by considering both shape and metamorphic pathway. Fierz et al. (2009) uses a system of major classes and subclasses communicated as four-letter abbreviations. The major class is the first two letters and the subclass, if used, is the following two lowercase letters. Major classes and subclasses used in this dissertation are listed in Table B.1 alongside a previous system published by Colbeck et al. (1992).

Hand Hardness: A hardness scale developed help field workers quickly determine the relative hardness of snow layers. Values in order of increasing hardness are, "fist","four fingers","one finger","pencil","knife" and "ice", and are determined by which object can penetrate the snow with moderate force.

Table B.1: *Grain type abbreviations. The full classification systems have major classes and subclasses. Only those subclasses used in the paper are included in the table. For a full list consult the relevant publication.*

Grain Type	**Fierz et al. (2009)**	**Colbeck et al. (1992)**
Precipitation Particles	PP	1
Decomposing forms	DF	2
Rounded grains	RG	3
Rounded grains, faceting	RGxf	3c
Rounded grains, wind packed	RGwp	9d
Faceted crystals	FC	4
Faceted crystals, rounding	FCxr	4c
Depth hoar	DH	5b
Surface hoar	SH	7
Melt freeze crust	MFcr	9e
Clustered grains	MFcl	6a
Refrozen polycrystals	MFpc	6b
Ice layer	IF	8,9c

Micro-Computed Tomography (μCT): A non-destructive imaging technique used to compute a physical model of an object, with resolution on the micron scale. In snow science the technique has been used to study structure, bonds and metamorphism of small snow samples in a lab.

Neck: Sometimes used to refer to bonds, so-called because of the constriction of the idealized bond (*example shown in Figure 1.2.*).

Optical Diameter (snow): For a given portion of the visible or near-infrared range of the electromagnetic spectrum, the diameter of a sphere (or collection of spheres) having the same optical properties as a snow crystal, or collection of crystals. Inversely proportional to the Specific Surface Area in the near-infrared range, and sometimes treated as an intrinsic property of snow in snowpack models.

Overburden: Refers to the column snow water equivalent overlying a particular layer within the snowpack. May be measured exactly by using a cylindrical tube of known diameter and extracting, then weighing a continuous core from the snow surface down to the layer, or may

be estimated from densities collected from a full or test snow profile.

Pore Intercept Length: A term used in stereological modeling to denote the ratio of element volume to area. The inverse of specific surface area.

Persistent Weak Layer: Sometimes abbreviated as *PWL*, describes a weak layer in the snowpack that persists for several weeks or months. These layers often go 'dormant' and become difficult to trigger for extended periods before suddenly becoming reactive dynamic loading from skiers, snowmobilers or cornices,

Propagation Saw Test (*PST*): A test of the propagation propensity of a layer in the seasonal snow pack, usually a persistent weak layer which must be identified beforehand. Formalized by Gauthier and Jamieson (2008) and studied further by a number of authors including Ross (2010). A column is 30 cm wide and either 90 cm or the depth of the weak layer, whichever is greater, is isolated. The blunt edge of a snow saw is run through the weak layer, starting from the downslope end of the column. Cutting is stopped once the fracture propagates ahead of the saw. Interpretation of the propagation propensity is based on the ratio of the cut length to the overall column length.

Radius of Curvature: Radius of a sphere that is (usually) used to approximate the shape and size of a grain of snow. Principally important due to the fact that equilibrium vapour pressure over ice increases as the radius of curvature decreases.

Rayleigh Number (critical): A dimensionless number used to describe the relative importance of convection and conduction in a fluid. The critical Rayleigh Number is the point at which convection dominates conduction.

Slab: A region of relatively stiff, supportable snow overlying a weak layer. Slab thickness, density and stiffness contribute to the propagation of failures in buried weak layers in the snowpack but may also bridge weak layers.

Scale: The physical distance over which phenomena are measured or over which natural processes act. Blöschl and Sivapalan (1995) defined a 'scale triplet' which define measurements

taken over a given scale. These include the spacing, the extent and the support. Schweizer et al. (2008) summarize the scale and scale triplets as they apply to snow avalanche studies.

Specific Surface Area: The ratio of an element's surface area to volume. Can be used as a proxy for observing structural changes in an aggregate of snow crystals. Typically the specific surface area will be large for new snow crystals with dendritic shapes, and will decrease with mechanical compaction and equilibrium metamorphism, or rounding. Inversely proportional to the optical diameter.

Temperature Gradient Metamorphism: *(see also: Equilibrium Metamorphism)*: Snow metamorphism that is driven by a gradient in temperature, resulting in a gradient in water vapour. Growth trends toward edged crystals with flat faces ('facets') and this process tends to produce a weaker, poorly-bonded snowpack.

Thermal Diffusivity: The ratio of the thermal conductivity to the product of density and specific heat capacity. In Fourier analysis of thermal conductivity the thermal diffusivity is measured directly and the thermal conductivity is derived from the measurement.

(Effective) Thermal Conductivity (k_{eff}) : The ability of a material to conduct heat. In modeling studies this is often broken down into separate terms representing the thermal conductivity due to sensible and latent heat transfer through the material. In field studies it is often impractical or impossible to distinguish between the two and thus a total effective conductivity is used. The terms *thermal conductivity*, *bulk thermal conductivity* and *effective thermal conductivity* are used interchangeably throughout this text.

Tortuosity: Defined by Kaempfer et al. (2005) as 'the square of the ratio of the effective path of diffusion through a porous medium to the length along the major diffusion axis'. The tortuosity may be used to describe how water vapour diffuses through the pore space within the snowpack. Samples with high values of tortuosity will tend toward lower values (and thus more direct thermal pathways) under an induced thermal temperature gradient.

Appendix C

Thermal Conductivity and Layer Characteristics

Table C.1: Layer characteristics for 2008-09 crusts. Labels and units: Temperature (T,[°C]); Grain Type (F); Layer Resistance (R); Density (ρ,[kg m^{-3}]); Layer Moisture (θ).

Crust	**Date**	**T**	**F**	**R**	ρ	θ
SR0127	09/02/02	-7.5	MFcr	K-	282	D
SR0127	09/02/10	-5.3	MFcr	K-	276	D
SR0127	09/02/21	-4.6	MFcr	K-	290	D
SR0127	09/03/05	-1.3	MFcr	K	280	D
SR0127	09/03/12	-3.5	MFcr	K	266	D
SR0127	09/03/21	-2.6	MFcr*	K*	300	D
SR0127	09/03/27	-1.0	MFcr*	P+*	318	D
SR0127	09/04/06	-0.3	MFpc	1F+	335	M
SR0127	09/04/11	0.0	MFpc*	P-*	313	M
SR0222	09/02/24	-2.5	Mfcr	K	290	D
SR0222	09/03/05	-1.8	Mfcr	K	331	D
SR0222	09/03/12	-5.3	Mfcr	K	290	D
SR0222	09/03/21	-3.0	Mfcr	K-	290	D
SR0222	09/03/27	-0.9	Mfcr	K-	311	D
SR0222	09/04/06	0.1	Mfcr*	P+*	306	M
*X: Not recorded. *: Variable*						

Table C.1 – continued from previous page

Crust	**Date**	**T**	**F**	**R**	ρ	θ
SR0222	09/04/11	0.1	Mfpc	1F-	346	M
SR0301	09/03/05	X	Mfcr	K-	281	D
SR0301	09/03/12	-4.9	Mfcr	K	262	D
SR0301	09/03/21	-2.8	Mfcr	K	280	D
SR0301	09/03/27	-0.7	Mfcr	K-*	289	D
SR0301	09/04/06	0.2	Mfcr	1F+	354	M
SR0301	09/04/11	0.2	Mfpc	1F-	373	M

Table C.2: Thermal conductivity and layer characteristics for 2009-10 crusts. Labels and units: Thermal conductivity (λ,[$Wm^{-1}k^{-1}$]); Temperature (T,[°C]); Grain Type (F); Layer Resistance (R); Density (ρ,[kg m^{-3}]); Layer Moisture (θ).

Crust	**L**	**Date**	λ	**T**	**F**	**R**	ρ	θ
BV0112	A	10/01/31	0.08	-2.6	RGxf	F+	164	M
BV0112	A	10/02/07	0.084	-4.0	FCxr	F+	122	D
BV0112	A	10/02/15	0.082	-0.2	RGsr	4F	221	D
BV0112	A	10/02/15	0.042	-0.2	RGsr	4F	221	D
BV0112	A	10/03/01	BAD	-0.4	MFpc	1F	254	M
BV0112	A	10/03/01	BAD	-0.4	MFpc	1F	254	M
BV0112	A	10/03/08	0.095	-2.0	FCxr	1F-	271	M
BV0112	A	10/03/08	0.724	-2.0	FCxr	1F-	271	M
*X: Not recorded. *: Variable*								

Table C.2 – continued from previous page

Crust	**L**	**Date**	λ	**T**	**F**	**R**	ρ	θ
BV0112	A	10/03/14	BAD	-2.7	FCso	1F-	229	M
BV0112	A	10/03/14	0.077	-2.7	FCso	1F-	229	M
BV0112	A	10/03/23	BAD	0.0	MFcr	P+	392	M
BV0112	A	10/03/23	0.056	0.0	MFcr	P+	392	M
BV0112	B	10/01/31	0.100	-3.1	FCxr	4F	257	M
BV0112	B	10/01/31	0.145	-3.1	FCxr	4F	257	M
BV0112	B	10/01/31	0.104	-3.1	FCxr	4F	257	M
BV0112	B	10/02/07	BAD	-3.5	Fcso	1F	249	D
BV0112	B	10/02/15	BAD	-0.4	MFpc	4F+	278	D
BV0112	B	10/02/15	0.058	-0.4	MFpc	4F+	278	D
BV0112	B	10/03/01	0.052	-0.6	MFCL	P-	311	M
BV0112	B	10/03/01	BAD	-0.6	MFCL	P-	311	M
BV0112	B	10/03/08	0.319	-3.0	FCxr	1F+	278	M
BV0112	B	10/03/08	0.189	-3.0	FCxr	1F+	278	M
BV0112	B	10/03/14	0.254	-1.4	FCxr	4F+	277	M
BV0112	B	10/03/14	BAD	-1.4	FCxr	4F+	277	M
BV0112	B	10/03/23	BAD	-0.1	MFpc	4F+	343	M
BV0112	B	10/03/23	BAD	-0.1	MFpc	4F+	343	M
BV0112	I	10/01/31	0.150	-2.9	MFcr	P+	321	D
BV0112	I	10/01/31	0.193	-2.9	MFcr	P+	321	D
BV0112	I	10/02/07	BAD	-3.9	MFcr	P-	306	D
BV0112	I	10/02/15	0.209	-0.3	MFpc	1F	335	D

*X: Not recorded. *: Variable*

Table C.2 – continued from previous page

Crust	**L**	**Date**	λ	**T**	**F**	**R**	ρ	θ
BV0112	I	10/02/15	0.079	-0.3	MFpc	1F	335	D
BV0112	I	10/03/01	BAD	-0.7	MFcl	P-*	298	M
BV0112	I	10/03/01	BAD	-0.7	MFcl	P-*	298	M
BV0112	I	10/03/08	0.062	-2.6	MF	P	272	D
BV0112	I	10/03/08	0.135	-2.6	MF	P	272	D
BV0112	I	10/03/14	BAD	-2.2	MFpc	P-*	223	M
BV0112	I	10/03/14	BAD	-2.2	MFpc	P-*	223	M
BV0112	I	10/03/14	0.206	-2.2	MFpc	P-*	223	M
BV0112	I	10/03/14	0.317	-2.2	MFpc	P-*	223	M
BV0112	I	10/03/23	BAD	0.0	MFcr	4F	367	M
BV0112	I	10/03/23	BAD	0.0	MFcr	4F	367	M
BV0112	V	10/03/08	5.136	0.0	X			D
BV0112	V	10/03/14	0.279	0.0	X			M
BV0112	V	10/03/23	BAD	0.0	X	X		M
FI0110	A	10/01/10	0.108	-4.1	PPrm	F	97	D
FI0110	A	10/01/10	BAD	-4.1	PPrm	F	97	D
FI0110	A	12/01/10	0.118	-3.0	MF	4F+	136	M
FI0110	A	18/01/10	0.139	-3.6	FCxr	1F	226	D
FI0110	A	18/01/10	0.147	-3.6	FCxr	1F	226	D
FI0110	A	25/01/10	0.140	-4.7	RGsr	P-	244	D
FI0110	A	25/01/10	0.160	-4.7	RGsr	P-	244	D
FI0110	A	25/01/10	0.175	-4.7	RGsr	P-	244	D

*X: Not recorded. *: Variable*

Table C.2 – continued from previous page

Crust	**L**	**Date**	λ	**T**	**F**	**R**	ρ	θ
FI0110	A	02/02/10	0.161	-4.1	FCxr	1F+	236	D
FI0110	A	02/02/10	0.156	-4.1	FCxr	1F+	236	D
FI0110	A	02/02/10	0.201	-4.1	FCxr	1F+	236	D
FI0110	A	08/02/10	0.179	-3.9	FCxr	1F+	284	D
FI0110	A	08/02/10	0.205	-3.9	FCxr	1F+	284	D
FI0110	A	17/02/10	0.176	-3.0	FCxr	P-	287	D
FI0110	A	17/02/10	0.213	-3.0	FCxr	P-	287	D
FI0110	A	28/02/10	0.208	-3.2	FCxr	P+	347	D
FI0110	A	28/02/10	0.201	-3.2	FCxr	P+	347	D
FI0110	A	09/03/10	0.192	-2.3	RGlr	P	345	D
FI0110	A	09/03/10	0.292	-2.3	RGlr	P	345	D
FI0110	A	15/03/10	0.212	-2.4	RGsr	P-	346	M
FI0110	A	15/03/10	0.236	-2.4	RGsr	P-	346	M
FI0110	A	10/03/22	0.222	-2.0	FCxr	P+	341	D
FI0110	A	10/03/22	0.261	-2.0	FCxr	P+	341	D
FI0110	A	10/03/28	BAD	-1.6	RGsr	P+	372	M
FI0110	A	10/03/28	0.356	-1.6	RGsr	P+	372	M
FI0110	A	10/04/07	0.354	-1.6	FCxr	P+	378	D
FI0110	A	10/04/14	0.320	-1.6	FCxr	K-	397	D
FI0110	A	10/04/14	BAD	-1.6	FCxr	K-	397	D
FI0110	B	10/01/10	0.046	-4.6	PP	F+	112	D
FI0110	B	10/01/10	0.040	-4.6	PP	F+	112	D

*X: Not recorded. *: Variable*

Table C.2 – continued from previous page

Crust	**L**	**Date**	λ	**T**	**F**	**R**	ρ	θ
FI0110	B	12/01/10	0.089	-2.9	FCxr	4F-	139	D
FI0110	B	12/01/10	0.096	-2.9	FCxr	4F-	139	D
FI0110	B	18/01/10	0.157	-3.6	FCxr	1F	223	D
FI0110	B	18/01/10	0.104	-3.6	FCxr	1F	223	D
FI0110	B	25/01/10	0.131	-4.8	FCxr	1F	248	D
FI0110	B	25/01/10	0.129	-4.8	FCxr	1F	248	D
FI0110	B	02/02/10	0.168	-4.2	FCxr	P-	269	D
FI0110	B	02/02/10	0.162	-4.2	FCxr	P-	269	D
FI0110	B	02/02/10	0.161	-4.2	FCxr	P-	269	D
FI0110	B	02/02/10	0.134	-4.2	FCxr	P-	269	D
FI0110	B	08/02/10	0.166	-3.9	FCxr	1F-	297	D
FI0110	B	08/02/10	0.170	-3.9	FCxr	1F-	297	D
FI0110	B	17/02/10	0.148	-3.1	RGsr	P	323	D
FI0110	B	17/02/10	0.215	-3.1	RGsr	P	323	D
FI0110	B	28/02/10	0.200	-3.3	FCxr	P+	364	D
FI0110	B	28/02/10	BAD	-3.3	FCxr	P+	364	D
FI0110	B	09/03/10	0.275	-2.3	FCxr	P+	375	D
FI0110	B	09/03/10	0.206	-2.3	FCxr	P+	375	D
FI0110	B	15/03/10	0.216	-2.5	RGsr	P	382	M
FI0110	B	15/03/10	0.221	-2.5	RGsr	P	382	M
FI0110	B	10/03/22	0.296	-2.0	FCxr	K-	356	D
FI0110	B	10/03/28	0.553	-1.6	RGsr	P+	393	M

*X: Not recorded. *: Variable*

Table C.2 – continued from previous page

Crust	**L**	**Date**	λ	**T**	**F**	**R**	ρ	θ
FI0110	B	10/03/28	0.489	-1.6	RGsr	P+	393	M
FI0110	B	10/04/07	0.428	-1.2	FCxr	K-	406	D
FI0110	B	10/04/14	0.467	-1.1	FCxr	K-	430	D
FI0110	B	10/04/14	0.275	-1.1	FCxr	K-	430	D
FI0110	I	08/02/10	0.188	-3.9	MFpc	1F+	X	D
FI0110	I	17/02/10	0.219	-3.1	MFpc	P	X	D
FI0110	I	28/02/10	0.175	-3.3	IFrc	P	X	D
FI0110	I	28/02/10	0.209	-3.3	IFrc	P	X	D
FI0110	I	09/03/10	0.265	-2.3	IFil	K-	X	D
FI0110	I	09/03/10	BAD	-2.3	IFil	K-	X	D
FI0110	I	15/03/10	0.221	-2.5	IFrc	M	X	M
FI0110	I	15/03/10	0.282	-2.5	IFrc	M	X	M
FI0110	I	10/03/22	0.279	-2.0	IFrc	K-	X	D
FI0110	I	10/03/22	0.258	-2.0	IFrc	K-	X	D
FI0110	I	10/03/28	BAD	-1.6	IFil	P+	X	M
FI0110	I	10/03/28	0.843	-1.6	IFil	P+	X	M
FI0110	I	10/04/07	0.220	-1.2	IFrc	P+	X	D
FI0110	I	10/04/14	BAD	-1.1	IFrc	K-	X	D
FI0110	I	10/04/14	0.421	-1.1	IFrc	K-	X	D
FI0308	A	10/03/15	0.106	-3.7	Mfpc	4F	185	M
FI0308	A	10/03/15	0.074	-3.7	Mfpc	4F	185	M
FI0308	A	10/03/22	0.115	-2.9	DFdc	1F	166	M

*X: Not recorded. *: Variable*

Table C.2 – continued from previous page

Crust	**L**	**Date**	λ	**T**	**F**	**R**	ρ	θ
FI0308	A	10/03/22	0.122	-2.9	DFdc	1F	166	M
FI0308	A	10/03/28	0.130	-1.8	MFcl	1F+	264	M
FI0308	A	10/03/28	0.166	-1.8	MFcl	1F+	264	M
FI0308	A	10/04/07	0.203	-2.5	RGsr	P	285	D
FI0308	A	10/04/14	0.262	-2.3	RGsr	P+	310	D
FI0308	A	10/04/14	0.290	-2.3	RGsr	P+	310	D
FI0308	B	10/03/15	0.088	-3.7	FCxr	4F+	228	M
FI0308	B	10/03/15	0.098	-3.7	FCxr	4F+	228	M
FI0308	B	10/03/22	0.143	-2.9	RGlr	P-	252	D
FI0308	B	10/03/22	0.163	-2.9	RGlr	P-	252	D
FI0308	B	10/03/28	0.158	-1.8	RGsr	1F	265	M
FI0308	B	10/03/28	BAD	-1.8	RGsr	1F	265	M
FI0308	B	10/04/07	0.243	-2.3	RGsr	P-	309	D
FI0308	B	10/04/14	0.301	-2.1	FCxr	P+	332	D
FI0308	B	10/04/14	0.256	-2.1	FCxr	P+	332	D
FI0308	I	10/03/15	0.055	-3.8	MFcr	P	X	M
FI0308	I	10/03/15	0.239	-3.8	MFcr	P	X	M
FI0308	I	10/03/22	0.183	-2.9	MFcr	P+	X	D
FI0308	I	10/03/22	0.204	-2.9	MFcr	P+	X	D
FI0308	I	10/03/28	0.186	-1.8	MFcr	1F	288	M
FI0308	I	10/03/28	2.103	-1.8	MFcr	1F	288	M
FI0308	I	10/04/07	0.178	-2.4	MFcr	P-	X	D

*X: Not recorded. *: Variable*

Table C.2 – continued from previous page

Crust	**L**	**Date**	λ	**T**	**F**	**R**	ρ	θ
FI0308	I	10/04/14	0.133	-2.3	MFcr	K	X	D
FI0308	I	10/04/14	0.218	-2.3	MFcr	K	X	D
FI0308	V	10/03/15	0.102	-3.8	MFcr	P	X	M
FI0308	V	10/03/22	0.170	-2.9	MFcr	P+	X	D
FI0308	V	10/03/28	0.290	-1.8	MFcr	1F	288	M
FI0308	V	10/03/28	0.173	-1.8	MFcr	1F	288	M
FI0308	V	10/04/07	0.180	-2.4	MFcr	P-	X	D
FI0308	V	10/04/14	0.233	-2.3	MFcr	K	X	D
FI0308	V	10/04/14	0.540	-2.3	MFcr	K	X	D
RP0112	A	10/01/19	0.100	-2.7	DFdc	4F	162	D
RP0112	A	10/01/25	0.137	-5.8	FCxr	4F	207	D
RP0112	A	10/02/02	0.144	-2.7	RGlr	1F-	260	D
RP0112	A	10/02/02	0.123	-2.7	RGlr	1F-	260	D
RP0112	A	10/02/09	0.129	-3.7	FCxr	1F-	277	D
RP0112	A	10/02/09	0.112	-3.7	FCxr	1F-	277	D
RP0112	A	10/02/15	0.118	-2.8	FCxr	1F+	273	D
RP0112	A	10/02/15	0.169	-2.8	FCxr	1F+	273	D
RP0112	A	10/02/27	0.199	-2.2	FCxr	1F+	277	M
RP0112	A	10/02/27	0.172	-2.2	FCxr	1F+	277	M
RP0112	A	10/03/08	0.164	-3.9	FCxr	1F+	300	D
RP0112	A	10/03/08	0.195	-3.9	FCxr	1F+	300	D
RP0112	A	10/03/14	0.193	-2.3	FCxr	1F+	327	M

*X: Not recorded. *: Variable*

Table C.2 – continued from previous page

Crust	**L**	**Date**	λ	**T**	**F**	**R**	ρ	θ
RP0112	A	10/03/14	0.174	-2.3	FCxr	1F+	327	M
RP0112	A	10/03/23	0.330	0.0	MFcr	P+	392	M
RP0112	A	10/03/23	0.203	0.0	MFcr	P+	392	M
RP0112	A	10/03/29	1.107	-0.3	FCxr	1F	317	M
RP0112	A	10/03/29	2.411	-0.3	FCxr	1F	317	M
RP0112	A	10/03/29	BAD	-0.3	FCxr	1F	317	M
RP0112	A	10/03/29	BAD	-0.3	FCxr	1F	317	M
RP0112	A	10/03/29	BAD	-0.3	FCxr	1F	317	M
RP0112	A	10/04/06	BAD	-0.3	FCxr	P-	314	M
RP0112	A	10/04/06	BAD	-0.3	FCxr	P-	314	M
RP0112	A	10/04/13	0.267	-0.4	FCxr	1F+	332	M
RP0112	B	10/01/19	0.110	-1.6	FCxr	1F	X	D
RP0112	B	10/01/25	0.154	-3.5	FCxr	P-	260	D
RP0112	B	10/02/02	0.160	-2.5	FCxr	P-	301	D
RP0112	B	10/02/02	0.158	-2.5	FCxr	P-	301	D
RP0112	B	10/02/09	0.140	-3.0	FCxr	1F	306	D
RP0112	B	10/02/09	0.125	-3.0	FCxr	1F	306	D
RP0112	B	10/02/27	0.194	-2.2	FCxr	P+	383	M
RP0112	B	10/02/27	0.196	-2.2	FCxr	P+	383	M
RP0112	B	10/03/08	0.269	-3.1	FCxr	P	354	D
RP0112	B	10/03/08	0.228	-3.1	FCxr	P	354	D
RP0112	B	10/03/08	0.173	-3.1	FCxr	P	354	D

*X: Not recorded. *: Variable*

Table C.2 – continued from previous page

Crust	**L**	**Date**	λ	**T**	**F**	**R**	ρ	θ
RP0112	B	10/03/08	0.147	-3.1	FCxr	P	354	D
RP0112	B	10/03/14	0.192	-2.1	FCXR	P	371	M
RP0112	B	10/03/14	0.196	-2.1	FCXR	P	371	M
RP0112	B	10/03/23	0.359	-0.1	MFpc	4F+	343	M
RP0112	B	10/03/23	0.408	-0.1	MFpc	4F+	343	M
RP0112	B	10/03/29	BAD	-0.3	FC	P+	396	M
RP0112	B	10/03/29	BAD	-0.3	FC	P+	396	M
RP0112	B	10/03/29	BAD	-0.3	FC	P+	396	M
RP0112	B	10/04/06	BAD	-0.3	FCso	P+	389	M
RP0112	B	10/04/06	BAD	-0.3	FCso	P+	389	M
RP0112	B	10/04/13	BAD	-0.3	FCxr	P+	407	M
RP0112	I	10/01/19	0.087	-2.0	MFcr*	P*	190	D
RP0112	I	10/01/19	0.064	-2.0	MFcr*	P*	190	D
RP0112	I	10/01/19	0.154	-2.0	MFcr*	P*	190	D
RP0112	I	10/01/19	0.236	-2.0	MFcr*	P*	190	D
RP0112	I	10/01/25	0.106	-4.8	MFcr*	P*	220	D
RP0112	I	10/01/25	0.156	-4.8	MFcr*	P*	220	D
RP0112	I	10/02/02	0.124	-2.3	MFcr*	P*	222	D
RP0112	I	10/02/02	0.135	-2.3	MFcr*	P*	222	D
RP0112	I	10/02/09	0.098	-3.3	MFpc	1F+*	229	D
RP0112	I	10/02/09	0.124	-3.3	MFpc	1F+*	229	D
RP0112	I	10/02/09	0.058	-3.3	MFpc	1F+*	229	D

*X: Not recorded. *: Variable*

Table C.2 – continued from previous page

Crust	**L**	**Date**	λ	**T**	**F**	**R**	ρ	θ
RP0112	I	10/02/15	0.220	-2.8	MFpc	P+	316	D
RP0112	I	10/02/15	0.239	-2.8	MFpc	P+	316	D
RP0112	I	10/02/27	0.180	-2.3	MFcr*	P+*	313	M
RP0112	I	10/02/27	0.076	-2.3	MFcr*	P+*	313	M
RP0112	I	10/03/08	0.109	-3.5	MFcr	P*	331	D
RP0112	I	10/03/08	0.142	-3.5	MFcr	P*	331	D
RP0112	I	10/03/14	0.179	-2.2	FCxr	4F+	332	M
RP0112	I	10/03/14	0.139	-2.2	FCxr	4F+	332	M
RP0112	I	10/03/23	BAD	-0.1	MFcr	4F	367	M
RP0112	I	10/03/23	0.079	-0.1	MFcr	4F	367	M
RP0112	I	10/03/29	BAD	-0.3	MFpc*	1F	343	M
RP0112	I	10/03/29	BAD	-0.3	MFpc*	1F	343	M
RP0112	I	10/04/06	BAD	-0.3	FC	1F+	344	M
RP0112	I	10/04/06	BAD	-0.3	FC	1F+	344	M
RP0112	I	10/04/13	BAD	-0.4	MFpc	1F-	318	M
RP0112	V	10/03/08	0.124	-3.5	MFcr	P+*	331	D
RP0112	V	10/03/08	0.117	-3.5	MFcr	P+*	331	D
RP0112	V	10/03/14	0.180	-2.2	FCxr	4F+	332	M
RP0112	V	10/03/14	0.213	-2.2	FCxr	4F+	332	M
RP0112	V	10/03/23	BAD	-0.1	MFcr	4F	367	M
RP0112	V	10/03/23	0.204	-0.1	MFcr	4F	367	M
RP0112	V	10/03/29	BAD	-0.3	MFpc*	1F	343	M
*X: Not recorded. *: Variable*								

Table C.2 – continued from previous page

Crust	**L**	**Date**	λ	**T**	**F**	**R**	ρ	θ
RP0112	V	10/04/06	BAD	-0.3	FC	1F+	344	M
RP0112	V	10/04/06	BAD	-0.3	FC	1F+	344	M
RP0112	V	10/04/13	BAD	-0.4	MFpc	1F-	318	M
LAB0312	I	13 12:00	BAD	0.0	X	X	X	W
LAB0312	I	13 12:37	0.089	-0.5	I	K	M	W
LAB0312	I	13 12:51	0.141	-0.5	I	K	M	W
LAB0312	I	13 13:26	0.648	-2.9	I	K	M	W
LAB0312	I	13 14:05	0.276	-0.5	I	K	M	M
LAB0312	I	13 15:10	0.142	0.0	I	K	M	D
LAB0330	A	30 09:30	BAD	-0.2	MFpc	K	X	M
LAB0330	B	30 09:30	BAD	-0.2	MFpc	K	X	M
LAB0330	I	30 09:30	BAD	-0.2	MFpc	K	X	M
LAB0330	I	30 09:30	BAD	-0.2	MFpc	K	X	M
LAB0330	V	30 09:30	0.094	-0.2	MFpc	K	X	M
LAB0330	V	30 10:30	0.034	-0.2	MFpc	K	X	M
LAB0330	V	30 10:30	0.065	-0.2	MFpc	K	X	M
LAB0330	V	30 12:20	0.285	-0.5	MFpc	K	X	M
LAB0330	V	30 12:20	BAD	-0.5	MFpc	K	X	M
LAB0330	V	30 14:12	0.249	-0.6	MFpc	X	X	M
LAB0330	V	30 14:12	BAD	-0.6	MFpc	X	X	M
LAB0330	V	30 16:55	0.122	-0.6	MFpc	K	X	M
LAB0330	V	30 16:55	0.193	-0.6	MFpc	K	X	M

*X: Not recorded. *: Variable*

Table C.2 – continued from previous page

Crust	**L**	**Date**	λ	**T**	**F**	**R**	ρ	θ
LAB0330	V	30 21:50	0.236	-1.5	MFpc	K	X	D
LAB0330	V	30 21:50	0.250	-1.5	MFpc	K	X	D
LAB0330	V	31 07:25	0.000	0.0	MFpc	K	X	D
LAB0330	V	31 07:25	0.000	0.0	MFpc	K	X	D
LAB0409	V	09 13:00	BAD	-0.2	MFpc	X	X	M
LAB0409	V	09 13:00	0.072	-0.2	MFpc	X	X	M
LAB0409	V	09 19:35	BAD	-0.2	MFpc	X	X	M
LAB0409	V	09 19:35	0.690	-0.2	MFpc	X	X	M
LAB0409	V	10 01:15	0.136	-1.5	MFpc	X	X	D
LAB0409	V	10 01:15	0.252	-1.5	MFpc	X	X	D
LAB0409	V	10 08:20	0.130	-7.8	MFpc	X	X	D
LAB0409	V	10 08:20	0.286	-7.8	MFpc	X	X	D
LAB0409	V	10 14:30	0.270	-13.0	MFpc	X	X	D
LAB0410	V	10 19:15	0.058	-0.1	MFpc	X	X	M
LAB0410	V	10 19:15	0.025	-0.1	MFpc	X	X	M
LAB0410	V	11 09:30	0.081	-7.0	MFpc	X	X	D
LAB0410	V	11 09:30	0.178	-7.0	MFpc	X	X	D
LAB0410	V	11 21:00	0.277	-12.5	MFpc	X	X	D
LAB0410	V	11 21:00	0.302	-12.5	MFpc	X	X	D
LAB0410	V	12 09:40	BAD	-14.4	MFpc	X	X	D
LAB0410	V	12 09:40	0.269	-14.4	MFpc	X	X	D
LAB0410	V	12 21:05	0.225	-14.9	MFpc	X	X	D

*X: Not recorded. *: Variable*

Table C.2 – continued from previous page

Crust	**L**	**Date**	λ	**T**	**F**	**R**	ρ	θ
LAB0410	V	12 21:05	0.246	-14.9	MFpc	X	X	D
LAB0410	V	13 09:35	0.273	-14.1	MFpc	X	X	D
LAB0410	V	13 09:35	0.409	-14.1	MFpc	X	X	D
LAB0413	V	10/04/13	0.080	-1.5	MFpc	1f+	400	M
LAB0413	V	10/04/13	BAD	-1.5	MFpc	1f+	400	M
LAB0413	V	10/04/14	BAD	-2.6	MFpc	K	X	D
LAB0413	V	10/04/14	0.293	-2.6	MFpc	K	X	D
LAB0413	V	10/04/15	0.414	-6.0	MFpc	K	X	D
LAB0413	V	10/04/15	0.330	-6.0	MFpc	K	X	D
LAB0413	V	10/04/16	0.253	-8.4	MFpc	K	X	D
LAB0413	V	10/04/16	0.302	-8.4	MFpc	K	X	D
LAB0413	V	10/04/17	0.144	-8.7	MFpc	K	X	D
LAB0413	V	10/04/17	0.248	-8.7	MFpc	K	X	D
LAB0413	V	10/04/18	0.136	-8.6	MFpc	K	X	D
LAB0413	V	10/04/18	0.241	-8.6	MFpc	K	X	D
SR0131	A	10/02/03	0.080	-3.5	PP	F	63	D
SR0131	A	10/02/03	0.065	-3.5	PP	F	63	D
SR0131	A	10/02/10	0.044	-4.5	FCxr	4F	251	D
SR0131	A	10/02/10	0.096	-4.5	FCxr	4F	251	D
SR0131	A	10/02/17	0.099	-2.4	FCxr	F	191	D
SR0131	A	10/02/17	0.096	-2.4	FCxr	F	191	D
SR0131	A	10/03/02	BAD	0.0	X	X	X	X

*X: Not recorded. *: Variable*

Table C.2 – continued from previous page

Crust	**L**	**Date**	λ	**T**	**F**	**R**	ρ	θ
SR0131	A	10/03/02	BAD	0.0	X	X	X	X
SR0131	A	10/03/09	BAD	0.0	X	X	X	X
SR0131	A	10/03/09	BAD	0.0	X	X	X	X
SR0131	A	10/03/22	BAD	0.0	X	X	X	X
SR0131	A	10/03/22	BAD	-0.2	MFpc	P-	318	M
SR0131	A	10/03/28	BAD	0.0	X	X	X	M
SR0131	A	10/04/07	BAD	0.0	X	X	X	M
SR0131	B	10/02/03	0.149	-3.8	FCxr	1F	168	D
SR0131	B	10/02/03	0.142	-3.8	FCxr	1F	168	D
SR0131	B	10/02/10	0.073	-4.0	FCxr	4F+	240	D
SR0131	B	10/02/10	0.080	-4.0	FCxr	4F+	240	D
SR0131	B	10/02/17	0.165	-2.3	FCXR	4F+	272	D
SR0131	B	10/02/17	0.131	-2.3	FCXR	4F+	272	D
SR0131	B	10/03/02	3.640	0.0	FCxr	P-	295	M
SR0131	B	10/03/02	1.727	0.0	FCxr	P-	295	M
SR0131	B	10/03/09	BAD	0.0	X	X	X	W
SR0131	B	10/03/09	BAD	0.0	X	X	X	W
SR0131	B	10/03/22	BAD	0.0	X	X	X	W
SR0131	B	10/03/22	BAD	0.0	X	X	X	W
SR0131	B	10/03/28	BAD	0.0	X	X	X	M
SR0131	B	10/04/07	BAD	0.0	X	X	X	W
SR0131	I	10/02/03	0.714	-3.4	MFcr	K-	238	D

*X: Not recorded. *: Variable*

Table C.2 – continued from previous page

Crust	**L**	**Date**	λ	**T**	**F**	**R**	ρ	θ
SR0131	I	10/02/03	0.148	-3.4	MFcr	K-	238	D
SR0131	I	10/02/10	0.311	-4.3	MFcr	K-	X	D
SR0131	I	10/02/10	0.109	-4.3	MFcr	K-	X	D
SR0131	I	10/02/17	0.158	-2.3	MFcr	K-	278	D
SR0131	I	10/02/17	0.175	-2.3	MFcr	K-	278	D
SR0131	I	10/03/02	BAD	0.0	X	X	X	M
SR0131	I	10/03/09	BAD	0.0	X	X	X	M
SR0131	I	10/03/09	BAD	0.0	X	X	X	M
SR0131	I	10/03/22	BAD	0.0	X	X	X	M
SR0131	I	10/03/22	BAD	0.0	X	X	X	M
SR0131	I	10/03/28	BAD	0.0	X	X	X	M
SR0131	I	10/03/28	0.134	-0.2	MFpc	F+	400	M
SR0131	I	10/03/28	0.055	-0.2	MFpc	F+	400	M
SR0131	I	10/04/07	BAD	0.0	X	X	X	M
SR0210	A	10/02/10	0.000	-4.5	PP	F-	60	D
SR0210	A	10/02/17	0.092	-2.6	DFdc	F-	126	D
SR0210	A	10/02/17	0.091	-2.6	DFdc	F-	126	D
SR0210	A	10/03/02	BAD	0.0	MFpc*	4F-	245	M
SR0210	A	10/03/02	0.082	0.0	MFpc*	4F-	245	M
SR0210	A	10/03/09	0.022	0.0	DFdc	F-	126	D
SR0210	A	10/03/09	BAD	0.0	X	X	X	M
SR0210	A	10/03/22	BAD	0.0	X	X	X	M

*X: Not recorded. *: Variable*

Table C.2 – continued from previous page

Crust	**L**	**Date**	λ	**T**	**F**	**R**	ρ	θ
SR0210	A	10/03/22	BAD	0.0	X	X	X	M
SR0210	A	10/03/28	BAD	0.0	X	X	X	M
SR0210	A	10/04/07	BAD	0.0	X	X	X	M
SR0210	B	10/02/10	0.044	-4.5	FCxr	1F+	179	D
SR0210	B	10/02/10	0.096	-4.5	FCxr	1F+	179	D
SR0210	B	10/02/17	0.099	-2.3	FCxr	F-	191	D
SR0210	B	10/02/17	0.096	-2.3	FCxr	F-	191	D
SR0210	B	10/03/02	BAD	0.0	MFpc*	4F+	X	M
SR0210	B	10/03/02	BAD	0.0	MFpc*	4F+	X	M
SR0210	B	10/03/09	BAD	0.0	X	X	X	M
SR0210	B	10/03/09	BAD	0.0	X	X	X	M
SR0210	B	10/03/22	BAD	0.0	X	X	X	M
SR0210	B	10/03/22	BAD	-0.1	MFpc	4F	300	M
SR0210	B	10/03/28	BAD	0.0	X	X	X	M
SR0210	B	10/04/07	BAD	-0.2	MfPc*	1F+	383	M
SR0210	I	10/02/10	0.225	-4.0	MFcr	P+	X	D
SR0210	I	10/02/10	0.209	-4.0	MFcr	P+	X	D
SR0210	I	10/02/17	0.134	-2.4	Mfcr	K	251	D
SR0210	I	10/02/17	0.098	-2.4	Mfcr	K	251	D
SR0210	I	10/03/02	BAD	0.0	MFcr	K	X	M
SR0210	I	10/03/09	BAD	0.0	X	X	X	M
SR0210	I	10/03/09	0.028	-1.5	MFcr	P-	298	M

*X: Not recorded. *: Variable*

Table C.2 – continued from previous page

Crust	**L**	**Date**	λ	**T**	**F**	**R**	ρ	θ
SR0210	I	10/03/28	BAD	0.0	X	X	X	M
SR0210	I	10/03/28	0.134	-0.2	MFpc	F+	400	M
SR0210	I	10/03/28	0.055	-0.2	MFpc	F+	400	M
SR0210	I	10/04/07	BAD	-0.2	MFcr	P+	323	D
SR09	I	10/02/05	0.081	X	X	X	X	D
SR09	I	10/02/05	0.087	X	X	X	X	D
SR09	I	10/02/05	0.115	X	X	X	X	D
SR09	I	10/02/05	0.093	X	X	X	X	D
SR09	I	10/02/05	0.084	X	X	X	X	D
SR09	I	10/02/05	0.114	X	X	X	X	D
SR09	I	10/02/05	0.111	X	X	X	X	D
SR09	I	10/02/05	0.092	X	X	X	X	D
SR09	I	10/02/05	0.113	X	X	X	X	D
SR09	I	10/02/05	0.085	X	X	X	X	D
SR09	I	10/02/05	0.165	X	X	X	X	D

Table C.3: All thermal conductivity measurements. Labels and Units: Sample Location (A = Above; B = Below; I = Crust Interior; V = Vertical through crust); Thermal Conductivity (λ, [W m^{-1} k^{-1}]); Goodness of linear fit to rate of warming versus heating power (R^2); Average heating power during measurement (P,[W m^{-1}]); Duration of heating period used for calculation (Δt [s]); Temperature rise during measurement (ΔT [°C])

Crust	**L**	**Date**	λ	R^2	**Δt**	**P**	**ΔT**
BV0112	A	10/01/31	0.078	0.995	35.4	0.383	1.4
BV0112	A	10/02/07	0.084	0.989	23.3	0.475	1.8
BV0112	A	10/02/15	0.082	0.998	47.5	0.447	1.5
BV0112	A	10/02/15	0.042	0.997	47.5	0.443	0.9
BV0112	A	10/03/01	BAD	X	X	0.455	0.0
BV0112	A	10/03/01	BAD	X	X	0.449	0.0
BV0112	A	10/03/08	0.095	0.993	35.4	0.445	1.3
BV0112	A	10/03/08	0.724	0.830	40.6	0.444	1.0
BV0112	A	10/03/14	BAD	X	X	0.419	0.0
BV0112	A	10/03/14	0.077	0.988	23.3	0.423	1.7
BV0112	A	10/03/23	BAD	X	X	0.563	0.0
BV0112	A	10/03/23	0.056	0.994	21.1	0.591	2.2
BV0112	B	10/01/31	0.100	0.981	20.9	0.372	1.8
BV0112	B	10/01/31	0.145	0.976	26.6	0.369	1.5
BV0112	B	10/01/31	0.104	0.985	24.5	0.366	1.6

*X: Not recorded. *: Variable*

Table C.3 – continued from previous page

Crust	**L**	**Date**	λ	R^2	**Δt**	**P**	**ΔT**
BV0112	B	10/02/07	BAD	X	X	0.000	0.0
BV0112	B	10/02/15	BAD	X	X	0.435	0.0
BV0112	B	10/02/15	0.058	0.987	45.3	0.432	1.0
BV0112	B	10/03/01	0.052	0.990	24.8	0.435	0.3
BV0112	B	10/03/01	BAD	X	X	0.423	0.0
BV0112	B	10/03/08	0.319	0.956	35.4	0.443	0.7
BV0112	B	10/03/08	0.189	0.962	23.3	0.439	1.3
BV0112	B	10/03/14	0.254	0.964	35.4	0.416	0.3
BV0112	B	10/03/14	BAD	X	X	0.413	0.0
BV0112	B	10/03/23	BAD	X	X	0.552	0.0
BV0112	B	10/03/23	BAD	X	X	0.544	0.0
BV0112	I	10/01/31	0.150	0.959	23.3	0.378	1.5
BV0112	I	10/01/31	0.193	0.958	29.7	0.375	1.2
BV0112	I	10/02/07	BAD	X	X	0.000	0.0
BV0112	I	10/02/15	0.209	0.964	29.7	0.439	0.9
BV0112	I	10/02/15	0.079	0.961	13.2	0.436	2.1
BV0112	I	10/03/01	BAD	X	X	0.440	0.0
BV0112	I	10/03/01	BAD	X	X	0.439	0.0
BV0112	I	10/03/08	0.062	0.995	47.5	0.442	1.8
BV0112	I	10/03/08	0.135	0.892	12.9	0.439	1.9
BV0112	I	10/03/14	BAD	X	X	0.422	0.0
BV0112	I	10/03/14	BAD	X	X	0.418	0.0

*X: Not recorded. *: Variable*

Table C.3 – continued from previous page

Crust	**L**	**Date**	λ	R^2	**Δt**	**P**	**ΔT**
BV0112	I	10/03/14	0.206	0.973	35.4	0.415	0.3
BV0112	I	10/03/14	0.317	0.000	47.5	0.416	0.2
BV0112	I	10/03/23	BAD	X	X	0.561	0.0
BV0112	I	10/03/23	BAD	X	X	0.559	0.0
BV0112	V	10/03/08	5.136	0.243	53.4	0.430	0.8
BV0112	V	10/03/14	0.279	0.991	106.5	0.411	0.3
BV0112	V	10/03/23	BAD	X	X	0.543	0.0
FI0110	A	10/01/10	0.108	0.993	35.4	0.762	3.2
FI0110	A	10/01/10	BAD	X	X	0.761	0.0
FI0110	A	12/01/10	0.118	0.986	59.8	0.360	1.6
FI0110	A	18/01/10	0.139	0.979	35.4	0.393	1.0
FI0110	A	18/01/10	0.147	0.966	29.7	0.388	1.0
FI0110	A	25/01/10	0.140	0.975	35.4	0.405	1.1
FI0110	A	25/01/10	0.160	0.988	45.3	0.398	0.9
FI0110	A	25/01/10	0.175	0.995	126.7	0.394	1.0
FI0110	A	02/02/10	0.161	0.989	45.3	0.416	0.9
FI0110	A	02/02/10	0.156	0.985	35.4	0.411	1.0
FI0110	A	02/02/10	0.201	0.982	40.6	0.407	0.9
FI0110	A	08/02/10	0.179	0.991	40.6	0.457	0.9
FI0110	A	08/02/10	0.205	0.985	40.6	0.454	0.9
FI0110	A	17/02/10	0.176	0.984	35.4	0.456	1.0
FI0110	A	17/02/10	0.213	0.966	26.9	0.453	0.8

*X: Not recorded. *: Variable*

Table C.3 – continued from previous page

Crust	**L**	**Date**	λ	R^2	**Δt**	**P**	**ΔT**
FI0110	A	28/02/10	0.208	0.969	47.5	0.484	0.8
FI0110	A	28/02/10	0.201	0.963	32.0	0.478	0.7
FI0110	A	09/03/10	0.192	0.984	45.3	0.039	0.9
FI0110	A	09/03/10	0.292	0.935	21.1	0.448	0.8
FI0110	A	15/03/10	0.212	0.991	56.9	0.435	0.6
FI0110	A	15/03/10	0.236	0.981	40.6	0.434	0.6
FI0110	A	10/03/22	0.222	0.901	17.2	0.477	0.8
FI0110	A	10/03/22	0.261	0.986	49.6	0.480	0.6
FI0110	A	10/03/28	BAD	X	X	0.000	0.0
FI0110	A	10/03/28	0.356	0.932	36.7	0.449	0.5
FI0110	A	10/04/07	0.354	0.918	27.9	0.503	0.7
FI0110	A	10/04/14	0.320	0.716	12.1	0.499	0.7
FI0110	A	10/04/14	BAD	X	X	0.475	0.0
FI0110	B	10/01/10	0.046	1.000	32.0	0.764	2.8
FI0110	B	10/01/10	0.040	0.999	50.0	0.762	4.3
FI0110	B	12/01/10	0.089	0.986	59.8	0.355	1.8
FI0110	B	12/01/10	0.096	0.986	29.7	0.352	1.4
FI0110	B	18/01/10	0.157	0.983	91.3	0.383	1.4
FI0110	B	18/01/10	0.104	0.991	35.4	0.378	1.2
FI0110	B	25/01/10	0.131	0.997	126.7	0.387	1.1
FI0110	B	25/01/10	0.129	0.991	35.4	0.382	1.1
FI0110	B	02/02/10	0.168	0.981	35.4	0.404	0.9

*X: Not recorded. *: Variable*

Table C.3 – continued from previous page

Crust	**L**	**Date**	λ	R^2	**Δt**	**P**	**ΔT**
FI0110	B	02/02/10	0.162	0.981	29.7	0.401	1.0
FI0110	B	02/02/10	0.161	0.987	40.6	0.399	0.9
FI0110	B	02/02/10	0.134	0.994	49.6	0.397	1.1
FI0110	B	08/02/10	0.166	0.989	35.4	0.450	1.0
FI0110	B	08/02/10	0.170	0.987	35.4	0.447	1.0
FI0110	B	17/02/10	0.148	0.996	34.7	0.449	0.7
FI0110	B	17/02/10	0.215	0.979	26.9	0.447	1.0
FI0110	B	28/02/10	0.200	0.995	24.8	0.469	0.6
FI0110	B	28/02/10	BAD	X	X	0.483	0.0
FI0110	B	09/03/10	0.275	0.916	26.6	0.441	0.7
FI0110	B	09/03/10	0.206	0.997	73.6	0.440	0.6
FI0110	B	15/03/10	0.216	0.990	53.4	0.439	0.6
FI0110	B	15/03/10	0.221	0.982	40.9	0.424	0.6
FI0110	B	10/03/22	0.296	0.977	40.6	0.483	0.6
FI0110	B	10/03/28	0.553	0.851	33.3	0.453	0.6
FI0110	B	10/03/28	0.489	0.840	35.4	0.457	0.5
FI0110	B	10/04/07	0.428	0.911	29.7	0.504	0.6
FI0110	B	10/04/14	0.467	0.960	45.3	0.493	0.5
FI0110	B	10/04/14	0.275	0.996	66.6	0.489	0.4
FI0110	I	08/02/10	0.188	0.985	48.3	0.444	0.9
FI0110	I	17/02/10	0.219	0.942	24.3	0.444	0.7
FI0110	I	28/02/10	0.175	0.976	21.8	0.476	0.7

*X: Not recorded. *: Variable*

Table C.3 – continued from previous page

Crust	**L**	**Date**	λ	R^2	**Δt**	**P**	**ΔT**
FI0110	I	28/02/10	0.209	0.981	19.4	0.472	0.8
FI0110	I	09/03/10	0.265	0.971	49.6	0.436	0.7
FI0110	I	09/03/10	BAD	X	X	0.437	0.0
FI0110	I	15/03/10	0.221	0.992	48.3	0.445	0.6
FI0110	I	15/03/10	0.282	0.805	16.3	0.441	0.6
FI0110	I	10/03/22	0.279	0.970	35.4	0.484	0.6
FI0110	I	10/03/22	0.258	0.976	40.6	0.480	0.7
FI0110	I	10/03/28	BAD	X	X	0.489	0.0
FI0110	I	10/03/28	0.843	0.593	40.6	0.470	0.6
FI0110	I	10/04/07	0.220	0.895	14.8	0.483	0.7
FI0110	I	10/04/14	BAD	X	X	0.477	0.0
FI0110	I	10/04/14	0.421	0.969	37.1	0.484	0.6
FI0308	A	10/03/15	0.106	0.997	47.5	0.445	1.1
FI0308	A	10/03/15	0.074	0.998	47.5	0.443	1.5
FI0308	A	10/03/22	0.115	0.993	35.4	0.505	1.3
FI0308	A	10/03/22	0.122	0.996	47.5	0.501	1.1
FI0308	A	10/03/28	0.130	0.999	76.1	0.506	0.9
FI0308	A	10/03/28	0.166	0.996	47.5	0.504	1.0
FI0308	A	10/04/07	0.203	0.949	17.1	0.501	0.8
FI0308	A	10/04/14	0.262	0.941	26.9	0.484	0.7
FI0308	A	10/04/14	0.290	0.954	35.4	0.485	0.7
FI0308	B	10/03/15	0.088	0.995	29.7	0.438	1.4

*X: Not recorded. *: Variable*

Table C.3 – continued from previous page

Crust	**L**	**Date**	λ	R^2	**Δt**	**P**	**ΔT**
FI0308	B	10/03/15	0.098	0.993	35.4	0.436	1.3
FI0308	B	10/03/22	0.143	0.985	23.3	0.496	1.1
FI0308	B	10/03/22	0.163	0.981	29.7	0.494	1.1
FI0308	B	10/03/28	0.158	0.981	29.7	0.502	1.2
FI0308	B	10/03/28	BAD	X	X	0.000	0.0
FI0308	B	10/04/07	0.243	0.980	35.4	0.503	0.8
FI0308	B	10/04/14	0.301	0.940	29.7	0.480	0.8
FI0308	B	10/04/14	0.256	0.956	35.4	0.479	0.8
FI0308	I	10/03/15	0.055	0.998	35.4	0.441	0.9
FI0308	I	10/03/15	0.239	0.966	35.4	0.439	1.0
FI0308	I	10/03/22	0.183	0.923	11.9	0.494	1.7
FI0308	I	10/03/22	0.204	0.980	35.4	0.498	1.3
FI0308	I	10/03/28	0.186	0.984	35.4	0.497	1.3
FI0308	I	10/03/28	2.103	0.024	8.6	0.503	1.6
FI0308	I	10/04/07	0.178	0.990	40.6	0.504	1.2
FI0308	I	10/04/14	0.133	0.943	13.2	0.483	2.0
FI0308	I	10/04/14	0.218	0.985	40.6	0.478	1.1
FI0308	V	10/03/15	0.102	0.994	35.4	0.451	1.1
FI0308	V	10/03/22	0.170	0.969	40.1	0.490	1.3
FI0308	V	10/03/28	0.290	0.916	34.3	0.480	1.0
FI0308	V	10/03/28	0.173	0.951	31.2	0.465	1.1
FI0308	V	10/04/07	0.180	0.965	12.1	0.740	1.2

*X: Not recorded. *: Variable*

Table C.3 – continued from previous page

Crust	**L**	**Date**	λ	R^2	**Δt**	**P**	**ΔT**
FI0308	V	10/04/14	0.233	0.933	23.3	0.481	0.6
FI0308	V	10/04/14	0.540	0.796	19.9	0.485	0.6
RP0112	A	10/01/19	0.100	0.975	29.7	0.395	1.4
RP0112	A	10/01/25	0.137	0.988	91.3	0.385	1.5
RP0112	A	10/02/02	0.144	0.989	45.3	0.404	1.0
RP0112	A	10/02/02	0.123	0.994	45.3	0.399	1.1
RP0112	A	10/02/09	0.129	0.996	47.5	0.446	1.0
RP0112	A	10/02/09	0.112	0.995	38.9	0.441	1.0
RP0112	A	10/02/15	0.118	0.993	18.2	0.430	0.7
RP0112	A	10/02/15	0.169	0.986	40.6	0.424	0.8
RP0112	A	10/02/27	0.199	0.973	29.7	0.470	1.0
RP0112	A	10/02/27	0.172	0.986	35.4	0.449	1.0
RP0112	A	10/03/08	0.164	0.992	35.4	0.431	0.8
RP0112	A	10/03/08	0.195	0.990	47.5	0.432	0.8
RP0112	A	10/03/14	0.193	0.993	57.0	0.434	0.8
RP0112	A	10/03/14	0.174	0.983	44.9	0.431	1.1
RP0112	A	10/03/23	0.330	0.979	57.0	0.534	0.9
RP0112	A	10/03/23	0.203	0.993	57.0	0.522	0.8
RP0112	A	10/03/29	1.107	0.863	46.6	0.534	0.2
RP0112	A	10/03/29	2.411	0.594	57.0	0.607	0.2
RP0112	A	10/03/29	BAD	X	X	0.561	0.0
RP0112	A	10/03/29	BAD	X	X	0.557	0.0

*X: Not recorded. *: Variable*

Table C.3 – continued from previous page

Crust	**L**	**Date**	λ	R^2	**Δt**	**P**	**ΔT**
RP0112	A	10/03/29	BAD	X	X	0.680	0.0
RP0112	A	10/04/06	BAD	X	X	0.482	0.0
RP0112	A	10/04/06	BAD	X	X	0.429	0.0
RP0112	A	10/04/13	0.267	0.991	103.8	0.550	1.6
RP0112	B	10/01/19	0.110	0.981	16.2	0.377	0.8
RP0112	B	10/01/25	0.154	0.989	91.3	0.369	1.2
RP0112	B	10/02/02	0.160	0.993	53.4	0.388	0.8
RP0112	B	10/02/02	0.158	0.991	45.3	0.385	0.9
RP0112	B	10/02/09	0.140	0.991	38.9	0.440	0.9
RP0112	B	10/02/09	0.125	0.991	17.8	0.436	0.8
RP0112	B	10/02/27	0.194	0.983	35.4	0.433	1.1
RP0112	B	10/02/27	0.196	0.978	35.4	0.431	0.8
RP0112	B	10/03/08	0.269	0.953	29.7	0.416	0.9
RP0112	B	10/03/08	0.228	0.985	47.5	0.415	0.8
RP0112	B	10/03/08	0.173	0.992	47.5	0.428	0.8
RP0112	B	10/03/08	0.147	0.992	47.5	0.420	0.9
RP0112	B	10/03/14	0.192	0.990	57.0	0.434	0.7
RP0112	B	10/03/14	0.196	0.992	57.0	0.426	0.6
RP0112	B	10/03/23	0.359	0.978	57.0	0.531	0.7
RP0112	B	10/03/23	0.408	0.965	47.5	0.521	0.7
RP0112	B	10/03/29	BAD	X	X	0.521	0.0
RP0112	B	10/03/29	BAD	X	X	0.513	0.0

*X: Not recorded. *: Variable*

Table C.3 – continued from previous page

Crust	**L**	**Date**	λ	R^2	**Δt**	**P**	**ΔT**
RP0112	B	10/03/29	BAD	X	X	0.522	0.0
RP0112	B	10/04/06	BAD	X	X	0.513	0.0
RP0112	B	10/04/06	BAD	X	X	0.500	0.0
RP0112	B	10/04/13	0.000	0.000	0.0	0.000	0.0
RP0112	I	10/01/19	0.087	0.990	29.7	0.390	1.6
RP0112	I	10/01/19	0.064	0.994	24.3	0.386	1.8
RP0112	I	10/01/19	0.154	0.987	35.4	0.383	1.0
RP0112	I	10/01/19	0.236	0.976	46.2	0.380	0.8
RP0112	I	10/01/25	0.106	0.992	91.3	0.379	1.8
RP0112	I	10/01/25	0.156	0.987	91.3	0.373	1.3
RP0112	I	10/02/02	0.124	0.995	45.3	0.393	1.1
RP0112	I	10/02/02	0.135	0.996	56.9	0.390	0.9
RP0112	I	10/02/09	0.098	0.996	38.9	0.446	1.1
RP0112	I	10/02/09	0.124	0.993	38.9	0.441	1.0
RP0112	I	10/02/09	0.058	0.998	47.5	0.434	1.6
RP0112	I	10/02/15	0.220	0.968	29.7	0.422	0.7
RP0112	I	10/02/15	0.239	0.989	47.5	0.421	0.8
RP0112	I	10/02/27	0.180	0.981	35.4	0.452	1.2
RP0112	I	10/02/27	0.076	0.992	23.3	0.437	2.0
RP0112	I	10/03/08	0.109	0.983	26.6	0.429	1.6
RP0112	I	10/03/08	0.142	0.995	47.5	0.423	1.0
RP0112	I	10/03/14	0.179	0.991	57.0	0.429	0.7

*X: Not recorded. *: Variable*

Table C.3 – continued from previous page

Crust	**L**	**Date**	λ	R^2	**Δt**	**P**	**ΔT**
RP0112	I	10/03/14	0.139	0.995	57.0	0.425	0.8
RP0112	I	10/03/23	BAD	X	X	0.528	0.0
RP0112	I	10/03/23	0.079	0.995	75.0	0.526	1.4
RP0112	I	10/03/29	BAD	X	X	0.519	0.0
RP0112	I	10/03/29	BAD	X	X	0.523	0.0
RP0112	I	10/04/06	BAD	X	X	0.487	0.0
RP0112	I	10/04/06	BAD	X	X	0.498	0.0
RP0112	I	10/04/13	0.000	0.000	0.0	0.000	0.0
RP0112	V	10/03/08	0.124	0.985	39.1	0.409	1.2
RP0112	V	10/03/08	0.117	0.978	29.4	0.411	1.7
RP0112	V	10/03/14	0.180	0.995	138.8	0.419	0.8
RP0112	V	10/03/14	0.213	0.979	81.8	0.416	1.0
RP0112	V	10/03/23	BAD	X	X	0.529	0.0
RP0112	V	10/03/23	0.204	0.990	114.6	0.568	1.1
RP0112	V	10/03/29	BAD	X	X	0.796	0.0
RP0112	V	10/04/06	BAD	X	X	0.484	0.0
RP0112	V	10/04/06	BAD	X	X	0.467	0.0
RP0112	V	10/04/13	0.000	0.000	0.0	0.000	0.0
LAB0312	I	13 12:00	BAD	X	X	0.432	0.0
LAB0312	I	13 12:37	0.089	0.919	9.0	0.433	0.3
LAB0312	I	13 12:51	0.141	0.890	4.4	0.425	0.3
LAB0312	I	13 13:26	0.648	0.901	49.9	0.421	0.1

*X: Not recorded. *: Variable*

Table C.3 – continued from previous page

Crust	**L**	**Date**	λ	R^2	**Δt**	**P**	**ΔT**
LAB0312	I	13 14:05	0.276	0.969	40.0	0.413	0.2
LAB0312	I	13 15:10	0.142	0.996	52.1	0.421	0.7
LAB0330	A	30 09:30	BAD	X	X	0.569	0.0
LAB0330	B	30 09:30	BAD	X	X	0.559	0.0
LAB0330	I	30 09:30	BAD	X	X	0.567	0.0
LAB0330	I	30 09:30	BAD	X	X	0.562	0.0
LAB0330	V	30 09:30	0.094	0.769	4.6	0.555	3.0
LAB0330	V	30 10:30	0.034	0.995	13.2	0.546	1.6
LAB0330	V	30 10:30	0.065	0.979	13.2	0.541	0.8
LAB0330	V	30 12:20	0.285	0.979	31.2	0.571	0.3
LAB0330	V	30 12:20	BAD	X	X	0.565	0.0
LAB0330	V	30 14:12	0.249	0.927	19.2	0.527	0.3
LAB0330	V	30 14:12	BAD	X	X	0.522	0.0
LAB0330	V	30 16:55	0.122	0.987	71.3	0.527	1.8
LAB0330	V	30 16:55	0.193	0.975	83.8	0.521	1.9
LAB0330	V	30 21:50	0.236	0.989	85.7	0.546	1.5
LAB0330	V	30 21:50	0.250	0.978	81.8	0.538	1.6
LAB0330	V	31 07:25	0.000	0.000	0.0	0.000	0.0
LAB0330	V	31 07:25	0.000	0.000	0.0	0.000	0.0
LAB0409	V	10 13:00	BAD	X	X	0.486	0.0
LAB0409	V	09 13:00	0.072	0.816	4.6	0.496	2.5
LAB0409	V	09 19:35	BAD	X	X	0.491	0.0

*X: Not recorded. *: Variable*

Table C.3 – continued from previous page

Crust	**L**	**Date**	λ	R^2	**Δt**	**P**	**ΔT**
LAB0409	V	09 19:35	0.690	0.910	45.2	0.491	0.4
LAB0409	V	10 01:15	0.136	0.995	52.1	0.499	0.8
LAB0409	V	10 01:15	0.252	0.963	40.0	0.497	0.4
LAB0409	V	10 08:20	0.130	0.988	17.8	0.471	1.1
LAB0409	V	10 08:20	0.286	0.971	81.8	0.480	1.5
LAB0409	V	10 14:30	0.270	0.979	81.8	0.496	1.2
LAB0410	V	10 19:15	0.058	0.997	47.0	-0.282	3.3
LAB0410	V	10 19:15	0.025	1.000	52.1	0.533	2.8
LAB0410	V	11 09:30	0.081	0.967	25.2	0.521	1.7
LAB0410	V	11 09:30	0.178	0.988	95.9	0.523	1.6
LAB0410	V	11 21:00	0.277	0.966	69.1	0.518	1.8
LAB0410	V	11 21:00	0.302	0.987	109.1	0.515	1.2
LAB0410	V	12 09:40	BAD	X	X	0.511	0.0
LAB0410	V	12 09:40	0.269	0.780	71.3	0.460	1.6
LAB0410	V	12 21:05	0.225	0.986	54.8	0.517	1.4
LAB0410	V	12 21:05	0.246	0.987	109.1	0.512	1.9
LAB0410	V	13 09:35	0.273	0.987	100.5	0.550	1.7
LAB0410	V	13 09:35	0.409	0.000	91.1	0.546	1.7
LAB0413	V	10/04/13	0.080	0.997	50.3	0.520	1.7
LAB0413	V	10/04/13	BAD	X	X	0.514	0.0
LAB0413	V	10/04/14	BAD	X	X	0.559	0.0
LAB0413	V	10/04/14	0.293	0.968	91.1	0.538	0.7

*X: Not recorded. *: Variable*

Table C.3 – continued from previous page

Crust	**L**	**Date**	λ	R^2	**Δt**	**P**	**ΔT**
LAB0413	V	10/04/15	0.414	0.950	69.1	0.632	1.0
LAB0413	V	10/04/15	0.330	0.975	91.1	0.566	1.3
LAB0413	V	10/04/16	0.253	0.989	100.5	0.528	1.4
LAB0413	V	10/04/16	0.302	0.984	100.5	0.521	0.7
LAB0413	V	10/04/17	0.144	0.983	61.2	0.332	0.8
LAB0413	V	10/04/17	0.248	0.947	100.5	0.355	0.7
LAB0413	V	10/04/18	0.136	0.978	61.2	0.356	1.3
LAB0413	V	10/04/18	0.241	0.838	49.4	0.325	1.1
SR0131	A	10/02/03	0.080	0.987	16.3	0.488	2.4
SR0131	A	10/02/03	0.065	0.995	23.3	0.482	2.6
SR0131	A	10/02/10	0.044	0.998	34.3	0.431	2.3
SR0131	A	10/02/10	0.096	0.984	27.9	0.428	1.5
SR0131	A	10/02/17	0.099	0.992	27.9	0.463	1.6
SR0131	A	10/02/17	0.096	0.994	40.0	0.461	1.6
SR0131	A	10/03/02	BAD	X	X	0.467	0.0
SR0131	A	10/03/02	BAD	X	X	0.464	0.0
SR0131	A	10/03/09	BAD	X	X	0.464	0.0
SR0131	A	10/03/09	BAD	X	X	0.460	0.0
SR0131	A	10/03/22	BAD	X	X	0.521	0.0
SR0131	A	10/03/22	BAD	X	X	0.510	0.0
SR0131	A	10/03/28	0.000	0.000	0.0	0.000	0.0
SR0131	A	10/04/07	BAD	X	X	0.000	0.0

*X: Not recorded. *: Variable*

Table C.3 – continued from previous page

Crust	**L**	**Date**	λ	R^2	**Δt**	**P**	**ΔT**
SR0131	B	10/02/03	0.149	0.974	23.3	0.470	1.5
SR0131	B	10/02/03	0.142	0.985	23.3	0.467	1.5
SR0131	B	10/02/10	0.073	0.994	23.3	0.421	1.6
SR0131	B	10/02/10	0.080	0.931	13.2	0.419	1.9
SR0131	B	10/02/17	0.165	0.970	23.3	0.454	1.2
SR0131	B	10/02/17	0.131	0.994	47.5	0.452	1.0
SR0131	B	10/03/02	3.640	0.491	70.1	0.461	0.5
SR0131	B	10/03/02	1.727	0.634	52.1	0.459	0.6
SR0131	B	10/03/09	BAD	X	X	0.451	0.0
SR0131	B	10/03/09	BAD	X	X	0.448	0.0
SR0131	B	10/03/22	BAD	X	X	0.503	0.0
SR0131	B	10/03/22	BAD	X	X	0.500	0.0
SR0131	B	10/03/28	0.000	0.000	0.0	0.000	0.0
SR0131	B	10/04/07	BAD	X	X	0.000	0.0
SR0131	I	10/02/03	0.714	0.459	8.6	0.478	1.7
SR0131	I	10/02/03	0.148	0.939	16.3	0.474	1.6
SR0131	I	10/02/10	0.311	0.625	13.2	0.426	1.2
SR0131	I	10/02/10	0.109	0.924	10.9	0.423	1.2
SR0131	I	10/02/17	0.158	0.971	23.3	0.458	1.5
SR0131	I	10/02/17	0.175	0.981	34.3	0.456	1.3
SR0131	I	10/03/02	0.000	0.000	0.0	0.000	0.0
SR0131	I	10/03/09	BAD	X	X	0.454	0.0

*X: Not recorded. *: Variable*

Table C.3 – continued from previous page

Crust	**L**	**Date**	λ	R^2	**Δt**	**P**	**ΔT**
SR0131	I	10/03/09	BAD	X	X	0.448	0.0
SR0131	I	10/03/22	BAD	X	X	0.155	0.0
SR0131	I	10/03/22	BAD	X	X	0.505	0.0
SR0131	I	10/03/28	BAD	X	X	0.525	0.0
SR0131	I	10/03/28	0.134	0.976	23.3	0.529	0.3
SR0131	I	10/03/28	0.055	0.999	36.7	0.516	1.9
SR0131	I	10/04/07	BAD	X	X	0.000	0.0
SR0210	A	10/02/10	0.000	0.000	0.0	0.000	0.0
SR0210	A	10/02/17	0.092	0.990	24.5	0.474	2.0
SR0210	A	10/02/17	0.091	0.982	17.2	0.471	2.1
SR0210	A	10/03/02	BAD	X	X	0.475	0.0
SR0210	A	10/03/02	0.082	0.995	34.3	0.470	1.9
SR0210	A	10/03/09	0.022	0.997	47.5	0.468	2.0
SR0210	A	10/03/09	BAD	X	X	0.464	0.0
SR0210	A	10/03/22	BAD	X	X	0.522	0.0
SR0210	A	10/03/22	BAD	X	X	0.518	0.0
SR0210	A	10/03/28	0.000	0.000	0.0	0.000	0.0
SR0210	A	10/04/07	0.000	0.000	0.0	0.000	0.0
SR0210	B	10/02/10	0.044	0.998	34.3	0.431	2.3
SR0210	B	10/02/10	0.096	0.984	27.9	0.428	1.5
SR0210	B	10/02/17	0.099	0.992	27.9	0.463	1.6
SR0210	B	10/02/17	0.096	0.994	40.0	0.461	1.6

*X: Not recorded. *: Variable*

Table C.3 – continued from previous page

Crust	**L**	**Date**	λ	R^2	**Δt**	**P**	**ΔT**
SR0210	B	10/03/02	BAD	X	X	0.467	0.0
SR0210	B	10/03/02	BAD	X	X	0.464	0.0
SR0210	B	10/03/09	BAD	X	X	0.464	0.0
SR0210	B	10/03/09	BAD	X	X	0.460	0.0
SR0210	B	10/03/22	BAD	X	X	0.521	0.0
SR0210	B	10/03/22	BAD	X	X	0.510	0.0
SR0210	B	10/03/28	0.000	0.000	0.0	0.000	0.0
SR0210	B	10/04/07	BAD	X	X	0.000	0.0
SR0210	I	10/02/10	0.225	0.726	13.2	0.438	1.3
SR0210	I	10/02/10	0.209	0.881	5.7	0.434	1.1
SR0210	I	10/02/17	0.134	0.992	47.6	0.468	1.1
SR0210	I	10/02/17	0.098	0.981	13.2	0.465	1.8
SR0210	I	10/03/02	0.000	0.000	0.0	0.000	0.0
SR0210	I	10/03/09	BAD	X	X	0.465	0.0
SR0210	I	10/03/09	0.028	0.992	8.6	0.478	2.9
SR0210	I	10/03/28	BAD	X	X	0.525	0.0
SR0210	I	10/03/28	0.134	0.976	23.3	0.529	0.3
SR0210	I	10/03/28	0.055	0.999	36.7	0.516	1.9
SR0210	I	10/04/07	BAD	X	X	0.000	0.0
SR09	I	10/02/05	0.081	0.992	23.3	0.458	2.2
SR09	I	10/02/05	0.087	0.995	47.5	0.451	1.7
SR09	I	10/02/05	0.115	0.993	29.7	0.446	1.5

*X: Not recorded. *: Variable*

Table C.3 – continued from previous page

Crust	**L**	**Date**	λ	R^2	**Δt**	**P**	**ΔT**
SR09	I	10/02/05	0.093	0.968	16.3	0.441	1.8
SR09	I	10/02/05	0.084	0.992	23.3	0.437	1.9
SR09	I	10/02/05	0.114	0.974	23.3	0.420	1.8
SR09	I	10/02/05	0.111	0.993	35.4	0.434	1.3
SR09	I	10/02/05	0.092	0.988	23.3	0.430	1.5
SR09	I	10/02/05	0.113	0.982	23.3	0.428	1.5
SR09	I	10/02/05	0.085	0.963	8.6	0.427	2.2
SR09	I	10/02/05	0.165	0.982	35.4	0.423	1.2